THE UNIVERSITY OF QUEENSLAND

AUSTRALIA

Investigation of Pre-Combustion Shock Trains in a Scramjet Using a Shock Tunnel at Mach 8 Flight Conditions

Andrew Noel Ridings
B.Eng (Aerospace) (Hons 1) *UNSW*

A thesis submitted for the degree of Doctor of Philosophy at
The University of Queensland in 2014
School of Mechanical and Mining Engineering

Abstract

One of the major challenges to scramjet propulsion is the ability to operate over a wide range of Mach numbers. The dual-mode scramjet has the advantage that it can operate much like a ramjet at low Mach numbers, with subsonic flow entering the combustion chamber, and as a conventional scramjet at higher Mach numbers where the flow remains supersonic throughout the engine. A dual-mode scramjet is able to operate as a ramjet by allowing a shock train to form in the section between the inlet and combustor known as the isolator. This pre-combustion shock train, which is a series of intersecting shock and expansion waves, provides additional compression of the flow allowing subsonic flow to be supplied to the combustion chamber.

Free-piston shock tunnels, such as Stalker Tubes, are typically used to test scramjet engines due to the high enthalpy flows which these facilities can produce. However these impulse type wind tunnels have short test times of the order of milliseconds. As the pre-combustion shock train involves large regions of separated flow, which take longer than attached flow to establish, there is some question as to whether dual mode can be modelled in Stalker Tubes.

This work investigates whether pre-combustion shock trains can be studied in shock tunnels at the upper end of the dual-mode regime and if so, how this phenomenon affects scramjet performance. Experiments were conducted in the T4 Stalker Tube at The University of Queensland at a condition which represents flight at Mach 8 at an altitude of 26 km. This corresponds to a dynamic pressure of 105 kPa and a total enthalpy of 3.1 MJ kg^{-1}.

The experiments were conducted using a simple axi-symmetric scramjet, which comprised a short inlet, an isolator, fuel injectors and three interchangeable combustion chambers. The set of combustion chambers consisted of a constant area and two divergent combustors with half-cone angles of 1° and 2°. The different combustion chambers were tested to assess the effect which area expansion has on the shock train and on the overall combustion efficiency of the engine. The model was arranged in a semi-direct connect configuration to produce the desired conditions at the isolator entrance. Gaseous hydrogen was used as the fuel and was injected via six port-hole injectors equally spaced around the circumference. Wall static pressures were measured along the isolator and combustor walls. A quasi-one-dimensional cycle analysis code,

which is capable of modelling separated flow, is used to model the flow through the engine and provides estimates of the combustion efficiency and distribution of heat release.

Robust combustion was observed in the experiments over a range of fuel equivalence ratios between 0.5 and 1.35, for all three combustor configurations. Results for the constant area combustor show that at an equivalence ratio approximately equal to 0.7 the boundary layer separates due to the pressure rise generated from combustion, forming a shock train upstream of fuel injection. With increasing equivalence ratio the shock train grows in scale. The transient data reveal that there is sufficient time for the shock train to establish at equivalence ratios at or below 1.35. This is indicated by the steady pressure at the rear of isolator. At equivalence ratios above 1.35, the pressure in the rear of the isolator never reaches a steady level and for these cases the test time is not sufficiently long for the shock train to establish. The transient characteristics of the shock train are similar for all three combustors with the initial separation occurring at similar fuelling levels. The pressure distributions also show that the shock train length and position are similar for all three combustors. This indicates that the area divergence of the two divergent combustors does not have an effect on pre-combustion shock train for this engine.

Cycle analysis of the experimental data reveals a number of aspects. First, for lean mixtures up to an equivalence ratio of 0.9, all three combustors have combustion efficiencies around 100%. Above this there is a steady decrease in combustion efficiency. For the non-separated cases, the combustion length is similar to the combustion chamber length. However, for the separated cases, there is a dramatic shortening of the combustion length. This indicates that the shock train improves combustion through higher compression of the combustor inflow but also through enhanced mixing. The results from the cycle analysis reveal that for the separated cases both the reattachment point and point of complete combustion are well upstream of the divergence point of both divergent combustors. This is consistent with the observation from the experiments that the area divergence had no effect on the shock train for either of the divergent combustors.

Declaration by author

This thesis is composed of my original work, and contains no material previously published or written by another person except where due reference has been made in the text. I have clearly stated the contribution by others to jointly-authored works that I have included in my thesis.

I have clearly stated the contribution of others to my thesis as a whole, including statistical assistance, survey design, data analysis, significant technical procedures, professional editorial advice, and any other original research work used or reported in my thesis. The content of my thesis is the result of work I have carried out since the commencement of my research higher degree candidature and does not include a substantial part of work that has been submitted to qualify for the award of any other degree or diploma in any university or other tertiary institution. I have clearly stated which parts of my thesis, if any, have been submitted to qualify for another award.

I acknowledge that an electronic copy of my thesis must be lodged with the University Library and, subject to the policy and procedures of The University of Queensland, the thesis be made available for research and study in accordance with the Copyright Act 1968 unless a period of embargo has been approved by the Dean of the Graduate School.

I acknowledge that copyright of all material contained in my thesis resides with the copyright holder(s) of that material. Where appropriate I have obtained copyright permission from the copyright holder to reproduce material in this thesis.

Publications during candidature

Conference Papers

Ridings, A.N. and Smart, M.K. (2009)
"Experimental Studies of Divergent Supersonic Combustors." In *47th AIAA Aerospace Sciences Meeting including the New Horizons Forum and Aerospace Exposition, Orlando, FL, United States of America*, 2009. AIAA-2009-1425.

Mee, D.J.; Stalker, R.J.; Suraweera, M.V.; Tanimizu, K., Kirchhartz, R.M., Ridings, A.N. and **Chan, W.Y.K.** (**2008**) .
"Force measurements and drag reduction." In *Proceedings of the Australian Hypersonics Capabilities and Future Directions Workshop, Brisbane, QLD, Australia, 2008*.

Conference Presentations

Ridings, A.N. (2012)
"UQ's T4 Shock Tunnel Data Acquisition System." At the *2012 National Instruments Technical Symposium, Brisbane, QLD, Australia, 23rd February 2012*.

Ridings, A.N. (2006)
"Scramjet Experiments Using Divergent Circular Combustors." At the *10th International Workshop on Shock Tube Technology, The University of Queensland, Brisbane, QLD, Australia, 2nd – 3rd November* 2006.

Publications included in this thesis

No publications included.

Contributions by others to the thesis

- Design of the diffuser flow field - Michael K. Smart - 100%
- CFD simulation of the diffuser flow field - Michael K. Smart - 100%
- CFD simulation of the Mach 4 nozzle flow field - Philipe Lorrain - 100%
- Interpretation of cycle analysis results - Michael K. Smart - 20%

Statement of parts of the thesis submitted to qualify for the award of another degree

None.

Acknowledgements

This thesis represents the culmination of a long and hard journey with many trials and tribulations. I would not have made it to the end without the kind support of a great many people.

I would first like to acknowledge and thank my supervisor Professor Michael Smart for taking me on as his student, sharing his knowledge, providing support and endless encouragement. A particular thank you for reading those very rough early drafts. You've help me find my way in a number of respects.

I would also like to acknowledge and thank my associate supervisor Professor David Mee for always making the time to provide advice and support, particularly at critical times.

Thank you to Keith Hitchcock for all your support and guidance during my multiple T4 campaigns. You definitely go beyond the call of duty.

I must say a big thank you to my fellow T4 tunnel operators: Rainer, Katsu, James, Sarah, Tom, Wilson, Luke, Philipe, Arman and Daniel. It is a hard beast but you all tamed it well. Thank you and apologies to all my office buddies over the years: Rainer, Sarah, Tom, Katsu, Jenny, Wilson, Luke, Ben, Kevin and Zac. Thank you for your patience and tolerance and the many thoughtful discussions. A special thank you to Rainer: you really lifted the bar and by doing so challenged me to become a better scientist. Another special thank you to Ben Shoesmith who provided many great conversations on the absurdities of human behaviour and those infernal shock boundary layer interactions. You re-instilled a passion for the theoretical side of my work. Mark and Wilson, thank you to you both for lending a kind ear and your encouragement along the way.

A general thank you to everyone in the wider Centre for Hypersonics. It is a great community we have here which fosters some great discussions and interesting science. Specifically I wish to thank some people who have gone out of their way to help me out: Rainer Kirchhartz, Wilson Chan, Mark Bateup, Philippe Lorain, Paul van Staden, Sarah Razzaqi, Luke Doherty, Dhananjay Gangurde, James Turner, Fabian Zander,

Sandy Tirtey, Andrew Dann, Milinda Suraweera, Greg Fairburn, and Troy Eichmann.

And thank you to all the guys in the machine and electrical workshops. I appreciate the great work you do and your valued advice in the design process. Thank you to Brianne and Katie in the school office for going into bat for me on more than one occasion.

Thank you to the School of Mechanical and Mining Engineering and to University of Queensland for the scholarships that supported my study.

To my many many many flatmates over the years. Thank you for putting up with a tired, greasy, exhausted, sometimes dejected, non-existent flatmate when I was in the tunnel. I hope the good times more than just balanced out those days.

To my dear friends, whom I am very lucky to have such wonderful people to call my friends. Thank you to the Graceville crew for all those wonderful dinners and get-togethers. Thank you Matt for sharing such fine wine with such fine company with me. To Nick thank you for dragging me out of Brisbane suburbia to the city for some good fun nights out. To the Stanfran alumni, thank you for keeping me young at heart. A special thank you to my dear friend Sita for taking me into the other worlds of Brisbane. I don't think you realise how much our time together kept things in perspective for me. To Kirsty: you were my lifeline at some of the toughest times. Thank you for being on the other end of the phone with always very wise words. A very special thank you to David who saw me first hand through my highs and lows at lunch. Thank you for forcing me to take a break each day and suffering through my tribulations with me.

And finally, a most loving thank you to my family. Thank you to my sister Joanna for your words of support and encouragement. A dear thank you to my mother and father. I cannot begin to say how grateful I am for all your love and support throughout not just my studies but all my life. I would not have made it without you being there always.

Keywords

dual-mode scramjet, pre-combustion shock train, shock tunnel, hypersonics, airbreathing propulsion

Australian and New Zealand Standard Research Classifications (ANZSRC)

ANZSRC code: 090107, Hypersonic Propulsion and Hypersonic Aerodynamics 100%

Field of Research (FoR) Classification

FoR code: 0901, Aerospace Engineering 100%

"For what then matters is to bear witness to the uniquely human potential at its best, which is to transform a personal tragedy into a triumph, to turn one's predicament into a human achievement." – Viktor E. Frankl

Contents

Abstract **ii**

List of Figures **xvii**

List of Tables **xxvii**

Nomenclature **xxxi**

1 Introduction **1**

1.1 Research Aims 7

1.2 Thesis Outline 7

2 Literature Review **9**

2.1 Shock Train and Pseudo-Shock Experiments 9

2.1.1 Shock trains and non-circular cross sections 23

2.1.2 Shock trains and asymmetric boundary layers 23

2.1.3 Oscillatory nature of shock trains 24

2.1.4 Flow establishment times for shock-trains and pseudo-normal-shock 26

2.2 Pseudo-Shock and Shock Train Analytical Models 28

2.3 Scramjet Ground Test Facilities 31

2.4 Shock Trains and Combustion 33

2.4.1 Pre-combustion shock trains and shock tunnel testing 42

2.5 Summary 45

3 Experimental Apparatus and Methodology **47**

3.1 Model 47

3.1.1 Diffuser 48

3.1.2 Isolator 51

3.1.3 Combustion chambers 52

3.1.4 Model instrumentation 53

3.1.5 Fuel system 57

3.1.6 Mounting and shielding 61

3.2 The T4 Stalker Tube 64

3.2.1 Operating principle 65

3.2.2 Tunnel instrumentation 67

3.2.3 M4 nozzle 68

3.3 Test Flow Conditions 75

3.3.1 Calculation of freestream properties 77

3.3.2 Boundary layer analysis through the diffuser 79

3.4 Data Reduction 79

3.4.1 Test time 79

3.4.2 Uncertainty analysis 83

3.4.3 Repeatability 84

4 Experimental Results **87**

4.1 Investigation of Separated Flow Establishment 87

4.1.1 Conventional test time window 87

4.1.2 Isolator pressure traces for non-separated cases 89

4.1.3 Combustion chamber pressure traces for non-separated cases . . 94

4.1.4 Isolator pressure traces for separated cases at moderate ϕ 95

4.1.5 Combustion chamber pressure traces for separated cases at moderate ϕ . . . 98
4.1.6 Isolator pressure traces for cases at high ϕ . . . 99
4.1.7 Combustion pressure traces for cases at high ϕ . . . 101
4.1.8 Methodology for determining establishment time of separated flow . . . 103
4.1.9 Establishment time versus shock train length . . . 106
4.1.10 Establishment time versus equivalence ratio . . . 106
4.1.11 Separation time for the furthest downstream isolator sensor . . . 106
4.1.12 Summary of establishment times . . . 112
4.2 Pressure Distributions . . . 113
4.2.1 Constant area combustor . . . 113
4.2.2 2° divergent combustor . . . 120
4.2.3 1° divergent combustor . . . 126
4.3 Shock Train Characteristics . . . 134
4.3.1 Shock train length versus isolator exit pressure . . . 134
4.3.2 Isolator exit pressure versus equivalence ratio . . . 134
4.3.3 Shock train length versus equivalence ratio . . . 135
4.3.4 Summary of shock train characteristics . . . 136
4.4 Summary and Conclusions . . . 137

5 Cycle Analysis Methodology and Results **139**

5.1 Dual-mode Cycle Analysis Methodology . . . 139
5.1.1 Combustion model . . . 140
5.1.2 Ortwerth's diffuser model . . . 141
5.1.3 Code logic . . . 142
5.1.4 Parameter selection and optimisation . . . 142

5.2 Dual-mode Cycle Analysis Results 143
5.2.1 Constant area combustor 143
5.2.2 2° divergent combustor 154
5.2.3 1° divergent combustor 160
5.2.4 Separation characteristics and key Mach numbers 163
5.2.5 Trends in combustion efficiency, air-based combustion efficiency and mixing-length 164
5.3 Summary and Conclusions 169

6 Conclusions **171**
6.1 Recommendations for Future Studies 175

References **179**

A Additional Theory and Results **199**
A.1 Aerothermodynamics of Dual Mode Scramjets 199
A.2 Chemical Reaction Kinetics 204
A.3 Hydrogen-Oxygen Reaction Scheme 207
A.4 CFD of Mach 4 nozzle 208
A.5 Shock Train Characteristics 210
A.5.1 Location of the leading edge of the shock train 210
A.5.2 Shock train establishment time versus equivalence ratio for the divergent combustors 211
A.5.3 Isolator exit pressure versus equivalence ratio 212
A.5.4 Shock train length versus isolator exit pressure 213
A.5.5 Shock train length versus equivalence ratio 215
A.6 Propagation Rate of Separation 217

B Fuel System **219**

B.1 Calculation of Fuel Mass Flow Rate 219

B.2 Effect of Pre-Test Fuel on Data Reduction 221

B.3 Jet Penetration Parameter Model 223

C Uncertainty and Repeatability **225**

C.1 Uncertainties in the Freestream Test Conditions 225

C.2 Uncertainties in the Fuelling Conditions 227

C.3 Repeatability of Test Conditions 229

C.4 Repeatability of Flow Phenomena 230

D Experimental Runs **233**

E Cycle Analysis Optimisation **239**

E.1 Optimisation of Performance Parameters 239

E.1.1 Constant area combustor 239

E.1.2 2° divergent combustor 245

E.1.3 1° divergent combustor 247

E.1.4 High sensitivity to combustion efficiency and Mach number . . . 249

E.1.5 Non-established maximum fuelling cases 251

E.2 Discussion on Mixing Curves 253

F Technical Drawings **259**

List of Figures

1.1 Typical transatmospheric accelerator trajectory. 2

1.2 Schematic of a conventional ramjet, dual-mode ramjet and scramjet. . . 5

2.1 Sketch of a normal shock wave/turbulent boundary layer interaction in a constant area duct from Matsuo et al. (1999)). 10

2.2 Schlieren photograph showing a shock train in a rectangular duct ($M_i = 1.75$) from Ikui and Matsuo (1969). 11

2.3 Schlieren photographs from Carroll and Dutton (1990) for a Mach 1.6 flow with increasing flow confinement by the boundary layer (δ/H). . . 12

2.4 Static pressure distributions and flow structure sketch for a shock train in constant area duct from Matsuo et al. (1999). 14

2.5 Simplified representation of shock structure of a shock train and comparison with Pitot pressure surveys from Waltrup and Billig (1973). . . . 15

2.6 Experimental results from Waltrup and Billig (1973) illustrating the superposition of the shock structure in a cylindrical duct. 16

2.7 Pseudo-shock model by Tamaki et al. (1971). 18

2.8 Waltrup and Cameron's (1974) shock train experiment 18

2.9 Schematic of static pressure along centreline and wall of pseudo-normal-shock in a duct from Matsuo et al. (1999). 20

2.10 Sketch of the flow re-acceleration and deceleration processes inside a shock train from Carroll and Dutton (1992). 21

2.11 Colour schlieren photographs of a shock train from Sugiyama et al. (2006). 22

2.12 Shockless model of pseudo-shock by Crocco (1958). 29

2.13 Validation data for the Ortwerth (2000) diffusion model for the length of a pseudo-normal-shock. 31

2.14 Application of the Ortwerth (2000) diffusion model using Smart's (2007) methodology to data from Kobayashi et al. (2006) by Doherty (2007). . . 31

2.15 Total pressures of ground hypersonic flow facilities from Anderson (2001). 32

2.16 Experimental wall pressure measurements from H_2-air combustion in a short cylinder-cone scramjet combustor from Billig et al. (1972). 34

2.17 The stages of transition from ramjet to scramjet for The University of Michigan Dual-Mode Combustor (MDMC) from Fotia and Driscoll (2013). 41

3.1 Schematic of the experimental rig with the constant area combustor. . . 49

3.2 Mach number contour plot of diffuser flow field 50

3.3 Manufacturing drawing of the three combustors. 53

3.4 Types of mounting for the pressure transducers used in the experimental model. 55

3.5 Original constant area combustor with mounting block attached. 56

3.6 Transducer mounting blocks for the combustors. 56

3.7 Overall schematic of the fuel system. 57

3.8 Timing of fuel for shot 10832. 59

3.9 Jet penetration based on Portz and Segal's (2006) correlation at various fuelling rates 61

3.10 CAD model of the experimental rig with the constant area combustor . . 62

3.11 Photographs of the model mounted in the test section 63

3.12 Schematic of the T4 Stalker Tube. 64

3.13 Operating principle of the T4 Stalker Tube. 66

3.14 Shock timing stations on the T4 Stalker Tube. 68

3.15 Schematic of the Mach 4 nozzle 69

3.16 Recent Pitot pressure surveys of the Mach 4 nozzle 70

3.17 Contour plots of both the Mach number and pressure from the *CFD++* simulation of flow through the Mach 4 nozzle for the nominal shot condition. 74

3.18 Scramjet powered vehicle flight corridor in terms of flight Mach number and altitude bounded by trajectories at constant dynamic pressures from Heiser and Pratt (1994). 75

3.19 Pressure traces from the nozzle-supply region and an isolator sensor (DT2) annotated with considerations for the selection of the test time for an attached flow along the isolator. 80

3.20 Time for 10% driver gas contamination to occur in the T4 Stalker Tube. . 82

4.1 Sensor labels and locations along the engine for all three combustor configurations 90

4.2 Time-history of the isolator pressures sensors (DT1–DT9 and DB1–DB8) for the constant area combustor where no separation is evident in the isolator for the fuel-off case. 92

4.3 Time-history of the isolator pressures sensors (DT1–DT9 and DB1–DB8) for the constant area combustor where no separation is evident in the isolator for a mid-range fuelling case. 93

4.4 Time-history of a single front edge (FE) sensor and the two sets of combustor pressures sensors (C0FC and C0R) for a fuelled case where no separation is evident in the isolator. 95

4.5 Time-history of the isolator pressures sensors (DT1–DT9 and DB1–DB8) for the constant area combustor for a fuelled case where some separation is evident in the isolator. 96

4.6 A second example showing the time-history of the isolator pressures sensors (DT1–DT9 and DB1–DB8) for the constant area combustor for a fuelled case where some separation is evident in the isolator. 98

4.7 Time-history of a single front edge (FE) sensor and the two sets of combustor pressures sensors (C0FC and C0R) for a fuelled case where no separation is evident in the isolator. 99

4.8 Time-history of the isolator pressures sensors (DT1–DT9 and DB1–DB8) for the constant area combustor for a fuelled case where the separation does not reach steady state. 100

4.9 Time-history of a single front edge (FE) sensor and the two sets of combustor pressures sensors (C0FC and C0R) for a fuelled case for the constant area combustor at an equivalence ratio (ϕ) of 1.52 where the flow does not reach steady state in the isolator. 102

4.10 Chart showing the type of flow over the full range of equivalence ratios for all three combustors. 103

4.11 Examples of tests for the constant area combustor configuration of how flow establishment time was determined for the separated cases. 105

4.12 Plots showing flow establishment time (t_{est}) for the isolator versus shock train length (S_o) for all three combustors. 107

4.13 Establishment times (t_{est}) for the isolator plotted against the fuel equivalence ratio (ϕ) for the constant area combustor. 108

4.14 Plot illustrating the time it takes for the flow at the furthest downstream isolator sensor (DT9) to separate ($t_{sep_{DT9}}$) after flow onset at that sensor. . 109

4.15 Plots showing flow establishment time for the furthest downstream sensor (DT9) in the isolator ($t_{sep_{DT9}}$) versus pre-injector shock train length (S_o) for all three combustors. 110

4.16 Plots showing the flow establishment time for the most downstream sensor (DT9) in the isolator ($t_{sep_{DT9}}$) versus P_{DT9}/P_∞ and ϕ for all three combustors. 111

4.17 Pressure and area profiles for the fuel-off and the combustion-suppressed tests for the constant area combustor. 114

4.18 Pressure profile for a non-separated case for the constant area combustor (ϕ = 0.6). 115

4.19 Pressure profile for a moderately separated case for the constant area combustor (ϕ = 0.76). 117

4.20 Pressure profile for a second example of a moderately separated case for the constant area combustor (ϕ = 0.94). 117

4.21 Pressure profile for a highly separated case for the constant area combustor (ϕ = 1.06). 118

4.22 Pressure profile for a second example of a highly separated case for the constant area combustor (ϕ = 1.22). 119

4.23 Pressure profile for a third example of a highly separated case for the constant area combustor (ϕ = 1.29). 119

4.24 Pressure profiles for the fuel-off and combustion-suppressed tests for the 2° divergent combustor. 121

4.25 Pressure profile for a non-separated case for the 2° divergent combustor ($\phi = 0.56$). 122

4.26 Pressure profiles for the key results of the 2° divergent combustor. 123

4.27 Comparison of the pressure profiles for the constant area and 2° divergent combustors. 125

4.28 Pressure profiles for the fuel-off and combustion-suppressed tests for the 1° divergent combustor 126

4.29 Pressure profile for a non-separated case for the 1° divergent combustor 127

4.30 Pressure profiles for the key results of the 1° divergent combustor. 128

4.31 Comparison of the pressure profiles for the 2° and 1° divergent combustors. 131

4.32 Comparison of the pressure profiles for all three combustors. 133

4.33 Plots showing normalised isolator exit pressure (P_{DT9}/P_{∞}) versus pre-injector shock train length (S_o) for all three combustors. 134

4.34 Plots showing normalised isolator exit pressure (P_{DT9}/P_{∞}) versus equivalence ratio (ϕ) for all three combustors. 135

4.35 Plots showing shock train length (S_o) versus equivalence ratio (ϕ) for all three combustors. 136

5.1 Cycle analysis results for the fuel-off case for the constant area combustor. 144

5.2 Cycle analysis results for the combustion-suppressed case for the constant area combustor. 145

5.3 Cycle analysis result of a non-separated case for the constant area combustor showing both pressure and Mach number distributions along the isolator and combustion chamber ($\phi = 0.60$). 146

5.4 Cycle analysis result of a separated case for the constant area combustor ($\phi = 0.76$). 147

5.5 Cycle analysis result of a second separated case for the constant area combustor ($\phi = 0.86$). 148

5.6 Cycle analysis result of a third separated case for the constant area combustor ($\phi = 0.94$). 151

5.7 Cycle analysis result of a highly separated case for the constant area combustor ($\phi = 1.06$). 151

5.8 Cycle analysis result of a highly separated case for the constant area combustor ($\phi = 1.1$). 152

5.9 Cycle analysis result for the maximum fuelling of an established flow for the constant area combustor ($\phi = 1.29$). 153

5.10 Cycle analysis results of key cases for the 2° divergent combustor 156

5.11 Cycle analysis results of key cases for the 1° divergent combustor 162

5.12 Combustion efficiency ($\eta_{c,f}$) versus equivalence ratio (ϕ) for all three combustors. 164

5.13 Air-based combustion efficiency (η_{air}) versus equivalence ratio (ϕ) for all three combustors. 166

5.14 Point of complete mixing (x_{fe_1}) versus equivalence ratio (ϕ) for all three combustors. 166

A.1 Dimensionless kinetic energy versus dimensionless static enthalpy (H-K diagram) depicting constant property isolines and idealised compressible flow. 200

A.2 H-K diagrams for a ramjet and scramjet. 201

A.3 H-K diagram for a dual-mode scramjet engine with a constant area isolator and constant area combustor. 202

A.4 Ignition and reaction times with corresponding lengths for a flow speed of 2122 m s^{-1} 205

A.5 Key results from the CFD simulation of the Mach 4 nozzle flow. 208

A.6 The CFD solution sensitivity to mesh refinement for various key flow parameters 209

A.7 Establishment times (t_{est}) for the isolator plotted versus the fuel equivalence ratio (ϕ) for the 2° divergent combustor 211

A.8 Establishment times (t_{est}) for the isolator plotted versus the fuel equivalence ratio (ϕ) for the 1° divergent combustor 212

A.9 Plots showing the normalised isolator exit pressure (P_{DT9}/P_∞) versus equivalence ratio (ϕ) for the constant area combustor. 212

A.10 Plots showing the normalised isolator exit pressure (P_{DT9}/P_∞) versus equivalence ratio (ϕ) for the 2° divergent combustor. 213

A.11 Plots showing the normalised isolator exit pressure (P_{DT9}/P_∞) versus equivalence ratio (ϕ) for the 1° divergent combustor. 213

A.12 Plots showing the shock train length (S_o) versus normalised isolator exit pressure (P_{DT9}/P_∞) for the constant area combustor. 214

A.13 Plots showing the shock train length (S_o) versus normalised isolator exit pressure (P_{DT9}/P_∞) for the 2° divergent combustor. 214

A.14 Plots showing the shock train length (S_o) versus normalised isolator exit pressure (P_{DT9}/P_∞) for the 1° divergent combustor. 215

A.15 Plot showing shock train length (S_o) versus equivalence ratio (ϕ) for the constant area combustor. 215

A.16 Plot showing shock train length (S_o) versus equivalence ratio (ϕ) for the 2° divergent combustor. 216

A.17 Plot showing shock train length (S_o) versus equivalence ratio (ϕ) for the 1° divergent combustor. 216

A.18 Time history of the isolator pressures sensors (DT1–DT9 and DB1–DB8) for a highly separated case of the constant area combustor at $\phi = 1.29$ with propagation line of separation. 217

A.19 Time history of the isolator pressures sensors (DT1–DT9 and DB1–DB8) for a highly separated case of the constant area combustor at $\phi = 1.46$ with propagation line of separation. 218

A.20 Time history of the isolator pressures sensors (DT1–DT9 and DB1–DB8) for a second highly separated case of the constant area combustor at $\phi = 1.52$ with propagation line of separation. 218

B.1 Schematic of ASCO/JOUCOMATIC® fast-acting solenoid valve. 223

C.1 Plots showing repeatability of testing with combustion in the constant area combustor at mid and high fuelling levels 230

C.2 Plots showing repeatability of testing with combustion in the 2° divergent combustor at mid and high fuelling levels 231

C.3 Plots showing repeatability of testing with combustion in the 1° divergent combustors at mid and high fuelling levels 231

E.1 Parameter study of the cycle analysis result of the non-separated case for the constant area combustor 240

E.2 Parameter study of the cycle analysis result of a separated case for the constant area combustor 243

E.3 Parameter study of the cycle analysis result of a highly separated case for the constant area combustor 244

E.4 Parameter study of the cycle analysis result of a non-separated case for the 2° divergent combustor 245

E.5 Parameter study of the cycle analysis result of a moderately separated case for the 2° divergent combustor 246

E.6 Parameter study of the cycle analysis result of a highly separated case for the 2° divergent combustor 246

E.7 Parameter study of the cycle analysis result of a non-separated case for the 1° divergent combustor 247

E.8 Parameter study of the cycle analysis result of a moderately separated case for the 1° divergent combustor 248

E.9 Parameter study of the cycle analysis result of a highly separated case for the 1° divergent combustor 248

E.10 Parameter study of the cycle analysis results for two highly separated cases for the constant area combustor showing the particularly high sensitivity to: (a) combustion efficiency ($\eta_{c,f}$) and (b) the Mach number of the isolator inflow. 250

E.11 Best fit of cycle analysis result of the maximum fuelling case for all three combustors by varying inflow conditions 252

E.12 Plots showing the effect on the combustion efficiency curve by varying the mixing rate parameter (ϑ) and the mixing length parameter (x_{fe_1}). . . 254

E.13 Plot showing a comparison of the mixing-combustion models of Heiser and Pratt (1994), Diskin and Northam (1987) and Noda et al. (2011a). . . 256

E.14 A plot showing how the point of complete combustion (x_ϕ) in the combustion model by Diskin and Northam (1987) varies with equivalence ratio (ϕ). 257

List of Tables

2.1 Experimental constants in Equation (2.4) from Noda et al. (2011a) 38

3.1 Key parameters of the diffuser 48

3.2 Nominal flow conditions exiting the diffuser (i.e. entering the isolator) . 51

3.3 Combustion chamber parameters 53

3.4 Inflow conditions for CFD simulation of the Mach 4 nozzle (based on the stagnation conditions of the nominal Shot 10816) 72

3.5 Freestream conditions from the Mach 4 nozzle from *CFD++* and *NENZF* 73

3.6 Flow conditions for flight at Mach 8 at a dynamic pressure of 95 kPa of the freestream and at the post forebody and isolator entrance stations. . 77

3.7 Nozzle-supply conditions and shock speed for the nominal condition. . 78

3.8 Nominal test flow conditions using *ESTCj* & *NENZF*. 78

3.9 State of the boundary layer at the diffuser exit (i.e. isolator entrance). . . 79

3.10 uncertainty in the nominal test flow conditions as computed by *ESTCj* & *NENZF*. 83

3.11 Relative uncertainties in the fuelling conditions. 84

3.12 Shots used to demonstrate repeatability of flow phenomenon for each of the combustors. 85

4.1 The peak pressure, normalised by the freestream pressure (P_∞), measured in the 2° and 1° divergent combustors. 130

5.1 Key values relating to the separation from the cycle analysis for all three combustors at similar equivalence ratios. 163

5.2 Key Mach numbers from the cycle analysis for all three combustors at similar equivalence ratios. 164

A.1 Ignition and reaction times based on the properties of flow entering the isolator (P_2=118 kPa, T_2=885 K, u_2=2122 m s^{-1}) 205

A.2 Hydrogen-oxygen chemical reaction scheme used by Pergament (1963) . 207

A.3 Location of furthest upstream sensor in the isolator where flow separated and remained separated over the test time for the constant area combustor. 210

A.4 Location of furthest upstream sensor in the isolator where flow separated and remained separated over the test time for the 2° divergent combustor. 210

A.5 Location of furthest upstream sensor in the isolator where flow separated and remained separated over the test time for the 1° divergent combustor. 211

B.1 Penetration equation parameters as a function of the air Mach number from Portz and Segal (2006). 223

C.1 Fundamental relative uncertainties of the measured quantities. 226

C.2 Sensitivity $\left(\partial X_F / \partial X_{\psi_i}\right)$ of the freestream conditions to the measured quantities. 226

C.3 Components $\left(\left(X_F\right)_{\psi_i}\right)$ of the total uncertainties (X_F) of the test condition. 227

C.4 Fundamental relative uncertainties of the measured quantities relating to the fuel system. 228

C.5 Sensitivity $\left(\partial X_F / \partial X_{\psi_i}\right)$ of the discharge coefficient (α) due to the measured and calculated quantities. 228

C.6 Sensitivity ($\partial X_F / \partial X_{\psi_i}$) of the fuel mass flow rate ($\dot{m}_F$) due to the measured quantities 228

C.7 Relative uncertainties of the fuelling conditions. 229

C.8 Repeatability of the test flow conditions (for air as the test gas) expressed as a 95% confidence interval. 229

D.1 Shock tunnel operational parameters and the resulting free-stream flow properties. 234

D.2 Measured and calculated key properties of the fuel system. 236

E.1 Experimental constants in Equation (E.5) from Noda et al. (2011a) 255

F.1 Tool path for the diffuser 290

Nomenclature

Roman

a	Speed of sound
A	Area
A	Penetration coefficient (in Portz and Segal (2006))
A_c	Inlet capture area
c_f	Skin friction coefficient
c_{f_0}	Skin friction coefficient at point of separation
D	Diameter
D_H	Hydraulic diameter
$F(\psi_{i..n})$	Derived quantity
h_f	Flight altitude
h, H	Duct height
H	Enthalpy
H	Dimensionless static enthalpy ($H = C_pT/C_pT_{t_0}$)
I	95% Confidence interval
K	Dimensionless kinetic energy ($K = V^2/2C_pT_{t_0}$)
L	Length
L_{int}	Length of interaction
$\dot{m}$	Mass flow rate
$\dot{m}_{air}$	Mass flow rate of air entering the isolator
M	Mach number
M_{1e}	Mach number just upstream of shock
$\mathcal{M}$	Molecular mass of a species
n_{exp}	Number of experiments
p, P	Pressure (static unless otherwise noted)
p_{Pitot}	Pitot pressure
p_f	Throttled pressure
p_S	Nozzle-supply pressure
P	Penetration of the jet (in Portz and Segal (2006))
q	Dynamic pressure ($q = \frac{1}{2}\rho\, u^2$)
r, R	Radius
R	Specific gas constant
Re	Reynolds number
Re_t	Transitional Reynolds number
Re_u	Unit Reynolds number
S	Shock train length
S_o	Length of shock train ahead of injectors
S_t	Total shock train length
t	Time
t_i	Ignition delay
t_r	Reaction time
t_{est}	Establishment time
$t_{flow\,onset}$	Time test flow arrives at a particular sensor
t_{sep}	Time taken to separate ($\equiv t_{2nd\,rise} - t_{flow\,onset}$)
$t_{2nd\,rise}$	Time of a 2$^{\text{nd}}$ rapid rise in pressure at a particular sensor

T	Temperature
u_{ss}	Incident shock speed in the shock tube
U	Flow velocity
U	Uncertainty
V	Volume
V	Velocity
w	dimensionless velocity (Crocco number, $\equiv u/\sqrt{2C_pT_0}$)
x, y	Coordinates
x_{fe_1}	Point of complete combustion (or mixing-length)
X	X-type shock train
X	Fraction of total combustor length
X_F	Normalised derived quantity
X_ψ	Normalised measured quantity
Y_i	Mass fraction of species i

Symbols

α	Discharge coefficient
α	Angle of attack
γ	Ratio of specific heats
δ	Boundary layer thickness
$\delta^\star$	Boundary layer displacement thickness
ζ	Mixing rate parameter (in Noda et al. (2011a))
η_{air}	Air-based combustion efficiency ($\eta_{air} \equiv \phi \times \eta_c$)
η_c	Combustion efficiency
$\eta_{c,f}$	Terminal combustion efficiency at end of combustor
η_{mix}	Mixing efficiency (in Noda et al. (2011a))
θ	Boundary layer momentum thickness
θ_{div}	Half cone angle of divergence of the combustion chamber
ϑ	Mixing rate parameter (from Heiser and Pratt (1994))
λ	λ-type shock train
ξ	Mixing rate parameter (in Noda et al. (2011a))
ρ	Density
σ	Standard deviation
τ	Ratio of total temperatures ($\tau \equiv T_t/T_{t_0}$)
ϕ	Fuel equivalence ratio
ϕ_{eff}	Effective fuel equivalence ratio ($\phi_{eff} \equiv \phi \times \eta_c$)
Φ	Constant impulse function
χ	Mass fraction
ψ	Measured quantity
ω	Wedge angle

Subscripts

a	Pertaining to the cross flow (in Portz and Segal (2006))
cc	Combustion chamber
CT	Compression tube
e	Immediately upstream of the interaction
f	Final value
$fill$	Fill value
i	Initial value
inj	Fuel injector
iso	Pertaining to the isolator entrance
j	Fuel jet property
LT	Ludwieg tube fuel supply
n	Pertaining to a normal shock
$plenum$	Fuel plenum chamber
PSW	Pertaining to the pseudo-shock
Res	Reservoir
$S, stag$	Nozzle-supply (stagnation) region
sep	Pertaining to the flow separation
ST	Shock tube
t_0	Stagnated or total property
w	Pertaining to the wall/surface
∞	Freestream property
0	Stagnated or total property
$1-6$	Axial stations along an engine flow field
θ	Based on the boundary layer momentum thickness

Superscripts

$\star$	Property at a reference temperature

Abbreviations

AFRL	Air Force Research Laboratory
APL	Applied Physics Laboratory
CAD	Computer aided design
CEA	Chemical equilibrium with application
CFD	Computational fluid dynamics
DAQ	Data acquisition system
diaph.	Primary diaphragm thickness
DLR	Deutsches Zentrum fr Luft- und Raumfahrt (German Aerospace Center)
DMCycle	Dual mode cycle analysis (in Smart (2007))
DSTO	Defence Science and Technology Organisation
EAH	Electric air heated
effc	Combustion efficiency (see η_c)
ER	Equivalence ratio
ERS	External rocket system

ESTC	Equilibrium shock tube conditions
ESTCj	ESTC Junior
GASL	General Applied Science Laboratory
HEG	High Enthalpy Shock Tunnel, Göttingen
HIEST	High Enthalpy Shock Tunnel
HRE	Hypersonic Research Engine
HSM	HYPULSE Scramjet Model
HTT	High Temperature Tunnel
HYPULSE	Hypersonic Pulse Facility
JAXA	Japan Aerospace Exploration Agency
KSPC	Kakuda Space Propulsion Center
LaRC	NASA Langley Research Center
LDV	Laser Doppler velocimetry
LENS	Large Energy National Shock Tunnel
LOX	Liquid oxygen
NENZF	Non-Equilibrium Nozzle Flow
PCB	PicoCoulomB (as in PCB Piezotronics® sensors)
RANS	Reynolds-averaged Navier-Stokes
REST	Rectangular to elliptical shape transition
RST	Reflected shock tunnel
SAH	Storage air heated
SBLI	Shock boundary layer interaction
SET	Shock-expansion tunnel
SI	Système International d'Unités
SST	Shear stress-transport turbulence model
STF	Scramjet Test Facility
TAU	DLR CFD Code
T4NIDAQ	T4 Shock Tunnel National Instruments® DAQ
UTRC	United Technologies Research Center
VAH	Vitiated air heated
VULCAN	Viscous upwind algorithm for complex flow analysis (LaRC)
1-D, 2-D	One or two-dimensional

Chapter 1

Introduction

Scramjets and ramjets offer an attractive means of powered hypersonic flight due to their high specific impulse compared with those of conventional rockets. However, despite over five decades of research effort from multiple countries, including flight experiments, a hypersonic air-breathing propulsion system does not form part of any space launch system currently in operation.

There are numerous phenomena that restrict scramjet design and limit performance. Some of them include: thermal choking, inlet unstart, extreme heating loads, significant skin friction (Heiser and Pratt, 1994), flow chemistry, boundary-layer effects, non-uniform flow conditions, shear-layer interaction, and three-dimensional effects (Andreadis, 2004). One of the many challenges to scramjets is being able to operate efficiently over an extraordinarily wide range of flight conditions. For a space launch a vehicle needs to accelerate through a large range of Mach numbers in order to reach orbital velocity.

A ram-type compression engine such as a scramjet cannot accelerate a vehicle from rest. The engine needs to be at a considerable speed initially in order that the inlet can compress the flow to a sufficient pressure and temperature suitable for combustion. Additionally, towards the end of the trajectory, at high altitude, the air becomes so thin that net thrust vanishes. At these velocities it is also hard to release the energy from the fuel and convert it into kinetic energy (Heiser and Pratt, 1994). Therefore a rocket is likely to be required for the final stage to achieve orbit. Following from these two restrictions the two likely scenarios which would include a scramjet in a space launch system are: (1) the scramjet replaces the middle stage in conventional multi-staged

rocket or (2) the scramjet is launched from a turbo-fan powered aircraft at high altitude and then a booster rocket places the payload into orbit. This second scenario is illustrated in Figure 1.1.

In order that the advantages of air-breathing engines be realised, the scramjet will need to operate over a section of the trajectory large enough such that the benefits outweigh the costs of replacing the rocket for that stage with a scramjet. These benefits may not come primarily from performance but may come from overall system benefits due to aircraft-like operation (i.e. rapid turn-around, re-usability, use of existing infrastructure for horizontal take-off) as highlighted by Mehta and Bowles (2001). However, any extension of the operating window of the scramjet is still expected to improve the performance of the system overall.

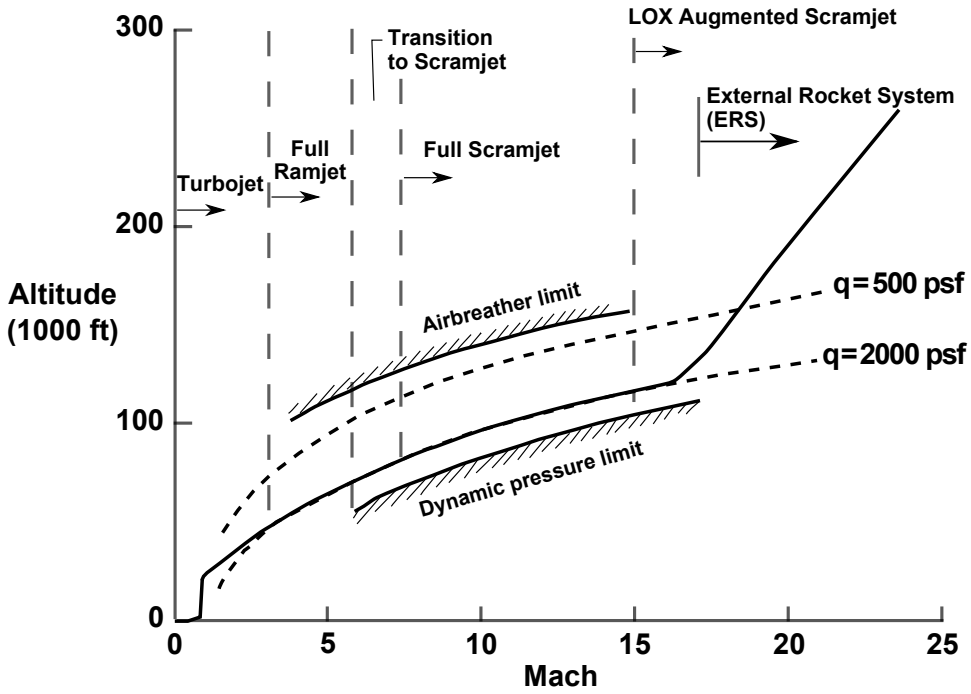

Figure 1.1: Typical transatmospheric accelerator trajectory. Over the Mach number range of 4 to 15 the trajectory follows a path of constant dynamic pressure (q) of 200 lb/ft^2. (Original figure from Hunt and Martin (2000) with adaptations from Gildfind (2012) and Razzaqi (2011)).

A conventional ramjet is not expected to deliver the performance required of such a system for the following reasons. First is that the upper limiting Mach number of a ramjet is too low. A conventional ramjet requires a physical throat to generate the pressures required for combustion and to achieve adequate performance from the nozzle of the engine. Whereas for a scramjet, which maintains supersonic flow throughout, such

a throat is not required. The second reason why the ramjet is an unlikely candidate for the second stage is that although a ramjet has superior performance than a scramjet at low Mach numbers, at higher Mach numbers the losses associated with decelerating the flow to subsonic quickly tip the scales in favour of a scramjet.

When it comes to scramjet design there are competing drivers. Weber and MacKay (1958) show that for a scramjet with a fixed geometry, superior performance over the entire trajectory is achieved when the peak performance point of the engine is selected to be at the terminal Mach number rather than its initial one (i.e. engines which have a design point at a high Mach number have a greater performance over the entire flight profile than engines which have a design point at a low Mach number). However scramjets which have been designed to operate most efficiently in the upper part of the regime typically suffer from choking at low Mach numbers (Mach 8 and below) (Billig, 1993; Turner and Smart, 2010).

Curran and Stull (1964) found that early research on scramjets focused on the Mach 8-25 range but little attention was given to speeds substantially below Mach 8. They envisaged that accelerating a scramjet powered vehicle up to Mach 8 was "a formidable problem" and argued that use of a turbine-style engine would be questionable. They deduced that any lowering of the take-over speed of the scramjet engine could be beneficial to overall vehicle performance. It was from this reasoning that they sought to explore the methods of extending the scramjet engine down into the flight regime typically dominated by ramjets, and thereby develop an engine which in effect could operate both as a ramjet and as a scramjet, that is a dual-mode engine.

In the literature on dual-mode operation of scramjets and ramjets there has been multiple definitions of this type of engine. Some (White et al., 1988) refer to dual-mode as a scramjet which can operate both in ramjet and scramjet modes at separate times and make the transition between the two modes via either a change in geometry, inflow conditions and/or fuelling rates and locations. Whereas other types (Vinogradov et al., 1990) incorporate two combustion chambers where combustion occurs subsonically in one and supersonically in the other. These combustion chambers may be in series, like Curran and Stull's (1964) early concept of a dual mode combustor or in parallel like the ramjet type missile designed by Billig et al. (1979, 1980). Also included in this wide definition of dual-mode are those which are occasionally termed mixed-flow combustors. These combustors mix subsonic flow with the core supersonic flow by a

number of means such as bypass flow or a surrogate flow device (Curran and Stull, 1964).

Another definition, the one adopted in this thesis and quite common in the literature (Sullins, 1993), is one in which a scramjet operates in a manner where the separation of the boundary layer causes a shock train to develop ahead of the fuel injectors (i.e. a pre-combustion shock train). This is best illustrated in Figure 1.2. In this mode the shock train, which contains a mixture of supersonic and subsonic flow, provides additional compression of the inflow and this improves the overall cycle performance.

It is important to note the nuance here in this definition of a dual-mode scramjet. It is the presence of subsonic flow in the separated flow associated with the shock train, which feeds flow to the combustion chamber, which allows it to be classified as dual-mode as both subsonic and supersonic combustion are present. Now, this separation may be strong enough that the core flow exiting from the pre-combustion shock train and entering the combustor is subsonic. In this case the flow must be accelerated through a thermal throat somewhere in or at the rear of the combustion chamber. In this scenario, the scramjet is operating much like a traditional ramjet but without the geometric throat at the exit of the combustion chamber. Although this type of scramjet would be able to operate in two distinctive modes (pseudo-ramjet and pure scramjet without a shock train) based on the state of the core flow, it is not this property which defines this engine as a dual-mode scramjet. It is rather the presence of the pre-combustion shock train which generates a mixture of subsonic and supersonic flow to the combustion chamber.

There are a number of advantages to a dual-mode scramjet. The main advantage is the additional compression which is generated from the shock-train that would otherwise be required of the inlet. This compression not only raises the pressure, which improves thrust performance, but also increases the temperature. This is advantageous as higher temperatures will improve the cycle efficiency of the engine and additionally, in conjunction with the higher pressures, will reduce the ignition and reaction times.

Ignition and reaction times are of critical importance to scramjets due to the high velocity of the internal flow through the engine. High velocities result in very short residence time of the flow in the engine (in the order of milliseconds for a metre long

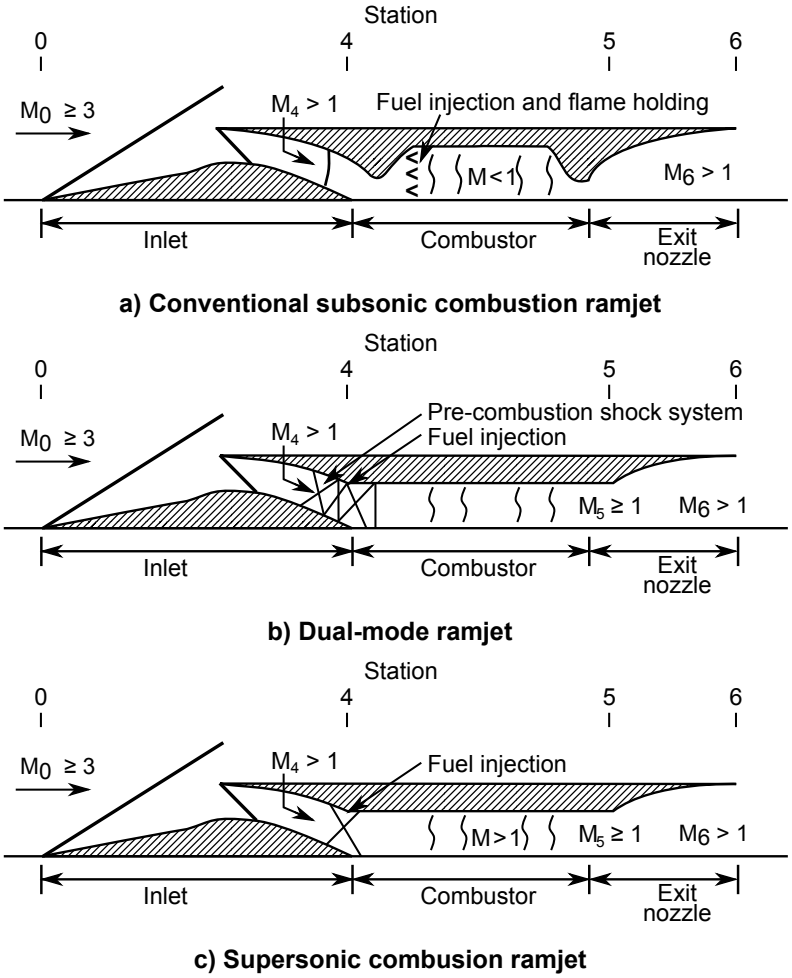

Figure 1.2: Schematic of (a) conventional ramjet, (b) dual-mode ramjet and (c) scramjet. (Reproduced from Sullins (1993)).

engine). As ignition length/delay is exponentially dependent on the temperature (Pergament, 1963), a scramjet which is designed for the upper region of the trajectory (i.e. at a high Mach number) may suffer from excessively long ignition times at the lower Mach number of the trajectory. The combustion chamber of a scramjet needs to be sufficiently long to give the flow enough time to mix with the fuel, ignite and burn sufficiently before reaching the nozzle of the engine. Although this issue grows as flight speeds increase, this is somewhat offset by the accompanying increase in temperature from a higher total enthalpy. This problem of ignition and reaction times can also be exacerbated at low flight speeds as, for a fixed geometry scramjet, operating at lower Mach numbers will be accompanied by lower temperatures. Curran and Stull (1964) from their cycle analysis, which incorporated empirical relations for ignition and reaction times for hydrogen (from Pergament (1963)), found that the low combustor temperatures which are due to the low flight speed lead to reaction times which

are excessive. This is despite the lower flow velocity which in itself results in a longer residence time of the flow within the combustor.

As mentioned, for a fixed geometry scramjet, operating in dual-mode improves the performance of the engine at lower Mach numbers through higher cycle temperatures. Shorter ignition and reaction lengths also allows a greater fraction of the fuel to be burnt before being expelled by the combustion chamber. Together these two aspects improve engine efficiency and would extend the operation of such a scramjet to a lower Mach number than would be otherwise possible.

While much of the previous research has been conducted on ramjet and scramjet engines, less attention has been on the dual-mode operation between ramjet and scramjet involving pre-combustion shock trains. Of the few dual-mode studies in the literature most have been focused on the lower end of the range at Mach numbers around 4 – 5 with little around the upper end of the dual-mode regime, which is at a flight Mach number around 8. Of these high Mach number studies, most have investigated dual-mode at conditions which have been at reduced enthalpies not representative of Mach 8 flight.

Shock tunnels, specifically the free-piston Stalker Tube class, generate high enthalpy flows such that flight conditions at Mach 8 and above can be produced on the ground. However these facilities, which are impulse wind tunnels, have short test times on the order of milliseconds. A critical issue in testing in these facilities is whether the fluid phenomenon being studied reaches equilibrium within the available test time such that the flow field can be considered established. Flow establishment is dependent on a number of factors including Reynold and Mach numbers, boundary layer thickness and model geometry. However, it generally reduces to a multiple of a characteristic length (such as the model diameter or length) in which the flow must first pass the model. Due to the high speeds produced in the shock tunnels, the short test time is generally sufficient for attached flow. However in regions of separated flow the flow takes longer to establish (Holden, 1971). As shock trains involve large scale separation it is anticipated that the presence of this phenomenon will increase the establishment time. As such, the question remains whether this phenomenon can be studied in these facilities. If possible, this would allow the testing of dual-mode scramjets in shock tunnels and this means that these engines can be tested at Mach

numbers towards the upper end of their anticipated regime at enthalpies representative of flight.

1.1 Research Aims

The overall aim of this thesis is: *To investigate the dual-mode operation of a scramjet in a shock tunnel at conditions representative of Mach 8 flight and to explore the effect that area divergence in the combustion chamber has on a scramjet in this mode.*

The specific research questions that this thesis aims to answer are:

At test conditions equivalent to Mach 8 flight:

1. Can dual-mode operation of a scramjet be studied experimentally in a shock tunnel and, if so, what is the establishment time of this phenomenon?
2. How does the pre-combustion shock train (the defining characteristic of dual-mode operation) affect mixing and thereby combustion efficiency of a scramjet?
3. Considering that scramjet engine designs are likely to incorporate an area expansion in the combustion chamber, how does area expansion of the combustion chamber affect the pre-combustion shock train and in turn the mixing and combustion efficiency of a scramjet?

1.2 Thesis Outline

This thesis comprises six chapters with appendices A through to F containing technical details and supporting data. The chapters are as follows:

Chapter 2 - Literature Review
Chapter 2 is a review of the literature of previous studies that relate to this thesis. The chapter begins with reviewing some of the earliest experiments involving shock trains and pseudo-shocks as well as the predominant shock train analytical models. The review covers the ground facilities used to test dual-mode engines and concludes with a

discussion of shock trains involving combustion.

Chapter 3 - Experimental Apparatus and Methodology
The test facility, experimental model, fuel system and instrumentation used to conduct these experiments are described in Chapter 3. Also described is the methodology of determining the test conditions and their associated uncertainties.

Chapter 4 - Experimental Results
This chapter presents the experimental results from the testing in the T4 Stalker Tube. The transient data of the pressure measurements taken along the isolator are presented first to show the flow establishment characteristics of the shock train. This is followed by pressure profiles along the entire engine in order of increasing fuelling rates. For each section, the data from the constant area combustor is presented first followed by the two divergent combustors in turn. The plots are categorised into non-separated and separated cases.

Chapter 5 - Cycle Analysis Methodology and Results
Chapter 5 presents the methodology and results from the cycle analysis which was applied to experimental results. Combustion efficiency and mixing-lengths are estimated for the key experimental results. A comparison of these parameters for all three combustors over the range of fuelling rates is presented at the end of this chapter.

Chapter 6 - Conclusions
Chapter 6 summaries the key findings of this study of the dual-mode operation of a scramjet in a shock tunnel. Finally, recommendations are made for improving upon this work as well as some suggestions for future studies.

Chapter 2

Literature Review

Scramjet engines have been the focus of numerous studies, however the dual-mode variant which involve a pre-combustion shock train has received relatively less attention. This chapter briefly reviews these previous studies which relate to the phenomenon of shock trains, that are encountered in a variety of flow fields. Next, the few pseudo-shock and shock train analytical models are introduced and discussed. The review also covers a selection of the ground test facilities which have been used to test dual-mode scramjets. Finally, the chapter reviews the shock train studies which involve combustion.

2.1 Shock Train and Pseudo-Shock Experiments

As outlined in the Chapter 1, the type of dual-mode scramjet of interest in this research is the fixed geometry, single combustion chamber, scramjet that can operate over a range of Mach numbers. A distinguishing feature of such an engine is the pre-combustion shock train which mainly resides within the isolator but can extend into the combustion chamber.

Shock trains have been the focus of numerous studies over the years (Cuffel and Back, 1976; Fejer et al., 1964; Ikui et al., 1980, 1974a,b; Neumann and Lustwerk, 1949, 1951; Ostras and Penzin, 1975; Sullins and McLafferty, 1992; Tamaki et al., 1970; Waltrup and Billig, 1973). They are frequently encountered in a number of devices which involve confined compressible flow such as ducts, pipelines, supersonic wind tunnels, supersonic inlets of aircraft engines and supersonic ejectors (Matsuo et al., 1999). The pressure rise across these shock trains can be as strong as the pressure rise across a

normal shock and the scale of these shock trains extend over a length equal to 8 to 12 duct diameters (Neumann and Lustwerk, 1949).

The causes and mechanisms of a shock train are best illustrated by first looking at the interaction of a normal shock and turbulent boundary layer in a constant area duct. According to Matsuo et al. (1999) from a review of previous studies (Ikui et al., 1974a, 1981; Nussdorfer, 1954; Shapiro, 1953) this interaction can be classified into four different possible configurations as shown in Figure 2.1.

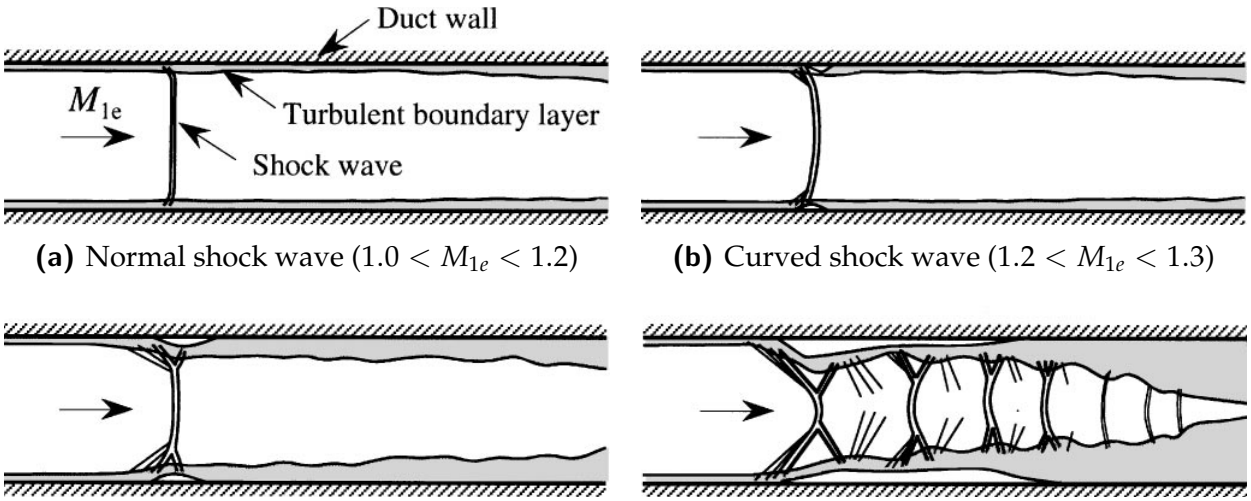

(a) Normal shock wave ($1.0 < M_{1e} < 1.2$)

(b) Curved shock wave ($1.2 < M_{1e} < 1.3$)

(c) Bifurcated shock wave ($1.3 < M_{1e} < 1.5$)

(d) Shock train ($1.5 < M_{1e}$)

Figure 2.1: Sketch of a normal shock wave/turbulent boundary layer interaction in a constant area duct. M_{1e} is the Mach number just upstream of the shock. (Figure sourced from Matsuo et al. (1999).)

At low Mach numbers ($1.0 < M < 1.2$) the transition from supersonic to subsonic flow is via a single normal shock. Where the shock meets the wall there is a shock boundary layer interaction, which is a highly complex fluid phenomenon in its own right. At low Mach numbers this interaction is small in scale compared with the duct height.

As the Mach number increases, through a range from 1.2 to 1.3, the normal shock begins to show some curvature (Figure 2.1b). This curvature is due to the growth of the localised boundary layer separation, which can manifest in a shock boundary layer interaction. Close to the wall, emanating from this separation, is an oblique shock and as this separation grows the oblique shock also grows as a proportion of the shock across

the duct leading to the curvature observed.

As the Mach number is increased to between 1.3 and 1.5 the normal shock bifurcates at the walls and the localised separation of the boundary layer is clearly evident. Above a Mach number of 1.5, the separation region grows to such a scale that a series of shocks ensues which form a shock train.

A schlieren image of a shock train by Ikui and Matsuo (1969) is shown in Figure 2.2. The apparatus which was used was a rectangular duct with an inflow at a Mach number of 1.75. The diamond shape structure is formed from the intersection of shock and expansion waves. Within the image it can be seen that the region near the wall, where the structure dissipates, is the boundary layer. This boundary layer grows in size along the duct and the shock structure causes it to mix with the main flow. By the end of the duct the structure of the shock train is no longer visible. This is where the flow has been reduced to below Mach 1 through a combination of the shock waves and the diffusion from the mixing of boundary layer with the main flow.

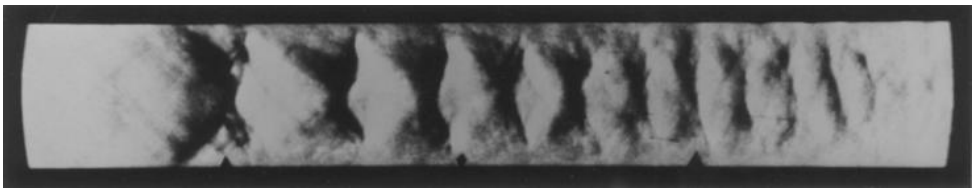

Figure 2.2: Schlieren photograph showing a shock train in a rectangular duct ($M_i = 1.75$). (Image sourced from Ikui and Matsuo (1969).)

This type of shock train is classed as a λ-type by Tamaki et al. (1970) as the feet of the interaction resemble the shape of that Greek letter. As the Mach number is further increased, the portion of the shock which is normal to the flow reduces to a point where it is indistinguishable, if present at all, and the shock train resembles a series of intersecting oblique shocks. These shock trains are classed as X-type by Tamaki et al. (1971).

A number of flow properties affect the formation of the shock train. Mach number effects have been investigated and well documented by Ikui and Matsuo (1969), Tamaki et al. (1970, 1971) and Neumann and Lustwerk (1949, 1951). The works by Lustwerk (1950), Merkli (1976), Mateer and Viegas (1980) and Carroll and Dutton

(1990) have demonstrated that flow confinement, as defined as the ratio of the boundary layer thickness (δ) to duct height (H), has a similar effect on shock trains as increases in Mach number does.

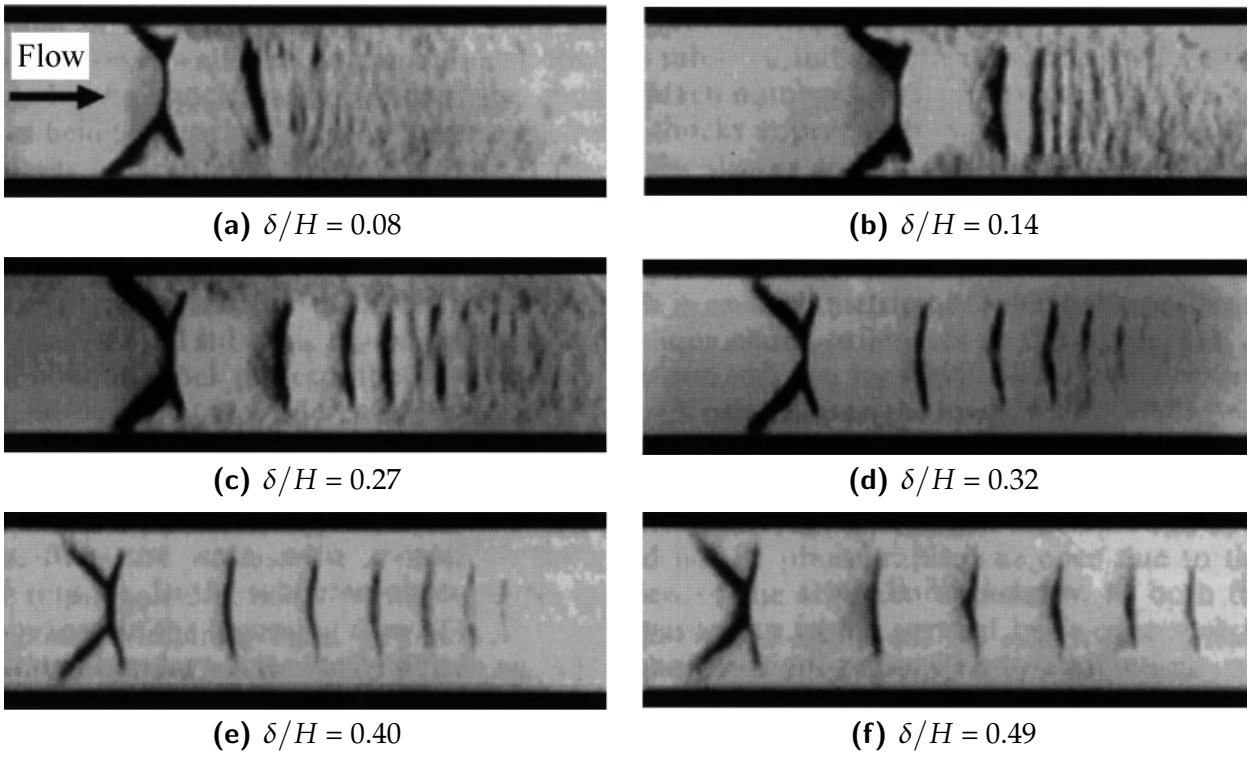

(a) $\delta/H = 0.08$ **(b)** $\delta/H = 0.14$

(c) $\delta/H = 0.27$ **(d)** $\delta/H = 0.32$

(e) $\delta/H = 0.40$ **(f)** $\delta/H = 0.49$

Figure 2.3: Schlieren photographs from Carroll and Dutton (1990) for a Mach 1.6 flow with increasing flow confinement by the boundary layer (δ/H). (Images sourced from Matsuo et al. (1999).)

Carroll and Dutton (1990) found that at low Mach numbers, the number of shocks and length of the interaction scales directly with the level of flow confinement. It was determined from the description of a previous experiment in Dutton and Carroll (1988) that the flow confinement at this facility is adjusted through a combination of a change in the duct height and a change in the thickness of the boundary layer of the incoming flow. For each series of experiments the Mach number and unit Reynold's number were held constant. In the schlieren images from their experiments, which are shown in Figure 2.3, it can be seen that for low levels of confinement ($\delta/H = 0.08$) the interaction begins with a bifurcated normal shock. This first shock system is followed by a single shock which does not extend to the walls and is free from bifurcation. This second shock is the terminating shock as the flow past this remains subsonic. As flow confinement increases additional shocks appear downstream and the spacing between these successive shocks also increases. An increase in flow confinement also increases

the scale of the bifurcation of the first shock system and reduces the proportion of the bifurcated shock which is normal to the flow. At a flow confinement of $\delta/H = 0.49$ (Figure 2.3f) the bifurcation has extended almost to the very centre of the duct. Carroll and Dutton (1990) also showed that the effect which the flow confinement has on the shock train structure is Mach number dependent. They found in their tests between Mach 1.6 and 2.4 that the effect which a change in flow confinement had on the shock structure reduces as the Mach number increases.

The first few investigations into this phenomenon of shock trains consisted mainly of schlieren photographs and measurements of the pressure along the wall of the duct (Fejer et al., 1964; Lustwerk, 1950; Neumann and Lustwerk, 1949, 1951). Measurements taken by Neumann and Lustwerk (1949) showed that the pressure at the wall rose gradually along the length of the shock train. However, wall pressures do not illuminate the complex process within the shock train. The large variations in pressure through the shock train, which are evident in the large variations in density in the schlieren photographs, are diffused near the wall by the boundary layer and as such do present on a distribution of pressure measurements taken at the wall.

A number of studies have conducted in-stream Pitot measurements to resolve the internal flow structure of the shock train (Tamaki et al., 1970, 1971; Waltrup and Billig, 1973). Tamaki et al.'s (1970) experiment was conducted at a Mach number of 1.62 where the shock train was of the λ-type. The results from Tamaki et al. (1970) are neatly reproduced by Matsuo et al. (1999) in Figure 2.4. Here it is clear by the large fluctuations along the centreline that the central flow is going through several compression and expansion waves. In the original data in Tamaki et al. (1970) the amplitude of the oscillation of pressure about the mean reduces with increasing distance away from the centreline. This continues out towards the wall until the pressure profile along the duct exhibits the same gradual increase as seen in the wall pressure measurements taken in the experiments of others.

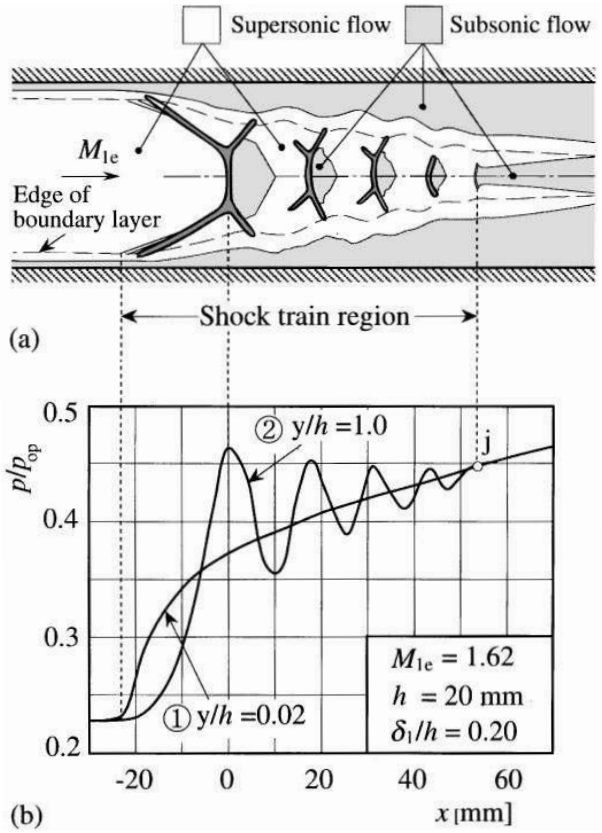

Figure 2.4: Static pressure distributions and flow structure sketch for a shock train in constant area duct. Figure (a) shows a sketch of the flow structure in the shock train region and figure (b) shows the static pressure distributions along the centreline ($y/h = 1.0$) and a line close to the wall ($y/h = 0.02$). (Figure sourced from Matsuo et al. (1999)), which is based on experimental data from Tamaki et al. (1970).)

Waltrup and Billig (1973) conducted similar experiments at a higher Mach number of 2.72 where the shock train was of the *X*-type. The results from these experiments are presented in Figure 2.5. As visualisations of the flow through the round duct were not able to be taken, Waltrup and Billig (1973) through oblique shock and expansion wave theory were able to resolve the shock structure based on Pitot pressure measurements taken along a line close to the centreline of the duct. This structure is shown in the upper portion of Figure 2.5 which shows that the flow goes through a series of shocks and expansion waves. The Pitot pressure profile calculated from this structure is overlaid on the measured Pitot pressure in the two graphs at the bottom. The agreement between the calculated and measured pressure profiles, for the peaks and troughs, is better along a line close to the centreline ($r = 0.125$ in) than along a line close to the wall ($r = 0.375$ in). This deterioration in the agreement between the measurements and the calculations with increasing distance from the centreline is attributed to the diffusion by the boundary layer and also to the interaction of the Pitot probe with the boundary

layer. From the comparison of the calculated and measured Pitot pressures, Waltrup and Billig (1973) were able to indicate the general character of the shock structure. They argued that "both the compression and expansion processes in reality consist of a multiplicity of waves which produce continuous rather than step changes in the [Pitot] pressure." Waltrup and Billig (1973) also noted that the calculated pressure ratio across the first shock compared well with the other separation criteria data from Mager (1956). This study by Waltrup and Billig (1973) also confirmed that the flow exiting the duct is primarily supersonic for pressure ratios less than the corresponding normal shock value.

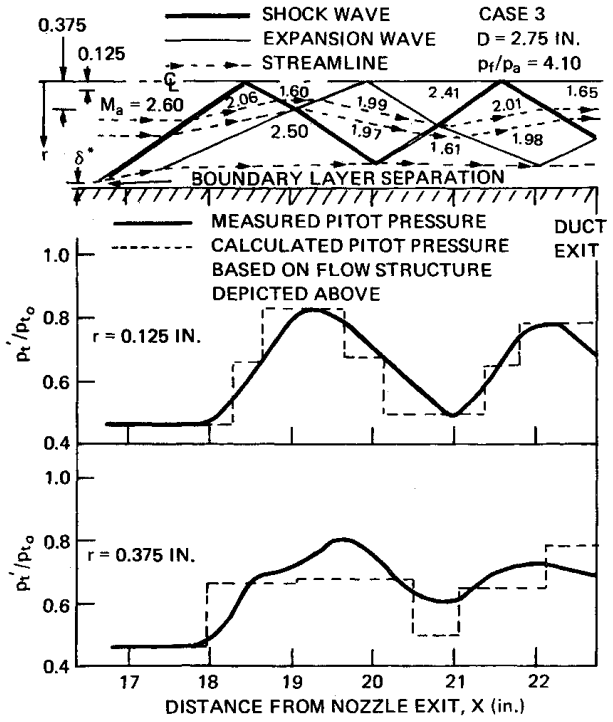

Figure 2.5: A simplified representation of the shock structure of a shock train (top figure) along with measurements from Pitot pressure surveys (bottom figure) from Waltrup and Billig (1973). (Figure sourced from Waltrup and Billig (1973).)

Following on from the comparison of calculated and measured Pitot pressures, Waltrup and Billig found a striking similarity in pressure profile along the duct across various cases tested in terms of the shape and slope. When they aligned each profiles by matching a point of the same pressure ratio they found that the curves would superpose. This is illustrated best in Figure 2.6a which shows the pressure distributions where they have been aligned by the point of separation. In this figure a selection of Waltrup and Billig's test cases are shown, which are grouped by the Mach number. For each Mach number group there are two tests where the imposed throttled pressure

(p_f) of one test is a fraction of the other. Here the superposition is quite clear with the tests of each pair being almost indistinguishable. From this superposition Waltrup and Billig argued that the wave structure of tests with a lower imposed pressure represents "a proportional part of the wave structure in the maximum case" and that this suggests that the shock structure is independent of its location of the duct.

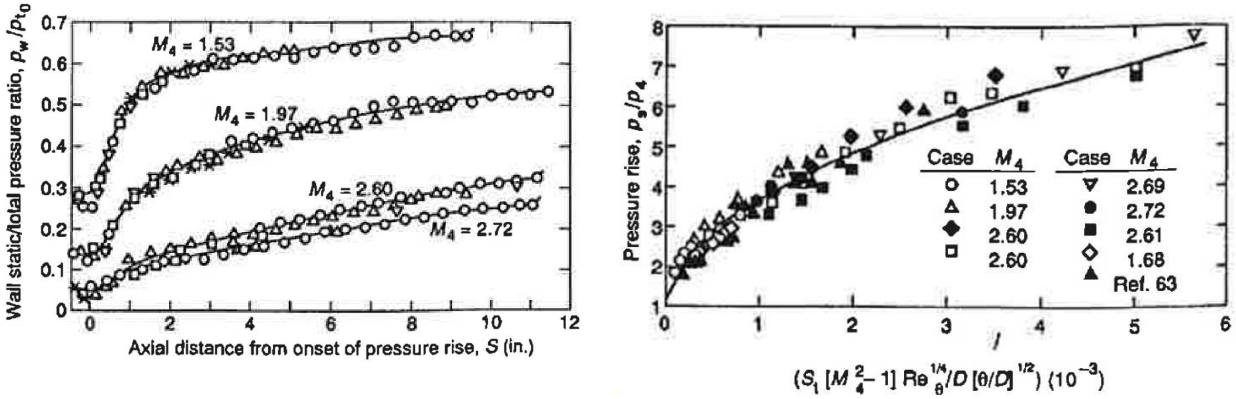

(a) Normalised wall pressure distributions. **(b)** Collapsed set of wall pressure data.

Figure 2.6: Experimental results from Waltrup and Billig (1973) illustrating the superposition of the shock structure in a cylindrical duct. Figure (a) shows the wall pressure distribution, normalised by the total pressure, through the shock train for selected pairs of tests. The pairs are represented by the △ and ○ symbols. In addition, a line is plotted which represents the average of each pair of tests. A total of four pairs are shown at different Mach numbers. For each pair, the Mach number was held constant and the throttled pressure (p_f) was adjusted. Figure (b) shows the duct exit pressure, normalised by the duct entry pressure, versus a quadratic equation (Equation 2.1) determined from a regression analysis of key test parameters including the shock train length (S_t). All tests collapse about this single curve prescribed by this quadratic equation. (Figures sourced from Billig (1993).)

Next, Waltrup and Billig explored the parameters that influence the shock structure. They argued that, for a given pressure ratio imposed, the shock structure is governed by the properties of the boundary layer. From their regression analysis, Waltrup and Billig were able to deduce a power-law relationship based on certain boundary layer parameters. They found that for a given pressure ratio across the entire length of the disturbance (p_f/p_i) that the length of the shock train (S_t) varied (approximately) directly with $\theta^{1/2}$ and $D^{1/2}$ and inversely with $M_i^2 - 1$ and $Re_\theta^{1/4}$ where θ is the boundary-layer momentum thickness of the undisturbed flow, D the duct diameter, M_i the Mach number of the incoming flow and Re_θ the Reynolds number based on the boundary-layer momentum thickness. From this they established an empirical quadratic relation for the shock train length for a constant area duct which is given in Equation (2.1).

When this equation is applied to their results, all the data collapse around a single curve as shown in Figure 2.6b.

$$\frac{S_t \left(M_i^2 - 1\right) Re_\theta^{1/4}}{D^{1/2}\,\theta^{1/2}} = 50 \left(\frac{p_f}{p_i} - 1\right) + 170 \left(\frac{p_f}{p_i} - 1\right)^2 \tag{2.1}$$

From their own investigations into X-type shock trains, Tamaki et al. (1971) developed a more refined sketch of the processes which the flow undergoes through this type of shock train, and this sketch is reproduced in Figure 2.7. This sketch was developed from schlieren photographs which indicate that the X-type shock train has more shocks and a longer shock region than the λ-type shock train. Interesting to note is that the sketch by Tamaki et al. (1971) includes the same features identified by Waltrup and Billig (1973) in that the compression and expansion processes consist of a multiplicity of waves. Tamaki et al. (1971) from their studies found that the total pressure decrease across the leading shock for the λ-type is about 70% of the overall pressure loss over the entire shock train whereas for the X-type the total pressure loss is about 25%. The reason for this is that the flow in the λ-type passes through a nearly normal shock wave while for the X-type the initial shock system is primarily made up of an oblique shock wave with only a small or non-existent normal shock wave (Section B–C in Figure 2.7a). Additionally, as there are additional shocks for the X-type shock train, compared with the λ-type, then there is further total pressure loss from these additional shocks, which reduces the proportion of the pressure loss of the first shock system.

Waltrup and Cameron (1974) investigated the skin friction along the separated region of a shock train using a JHU/APL designed floating head, strain-sensing skin-friction balance. They found that the magnitude of measured shear force in the separated zone was indeed negative indicating that the separated flow was recirculating. They found that the largest magnitude of the negative wall shear occurs immediately behind the initial oblique shock, which emanates from the fore position of the separated region. The smallest magnitude of the negative shear occurs immediately behind the first and strongest expansion wave. This trend continues down the duct for each reflection of the initial shock and expansion waves. Additionally, from a Pitot survey of the boundary layer they showed that the boundary layer ahead of the separation

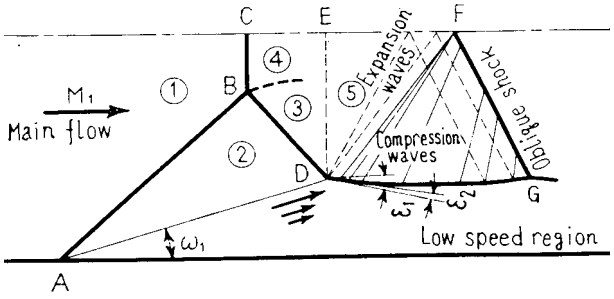

(a) Sketch of the flow processes through the initial shocks an oblique (X-type) shock train.

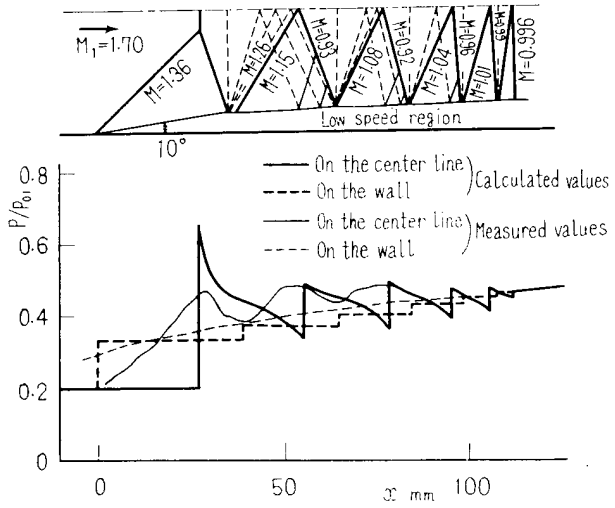

(b) Sketch of the flow field (upper) and the calculated and measured static pressure distributions (lower) through the entire shock train.

Figure 2.7: Pseudo-shock model by Tamaki et al. (1971) with (a) a sketch showing the flow processes through the initial shocks of an oblique (X-type) shock train and (b) a sketch of the flow field with the corresponding static pressure distributions (both measured and calculated from their model) through shock train to the terminal subsonic state. The Mach number of the incoming flow (M_1) was 1.70 and the assumed wedge angle (ω_1) is equal to 10°. (Figures sourced from Tamaki et al. (1971)).

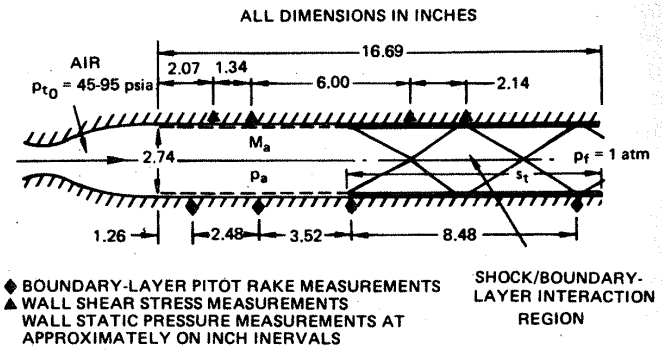

(a) Schemetic of test set-up, instrumentation and flow structure.

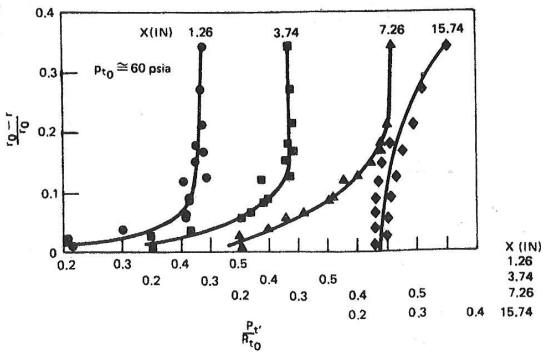

(b) Pitot pressure profiles of the boundary layer.

Figure 2.8: Waltrup and Cameron's (1974) shock train experiment which took measurements of shear stress at the wall and Pitot pressure across the boundary layer. (Figured sourced from Waltrup and Cameron (1974).)

develops as expected with the Pitot pressure increasing rapidly from near the wall towards the centre of the flow. This illustrates the power-law type velocity profile of a typical undisturbed boundary layer, whereas for the separated region the Pitot pressure was nearly constant which indicates a separated shear layer.

For the case of a shock train where the outflow of the duct is subsonic, the total pressure rise across the shock train proper does not account for all the pressure rise across the duct. There is additional pressure rise after the terminal shock due to mixing of the supersonic and subsonic flow. Figure 2.9 is reproduced from Matsuo et al.'s (1999) review paper in which they delineate the pressure rise from the shock train and the pressure rise from the subsequent dissipation. The shock train begins and ends by the series of identifiable shocks, which is then followed by a region of mixing of supersonic flow and subsonic flow. Subsonic flow resides in the detached boundary layer and in the small regions in the centre of the duct which lie behind sections of shock structure that are normal to the flow. Together the shock train and this region of diffusion from mixing make the pseudo-shock. It is called a "pseudo-normal-shock" by Matsuo (though commonly referred to in the literature as simply a 'pseudo-shock') as together the pressure rise is almost that which would have been generated by a single normal shock.

It is important to note that, for a constant area duct, if the outflow is subsonic then the shock train is classed as a pseudo-normal-shock. For the same duct, if the flow is also attached at the exit then only a single solution exists, which is the pressure ratio across a normal shock and hence a normal shock or pseudo-normal-shock exists somewhere in the duct (McLafferty, 1953). However if the flow is not attached at the end of the constant area duct (i.e. the boundary layer separates and does not reattach/reform) then there is a solution where the pressure ratio across the duct is less than that of a normal shock (Heiser and Pratt, 2000). Additionally, if there is heat exchange along the duct or mass addition, then again the flow is not limited to the single solution of a normal shock. It is under these last three scenarios (detached flow, heat exchange and/or mass addition) that allow for a shock train where the Mach number of the core flow exiting the duct can be supersonic.

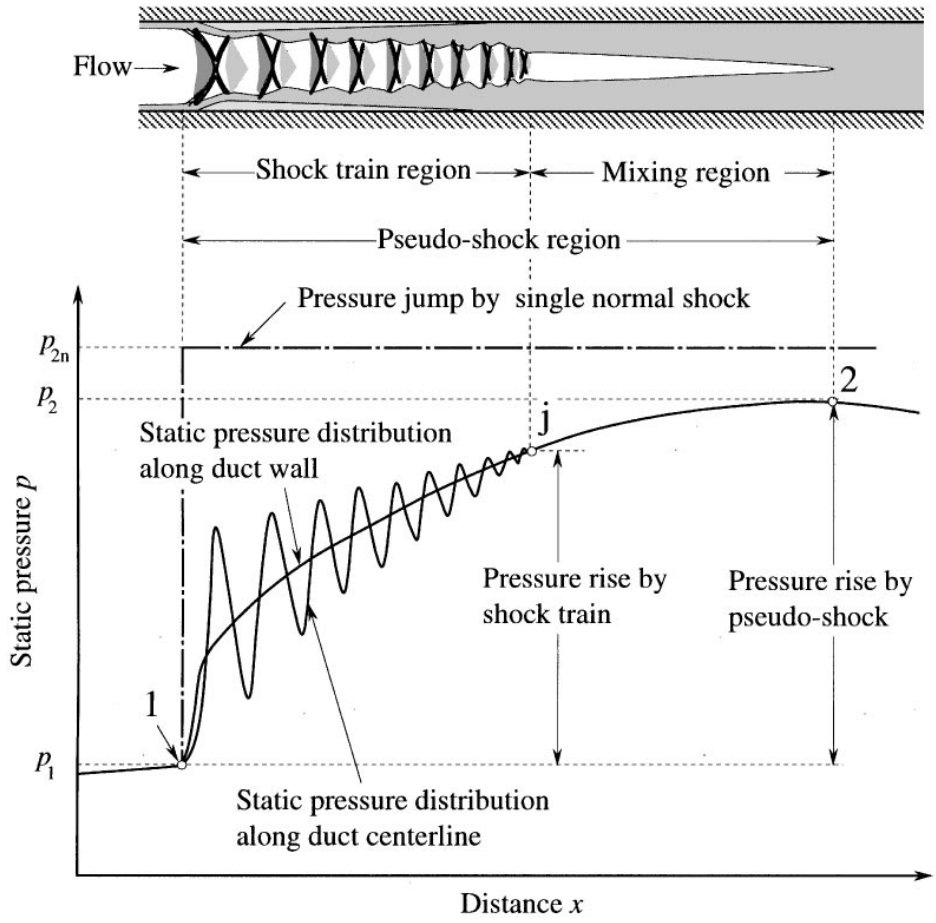

Figure 2.9: A schematic of the pseudo-normal-shock containing both an illustration of the flow structure and a depiction of the static pressure rise through the shock train along both the centreline and the wall of a duct. Grey areas represent regions of subsonic flow. (Figure sourced from Matsuo et al. (1999).)

In addition to the optical diagnostics and pressure measurements discussed, more sophistical optical techniques have been employed to investigate the velocity of the flow through the shock train. Using both schlieren and non-intrusive two-component laser Doppler velocimetry (LDV), Carroll and Dutton (1990, 1992) profiled the velocity of the flow through the shock train including the interaction with the boundary-layer. This provided great insight into the acceleration and deceleration process which the flow undergoes, particularly in the low speed areas near the wall. Their experiment consisted of a rectangular duct with an inflow at a Mach number of 1.6. With this setup they were able to generate multiple normal-shock boundary layer interactions along the duct. Their shock trains exhibited similar characteristics to the shock trains produced by Tamaki et al. (1970, 1971) where the first shock is a bifurcated normal shock, followed by non-bifurcated normal shocks which are increasingly weaker with distance downstream. Their velocity component data revealed that immediately behind the bifurcated and unbifurcated shocks that the flow is re-accelerated by two distinct expansion processes. The first expansion process is through a supersonic expansion fan which originates near the wall at the shock boundary layer interaction. The second expansion occurs through the displacement effect of the boundary layer which imposes on the core flow a flow field similar to a converging-diverging nozzle. These processes are illustrated in their sketch shown in Figure 2.10.

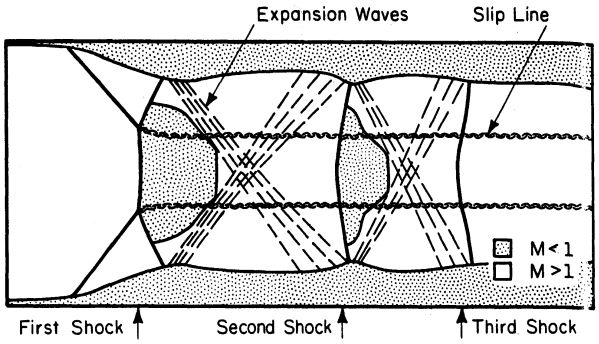

Figure 2.10: Sketch of the flow re-acceleration and deceleration processes inside a shock train. (Figure reproduced from Carroll and Dutton (1992).)

As seen in the work by Lustwerk (1950) and Ikui and Matsuo (1969), for sufficiently high Mach number and level of flow confinement, the separation of the boundary layer can lead to a highly complex flow where the system of shocks which forms around the incipient separation is repeated along the duct for many diameters. The results from Carroll and Dutton (1990, 1992), in conjunction with the sketch from Tamaki et al. (1970, 1971), help explain why the structure repeats itself along the duct. For high enough

Mach numbers the processes identified by Carroll and Dutton (1992) are sufficient to re-accelerate the flow back through one. Once above one, any subsequent boundary layer separation or sufficient growth in the boundary layer will result in another shock similar to the preceding one. This process of normal shocks, coupled with diffusion from mixing, repeats itself until the bulk of the flow reaches a limiting sonic state (similar to the terminal point on a Fanno flow diagram).

Colour schlieren is useful in distinguishing features that might not be possible in grey-scale schlieren (Settles, 2001). Sugiyama et al. (2006) took advantage of this when they employed a colour schlieren system, using a horizontal colour slit, to investigate both λ-type and X-type shock trains. Their experiments were run at Mach numbers of 2 and 4 using a blow down supersonic wind tunnel. Two of their results are shown in Figure 2.11. These images clearly show the λ shape of the shock train at Mach 2 and the X shape in the core flow at Mach 4. It is interesting to compare Figure 2.11a with the schematic in Figure 2.10 by Carroll and Dutton (1992) and to note the striking similar characteristics present in both images. For example, even the expansion wave emanating from the base of the second foot of the first λ shock as drawn in Figure 2.10 can be just made out in Figure 2.11a. In general, the results by Sugiyama et al. (2006) show there is a strong coupling between the separated boundary layer and the structure of the shock train, and that this coupling produces a highly complex flow. For the tests performed at the higher Mach number of 4 (Figure 2.11b) the results show that the separated boundary layer grows very rapidly from the point of separation and that this provides considerable compression of the core flow.

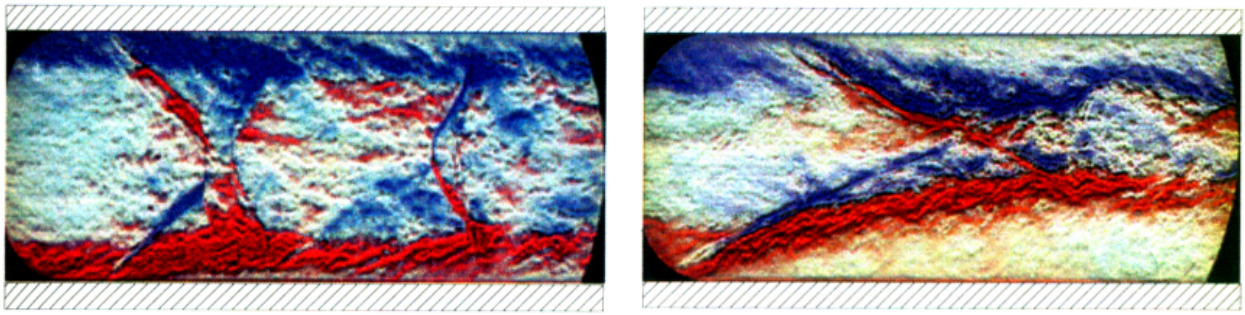

(a) Case B at Mach 2: $S_t/D \approx 7.9$, $\delta/H = 0.25$ **(b)** Case C at Mach 4: $S_t/D \approx 13.8$, $\delta/H = 0.47$

Figure 2.11: Colour schlieren photographs of a shock train. (Images sourced from Sugiyama et al. (2006).)

2.1.1 Shock trains and non-circular cross sections

The cross-sectional shape of a duct can have an effect on the formation of shock-trains and pseudo-normal-shocks (Penzin, 1995). Early studies focused on investigating shocks trains in circular ducts (Waltrup and Billig, 1973) and in rectangular ducts (Bement et al., 1990; Carroll and Dutton, 1990; Kawatsu et al., 2005; Merkli, 1976; Sullins and McLafferty, 1992). Some initial research has been carried out on novel cross-sectional shapes such as shape transition engines, for example the rectangular-to-elliptical transition (REST) inlet (Turner, 2010) and the racetrack-to-circular transition isolator (Bagaveyev et al., 2010), and on engines with chamfered corners (Grendell, 2004).

Lin (1993) and Lin et al. (2006) explore this effect of cross-sectional shape on shock trains numerically and experimentally respectively and found that a round isolator could withstand a higher back pressure before unstarting than could a rectangular isolator. Lin (1993) also found that shock train length scaled with the hydraulic diameter, which is in agreement with Waltrup and Billig's (1973) empirical relation. The general findings of Lin (1993) and Lin et al. (2006) are consistent with the findings of Nedungadi and Van Wie (2004) who, in their numerical study of shock trains, explored a number of rectangular isolators with a range of aspect ratios and identified that the flow in the corners was a critical feature. They found that the flow is separated in the corners for all cases where the Mach number is between 2 and 4. This corner flow mechanism identified by Nedungadi and Van Wie (2004) is critical to the formation of the shock train proper in the duct. However this mechanism by which initiate shock trains in planar ducts is poorly understood and warrants further study.

2.1.2 Shock trains and asymmetric boundary layers

The condition of the boundary layer upstream of the interaction has a strong influence on the formation of shock trains and hence, also on the characteristics of inlet/engine unstart. Do et al. (2011) investigated supersonic inlet unstart using a Mach 5 wind tunnel, in conjunction with wall pressure measurements, they employed planar laser Rayleigh scattering using CO_2 particles to visualise the flow dynamics. By using a central plate they were able to split the flow into two similar flows and generate a series of reflected shocks through the region of observation. They initiated the inlet

unstart by injecting additional air via a jet perpendicular to the main flow some distance downstream of the leading edge of the splitter plate. For these experiments, Do et al. (2011) found that the state of the incoming turbulent boundary layer and its degree of symmetry strongly affects the unstart dynamics. For relatively thick turbulent boundary layers they found that, for cases where the boundary layers were asymmetrical, a thick boundary layer leads to unstart shocks. Whereas for cases where the boundary layers were symmetrical a thick boundary layer leads to the propagation of weak compression waves, which forms a pseudo-shock system. This pseudo-shock system remains quasi-stable for a period of time before the flow structure breaks down completely, causing an inlet unstart. Do et al. (2011) also found that the behaviour of the shock train was influenced by whether the boundary layer was initially turbulent or laminar. For thin (initially laminar) boundary layers, they found that the shock train appears stable for approximately twice as long as the cases where the boundary layer was forced to be turbulent (by trips upstream). In general, the studies by Do et al. (2011) show that as the shock train involves shock waves which impinge the boundary layer, through which pressure disturbances can propagate, the state of the boundary layer can produce local conditions that can strongly affect the propagation speed of the disturbance.

2.1.3 Oscillatory nature of shock trains

An aspect of the shock train which has been of interest is their self-excited oscillatory nature. This nature was observed early on by Ikui et al. (1974b) and has continued to be the focus of studies more recently by Sugiyama et al. (1988), Le et al. (2008a,b), Tan et al. (2009) and Wagner et al. (2009). Ikui et al. (1974b) note that previous investigations into shocks trains were able to explain the time-mean static pressure distributions, however in reality the shock train oscillates about a mean position which results in fluctuations of the local static pressures. Ikui et al. (1974b) found from their own shock train experiments that the amplitude of the fluctuations in pressure due to the oscillation could amount up to 60% of the total pressure difference across the entire shock train. They also found that the strength of the oscillation of the shock train scales with Mach number. Ikui et al. (1974b) observed that the frequency of the oscillations depend on the geometry of the duct. From spectral density analysis of the data, they revealed that the oscillations of the shock trains in their tests had two prominent peaks of multiples of 10 Hz and 100–200Hz, which they note correspond to the Helmholtz resonance and the pipe resonance respectively. Ikui et al. (1974b), using a one-dimensional model where

the inflow was given a small perturbation, calculated the displacement of and pressure ratio across the shock train. The results from their calculations agree qualitatively with the amplitude of the oscillation of the shock train observed in their experiments. From this analysis, Ikui et al. (1974b) propose that the oscillation of the shock train may be caused by the interaction of the shock train with small perturbations in the supersonic flow upstream of the shock train.

Sugiyama et al. (1988) investigated, using high-speed schlieren photography in conjunction with wall pressure measurements, the oscillatory nature of the two types of shock trains (λ and X types) commonly encountered. They found that for the λ-type that the upstream location of the shock train would oscillate with an amplitude of $\Delta X/D = 0.2$ and at a low frequency of 40 Hz. For the X-type, the amplitude of the spatial oscillations were $\Delta X/D = 0.3$ and they oscillated at a low frequency of less than 70 Hz and also at high frequencies of about 150 Hz to 250 Hz. In the case of λ-type the fluctuations in pressure were greatest at the leading edge shock; whereas for the X-type the pressure fluctuation were greatest between the first and third shocks. As a fraction of the total pressure change across the pseudo-shock or shock train (ΔP_{PSW}), the largest pressure fluctuations for the λ and X-type shock trains were $0.35\Delta P_{PSW}$ and $0.55\Delta P_{PSW}$ respectively. Sugiyama et al. (1988) note that difference in the location of the largest pressure fluctuations between these two types of shock trains is explained by the fact that for the λ type, the majority of the pressure rise is across the first shock whereas for the X-type the majority of the pressure increase is spread over a greater number of shocks.

Although Ikui et al. (1974b) posed the possibility that the oscillatory nature of the shock train was in response to the perturbations in the flow upstream of the shock train, they were unable to conclude definitely that this was the case and not an inherent feature of the shock train phenomenon. Another (or contributing) cause argued by Li et al. (2007) and Le et al. (2008a,b) is that oscillations may be caused from acoustic waves generated by unsteady combustion which travel upstream via the subsonic boundary layer and recirculation zones (Choi et al., 2005). This is supported by the findings from Micka and Driscoll (2009) who found, in their study of a dual-mode scramjet with a cavity flameholder, that at the highest total temperature condition they tested that the reaction zone would oscillate between two different locations along the engine. Matsuo et al. (1999) note in their review paper of shock trains that the present understanding of these types of unsteady flows is rather limited as not enough of the

necessary basic data has been collected. They conclude their section on the oscillatory nature of shock trains with the statement: "The reason and flow mechanism of self-excited oscillation of the pseudo-shock have been left unsolved until now."

2.1.4 Flow establishment times for shock-trains and pseudo-normal-shock

If the shock trains are to be studied in impulse facilities, which have a short test time, then the question arises as to whether the test times will be sufficient for the shock train to reach a steady state within the available test time. There is little in the literature on the establishment times of shock trains, and as such, the general literature on separated flow is consulted.

Flow establishment times in shock tunnels have been investigated experimentally and numerically in previous studies (Davies and Bernstein, 1969; East et al., 1980; Jacobs et al., 1992). These studies correlate flow establishment time with the number of flow lengths. From these studies it is generally accepted that for the flow to reach steady state then 3.3 model lengths needs to flow past the model for an attached laminar boundary layer and 2 model lengths for an attached turbulent boundary layer. However for separated flow, such as behind a step or bluff body, the establishment time is much longer. Holden et al. (1997) found for flow behind a bluff body mounted on sting that it took between 35 to 50 body diameters for the flow to pass the model for the flow to establish. Findings of a similar magnitude were made by Hayne et al. (2005) who found that for recirculating zones behind a backward facing step that the number of flow lengths required was approximately 60 to 70 step heights. For the recirculating flow in the corner of an inclined wedge on a flat plate, where a shock boundary layer interaction exists, Holden (1971) reported the establishment flow time was the time it took for an acoustic wave to traverse the distance of the interaction.

From his experiments Holden (1971) distinguished that the general flow establishment process could be separated into two mechanisms. The first one would be the initial establishment associated with the propagation of an acoustic wave from the controlling point to the forward extremity of the interaction region. Examples of a 'controlling point' are the neck or throat of a base region, or where the boundary layer

reattaches downstream of a recirculating region. The second mechanism, which follows the first, was the time it took for the separated region to reach equilibrium through viscous and inviscid interactions. Holden argued that these two mechanisms in hypersonic flows are of the same order. From an argument of similitude, Holden proposed that the characteristic establishment time could be described as:

$$(t_{\text{est}} \cdot U/L) = T\left(M_e, Re_L, T_w/T_o\right) \tag{2.2}$$

where t_{est} is the establishment time defined as reaching 98% of the steady state value, U the local speed of sound, L the characteristic dimension related to the length of the interaction region, M_e the Mach number of freestream, Re_L the Reynolds number (based on L), and T_w/T_o the temperature ratio at the wall. From his study of flow over spheres, Holden found that over the range of conditions studied that the non-dimensional establishment time is weakly dependent on the Mach and Reynolds numbers of the freestream, is directly proportional to the scale of the separated region and is inversely proportional to flow velocity. Holden concludes that as the flow establishment time was significantly longer than the acoustic time, then the dominant mechanism in attaining flow equilibrium in the large separated regions is the establishment of viscous mixing. Holden notes that, however for the shock-wave boundary layer interaction, the length scales of the interactions are very small in comparison with those in the case of the spheres and so the additional time required beyond the acoustic propagation time is small. In these cases, the speed of sound at the wall (a_{w}) could be substituted for the flow velocity (U) in the non-dimensional establishment time ($t_{\text{est}} \cdot U/L$). This indicated to Holden that for shock-boundary layer interactions in high temperature hypersonic flows the establishment time is strongly dependent on the size and geometry of the interaction; whereas for separated base flows (such as behind a sphere) the establishment time is dominated by the viscous mixing process.

It is not known how these correlations might apply to shock trains. The characteristic length could be either the height of the separation or its length. If the characteristic length of a shock train were to be based on the height then for the largest permissible separation, one which has a height of half the duct, then 60 to 70 flow lengths would correspond to 30 to 35 duct diameters. This flow length is achievable in impulse facility despite the fact that the models are generally long and slender. However, if the characteristic length for the establishment time of a shock train were to be based on the longitudinal length of a train, then for a shock train which exhibits a similar length to

that found by previous researchers in other facilities of 8 to 12 duct diameters (Neumann and Lustwerk, 1949) then the resultant establishment flow length of 480 to 840 duct diameters would be well outside the test time of a shock tunnel.

Another characteristic of shock trains which may pose a problem for experiments in impulse facilities is the self-excited oscillations observed of shock trains and pseudo-normal-shocks, as discussed in Section 2.1.3. Ikui et al. (1974b) and Sugiyama et al. (1988), from observations of pseudo-shock oscillations in constant area ducts, have found that the amplitude of the shock oscillation, and the corresponding pressure fluctuations, both increase with an increase in the Mach number of the flow upstream of the shock. If this trend in the oscillatory nature of a shock train continues into the higher Mach numbers, then this oscillatory nature may be substantially amplified due to the relatively unsteadiness of the test flow of shock tunnels (compared with other facilities). Finally, for scramjet engines, the strength of the shock train also influences the flow entering the combustion region and this in-turn affects combustion. This can add yet another feedback mechanism which may futher extend the establishment time of a pre-combustion shock train.

Given the lack of data on the establishment time of shock trains and that the amplitude of the oscillations scale with Mach number, at least at low Mach numbers, then the question still remains as to whether the study of pre-combustion shock trains is feasible in short duration shock tunnels at high Mach numbers.

2.2 Pseudo-Shock and Shock Train Analytical Models

There are a number of pseudo-normal-shock and shock train models in the literature, with varying degrees of agreement with experimental data; such as the diffusion model (Ikui et al., 1974a), the modified diffusion model (Ikui et al., 1981), the submerged jet model (Zimont and Ostras, 1976), the momentum balanced model (Kanda and Tani, 2005) and the shock reflection model (Tamaki et al., 1971) to name a few.

Crocco (1958) was the first to propose a shock train model, which is depicted in Figure 2.12. He postulated a 'shock-less' or 'jump-less' model of the phenomenon. Crocco considered that the total entropy increase due to successive shocks would be

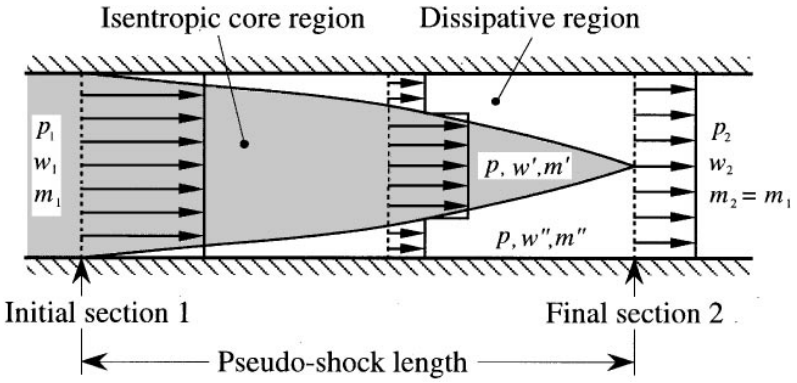

Figure 2.12: Shockless model of pseudo-shock by Crocco (1958). (Figure sourced from Matsuo et al. (1999))

negligible compared with a single normal shock. Crocco also assumed that the dissipation of kinetic energy change across the shock(s) is also negligible compared with the dissipation due to viscous mixing in the turbulent flow. From this he disregarded the presences of shocks entirely and considered that the core flow to be uniform and that it undergoes isentropic compression over the pseudo-shock region. The remaining non-uniform dissipative region near the wall was treated by Crocco as an equivalent uniform region which grows with distance downstream. Using this model, appropriate average values can be calculated for each region of flow along the pseudo-shock interaction.

Ikui et al. (1974a) found through their analysis of their experimental results that the prevailing theoretical model of the pseudo-shock system at the time, Crocco's (1958) shock-less model, was insufficient in explaining all the aspects of the flow. Ikui et al. (1974a) identified the following problems with Crocco's (1958) model for shock-train phenomena: (1) it does not allow the prediction of the distribution of various quantities along the duct as all quantities are a "function of the flow rate of the dissipative low velocity region to the total flow rate," and (2) "there is [a] discrepancy of velocities between the high and low speed regions at the final section of pseudo-shock." Ikui et al. (1974a) argued that the pseudo-shock should not be regarded as a shock but as "dissipative phenomenon of the high speed flow in the central region with the low speed flow near the wall." From this reasoning, Ikui et al. introduce a 'diffusion model' (Ikui et al., 1974a), followed by the 'modified diffusion model' (Ikui et al., 1981), and they found favourable agreement with their experimental data for both models. Both the shock-less model by Crocco (1958) and the diffusion model by Ikui et al. (1974a), which is a modified form of the shock-less model, both give the same flow properties

at the end of the pseudo-shock, which is the same as the flow downstream of a normal shock. This is because both models assume the wall friction along the pseudo-shock region has no effect and that the flow is uniform both upstream and downstream of the shock (i.e. the models neglect the effects of the state of the upstream boundary-layer).

Another shock train model, which is used by dual-mode engine designers (Smart, 2007), is the empirical relation (Equation 2.3) by Ortwerth (2000). Ortwerth (2000) determined from experiments that the pressure rise through the entire shock train region is proportional to the dynamic pressure (ρV^2) and to the coefficient of skin friction at the point of separation (C_{f_0}), and inversely proportional to the hydraulic diameter (D_H) of the duct.

$$\frac{dP}{dx} \approx \frac{89}{D_H} C_{f_0} \left(\frac{\rho V^2}{2} \right) \tag{2.3}$$

The validation data for this model is shown in Figure 2.13. When Tu and Segal (2010) applied this model to their combustor-isolator interaction experiments, they found that the model predicted the shock train length within an accuracy of 20% over a range of isolator entrance Mach numbers from 1.5 to 5, which included ducts of various shapes, differing Reynolds numbers and friction coefficients. The model is implemented in the cycle analysis code by Smart (2007) and has been used to analyse the performance of scramjet engines by Turner and Smart (2010) and by Doherty (2007), who used this code to analyse the experimental results out of *JAXA* from Kobayashi et al. (2006), where he found good agreement (see Figure 2.14).

A common requirement of some of the aforementioned models is that detailed information about the boundary layer is required, however this information can be difficult to obtain from experiments. As such there can be a large degree of scatter about these correlations. This is partially avoided with Ortwerth's model as there is only a single parameter pertaining to the boundary layer which needs to be calculated/estimated prior, which is the skin coefficient at the point of separation (C_{f_0}). This value can be determined from similar experiments or from boundary layer codes without too great a variation in results. As there is validation data for this model up to a local Mach number of 5, it this model which has been adopted for this research and is used in the subsequent cycle analysis of the experimental results.

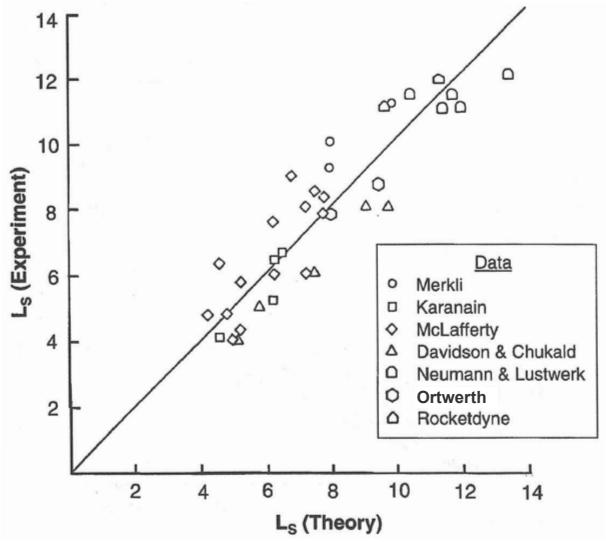

Figure 2.13: Validation data for the Ortwerth (2000) diffusion model for the length of a pseudo-normal-shock. (Sourced from Ortwerth (2000))

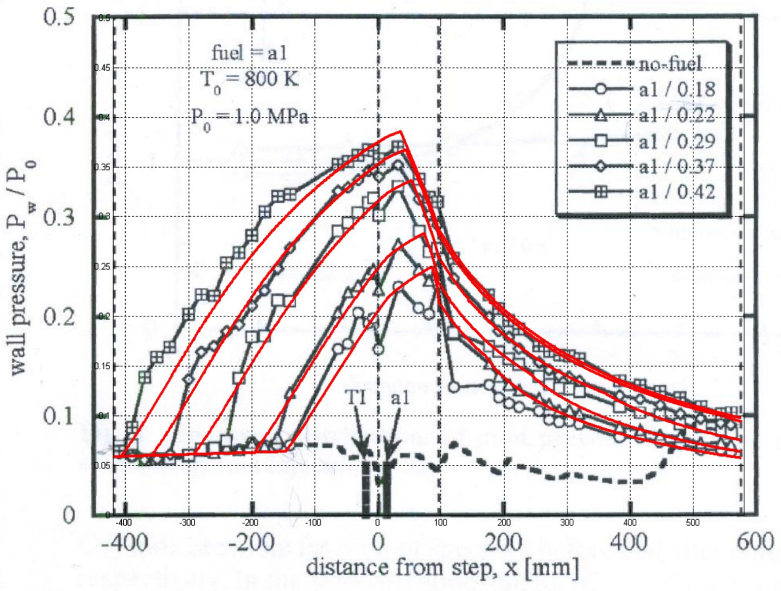

Figure 2.14: Application of the Ortwerth (2000) diffusion model using Smart's (2007) methodology to data from Kobayashi et al. (2006) by Doherty (2007). The red lines represent the pressure profile as computed by the cycle analysis in Doherty (2007).

2.3 Scramjet Ground Test Facilities

Before discussing the research of shock trains and combustion, it is worth first reviewing the type of facilities which are capable of producing conditions suitable for scramjet testing. Scramjet research is generally conducted in non-continuous wind tunnels due to the large power required to generate hypersonic flow (Lu and Marren, 2002b). Fig-

ure 2.15 plots the various facilities which can produce hypersonic flight test conditions. As indicated in Figure 2.15, the simulation of combustor flows, towards the lower end of the scramjet flight regime, can be performed with test flows which are not necessarily hypersonic when direct or semi-direct connect testing is employed. (However high total enthalpies and total pressures are still required.) Due to the use of such techniques and the prevalence of blow-down facilities, the majority of the testing to date on dual-mode scramjet combustors have been performed in blown-down tunnels and relatively few in hypersonic shock tunnels. Both types of facilities are briefly reviewed next in regards to their applicability to and history of research relating to dual-mode scramjets.

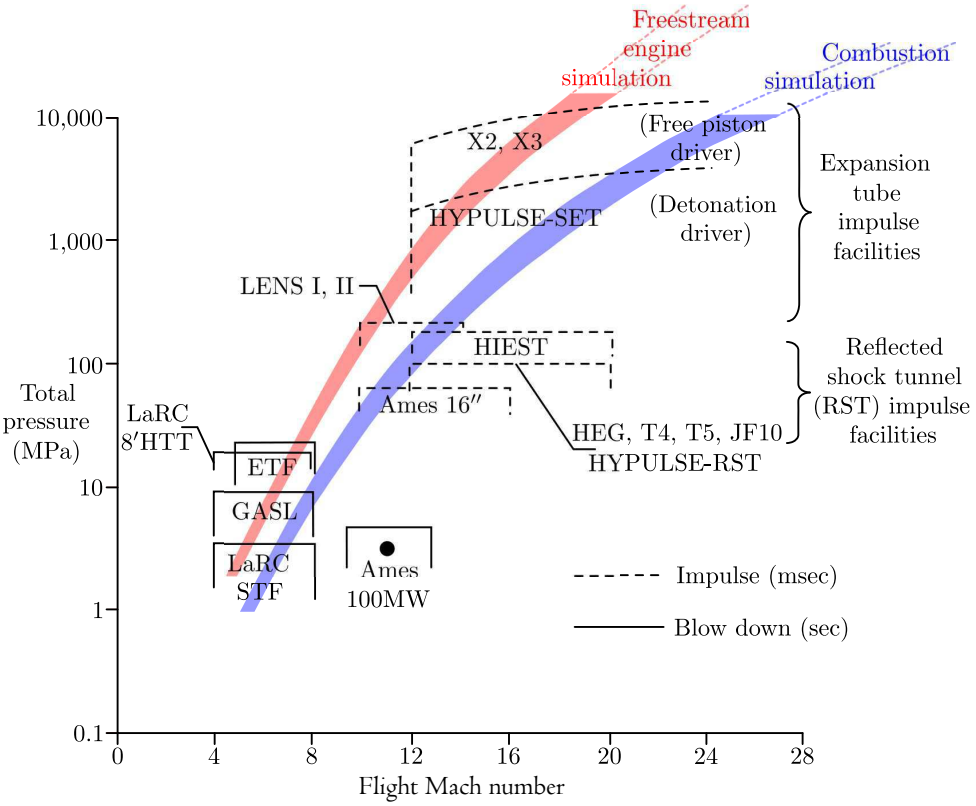

Figure 2.15: Total pressures of ground hypersonic flow facilities. (Original figure from Anderson (2001) with adaptations from Lu and Marren (2002a).)

Within the class of non-continuous wind tunnels are blow-down facilities and impulse facilities. Blow-down tunnels generate the required total pressures by compressing air into a reservoir over a relatively long time. This flow is then released through a nozzle to produce supersonic to hypersonic flows. To avoid liquefaction of the air when simulating hypersonic flows, the stagnation temperature needs to be raised above ambient. In order to minimise the pressure vessel requirements of the

reservoir, the fluid is usually heated downstream of the nozzle and upstream of the test section. This heating can be achieved via a number methods including electric arcs, lattice of heated stones/bricks or through combustion of the flow with an introduced fuel. In this last type of heating, the oxygen consumed during the heating process by combustion must be replaced to match the original gas composition of air. Although heated blow-down tunnels can achieve higher stagnation temperatures, the stagnation pressures are generally too low for true aerodynamic simulation. Additionally, these heated tunnels suffer from high contamination emanating from the various heating processes. Pellett et al. (2006) found that the large concentrations of water vapour which occur in vitiated air affects the bulk thermodynamic properties of the test gas. Also affected are the chemical kinetics of the gas by either the arc heating process or from combustion (Lu and Marren, 2002a). These kinetic effects can have a large effect on the reactions of the combustion experiments (Pellett et al., 2006).

Another form of non-continuous wind tunnels are the impulse type. Examples of such are gun tunnels, shock tunnels and expansion tubes. A number of the drawbacks of the cold and heated blow-down types of non-continuous tunnels are partially avoided by such facilities. Shock tunnels and expansion tubes achieve the high total pressures and total temperatures by processing the flow through one or more shock waves. Reflected shock tunnels stagnate the gas which supplies the nozzle. This allows for longer test time (1–5 milliseconds) compared with their non-reflected counterparts and expansion tubes. Within this class of reflected shock tunnels are Stalker Tubes. These tunnels use a free-piston, driven by gas from a reservoir, to achieve the high pressures in the driver tube which feed the reflected shock tube. It is this type of facility which is used in this study to achieve the high enthalpy flows required to conduct combustion experiments at Mach 8 flight conditions.

2.4 Shock Trains and Combustion

Many of the investigations into shock trains have involved imposing a back pressure, usually via a mechanical throttle, to generate the conditions suitable for a shock train to form (Emami et al., 1995; Ikui et al., 1980; Sullins and McLafferty, 1992; Tamaki et al., 1970, 1971; Waltrup and Billig, 1973, 1972). In the case of scramjets, this throttling has been used to simulate the back pressure generated by combustion and thereby study the pre-combustion shock train in isolation. This has allowed studies to be performed

in continuous flow facilities where the flow through the engine is cold compared with that which would be experienced in flight. Due to the predominance and lower costs of these facilities compared with hot flow facilities, relatively few studies have investigated shock trains which involve combustion. Billig and Dugger (1969) and Billig et al. (1971) conducted some of the earliest experiments involving supersonic combustion. In their experiments, they found a shock system would establish upstream of the injection point and this system could adversely interact with the intake of the engine. They defined this system as a "pre-combustion shock train" and they argued that the effects of the combustion, which cause this shock system, were being transmitted upstream through the subsonic boundary layer. In later tests, Billig et al. (1972) found that by introducing a section of constant-area, later called an 'isolator', between the inlet and the combustor that this provided adequate isolation between the combustor and intake. With this isolator installed they could extend the operation of the engine up to near-stoichiometric fuelling rates without unstarting the engine.

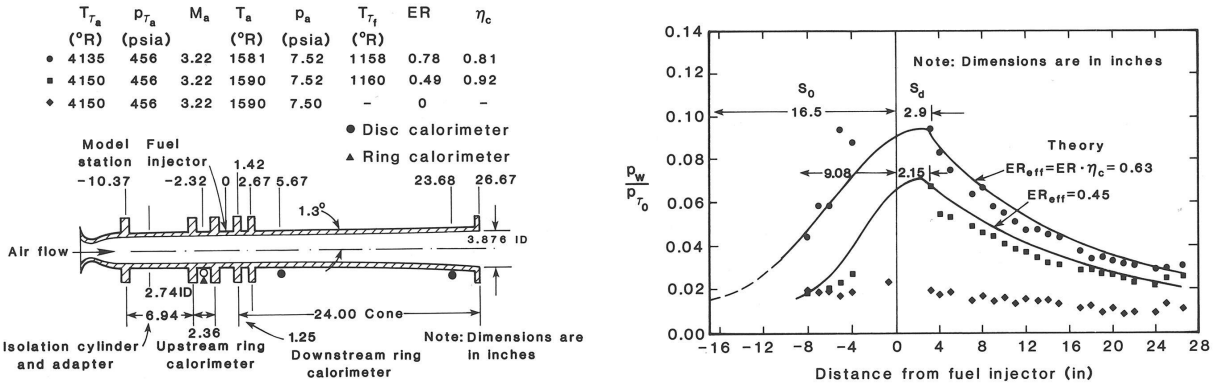

(a) Schematic of burner. **(b)** Axial pressure distribution.

Figure 2.16: Experimental wall pressure measurements from H_2-air combustion in a short cylinder-cone scramjet combustor from Billig et al. (1972) experiment. (Sourced from Fig. 6.26 of Heiser and Pratt (1994).)

Bement et al. (1990) extended Billig et al.'s (1972) investigation of pre-combustion shock trains in cylindrical ducts to rectangular ducts. The found in their semi-free jet tests, that the length of the shock train predicted by the empirical correlation (Equation 2.1) from Waltrup and Billig (1972) for cylindrical ducts compared well with the experimental results for their rectangular duct when the duct height was substituted for the duct diameter for the characteristic dimension.

Research by Kay et al. (1992a,b) is the first to appear in the literature which uses a hydrocarbon as the fuel instead of hydrogen in a dual-mode scramjet (both ethylene and JP-5 were tested in their experiments). At the United Technologies Research Center (UTRC) Ramjet/Scramjet Test Facility, Kay et al. used a novel air-breathing pilot flame and a combination of primary and secondary fuel injectors to achieve efficient supersonic combustion over a range of conditions equivalent to flight from Mach 3.5 to 7. They also demonstrated smooth transition from fully attached to separated boundary-layer flow.

Sullins (1993) tested an isolator-combustor in a direct-connect configuration using a vitiated air heated (VAH) wind tunnel at the John Hopkins University Applied Physics Laboratory (APL). Sullins (1993) was able to make the transition from ramjet to scramjet mode by holding the fuel-air equivalence ratio constant of 0.6 and accelerating the test flow from Mach 5.9 to 6.2. The pre-combustion shock, which was present in the ramjet mode, dissipated fully at the upper Mach number range with the engine operating in pure scramjet mode.

A substantial amount of dual-mode scramjet research has been conducted at the Japan Aerospace Exploration Agency's (JAXA) Kakuda Space Propulsion Center (KSPC), which has been well documented (Kanda et al., 2001; Kato et al., 2006; Kobayashi et al., 2006; Tomioka et al., 2006). The main facility used for their dual-mode scramjet work was the Mach 2.5 blowdown-type wind tunnel at KSPC. This facility is heated by way of combustion of the test flow with hydrogen. Additional oxygen is added to replenish the amount consume in combustion. A focus of much of the research at this institute has been on the tailoring of the location of fuel injectors to improve scramjet engine performance, particularly injecting in the divergent section of the combustion chamber. Their aim was to achieve combustion of the unburnt air through subsonic combustion in the divergent section rather than in the upstream constant area section of the combustion chamber. The motivation for this approach was that by tailoring the pressure release from the additional combustion to occur in the divergent section they could reduce the peak pressure of the engine. This has the advantage that more fuel can be burnt without increasing the size of the pre-combustion shock train and thereby increase the operational range of the engine. The experiments by Kato et al. (2006) demonstrates that when combustion occurs in the constant area section of the combustion chamber, the thrust produced by the engine is 20% to 30% higher than injecting the same amount of fuel in the divergent section of the combustion chamber.

However, when they injected in the divergent section, they were able to inject a larger amount of fuel before unstarting engine. The lower combustion efficiency associated with this injection scheme was more than offset by the increase in total combustion from the additional fuel. So by using this approach, Kobayashi et al. (2007), at Mach 4 flight equivalent conditions, were able to increase the maximum thrust by 62% for their engine. When fuel was injected in both the constant area and the divergent section, the maximum thrust is increased by a further 39%.

Shocks trains involving combustion have been investigated as part of a number of transition studies of dual-mode scramjets (Bagaveyev et al., 2010; Denis et al., 2003; Goyne et al., 2007; Haw et al., 2011; Le et al., 2005; Masumoto et al., 2009; Rockwell et al., 2010; Sullins, 1993). As discussed in Section 2.3, in which scramjet test facilities are reviewed, Pellett et al. (2006) found that the large concentration of water vapour in vitiated air affects the bulk thermodynamic properties of the test gas. This is important regarding scramjet tests as Edelman and Spadaccini (1969) have demonstrated that changes in the bulk thermodynamic properties of the fluid (through vitiation) lowers both the combustor exit temperature and the internal thrust generated for a scramjet engine. These vitiation effects on supersonic combustion have been further investigated by Mitani et al. (1997) who compared the performance of a scramjet in a storage air heater (SAH) facility with the performance in a VAH facility. They demonstrated that at a Mach 6 flight enthalpy that there were significant differences in performance for this engine between these two facilities. Mitani et al. (1997) found that the engine would self-ignite with vitiated air but not with clear air for a given fuelling equivalence ratio. This was attributed to the presence of radicals, such as H, O, OH and NO, in the vitiated flow.

Goyne et al. (2007, 1999, 2001) through numerous studies have explored these vitiation effects on the transition point of a dual-mode scramjet from one mode to the other. Goyne et al.'s work follows on from Mitani et al.'s work by specifically investigating the effects which water vapour and carbon dioxide have on this transition point. They achieve this by comparing the results from a scramjet combustor tested in an electric air heated (EAH) facility using dry air with the results in the same facility but with additional contaminates intentionally added to the flow. These additives were used to simulate the vitiation effects of a VAH facility. Goyne et al. (2007) demonstrate that at a Mach 5 flight enthalpy the combustion pressures, when compared with the baseline clean dry test flow were 10% lower for air vitiated with 5% H_2O and 12% lower for air

vitiated with a combination of 5% H_2O and 2.5% CO_2. This effect on combustion has a corresponding effect on the transition point of a dual-mode scramjet. Goyne et al. have shown in their tests that dual-mode operation occurs at a higher equivalence ratio for vitiated air than for dry air. Haw et al. (2011) and Rockwell et al. (2011) extend Goyne et al.'s (2007) investigation by lengthening the isolator which allows for higher equivalence ratios to be tested. They found that these trends in the effects of vitiation on the transition point continue up into the higher equivalence ratios.

Research by Noda et al. (2011a) extends the work by Rockwell et al. (2011) by taking the same engine design tested in the EAH facility to a VAH facility. The purpose of these tests was to investigate the effects of vitiation whilst matching total enthalpy, which were not matched in previous comparative study by Mitani et al. (1997). When Noda et al. compared their results from the VAH with those from the EAH by Rockwell et al. (2010), they found that when the conditions were matched for total temperature ($T_0 = 1200\,\mathrm{K}$) that the transition from supersonic to subsonic occurs at a much lower equivalence ratio (ϕ) for the EAH facility compared with the VAH facility. This also held true for a second VAH condition which was matched for total enthalpy (on a per molar basis) to the EAH condition. Noda et al. attribute this to vitiation effects promoting stronger combustion through a thermodynamic and/or chemical kinetic effect. The authors also noted that the difference between the tests from the VAH and EAH facilities when matched for total temperature were greater than the differences between these facilities when matched for total enthalpy. From this, they conclude that matching total flow enthalpy is more important than matching total temperature when replicating the distribution of wall pressures.

As part of their investigation into vitiation effects, Noda et al. (2011a) employed a quasi-one dimensional chemical kinetic code to estimate these effects quantitatively and through this approach they explored how the mode of combustion (supersonic vs subsonic) affects the mixing and combustion efficiency. In the code combustion was control via a mixing model from Diskin and Northam (1987). They found that the model by Diskin and Northam (1987) underpredicts the mixing efficiency, as determined from gas sampling of the combustion products, for both the supersonic and subsonic combustion type cases. They implemented a modification to the Diskin and Northam (1987) mixing model by introducing an additional linear term. This model is provided in Equation (2.4) where η_{mix} is the mixing efficiency, x the distance along the combustor, x_ϕ the complete mixing distance and ξ, ϕ and ζ are constants determined

from matching the pressure profile from the code to the experiment. The parameters determined from their tests are given in Table 2.1.

$$\eta_{mix}(x) = \xi + \psi\frac{x}{x_\phi} + \zeta ln\frac{x}{x_\phi} \tag{2.4}$$

Table 2.1: Experimental constants in Equation (2.4) from Noda et al. (2011a)

mode	ξ	ψ	ζ
supersonic	0.9248	0.5289	0.1241
subsonic	1.0979	0.2066	0.1448

Using this approach, they found that when the engine switches from supersonic to subsonic combustion the offset component (ξ) of the combustion efficiency curve increases from approximately 0.92 to 1.1. However, regardless of the combustion mode, by the end of the combustor the combustion efficiency is the same for both cases with $\eta_{mix} = 100\%$. This change in ξ indicates stronger initial combustion yet similar overall efficiency for the subsonic case compared with the supersonic case. This suggests that the combustion efficiency is enhanced during subsonic mode (when a strong pre-combustion shock train is present) mainly through enhanced mixing, most of which occurs in the near field close to the injection ramp, and less through higher pressures and temperatures at the combustor entrance. These findings by Noda et al. (2011a) are encouraging in that this improvement in mixing could allow for a shorter combustor design. Their findings regarding the comparison of tunnel conditions also highlights the need for dual-mode combustion studies to be conducted in facilities which can reproduce the total flight enthalpies.

Recent studies by Fotia and Driscoll (2012, 2013) have looked further into the complexities of the flow interactions between the isolator and combustor during dual-mode. Both these studies used the University of Michigan's Dual-Mode Combustor facility, which is an EAH type facility with $H_2 - O_2$ combustion and O_2 replenishment, operated in direct-connect configuration. For their tests the isolator had an entrance Mach number of 2.2 and stagnation temperature between 1000 K and 1400 K. Hydrogen was used as the fuel, which was injected from the wall normal to the main flow and the combustor contained a cavity towards the rear which acted as a flame holder.

Fotia and Driscoll (2012) recognise that, for this type of dual-mode scramjet, the backpressure on the isolator is a combination of both a fluid-mechanical blockage and a combustion-induced blockage, with the former blockage being due to the injection of the fuel into the main cross flow. In their experiments they observed that the fluid-mechanical blockage influences the effectiveness and location of the combustion blockage. They find that this leads to a situation where these two blockages are either reinforcing or destructive and that the nature of this relationship is dependant on both the geometry of the isolator and the inlet stagnation conditions.

To understand this observation, Fotia and Driscoll introduce an injector parameter to quantify this fluid-mechanical blockage from injection. This parameter is defined as the momentum flux ratio of the fuel fluid to that of the isolator entrance flow. From this they developed a coupling map which allows them to quantify the impact of the fuel-injector pressure on the required pressure recovery demanded of the isolator. From this map Fotia and Driscoll demonstrate that the "momentum ratio plays an important role in driving both an increase in the length of the pseudoshock and the maximum pressure it will recover over that length."

The above work is continued in Fotia and Driscoll (2013) where they apply high-speed laser interferometry to elicit insights into the processes which cause transition. In these experiments Fotia and Driscoll initiated the transition from one mode to the other by either reducing the fuelling or by allowing the temperature of the engine walls to increase. In the former method the mode switched from ramjet to scramjet, and in the latter method the reverse occurred.

When fuelling was reduced slowly the engine made a clear transition from ramjet to scramjet. They found in tracing the interferometry images that the reduction in the fuel lead to a transition from ramjet to scramjet through five quasi-stable stages, which are illustrated in Figure 2.17. In general they found that: (a) in ramjet mode the shock train consists of a series of nearly normal shocks, (b) the transition is marked by a shift in the anchor of the flame from one stable position to another, and (c) in scramjet mode an oblique shock train extends well into the combustor. When these tests were repeated but instead the fuelling was decreased rapidly (over a period of 90 ms), the flow structures seen in the interferometry images of the steady-state tests were seen in the images of the intermediate states of this rapid test. Fotia and Driscoll (2013) argue that this indicates that the flow structures and combustion adjust quickly and that "the

transition between combustion modes is quasi-steady-state."

Fotia and Driscoll (2013) also observed similar behaviour seen in the fuel-triggered transition tests in other tests where the transition was initiated not by a change in fuelling but by allowing the wall temperature to increase. In this test, although the transition occurred in reverse (from scramjet to ramjet), the five intermediate stages, marked by a shift in the flame anchor, were quite similar to the previous tests which were controlled by a change in fuelling. The key finding of these experiments is that transition in this engine was not just driven by a change in the heat generated from combustion, but that the shift in the anchor of the flame also changed the effective blockage from combustion.

In addition to these findings, Fotia and Driscoll (2013) observed behaviour under certain conditions in which both the flame and the shock train underwent low-frequency oscillation. They believe that the mechanism causing this behaviour is associated with the shear-layer instability across the cavity where "the flame enters into an oscillatory regime in which there appears to be a competition between the jet-wake and cavity stabilization modes." As discussed, the position of the flame anchor changes the effective blockage from combustion, which in turn affects the shock train. However the nature and structure of the upstream shock train affects the flame speed and so these two aspects are highly coupled in this type of engine. From looking at the spectra of the pressure traces, they found that these oscillations are quite periodic and so they are not considered to be random motions associated with any unsteadiness of the test flow. But more importantly, they found from the pressure spectra that the leading edge of pseudoshock has the same periodicity as flame position. Whilst there was a clear phase difference between isolator sensors and flame front position, all isolator transducers were in phase. This means that the shock train in their engine moves as a single entity. The phase offset between the flame position and shock train represents the time it takes for a shift in the position of the flame to be transmitted through the subsonic boundary layer through the isolator (i.e. the propagation speed). These findings are important to keep in mind when reviewing results from other dual-mode engine studies which use a cavity as a flameholder, as this cavity could be introducing or amplifying any oscillations that are observed in behaviour of the pre-combustion shock train.

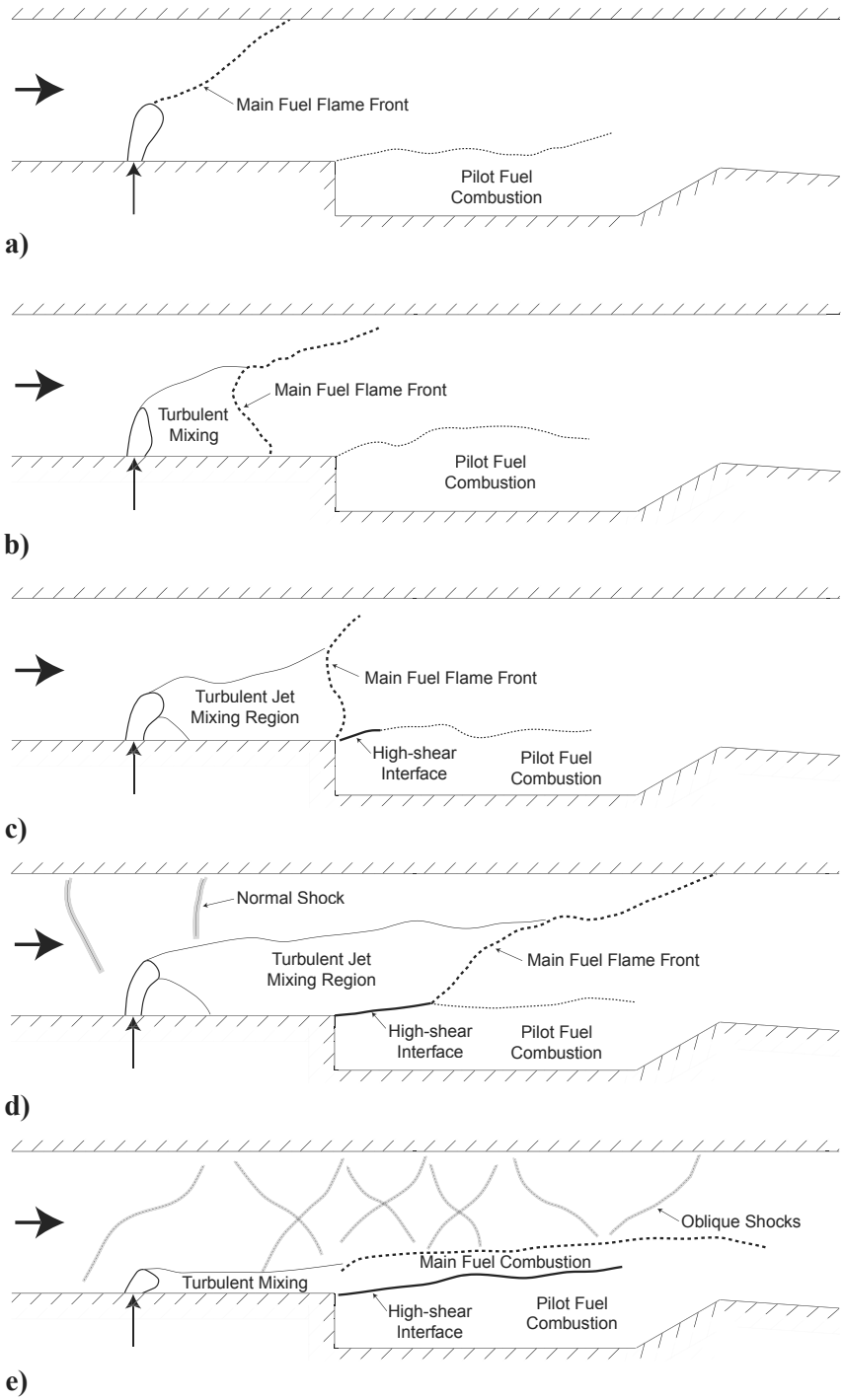

Figure 2.17: The stages of transition from ramjet to scramjet observed by Fotia and Driscoll (2013) in their steady-state tests of The University of Michigan Dual-Mode Combustor (MDMC). Cases: (a) jet-wake flame stabilised ramjet, (b) lifted-jet flame ramjet, (c) mid-combustor flame ramjet, (d) cavity flame stabilised ramjet and (e) scramjet. (Figure sourced from Fotia and Driscoll (2013).)

In summary, the work by Fotia and Driscoll (2012, 2013) make important contributions to the understanding of the complex coupling between fuel injection, combustion and shock train characteristics and to the understanding of the mechanisms which lead to transition from ramjet to scramjet. However these studies were performed, like many previous studies on this topic, towards the lower part of the dual-mode regime where the transition from ramjet to scramjet occurs. In order to map out the full dual-mode regime, then the study of this highly coupled behaviour between the shock train and combustion needs be extended to facilities which can generate much higher stagnation temperatures and total enthalpies.

2.4.1 Pre-combustion shock trains and shock tunnel testing

As discussed in the introductory of Section 2.4, much of the early early work on shock trains in scramjets used mechanical throttling to simulate the pressure rise from combustion. The majority of recent work which does involve both shock trains and combustion has been in continuous flow facilities in which the air is heated by some means to produce the temperatures required for combustion (Baurle and Eklund, 2001; Goyne et al., 1999; Le et al., 2008a, 2006, 2005; Noda et al., 2011a,b). Unfortunately these flow facilities suffer from contamination from the heating process and this can affect combustion, as discussed in Section 2.4. Additionally, a number of constraints usually limit these facilities from being able to simulate conditions above Mach 6 flight whilst still matching total enthalpy. Shock tunnels, more specifically Stalker Tubes, provide the capability to test at conditions above a flight Mach number of 6. However much of the early work on scramjets in shock tunnels was focussed on demonstrating that combustion was stable at the high flight Mach numbers which these types of facilities can produce (Stalker and Morgan, 1984). Little attention was given initially to the upper part of the dual-mode regime, which is towards the bottom end of shock tunnel range.

Despite the general focus on pure scramjet engines in shock tunnels, pre-combustion shock trains have been observed or suspected to have occurred in a few shock tunnel experiments. For example, Boyce et al. (2000) conducted an experiment in the T4 Stalker Tube in order to compare the behaviour of supersonic combustion in a shock tunnel and with that in a vitiated air heated facility (VAH). Boyce et al. (2000) found in their scramjet experiments, which had a constant area combustor, that they were limited to fuelling levels at or below an equivalence ratio of 0.3 due to boundary-layer

separation choking the engine. The only indication of this separation was the raised pressures at the injectors. Although, Boyce et al. (2000) were able to find favourable agreement between the results from the shock tunnel and the VAH facility, the focus of these experiments was not on pre-combustion shock trains per se but on the vitiation effects on supersonic combustion. As such instrumentation was not placed in the isolator section to study this shock train.

In other experiments in the T4 Stalker Tube, Frost et al. (2009) and Turner (2010) both observed boundary layer separation due to adverse combustion pressures. Frost et al.'s (2009) experiments were performed using a scaled model of the HyShot flight scramjet and the experiments by Turner (2010) were tests of his rectangular-to-elliptical shape transition (REST) inlet scramjet engine. A focus of Frost et al.'s (2009) research was to determine the critical pressure rise required to separate the boundary layer and cause an engine unstart. From their experimental results, Frost et al. (2009) argue that the separation criteria provided by Korkegi (1975), which is the critical pressure across a shock required to separate a turbulent boundary layer, could also be applied to the more gradual pressure rise experienced in a scramjet combustor to predict choking initiated by separation of the boundary layer. Though, as discussed later, Laurence et al. (2013) makes a case that this assumption is not valid. Nevertheless, for the experiments by Frost et al. (2009), as with the experiments by Boyce et al. (2000), pressure sensors were not placed along the isolator which precluded measurement of the size of the pre-combustion shock train. However, the experiments by Turner (2010) of a REST inlet scramjet did include pressure sensors along the isolator. In some of his tests the high pressures in the isolator indicated that the boundary layer had separated and that an oblique shock train formed in the isolator. In these tests the engine was operating in dual-mode. However those test fell outside the scope of that work and so few shots were performed in this mode.

More recently, work has been performed in the High Enthalpy Shock Tunnel (HEG) reflected-shock wind tunnel by Laurence et al. (2013) who have investigated transient fluid-combustion phenomena in a model of the HyShot II flight experiment. In agreement with Frost et al. (2009), they found the stable combustion could be achieved up to an equivalence ratio of 0.33. Above which the engine would begin to unstart during the test time. Much of the focus of Laurence et al. (2013) work is on the transient nature of this unstart. Laurence et al. employed high-speed schlieren and OH^* chemiluminescence visualisation in conjunction with time-resolved surface pressure measurements.

Laurence et al. observed in their experiments transient flow features, including the onset of unstart which was caused by a shock-train propagating upstream. They also found that the physical nature of the incipient shock system appears to be similar for different equivalence ratios. From a plot of the pressure traces during an unstart on a space-time ($x - t$) diagram they were able to measure the propagation speed of the unstart. They found that the propagation speed, and the location of where the shock train originates from, depends strongly on equivalence ratio.

From a combination of OH^* chemiluminescence visualisations and unsteady numerical simulations (using the *DLR TAU* code), Laurence et al. identify the initiating mechanism for the propagating shock train. They found that, although localised boundary-layer separation accompanies the shock system as it moves upstream, the primary mechanism for the transient behaviour is localised thermal choking. They found in the numerical simulations that "the global choking behaviour is dictated by the limited region of maximum heat release around the shear layer between the injected hydrogen and the incoming air flow." This lead them to the idea of 'local' thermal choking which results in a lower choking limit than is predicted by a simple integral analysis. This is where the aforementioned disagreement with Frost et al. (2009) arises. Laurence et al. make the case that "although boundary-layer separation may have occurred at some point during the choking development in the experiments of Frost et al. (2009), their assumption that it was the driving mechanism is likely to be in error."

Finally, Laurence et al. propose a novel quasi-unsteady one-dimensional analytical model (based on Rayleigh flow) to quantify the additional contribution to the stagnation temperature which is generated from a shock moving forward. From their quasi-unsteady one-dimensional analytical model they predict that the shock train slows as it moved upstream, which agrees with the observations from their experiment. The model also predicts the initial shock-propagation speed to be very sensitive to the total heat release, which they suggest may explain the large discrepancies that they found between experimental and numerical shock speeds.

Although the work by Laurence et al. (2013) provides insights into the transient nature of the unstart process, as the tests in which a shock train was formed also resulted in an unstart of the HyShot II engine, the question remains as to whether a stable shock train can form in the short test time of a shock tunnel.

2.5 Summary

From a review of the literature it can be seen that there is still much to be learnt about the highly complex flow that is characteristic of dual-mode scramjet engines. Despite a concerted effort in the specific areas of shock trains and pseudo-normal-shocks, a flow model has yet to be formulated which satisfactory predicts the shock train length and resolves its structure completely for the wide range of conditions present at the entrance of a scramjet isolator over an access-to-space trajectory. This is because the highly distorted flow which is produced by a pre-combustion shock train adds further complexity to the already highly complex flow in the combustion chamber. Much of the experimental data to date has been in wind-tunnels which simulate combustion via mechanical throttling and/or do not match the enthalpy of Mach 8 flight. The few experiments which have been performed at these higher Mach numbers, such as in shock tunnels where the flight enthalpy can be matched, have involved engines with short isolators where the formation of a pre-combustion shock train results in an engine unstart. The question remains whether this phenomenon can be studied in these short duration impulse facilities at a Mach number and matching enthalpy towards the upper end of the dual mode regime.

Chapter 3

Experimental Apparatus and Methodology

This chapter describes the experimental approach taken to investigate dual-mode supersonic combustion in a scramjet in a shock tunnel. First the experimental model is described including the fuel system. Following this, an overview of the wind tunnel facility is given, including the operating principle, instrumentation, data acquisition system and test flow conditions. Finally the method by which the data was processed is outlined along with the results from an analysis of the uncertainty in the test and fuelling conditions.

3.1 Model

The experimental model used in this study was an axi-symmetric engine with a circular cross section. It has been designed to operate at tunnel conditions equivalent to Mach 8 flight with an investigative focus on the phenomenon of pre-combustion shock trains which are characteristic of dual-mode scramjets. The model consists of a diffuser, an isolator, the fuel system, three interchangeable combustion chambers, external supports and shielding. The set of combustors comprise a constant area combustor and two divergent combustors. The experimental data was acquired from the model in the form of wall pressures measurements along the isolator and combustion chambers as well as measurements of fuel plenum pressures. The assembled model, with the constant area combustor installed, is shown in Figure 3.1. A number of components of the apparatus were taken from the base model used in the experiments by Chan (2012); Kirchhartz (2009); Rowan (2003); Tanno et al. (2001) and Paull et al. (1995), namely the

fuel block and the instrumented constant area combustor and the reader is directed to those references for the design rationale of those components.

3.1.1 Diffuser

The term 'diffuser' refers to the contracting section at the front of the model that precedes the isolator. The diffuser is designed to compress the Mach 4 freestream test flow down to the desired isolator entry conditions, as given in Table 3.6. In designing the diffuser the aim was to compress the flow with minimal losses and shock generation. The shape was chosen such that the incident shock would be cancelled by the expansion wave, which is generated as the area expands slightly past the throat, to produce relatively uniform shock-free flow to the isolator. The key parameters of the diffuser are given in Table 3.1 and a detailed drawing along with the tabulated profile, can be found in Appendix F. The method employed for the design of the diffuser is described in the next section.

Table 3.1: Key parameters of the diffuser

Property	Value	Units
Inlet Diameter	43.6	mm
Throat Diameter	32.8	mm
Exit Diameter	33.2	mm
Length	172.7	mm
Area Contraction Ratios		
inlet-to-throat	1.767	-
inlet-to-exit	1.725	-

3.1.1.1 Diffuser design methodology

The aerodynamic design of the diffuser was performed using the "reversed expander" method described in Smart (1999). The goal of this method was to design an axisymmetric compression field that, given a specified inflow Mach number, performs a desired amount of compression with a relatively uniform outflow. This method was developed for hypersonic inlets with a relatively high compression ratio. The current diffuser has a very modest compression ratio, so the method worked very well. Once an inviscid shape was determined, a boundary layer correction was performed using the code by Cebeci and Bradshaw (1984), with the assumption of fully turbulent flow.

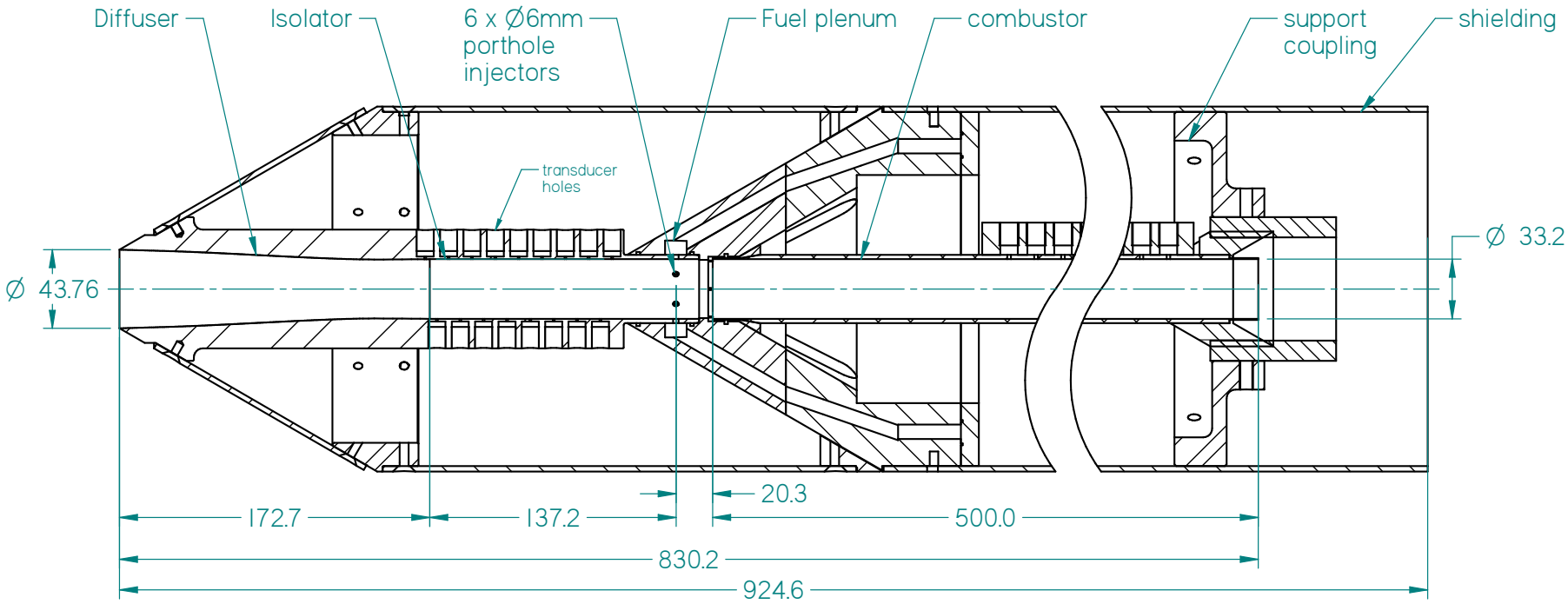

Figure 3.1: Schematic of the experimental rig with the constant area combustor (dimensions in mm).

3.1.1.2 CFD simulation of diffuser flow path

To assess the performance of the diffuser, a numerical simulation was performed using the NASA Langley computational fluid dynamics (CFD) code *VULCAN* (White and Morrison, 1999). This code solves the three-dimensional compressible Navier-Stokes equations for turbulent, non-equilibrium, chemically reacting flows using structured grids. A $k-\omega$ model was used to model the turbulent flow with transition specified at all leading edges. Grid clustering was used at wall boundaries and the wall functions of Wilcox were also applied (White and Morrison, 1999). This allowed the boundary layer to be resolved for wall cells with a y+ of approximately 25.

The inflow conditions for the simulation were based on the nominal shot conditions selected for this study and were taken directly from a stream thrust average of the results from the numerical simulation of the Mach 4 nozzle, which is discussed in Section 3.2.3.1. The result from the numerical simulation of the diffuser is presented in Figure 3.2, which shows a contour plot of the Mach number. One of the design objectives of the diffuser was to provide flow to the isolator which, along with having the desired pressure, temperature and Mach number, had a minimal shock structure downstream of the throat. From the contour plot it can be seen that this objective was met as the initial shock emanating from the leading edge is attenuated by the expansion at the throat of the diffuser.

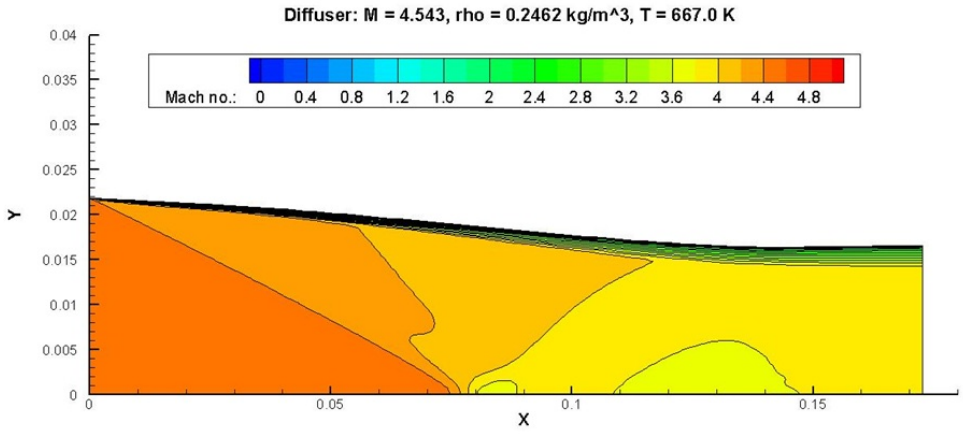

Figure 3.2: Mach number contour plot of diffuser flow field (CFD code: *Vulcan*)

In addition to assessing the uniformity of the outflow of the diffuser, the numerical simulation of the diffuser was carried out to obtain performance parameters for use in the subsequent cycle analysis of the experiments. These performance parameters

are in the form of the pressure and temperature exiting the diffuser as a ratio of the freestream test values. These performance parameters, which are listed in Table 3.2, were then applied to the table of freestream conditions, as generated from the relatively rapid analytical and numerical codes used to determine the freestream tunnel conditions (Section 3.3.1), to determine the stream-thrust average isolator entrance conditions for each shot. This approach was taken as the numerical simulation of every shot, which would require the simulation of both the nozzle of the facilities and the diffuser, was considered prohibitively expensive for this research.

Table 3.2: Nominal flow conditions exiting the diffuser (i.e. entering the isolator)

Property	p_{iso}	T_{iso}	ρ_{iso}	u_{iso}	M_{iso}	p_{iso}/p_∞	T_{iso}/T_∞
Value	118.8	884.7	0.4679	2122	3.63	2.5210	1.326
Units	kPa	K	kg/m^3	m/s	-	-	-

3.1.2 Isolator

Immediately downstream of the diffuser is a section of constant area which is referred to as the isolator. The diffuser and isolator form one piece and the downstream end slots into the front of the fuel-block. The isolator has an internal diameter (D_{iso}) of 33.20 mm and a length (L_{iso}) of 150.0 mm giving an $L/D \approx 4.5$. The isolator section also houses the port-hole injectors which are located 13 mm upstream from the downstream end. The presence of these injectors shortens the 'literal' length of the isolator to 137 mm and effectively lengthens the combustion chamber. The isolator piece was designed to be long enough to study a range of shock train lengths. The diffuser and isolator are manufactured from a single piece to eliminate an interface which may have potentially disturbed the flow. The isolator is instrumented with 9 pressure transducers along the top and 8 pressure transducers along the bottom. Both rows of transducers have a spacing 13 mm and the top row is offset from the bottom by half that spacing. This gives a spatial resolution along the length of the isolator of 6.5 mm. A detailed drawing the of isolator can be found in Appendix F.

3.1.3 Combustion chambers

Three combustion chambers were tested, one constant area combustor and two divergent combustors, which are shown in Figure 3.3 and a summary of their key dimensions are listed in Table 3.3. It was anticipated that the constant area combustor would have the highest peak pressure and therefore was used as an initial baseline to establish whether a pre-combustion shock train could be generated at these test conditions. The divergent combustors were used to investigate the effect that the shape of the combustion chamber has on the formation and position of the pre-combustion shock train.

The constant area combustor is the same combustor which was used in the experiments by Chan (2012). This combustor was selected as the previous experiments by Chan (2012), Kirchhartz (2009) and Rowan (2003) had shown near-complete burning of the fuel at stoichiometric levels with a combustor of this length at similar conditions. As the strength of the pre-combustion shock train is driven by the peak back pressure in the combustion chamber (Billig, 1993), it was desirable that the combustion chamber be long enough to achieve near-complete combustion of the fuel at stoichiometric levels to give the largest achievable range in peak combustion pressure.

Two divergent combustors were also manufactured and both of these consisted of a straight section followed by a diverging section of different angles. The two divergent combustors are referred to by their half cone angle of divergence which are 1^o and 2^o respectively. For a number of reasons outlined below, the combustors had the following design criteria:

- all to have the same length and inlet diameter,
- both divergent combustors to have the same exit-to-inlet area ratio of 2, and
- for the 1° divergent combustor to diverge well upstream of the 2° divergent combustor.

The decision for a common length for all three combustors was made so that the region over which mixing would occur would be similar for all three combustors. All three combustor chambers were held at the front by the fuel block and at the rear by a coupling arrangement. A common inlet diameter across all three combustors and a common exit diameter for the divergent combustors simplified the design by allowing common interfaces. As the exit-to-entrance area ratio for the divergent combustors

was the same and they were of the same length, this resulted in different length of the straight section for the divergent combustors. For the 1° divergent combustor the point of divergence is 106.1 mm from the leading edge of the combustor, whereas for the 2° divergent combustor this point is further downstream at 303.1 mm.

Table 3.3: Combustion chamber parameters

Combustion Chamber	Constant Area	2°	1°
Length [mm]	500	500	500
Length [L/D]	15.1	15.1	15.1
Entry diameter [mm]	33.2	33.2	33.2
Exit diameter [mm]	33.2	46.95	46.95
Area ratio	-	2	2
Constant area section length [mm]	500	303.1	106.1
Constant area section length ratio [L/D]	15.1	9.1	3.2
Divergence section length [mm]	-	196.9	393.9
Divergence section length ratio [L/D]	-	5.9	11.9

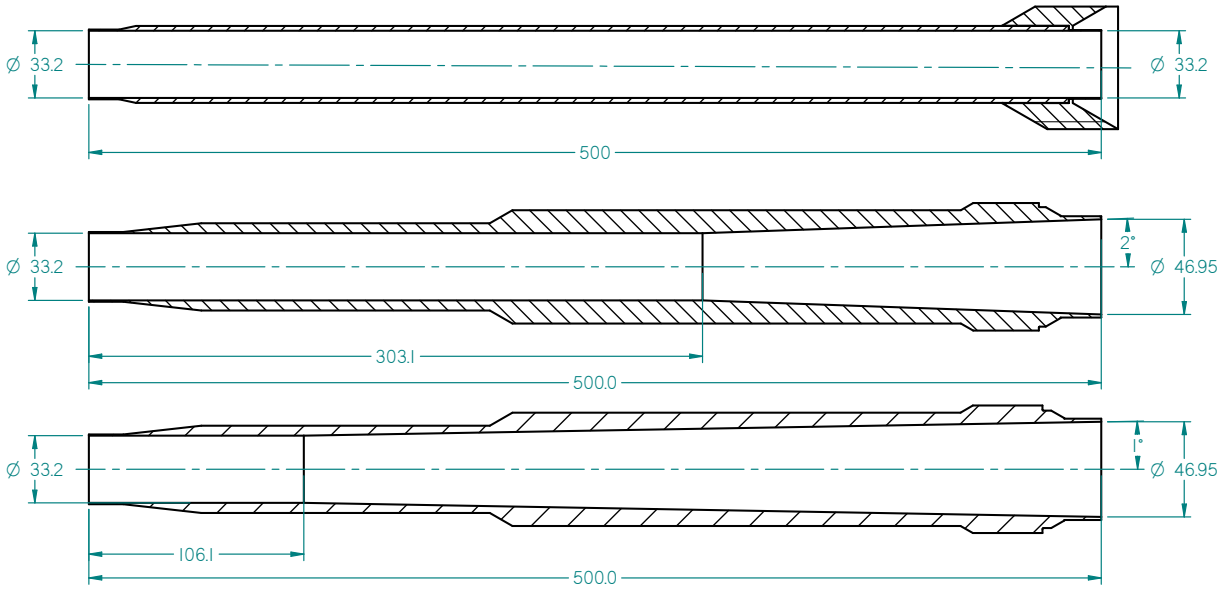

Figure 3.3: Manufacturing drawing of the three combustors. (Dimensions in mm.)

3.1.4 Model instrumentation

The sensors selected for this model were of two types: piezo-electric made by PCB Piezotronics® and piezo-resistive made by Kulite™. Both sensor types offer the short response time ($\leq$2 µs) required for short duration impulse facilities.

The PCB's were used along the isolator and combustor as well as in the fuel plenum chamber. The PCB model types used in this model were 111A21, 111A22 and 111A26 and were selected due to their long discharge time constant ($\geq$1.0 s). The standard mounting of a PCB sensor in a transducer hole was developed by Jacobs et al. (1992) with refinements by Bateup (2004) and is depicted in Figure 3.4a. This mounting arrangement has been designed to minimise vibration effects on the transducer, which can appear as noise on top of the signal. A thermal barrier, in the form of cellophane was used to protect the face of the sensor.

The Kulites were used in the fuel block, which also holds the front of the combustor, to measure the pressure around the front edge of the combustor. Six Kulites, from the XTEL-190M series, were spaced equally around the circumference. The mounting of a Kulite, as developed by Suraweera (2006), is shown in shown Figure 3.4b. The fuel block which contained these Kulites was originally designed and manufactured for a previous experiment by Paull et al. (1995) with subsequent modifications made by Kirchhartz (2009). These previous experiments required a measurement of pressure on the forward face of the combustor (Rowan, 2003) and as such there is a small recess in the interface been the combustor and the fuel-block where the pressure is measured by the Kulites. This recess, measuring 1 mm by 1 mm and which forms an annulus, is very small compared with the radius of the diameter of the combustor inlet (33.2 mm).

Although the design feature of the recess and the arrangement of Kulites was dictated by the requirements of the previous experiment, it was advantageous for these experiments as it provides a measurement of the pressure much closer to the injectors than either the furthest downstream sensor in the isolator or the most upstream sensor in the combustor proper. This was an advantage as separation associated with the pre-combustion shock train was anticipated to initiate around the injectors, and by providing a measurement as close as possible to the injectors this allowed separation of a smaller scale to be detected.

3.1.4.1 Transducer blocks

Due to the thin walls of all three combustion chambers, transducer blocks were manufactured to providing mounting for the transducers. The existing constant area combustor (taken from Kirchhartz's (2009) experiment) already had a rear transducer block attached as shown in Figure 3.5. However the first sensor of that block was considered

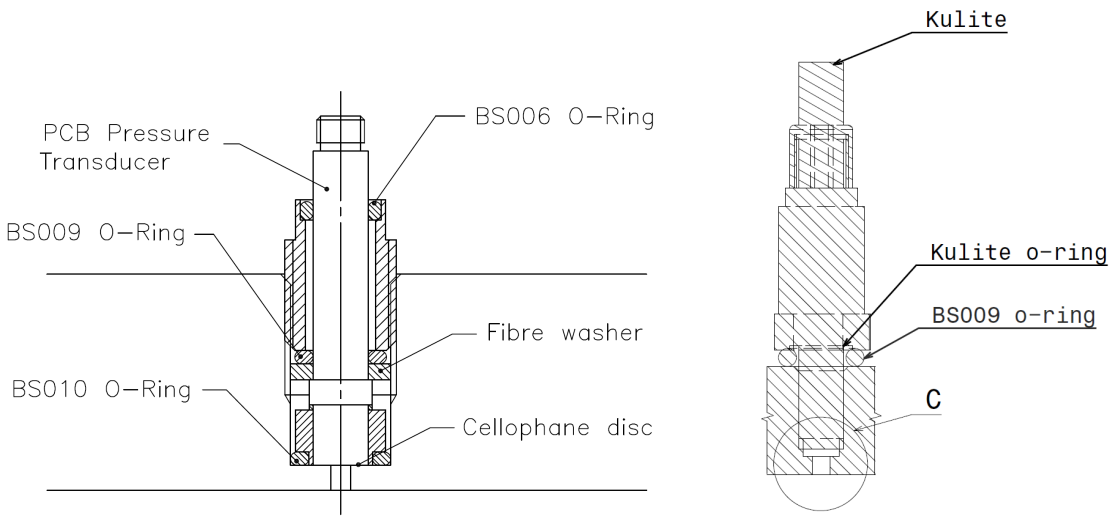

(a) PCB Piezoelectric mount (sourced from Rowan (2003))

(b) Kulite mount (sourced from Suraweera (2006))

Figure 3.4: Types of mounting for the pressure transducers used in the experimental model.

too far downstream of where the reattachment point of the separated flow may occur. As such, a forward transducer block was designed to slide on over the front part of the combustor to house transducers closer to the upstream end of the combustor. A drawing of this mount can be seen in Figure 3.6a. A similar forward block was used on the divergent combustors in addition to a rear transducer block designed specifically for the divergent combustors, shown in Figure 3.6b. Detailed drawings of all of the transducer blocks can be found in Appendix F.

The transducers in the forward block were mounted at an angle to fit within the space confines of the fuel block. To measure the flow in the combustion chamber two small intersecting pilot holes were drilled. One radially through the block into the combustion chamber. The second pilot hole was drilled along the axis of the transducer hole from the base of this transducer hole to intersect with the aforementioned pilot hole. The top portion of the radial pilot hole was plugged to form a closed passage from the transducer face to the combustion chamber internal wall.

The forward block has three sides each containing a row of transducer holes denoted in the detailed drawings A, B and C. The normal of each side is angled at 120° from the next about the axis. Each row is offset by a third of the regular spacing from the other sides to allow for increase in resolution. Only the one row was used during testing due to the limited supply of transducers. Referring to the detailed technical

drawings in the appendices, the row labelled A was used for the tests of the divergent combustors and the row labelled C for the constant area combustor.

This rear transducer blocks used on the divergent combustors have two rows of transducer holes, 17 holes on the top side and 15 on the bottom side. Along each row the holes have a spacing of 13 mm and one row is offset from the other by half this spacing (i.e. 6.5 mm) to increase overall resolution. Again, due to a limited number of transducers only one side was populated with sensors with the empty holes plugged during the tests.

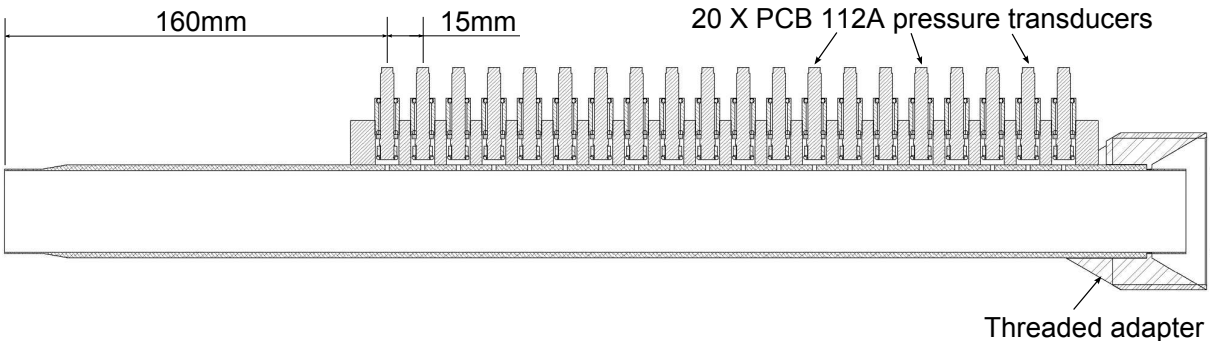

Figure 3.5: Original constant area combustor with mounting block attached (sourced from Chan (2012))

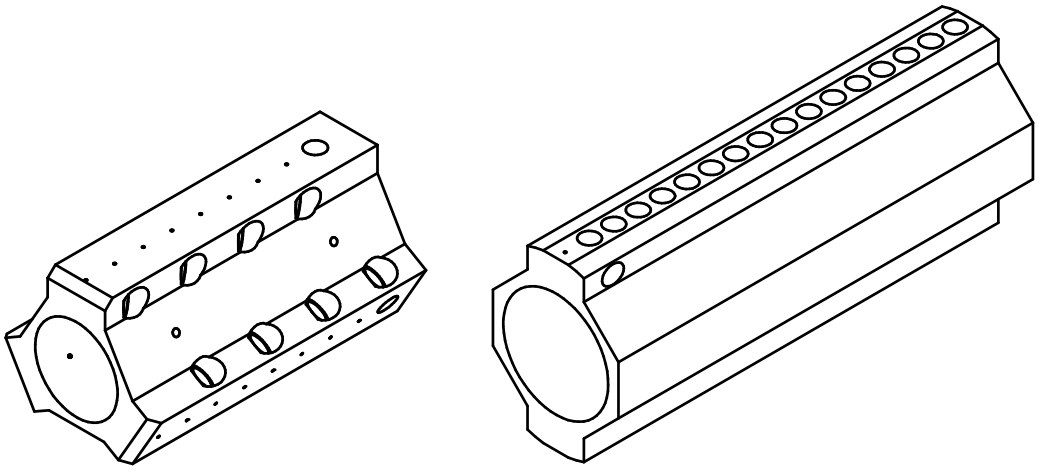

(a) Forward mounting block. **(b)** Rear mounting block.

Figure 3.6: Transducer mounting blocks for the combustors. The forward block (a) was used on all three combustors. The rear mounting block (b) shown was used on the two divergent combustors.

3.1.5 Fuel system

A fuel system was used to inject gaseous hydrogen as the fuel for these experiments. The fuel system comprises the port-hole injectors, an instrumented fuel block, a fast acting valve and the fuel supply system. A schematic of the overall fuel system is shown in Figure 3.7. Each of these parts are discussed in the following sections.

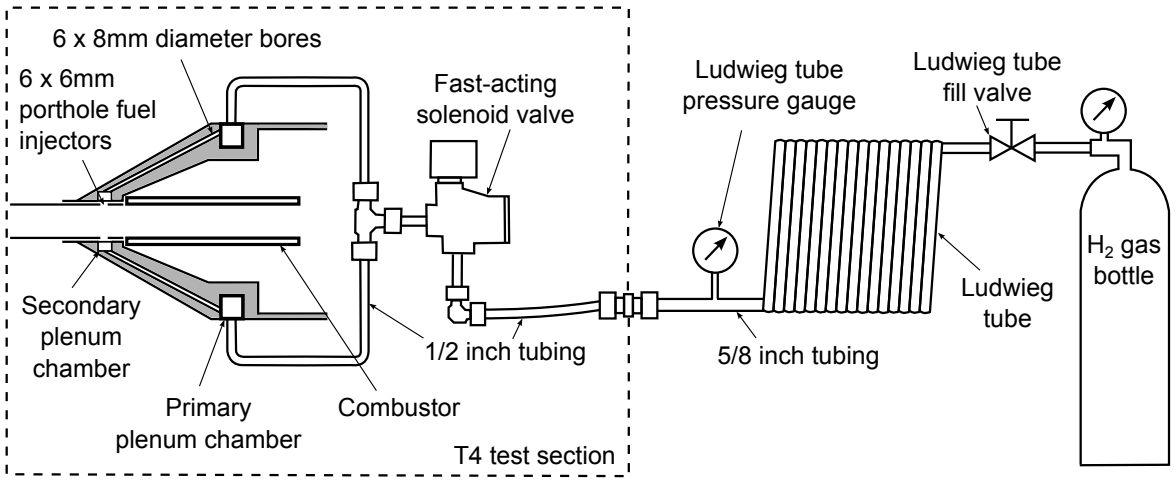

Figure 3.7: Overall schematic of the fuel system. (Figure adapted from Chan (2012).)

3.1.5.1 Injectors

The fuel was injected perpendicular to the flow via six port-hole injectors which are located 137 mm ($4.1D_{iso}$) downstream from the start of the isolator. Each port-hole has a diameter of 3 mm and were equally spaced around the circumference of the isolator. In sizing the injectors, the aims were to ensure sonic injection and to provide sufficient jet penetration. Sonic injection was required for the calculations relating to the fuel flow rate to be valid (as discussed in Section 3.1.5.5). Sufficient jet penetration was required to ensure fuel escaped the boundary layer and mixed sufficiently with the main flow. An estimation of this jet penetration is presented in Section 3.1.5.6.

3.1.5.2 Fuel block and plenum chamber

The injectors were supplied with fuel via a primary and a secondary plenum chamber as illustrated in Figure 3.7. The primary chamber feeds fuel to the secondary chamber via 6 equally spaced bores which have a diameter of 8 mm. The primary plenum

chamber was supplied by two $\frac{1}{2}$ inch tubes which branched off near the outlet of the fast acting solenoid valve. Two PCB piezo-electric transducers measured the pressure in the secondary plenum chamber over the test time. A detailed drawing of this fuel block can be found in Appendix F.

3.1.5.3 Fuel supply system

The fuel supply system of the T4 Stalker Tube comprises a Ludwieg tube, a cylinder of compressed fuel, a fast acting valve and a control board. A schematic of the system is shown in Figure 3.7. The Ludwieg tube for the T4 Stalker Tube consists of $\frac{3}{8}$ inch stainless steel tube which is 14.2 m long. The majority of the tube is coiled to save space. The length of this Ludwieg tube is sufficient to provide steady rate of fuel for over 20 milliseconds (ms). The Ludwieg tube is separated from the fuel block in the model by a fast acting valve. This valve is controlled by a solenoid and utilises a pilot tube to achieve the fast opening time. The value is triggered by the data acquisition system approximately 15 ms to 20 ms before the main flow reaches the model. This early triggering is to allow the flow of fuel to reach steady flow before onset of the main tunnel flow as shown in Figure 3.8. The valve was required to have a fast opening time to minimise the amount of fuel present within the test section before the main flow arrived so that the test section pressure remained low in order that the nozzle of the tunnel started properly. The valve used in these experiments was the SCD223A3 model from ASCO/JOUCOMATIC. A schematic of the valve can be found in Appendix B. A one-dimensional simulation of the fluid dynamics of the Ludwieg tube used in the T4 Stalker Tube can be found in Gangurde (2007).

3.1.5.4 Calculation of fuel mass flow rate

The fuel mass flow rate through the injectors can be described as a function of the instantaneous pressure in the plenum chamber, the initial fill pressure of Ludwieg tube and an effective discharge coefficient and is given in Equation (3.1):

$$\dot{m}_{\mathrm{H}} = \alpha \, p_{LT_i}^{\frac{\gamma-1}{2\gamma}} \; p_{plenum}^{\frac{\gamma+1}{2\gamma}} \tag{3.1}$$

where $\dot{m}_{\mathrm{H}}$ is the instantaneous mass flow rate of fuel, α an experimentally determined calibration constant, p_{LT_i} the initial pressure measured in the Ludwieg tube,

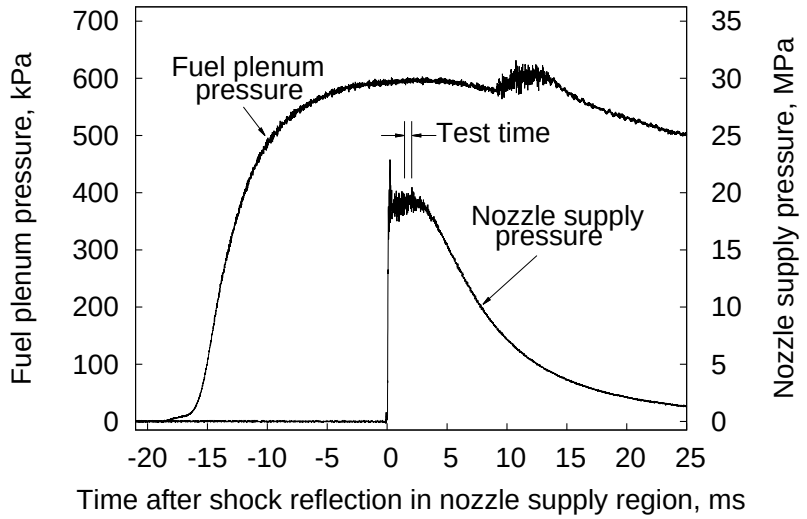

Figure 3.8: Timing of fuel for shot 10832.

p_{plenum} the pressure measured in the plenum chamber and γ the ratio of specific heats for hydrogen.

The value of the discharge coefficient (α) is determined prior from a calibration which is outlined in the T4 Stalker Tube Operator's Manual (Robinson et al., 2003) and is reproduced in Appendix B. This calibration method determines α by first calculating the total mass flow through the injectors over the calibration, which can be determined from a measure of the initial and final Ludwieg tube pressures and by knowing the volume and assuming the initial temperature of the Ludwieg tube. The coefficient α is then determined by relating this total mass flow to the measured pressure in the plenum chamber integrated over the calibration test time.

3.1.5.5 Calculation of equivalence ratio

For each experiment the amount of fuel which was injected into the test flow was expressed as an equivalence ratio, which is a ratio of the injected hydrogen to the stoichiometric amount of hydrogen required to burn all the oxygen in the flow passing through the engine. The calculation of this equivalence ratio comes directly from the stoichiometric chemical reaction of hydrogen with air and given by Equation (3.2),

$$\phi = 8\frac{\dot{m}_{\mathrm{H}}}{\dot{m}_{\mathrm{O}}} \tag{3.2}$$

where $\dot{m}_O$ is the mass flow rate of oxygen, which is a proportion of the air that is captured by the diffuser as calculated by Equation (3.3),

$$\begin{aligned} \dot{m}_O &= Y_O \, \dot{m}_{air} \\ &= Y_O \, A_c \, \rho_\infty \, u_\infty \end{aligned} \tag{3.3}$$

where Y_O is the mass fraction of oxygen in air (= 0.232), A_c is the capture area of the diffuser, ρ_∞ is the density of flow into the diffuser and u_∞ is the freestream flow velocity. For these experiments it assumed that due to the sharp leading edge of the diffuser no spillage occurs and so the mass capture by the diffuser is 100% of its inlet area.

3.1.5.6 Fuel penetration

An estimation of the fuel penetration is made using the correlations outlined in Portz and Segal (2006). Portz and Segal (2006) evaluated previous studies of gas jets into supersonic flows with established boundary layers over various Mach numbers. From this evaluation they proposed a new jet penetration correlation using coefficients based on the Mach number of the cross flow. The correlation, using the values specific to fuel injectors used for this study, is given in Equation (3.4)

$$\frac{P}{D} = A \left(\frac{q_j}{q_a} \right)^{0.319} \cdot \left(\frac{x}{D} - 0.63 \right)^{0.639} \cdot \left(\frac{\delta}{D} \right)^{0.077} \cdot \left(\frac{\mathcal{M}_j}{\mathcal{M}_a} \right)^{-0.025} \tag{3.4}$$

where P is the penetration of the jet measured from the wall, D is the diameter of the injector, A is a coefficient based on the incoming Mach number ($A = 3.616$ in this case), q_j and q_a are the dynamic pressure of the jet and cross flow respectively, δ is the boundary layer thickness along the wall (mm), x is the downstream distance from the injector centre (mm), and $\mathcal{M}_j$ and $\mathcal{M}_a$ are the respective molecular mass of species of the jet and cross flow.

A plot of the results is shown in Figure 3.9. For this calculation, δ is taken from the result of a boundary layer analysis of the flow through the diffuser which is presented in Section 3.3.2. From this figure it can be seen that the penetration of fuel reaches the centreline of the duct (16.6mm) almost immediately downstream of the injection

(between 5 mm to 10 mm downstream of injection). This is due to the very high dynamic pressure ratio of the fuel jet to the incoming flow ($q_j/q_a \approx 2.8$) and also from the high Mach number of the cross flow ($M = 3.6$). The P/D profile plotted here is consistent with the profiles shown in Portz and Segal (2006). The large penetration of jet across the middle of duct is encouraging in that a high combustion efficiency will be achievable and will allow for a wide range of combustion pressures to be tested. The original correlation and the detailed application to this study is outlined in Appendix B.

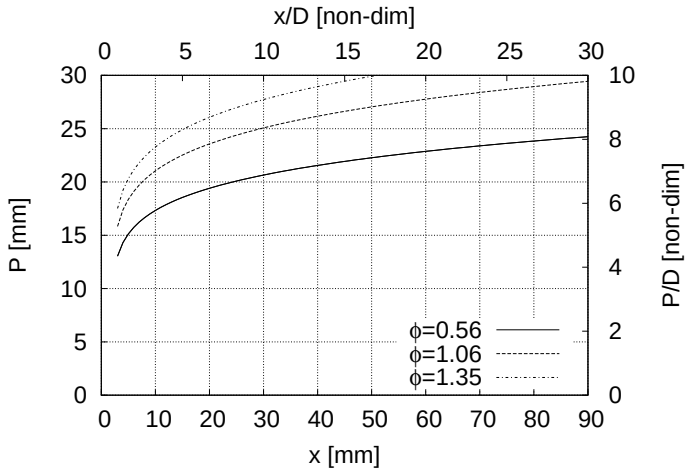

Figure 3.9: Jet penetration based on Portz and Segal's (2006) correlation given in Equation (3.4) at various fuelling rates as specified by the equivalence ratio (ϕ) for the following parameter values: $D = 3.0\,\text{mm}$, $A = 3.616$, $q_a = 2.12 \times 10^2\,\text{kPa}$, $\delta = 4.05\,\text{mm}$, $\mathcal{M}_j = 2.0156\,\text{kg kmol}^{-1}$ and $\mathcal{M}_a = 28.97\,\text{kg kmol}^{-1}$ and where the parameter q_j was $4.41 \times 10^2\,\text{kPa}$, $8.02 \times 10^2\,\text{kPa}$ and $10.94 \times 10^2\,\text{kPa}$ for the respective values for ϕ of 0.56, 1.06 and 1.35.

3.1.6 Mounting and shielding

The test section of the T4 Stalker Tube is harsh environment due to high dynamic pressures. As such external shielding is required to protect the sensors and associated cables. The brunt of the external flow is deflected by a 30° cone which connects to the outer face of the diffuser and to a tubular outer-shield which extends along to the fuel block. Another tubular outer-shield extends past the fuel block to a coupling at the very rear which holds the end of the combustor in place. Along the tubular outer-shield sections there are three pairs of contoured clamps which provide mounting points for the support structure. This support structure comprises side plates and C-section channels to mounted the whole model to the rails on the ceiling of the test section. A CAD image of the model, with the constant area combustor installed, is

shown in Figure 3.10 and photographs of the model installed in the test section are shown in Figure 3.11. Detailed drawings of the shielding and support structure are provided in Appendix F.

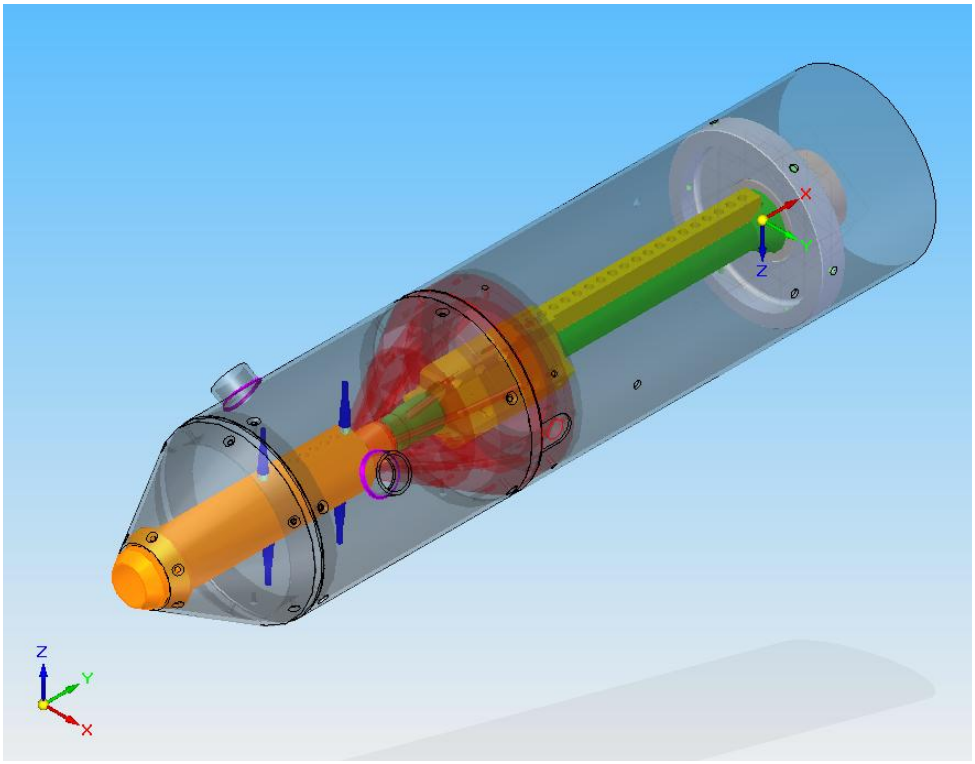

Figure 3.10: CAD model of the experimental rig with the constant area combustor

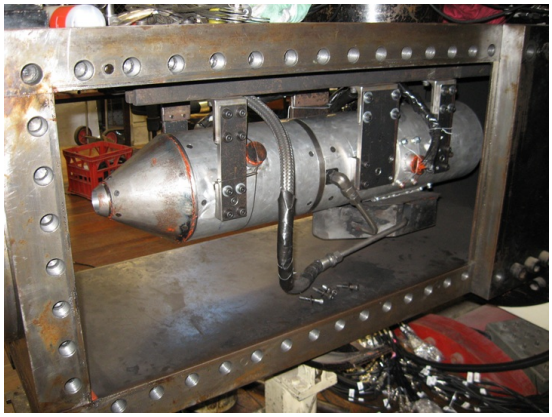

(a) Port side view

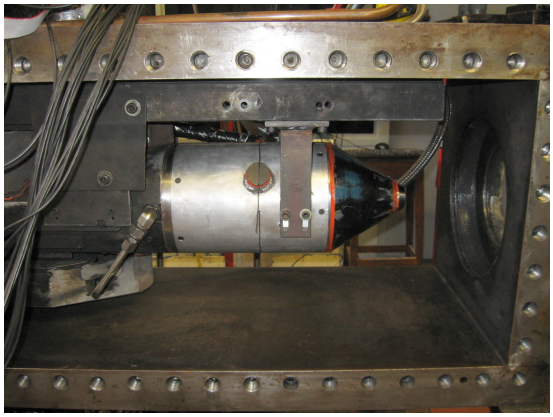

(b) Starboard side view

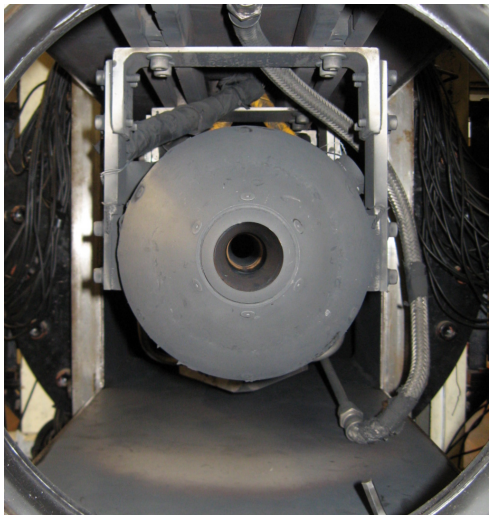

(c) Bow view

Figure 3.11: Photographs of the model mounted in the test section

3.2 The T4 Stalker Tube

For these experiments, the wind tunnel facility selected was the T4 Stalker Tube located at The University of Queensland, which is a free-piston reflected shock tunnel that provides steady hypersonic flow for approximately 2 ms to 4 ms. This facility has been extensively written about by Stalker (1966, 1990, 2006, 1987, 1967), Stalker and Crane (1978), Stalker and Morgan (1988), Jacobs and Stalker (1991) and Stalker et al. (2005). Whilst the facility is described below, for a history and a more detailed explanation of the design and operating principle the reader is directed to those aforementioned references.

The T4 Stalker Tube, a schematic of which is shown in Figure 3.12, comprises a high pressure reservoir, compression tube, shock tube, test section and dump tank.

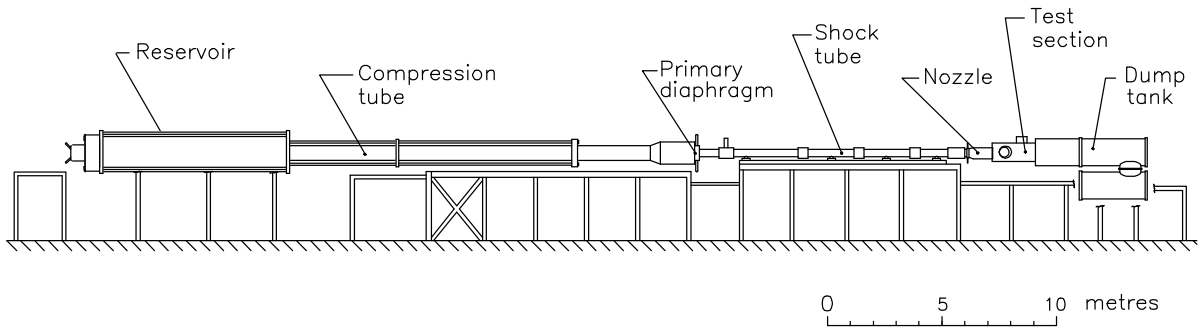

Figure 3.12: Schematic of the T4 Stalker Tube. (Figure sourced from Tanimizu (2008) and adapted by Kirchhartz (2009)).

The reservoir is an annular pressure vessel which sits around the compression tube. The compression tube is 26 m long and has an internal diameter of 299 mm and is followed by a shock tube which is 10 m long with an internal diameter of 75 mm.

A 92 kg stainless steel piston initially separates the high pressure gas in the reservoir from the compression tube and is held in place under vacuum on its rear face until firing. An unscored steel diaphragm separates the gases between compression tube and shock tube and is referred to as the primary diaphragm. A selection of primary diaphragms are available with a range in thickness of between 1 mm to 6 mm, resulting in burst pressures of between 12.5 MPa to 75 MPa. The secondary diaphragm, a

disc of Mylar, is located immediately downstream of the throat of the nozzle. This disc separates the shock tube gas from the initially evacuated test section.

A number of de Laval axi-symmetric nozzles are available to produce flows over a range of Mach number and enthalpies representative of hypersonic flight conditions. The nozzle used in these experiments was the Mach 4 nozzle, which has a throat diameter of 25 mm and an exit diameter of 135 mm. The downstream end of the nozzle lies inside the test section and sealed by o-rings. The test section has a square cross section with the dimensions 450 mm by 450 mm and is 1125 mm long. A large dump tank is connected to the back of the test section to collect the effluent of the tunnel during a shot.

3.2.1 Operating principle

The T4 Stalker Tube is operated in the following manner. A piston is driven down the compression tube by the high pressure in the reservoir. The gas in front of the piston is compressed up to the burst pressure of the primary diaphragm. Upon the bursting of the primary diaphragm a shock wave is formed in the shock tube. This shock wave then travels along the shock tube compressing the test gas contained within. Upon reaching the closed end of the shock tube, the shock wave is reflected back which further compresses the test gas. This region at the end of the shock tube is referred to as the stagnation region. The high pressure and temperature gas in this stagnation region burns through the secondary diaphragm, is driven through the throat of the nozzle and then accelerated by the nozzle to the desired freestream conditions in the test section.

Figure 3.13 illustrates the operating principle of the tunnel. The diagram in the top half of the figure shows the motion of the piston within the compression tube and the primary shock generated in the shock tube. The diagram in the bottom half of the figure is a space-time graph ($x - t$) of the compressible flow characteristics of the shock tube. Depicted in the $x - t$ graph is the primary shock wave as it travels down the shock tube and its reflection. Also shown are the contact surface between the driver gas and the test gas, the expansion fan and the piston trajectory.

In the bottom diagram in this figure, the boundaries to the test time can be seen on the far right. The flow commences when the incident shock burns through the Mylar diaphragm and ceases when the expansion wave reaches the model. The test time is truncated by the time it takes the nozzle to start and by driver gas contamination. All these effects are discussed in Section 3.4.

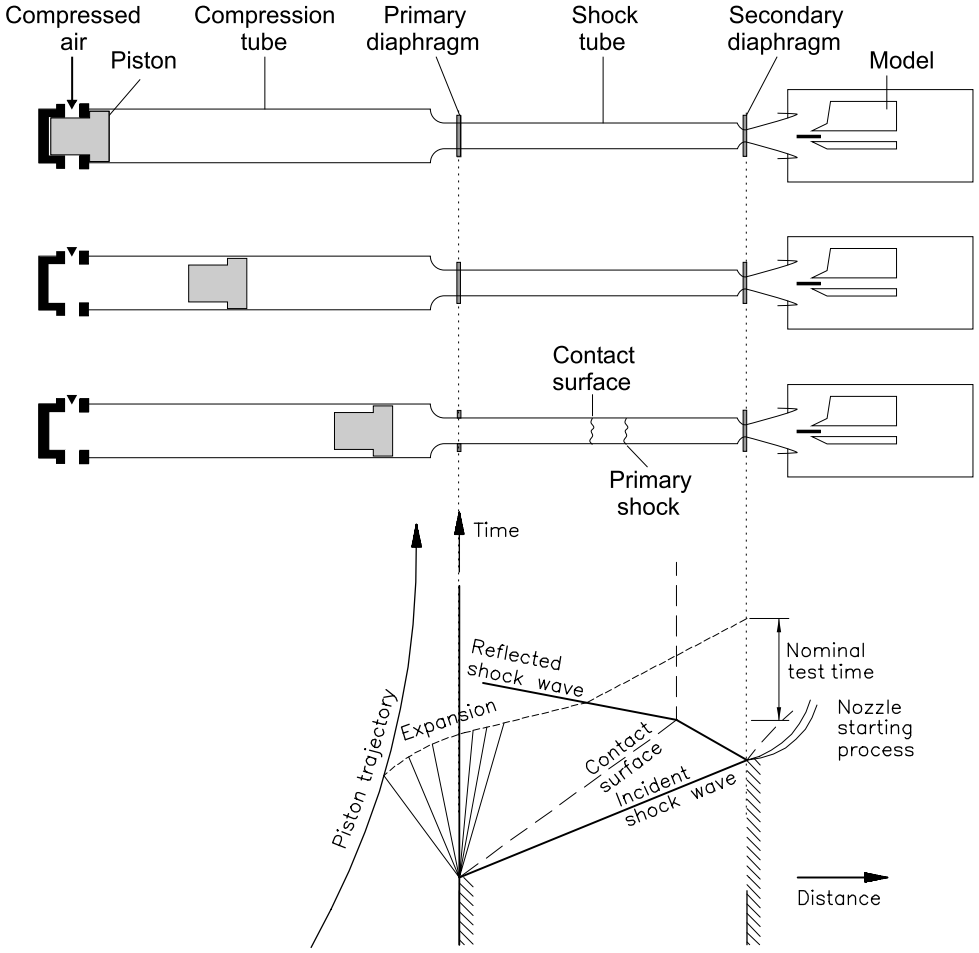

Figure 3.13: Operating principle of the T4 Stalker Tube. (Figure adapted from Kirchhartz (2009), Smith (1999) and Jacobs and Stalker (1991).)

An important consideration in operating a shock tunnel is the issue of tailoring and tuning. Tailoring refers to how steady the nozzle supply pressure is over the test time (Matsuo et al., 1975). Tuning refers to the piston motion at the end of its stroke. Tuning and tailoring of a shot are achieved by adjusting in tandem the ratio of the helium and argon in the compression tube and the fill pressures of the reservoir, compression tube and shock tube. A discussion on how tailoring and tuning are achieved for the T4 Stalker Tube can be found in Jacobs et al. (1993).

3.2.1.1 Semi-direct-connect mode

Although the tunnel is designed to produce flow up to Mach 12 and thereby allow scaled testing of an entire vehicle at that flight speed, the tunnel can also be configured to test a vehicle's sub-systems in isolation, such as the engine. This is achieved by running the tunnel in a semi-direct connect mode which operates on the same principle to direct-connect mode in other facilities; though in semi-direct connect mode the model is not connected directly to nozzle but sits some distance downstream. Direct and semi-direct connect mode is where a nozzle with a lower Mach number is selected but the total flight enthalpy is maintained in order to produce the incoming flow which the component would experience in flight. As the focus of this research was on the isolator and combustor chamber components, for these experiments the T4 Stalker Tube was run in semi-direct mode using the Mach 4 nozzle, which produces a flow with a Mach number closest to that which a typical scramjet combustor flying at Mach 8 would experience in flight (Billig, 1993). The specific test condition and the corresponding equivalent flight condition is discussed in Section 3.3.

3.2.2 Tunnel instrumentation

The tunnel has various instrumentation throughout to measure key parameters. A combination of analogue and digital gauges are used to measure the fill pressures of the reservoir, compression tube and shock tube. Mounted along the shock tube are three piezo-electric transducers used to measure the pressure in the shock tube, as shown in Figure 3.14. From the time history of these pressure traces, the time at which the shock wave passes each sensor can be determined and from this the shock speed can be calculated (Stalker and Morgan, 1988). The tunnel recoil is measured using a linear displacement transducer. This measurement is important for determining the exact position of the model in relation to the nozzle during the test time.

The pressure in the nozzle-supply region of the shock tunnel is measured using two piezo-electric pressure transducers which have ceramic thermal protection. Both the shock speed and the stagnation pressures are critical measurements as they are key parameters for the computer codes which are used to derive the properties of the freestream flow in the test section. These codes are discussed in Section 3.3.1. The signals from these tunnel sensors, along with the model sensors, were recorded using a National Instruments® 128-channel, 14-bit data acquisition system which can measure

up to 2.5 MS/s per channel (National Instruments, 2005).

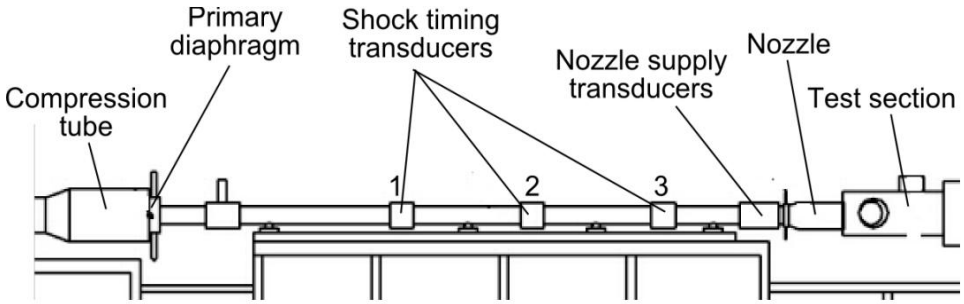

Figure 3.14: Shock timing stations on the T4 Stalker Tube (sourced from Freebairn (2010)).

The data acquisition system was run using three different sampling rates synchronously. The short time base recorded at 1 MHz the wall pressure transducers of the model, the transducers at the shock timing stations and the transducers measuring the stagnation region. The medium time base recorded at 200 kHz the transducers in the plenum chamber and the pulse which triggered the fuel valve, and the long time base recorded at 2.5 kHz the tunnel's recoil sensors. The signal from the Ludweig Tube pressure transducer was recorded on both the medium and long time base. The pulse which triggered the opening of the fuel valve was generated by the program when the tunnel recoil exceeded a certain threshold. The recoil trace is used so that the valve would have time to open fully just before the test flow arrived in the test section. The system was controlled via a program called *T4NIDAQ* (Ridings, 2012) written in the *LabVIEW*® programming language.

3.2.3 M4 nozzle

There are a range of contoured axi-symmetric hypersonic nozzles available for the T4 Stalker Tube ranging from Mach 4 to 12. For the present study the Mach 4 nozzle was used, a drawing of which is shown in Figure 3.15. The nozzle, designed by Jacobs (1989), produces parallel and uniform flow for the T4 Stalker Tube with a Mach number of around 4 for a broad range of stagnation pressures (13 MPa to 30 MPa) and total enthalpies (3 MJ kg^{-1} to 16 MJ kg^{-1}). Jacobs used a combination of a quasi-chemical kinetic program (*NENZF* by Lordi et al. (1966)) and a method-of-characteristics program (Jacobs, 1988) to design the nozzle contour taking into account the boundary layer growth along the wall. Detailed specifics of the nozzle, along with its performance, can be found in Jacobs (1989) and Jacobs and Stalker (1991).

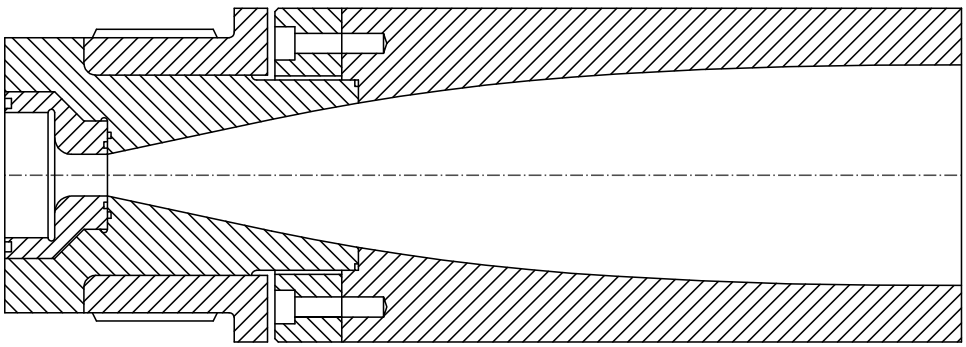

Figure 3.15: Schematic of the Mach 4 nozzle (sourced from Rowan (2003)).

A Pitot survey of the Mach 4 nozzle was conducted before the campaign in order to confirm that the flow characteristics of the nozzle had not deteriorated from previous use. The performance characteristics of a nozzle which are important are the size and shape of the core flow and the Pitot-to-stagnation ratio. The core flow is defined as the area on a plane parallel to the nozzle exit plane over which the flow is uniform and it is critical to characterise to ensure uniform flow is flowing into the model. An accurate measurement of the Pitot-to-stagnation ratio is critical as it is a key input to the codes which are used to compute the freestream properties, which are discussed in Section 3.3.1.

The Pitot survey consisted of an array of Pitot probes mounted in a rake which was positioned downstream of the nozzle exit. Within each probe a piezo-electric transducer was mounted. (A drawing of these instrumented probes can be found in Kirchhartz (2009).) These transducers measured the pressure behind a detached normal shock which forms over the upstream face of the probe during a shot. All transducers were calibrated in-situ before the commencement of the survey. The Pitot pressure measurements were normalised by the pressure measured in the stagnation region. This normalisation takes into account the time it takes for the flow in the stagnation region to reach the faces of the Pitot probes.

The Pitot rake was positioned at two locations downstream of the nozzle exit plane. One at 120 mm downstream and another at 156 mm. These two surveys were conducted at enthalpies of $3\,\mathrm{MJ\,kg^{-1}}$ and $5\,\mathrm{MJ\,kg^{-1}}$ respectively. The former position was chosen as this would allow direct comparison to previous surveys at a similar location and that this position lies close to the position at which the leading edge of the model

would be placed (107.5 mm). The latter position was taken as part of another experiment at a higher enthalpy, however it is included here as it affords a comparison at a similar enthalpy with the aforementioned previous surveys. These stated positions (denoted in Figure 3.16 by 'x') take into account the recoil of the tunnel, which is at its maximum at the onset of the test flow. For the 120 mm position, this meant that the probes would be sitting inside the nozzle at the time of filling and as such the outer probes had to be removed in order that the rake would fit within the nozzle. The flow is assumed to be axi-symmetric and the positions of the measurements are stated as the radial location of each probe from the centre line of the nozzle. At each position downstream of the nozzle the Pitot rake was also shifted vertically and horizontally to record pressures across a range of radial locations.

The results from the current survey are shown in Figure 3.16 along with the experimental results of Jacobs (1989) and Kirchhartz (2009). Also shown on these figures are the results from the CFD simulation of the nozzle which are discussed in Section 3.2.3.1. In these figures the results from this current survey are denoted as 'experiment'.

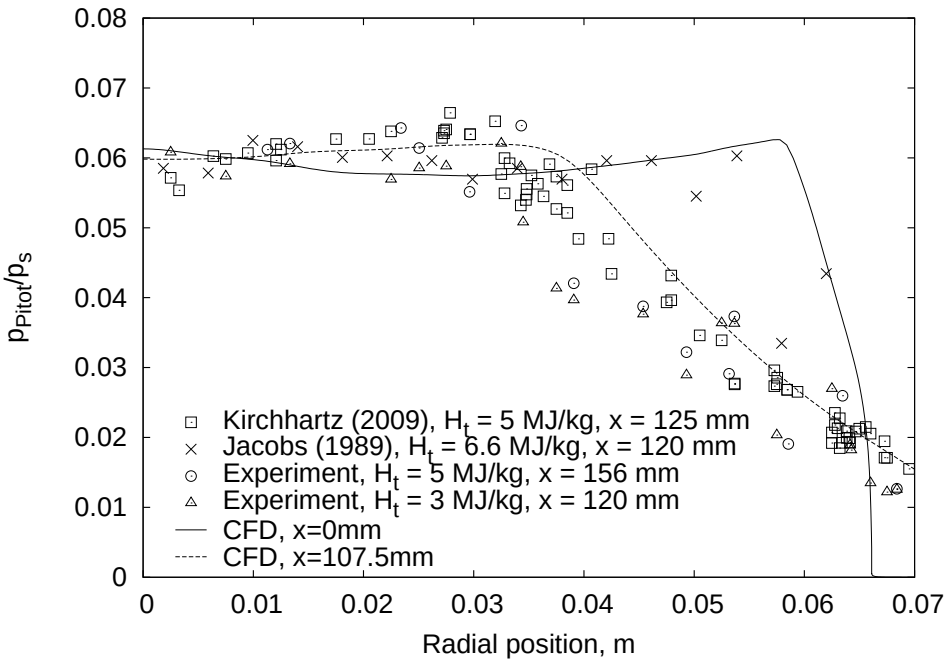

Figure 3.16: Recent Pitot pressure surveys of the Mach 4 nozzle along with the results from the CFD simulation of the nozzle flow. The x coordinate in the legend corresponds to the distance downstream of the nozzle exit plane where the leading face of the Pitot tubes were located.

Figure 3.16 shows results for various enthalpies and at different locations downstream of the nozzle. Comparing tests at the $5\,\mathrm{MJ\,kg^{-1}}$ condition, the result in this current study compare well with the those of Jacobs and Kirchhartz in terms of the Pitot-to-stagnation pressure ratio in the core area. The $5\,\mathrm{MJ\,kg^{-1}}$ in this current study is at location 156 mm, which is further downstream than both Kirchhartz and Jacob's experiments, however the Pitot-to-stagnation ratio of the core flow is relatively insensitive to changes in axial distance compared with the periphery flow. The survey conducted at the lower enthalpy of $3\,\mathrm{MJ\,kg^{-1}}$ shows that compared with the $5\,\mathrm{MJ\,kg^{-1}}$ by Kirchhartz, there is no appreciable change in the Pitot-to-stagnation ratio nor in the core size. For the study by Jacobs, the core flow is much larger, however it is noted in Kirchhartz (2009) that, from CFD simulations and discussions with Jacobs, the distance stated in Jacobs (1989) was likely to be in error and the true distance was more likely to be 60 mm. The CFD presented here, as does the CFD from Kirchhartz (2009), supports this conclusions as the slice taken at the very exit of the nozzle ($x = 0\,\mathrm{mm}$) matches the data by Jacobs (1989) very well at the extreme radial distances.

The key information to take from this current Pitot survey is that for the condition selected for this study, $3\,\mathrm{MJ\,kg^{-1}}$ at 120 mm - which lies close to where the leading edge of the model was placed ($x = 107.5\,\mathrm{mm}$), the core flow extends out to at least a radial distance of 30 mm. This corresponds to a diameter of 60 mm which provides a core flow 37% larger in diameter than the inlet of the diffuser. As the size of the diffuser precluded the use of a Pitot probe during the testing, the Pitot-to-stagnation ratio is taken from the Pitot survey for use in computing the freestream properties for this series experiments. The value used in the codes was taken from the average of the three most central measurements from this current survey, which is 0.0587. This ratio compares favourably with the previous established value of 0.0598 from Kirchhartz (2009) considering that this ratio is expected to be slightly lower at conditions with a lower total enthalpy.

3.2.3.1 CFD of Mach 4 nozzle

Whilst the use of *NENZF* is generally accepted for the calculation of the freestream properties of the T4 Stalker Tube for the interpretation of experimental data, a numerical simulation of the nozzle was required for the subsequent numerical simulation of the diffuser. The CFD code which was employed for the simulation of the flow through the Mach 4 nozzle was CFD++ (Goldberg et al., 2000). CFD++ is capable of

solving both the steady and unsteady 3-D Navier-Stokes equations for compressible flows including multi-species and finite-rate chemistry. CFD++ was selected as there has been considerable investment in code validation (Goldberg et al., 1997) and that it has been used with great success on cases ranging from ramp flow calculations (Reinartz et al., 2007) to combustion simulations (McGuire, 2007). Within the code, viscous effects are specified according to the Sutherland's law approximation. Turbulence is modelled by the solving the Reynolds-averaged Navier-Stokes (RANS) equations employing the two-equation ($k - \omega$) shear stress transport (SST) turbulence model, with a freestream turbulence level of 2%. The calculations performed were double precision and of second-order accuracy in both time and space. The specific details of the implementation of this code to the T4 Stalker Tube conditions are provided in Lorrain and Boyce (2011) and Lorrain et al. (2012), with the only addition being that the high temperature air chemistry model by Park (1985) was used for the simulations for these experiments.

The geometry of the nozzle that was modelled in the CFD++ simulation was extended upstream to include a short section of the stagnation region (which supplies the nozzle) and extended downstream to include a portion of the test section. The simulation was performed for the nominal shot only with the inflow conditions taken directly from the *ESTCj* calculations for that shot, as presented in Table 3.4.

Table 3.4: Inflow conditions for CFD simulation of the Mach 4 nozzle (based on the stagnation conditions of the nominal Shot 10816)

Property	Value	Units
Stagnation pressure (measured)	21.2	MPa
Stagnation temperature	2803	K
Total enthalpy	3.10	MJ/kg

The CFD solution of the flow field is shown in Figure 3.17 in contours of both Mach number and pressure. As shown in that figure on both contour plots, the Mach cone extends out to a distance of 0.78 m from the end of the throat of the nozzle and the flow is fairly uniform throughout this Mach cone.

At the position where the leading edge of the model is situated, 107.5 mm downstream from the exit of the nozzle (which corresponds to approximately 0.62 m on Fig-

ure 3.17), these contour plots show that the diameter of the core flow is approximately 90 mm. This is depicted more clearly in the same CFD results shown in Figure 3.16 where the Pitot pressures are plotted along a radial line perpendicular to the nozzle centreline at 107.5 mm downstream from the exit of the nozzle. Here the radius of the core flow extends out to approximately 0.038 m (or 76 mm in diameter). Taking the smaller of these two estimates of the core flow size of 76 mm, the core flow, as simulated by the CFD, at the entrance of the diffuser is at least 1.7 times the diameter of the entrance of the diffuser (43.6 mm). This supports the finding from the Pitot survey, that the model receives flow which is fairly uniform across the entire cross-sectional face of the diffuser.

The mass-averaged properties were extracted from the CFD solution across the core area at the 107.5 mm location and are presented in Table 3.5. These values from the CFD are tabled along with the freesteam properties computed by *NENZF* for that shot (which is discussed in Section 3.3.1) along with the deviation between the two calculations. Table 3.5 illustrates that there is good agreement between these two methods for calculating the properties of the freestream.

Table 3.5: Freestream conditions from the Mach 4 nozzle from *CFD++* and *NENZF*

Property	Units	*NENZF*	CFD	Difference (%)
Pressure	kPa	47.13	47.07	0.1
Temperature	K	667.0	651.7	2.3
Velocity	m/s	2325	2275	2.2
Mach No.	-	4.54	4.50	1.0
Density	kg/m^3	0.246	0.251	1.9

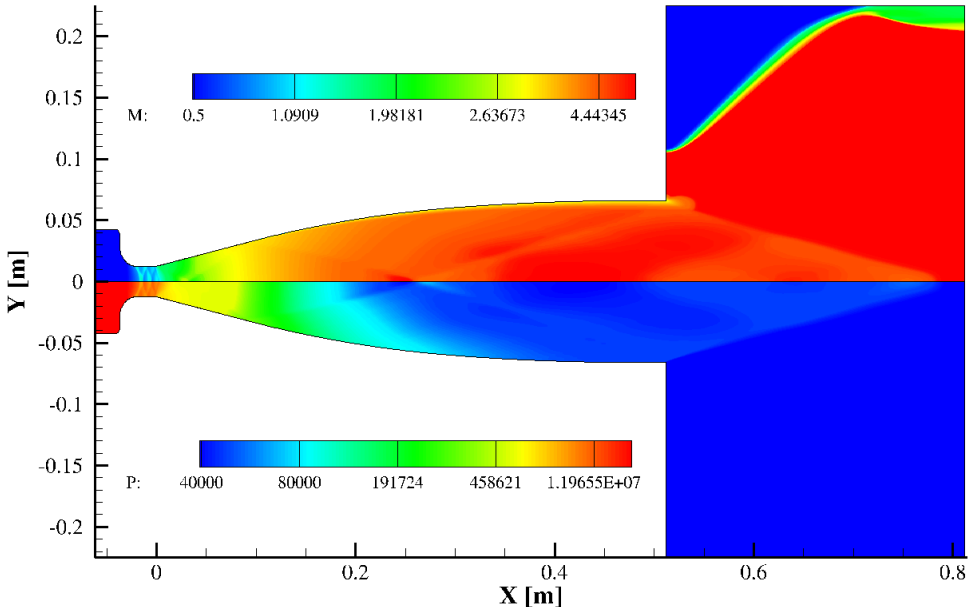

Figure 3.17: Contour plots of both the Mach number and pressure from the *CFD++* simulation of flow through the Mach 4 nozzle for the nominal shot condition. The top half of the figure shows the contours of Mach number and the bottom half shows the contours of pressure.

3.3 Test Flow Conditions

The tunnel test conditions are selected to represent the conditions which would exist in flight at Mach 8. To determine such flight conditions the approach taken in Heiser and Pratt (1994) was followed. Heiser and Pratt suggest a flight corridor bounded by trajectories of constant dynamic pressure as shown in Figure 3.18. The lower and upper bounding trajectories are at a dynamic pressures of between 95 kPa and 24 kPa respectively which represent, again respectively, a structural limit of the vehicle airframe and an aerodynamic limit (such that the wing is of a reasonable size). The target test condition for this study was for a flight Mach number of 8, which if placed on the median trajectory of $q = 50$ kPa of Figure 3.18 would be at an altitude of approximately 30 km. However, for scramjet powered flight it is advantageous to fly at the higher dynamic pressure limit as this provides a higher mass flow rate to the engine and will generate greater thrust. As such, for this study, the target condition was selected at the upper dynamic pressure limit of 95 kPa, similar to that adopted by Billig (1993), which for flight at Mach 8 would place the vehicle at an altitude of 26.1 km with a corresponding total enthalpy of 2.9 MJ kg^{-1}.

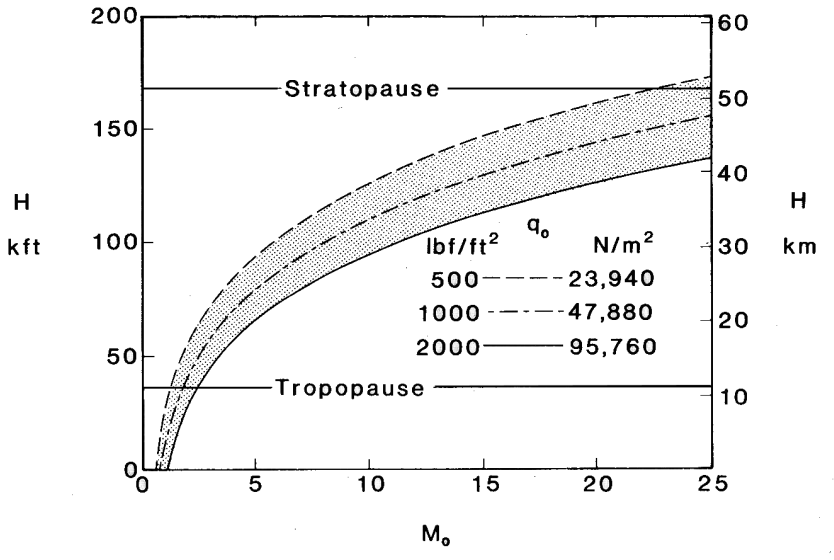

Figure 3.18: Scramjet powered vehicle flight corridor in terms of flight Mach number and altitude bounded by trajectories at constant dynamic pressures of 500 and 2000 lbf/ft^2. Trajectories use *U.S. Standard Atmosphere 1976*. (Figure sourced from from Heiser and Pratt (1994).)

As this is a semi-direct-connect study, where the vehicle forebody and part of the engine inlet are omitted, the conditions to match are those entering the isolator of the

scramjet. This is achieved primarily through matching the total enthalpies of the flight and ground test flows, along with the local Mach number and pressure. These target isolator conditions were estimated by assuming the vehicle's forebody deflection angle and selecting a representative engine.

The forebody deflection angle comes in tandem with the engine design selected, which for this research was the RESTM8 by Turner (2010). This engine is a rectangular-to-elliptical-shape-transition (REST) engine designed to operate at Mach 8 and has been substantially tested in the T4 Stalker Tube (Turner and Smart, 2008, 2010, 2009). The design of the RESTM8 engine assumes the flow undergoes pre-compression by the forebody of the vehicle, which for this engine was a planar surface with an angle of attack of 6° to the freestream. The same forebody angle is selected for the calculation of the target conditions for this study.

To determine the condition of the flow exiting the inlet of the RESTM8 engine, oblique shock theory is used for the flow across the forebody and then inlet performance parameters are applied to arrive at the isolator entrance conditions. These inlet performance parameters are taken directly from the numerical simulations from Turner (2010, Table 3.8) and are in the form of pressure and temperature ratios, along with the local Mach number at the isolator entrance.

The results from these calculations of the flow conditions at the target flight condition are listed in Table 3.6 which include the freestream and the post-forebody and isolator entrance stations. Also listed are the properties calculated for the flow entering the isolator for the nominal shot of the experiment (as discussed in Sections 3.1.1.2 and 3.3.1). When compared with the target the condition at the entrance of the isolator for the experiment is at a slightly higher total enthalpy and a larger static pressure. These differences result in the corresponding equivalent flight condition to be at higher dynamic pressure of 105 kPa and also at a higher Mach number of 8.3. These two parameters together dictate the altitude, which is adjusted down from 26.1 km to 26.0 km.

Table 3.6: Flow conditions for flight at Mach 8 at a dynamic pressure of 95 kPa of the freestream and at the post forebody and isolator entrance stations. Target isolator entrance conditions were calculated using the performance parameters of Turner's (2010) RESTM8 engine and a 6° forebody wedge. Experimental isolator conditions are estimated for the nominal shot.

	Units	Target			Experiment
		Free-stream	6° Fore-body	Isolator	Isolator
Mach no.		8.0	6.6	3.4	3.6
Static temperature	K	223	315	863	885
Static pressure	kPa	2.1	5.9	107	119
Dynamic pressure	kPa	95	181	843	1055
Static density	kg/m^3	0.033	0.065	0.43	0.47
Velocity	m/s	2390	2360	1970	2120
Stagnation enthalpy	MJ/kg	2.9	2.9	2.9	3.1
Unit Reynolds no.	$1/m$	5.5×10^6	8.0×10^6	2.7×10^7	2.6×10^7

3.3.1 Calculation of freestream properties

Direct measurement of freestream properties is difficult in hypersonic shock tunnels due to the short flow times, transient nature of phenomena, small core flows and the general harshness of the environment. Instead, the properties of the freestream must be computed based on the direct measurements which can be taken from the tunnel instruments such as the filling conditions, the shock speed and the nozzle-supply pressures. Two computer codes are used in series to calculate the freestream conditions of the T4 Stalker Tube and they are *ESTCj* and *NENZF*.

The code titled *Equilibrium Shock Tunnel Conditions Junior* (*ESTCj*) is a modified version of the original *ESTC* program written by McIntosh (1968) and is used to calculate the properties in the stagnation region at the end of the shock tube (also known as the nozzle supply region). The '*j*' at the end of '*ESTCj*' denotes that it incorporates the *CEA2* chemistry database (McBride et al., 2002). *ESTCj* is a one-dimensional model which assumes an inviscid mixture of reacting gases in thermodynamic equilibrium. The inputs for this program are the shock tube fill pressure (P_{ST}), the shock tube temperature (T_{ST}), the measured shock speed in the shock tube ($U_{S.T.}$) and the measured nozzle-supply pressure (P_S). The program then uses ideal normal shock relations to compute the flow properties in the stagnation region. Due to minor losses this method leads to higher estimations of stagnation pressures than those measured experimentally. To account for this difference *ESTCj* isentropically relaxes the initial estimate of the

stagnation pressures until they match those measured. The conditions in the nozzle-supply region of the T4 Stalker Tube, as computed by *ESTCj* for the nominal condition for this study, are shown in Table 3.7.

Table 3.7: Nozzle-supply conditions and shock speed for the nominal condition. The calculated properties were determined using *ESTCj*. (Nominal shot: 10816)

Property	Parameter	Value	Units
Stagnation pressure (measured)	P_S	19.59	MPa
Stagnation temperature (calculated)	T_S	2815	K
Shock speed (measured)	u_{ss}	1817	m/s
Total enthalphy (calculated)	H_0	3.12	MJ/kg

The results from *ESTCj* are then feed into a second computer code called *Non-Equilibrium NoZzle Flow (NENZF)*, written by Lordi et al. (1966). *NENZF* is a quasi-one-dimensional model which computes the inviscid expansion of the flow from the stagnation region through the nozzle. *NENZF* employs a set of 20 chemical species and 64 reactions set to model the chemical reactions occurring in the flow. The chemical reactions may be assumed to be either frozen, in equilibrium or to proceed at finite reaction rates (i.e. non-equilibrium). The input variables are the nozzle geometry, the measured nozzle-supply pressure, (P_S) and the computed nozzle-supply temperature, (T_S), as computed by ESTCj. The program calculates the expansion of the flow up to the area ratio as specified by the nozzle geometry. To account for boundary layer growth, the program is run iteratively and the nozzle area ratio is adjusted artificially such that the expanded flow matches the measured Pitot-to-nozzle-supply pressure ratio. This ratio may be from a Pitot probe installed on a model or, as in this case where space does not permit a probe, this ratio is taken from a prior Pitot survey of the nozzle. The conditions of the flow exiting the Mach 4 nozzle as computed by *NENZF* for this study are shown in Table 3.8 for the nominal condition.

Table 3.8: Nominal test flow conditions using *ESTCj* & *NENZF*. H_0 is stagnation enthalpy and the following relate to the freestream: p_∞ is the static pressure, T_∞ the static temperature, ρ_∞ the density, u_∞ the flow velocity and M_∞ the Mach number. (Nominal shot: 10816)

Parameter	H_0	p_∞	T_∞	ρ_∞	u_∞	M_∞
Nominal Value	3.12	43.6	671	0.226	2331	4.54
Units	MJ/kg	kPa	K	kg/m^3	m/s	-

3.3.2 Boundary layer analysis through the diffuser

Cebeci and Bradshaw's (1984) code was used to solved the coupled boundary layer equations along the wall of the diffuser and these results are given in Table 3.9. The input conditions were taken directly from results from *NENZF* for the nominal shot condition.

Table 3.9: State of the boundary layer at the diffuser exit (i.e. isolator entrance). Values are for a location which is 0.175 m from the leading edge. δ is the boundary layer thickness, δ^* the displacement thickness, θ momentum thickness and C_f the coefficient of skin friction.

Parameter	δ	δ^*	θ	C_f
Nominal Value	4.04	1.14	0.350	0.00152
Units	mm	mm	mm	-

3.4 Data Reduction

3.4.1 Test time

The test time is the period of time over which the flow being measured is a true representation of an established flow. The factors which affect the length of the test time are: the time for the nozzle to start properly, the time for the flow to establish along the model, the arrival of the driver gas and the tailoring of the nozzle supply pressure. These effects are discussed in the following sections and are depicted together in Figure 3.19.

3.4.1.1 Nozzle start up

A hypersonic nozzle is considered to be producing steady flow when the initial unsteady expansion has been swept out of the nozzle and the boundary layer along the nozzle walls have fully developed (Smith, 1966). The start up time for the Mach 4 nozzle used in this study, which had been previously established by Kirchhartz (2009), was taken as being approximately 0.5 ms after the rupture of the second diaphragm.

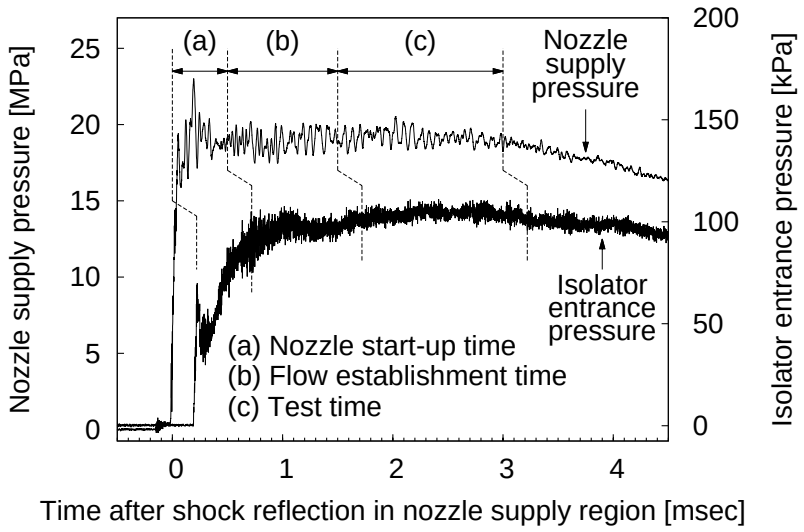

Figure 3.19: Pressure traces from the nozzle-supply region and an isolator sensor (DT2) annotated with considerations for the selection of the test time for an attached flow along the isolator. Vertical lines, indicating key periods of time, are shifted by 0.22 ms to the right from the nozzle supply pressure trace (upper trace) for the isolator entrance pressure trace (lower trace) to account for the time it takes for the flow to pass from the nozzle supply region to sensor DT2 in the isolator.

3.4.1.2 Flow establishment time

After the starting of the nozzle, the test time is still not considered to have begun. First the flow must establish itself and settle along the model. In short duration facilities this can consume a significant proportion of the time of steady flow. Flow establishment times in shock tunnels, as previously discussed in Chapter 2, have been investigated experimentally and numerically in previous studies (Davies and Bernstein, 1969; East et al., 1980; Jacobs et al., 1992). These studies correlate flow establishment time with the number of flow lengths. From these studies it is generally accepted that for attached flow to reach steady state a boundary layer would require 3.3 model lengths if laminar and 2 lengths if turbulent. Based on the parameters of the freestream, which has a flow velocity of approximately 2320 m s^{-1} and a model length of 0.7522 m (the distance from the leading edge to the position of the last sensor), the time it would take the flow to reach steady state at the last sensor would be approximately 1.1 ms for a laminar boundary layer and 0.64 ms for a turbulent boundary layer.

The point of transition of the boundary layer from laminar to turbulent has been estimated for this model based on transition studies specific to the T4 Stalker Tube (He and Morgan, 1994; Mee, 2002; Wise and Smart, 2012). Nagel (1968) found, that for

hypersonic flows, the Reynold's number where transition occurs (Re_t) is a function of the unit Reynold's number (Re_u). This correlation by Nagel (1968) was confirmed to hold true for higher enthalpy flows in the T4 Stalker Tube by He and Morgan (1994) and is given in Equation (3.5).

$$Re_t = 2687 \cdot Re_u^{0.4} \tag{3.5}$$

For the test condition for this study (3 MJ kg^{-1}, Mach 4 nozzle) the unit Reynold's number of the freestream flow is calculated to be 17.7×10^6 1/m. By the end of the diffuser Re_u has increased to 25.8×10^6 1/m. Using these two bounds with Equation (3.5), the Reynold's number at which transition is likely to occur is between 2.13×10^6 and 2.48×10^6. For a flat plate this would lie between 120 mm and 96 mm from the leading edge respectively. If taken to be true for these experiments, this would lie at least 53 mm upstream of the start of the isolator. It should be noted though that this estimation of the point of transition is based on the findings of He and Morgan (1994) who performed experiments at higher Mach numbers than this study. Additionally, the geometry they tested was an unconfined flat plate, whereas for this study the geometry of the diffuser is a converging circular duct. For the first of these differences, the lower Mach number of these experiments is expected to reduce Re_t (He and Morgan, 1994) and therefore the point of transition would lie further upstream than is estimated. The second of these differences, however, is difficult to quantify, though Kirchhartz (2009) adopted a similar value for Re_t of 2×10^6 for his experiments in the T4 Stalker Tube which involved a circular duct and he found good agreement between his experimental and numerical results.

Although only a minority of the flow along the model is expected to be laminar ($\approx$ 20%), a conservative flow establishment time of 1 ms is assumed as the establishment time for attached flow. For cases were the flow has separated then the time to reach steady state can be much longer (Holden, 1971). For these cases the time histories of the pressure traces in the region of the separated flow will need to be looked at directly to determine an establishment time. As this issue is a key question of this research, the determination of the establishment time for separated flows is left to Section 4.1 of Chapter 4 in which the experimental results are presented.

3.4.1.3 Driver gas contamination

The test time is terminated by one of two mechanisms: the arrival of the driver gas or a significant drop in the nozzle-supply pressure. A number of studies have been conducted to determine the arrival time of the driver gas for the T4 Stalker Tube over a range of enthalpies (Boyce et al., 2005; Paull, 1996; Paull and King, 1995; Skinner, 1994; Stalker and Crane, 1978). Due to mixing which occurs over a finite region between the test gas and driver gas the interface between these two gases is no longer discrete. Instead, the criterion chosen to note the arrival of the driver gas is when the driver gas represents 10% (by mole fraction) of the test gas composition (Boyce et al., 2005). The results from the most recent study (Boyce et al., 2005) are shown in Figure 3.20 and the S.I. base unit version of the relation in the figure is given in Equation (3.6).

$$t_{10\%\,\text{contamination}} = 1.268 \times 10^{9}\, H_0^{-1.7183} \pm 38\% \tag{3.6}$$

As shown in Figure 3.20, the driver gas arrival time is exponentially delayed with decreasing enthalpy. Extrapolating the curve to the condition run for these experiments, $3\,\text{MJ}\,\text{kg}^{-1}$, the arrival of the driver gas is calculated to be 8.8 ms ($\pm$3.4 ms) from the onset of flow. However, extrapolation may not hold true below $5\,\text{MJ}\,\text{kg}^{-1}$ due to an absence of experimental data at these low enthalpies. Therefore the value for the $5\,\text{MJ}\,\text{kg}^{-1}$ condition of 3.9 ms ($\pm$1.5 ms) is taken as a conservative estimate for $3\,\text{MJ}\,\text{kg}^{-1}$ condition.

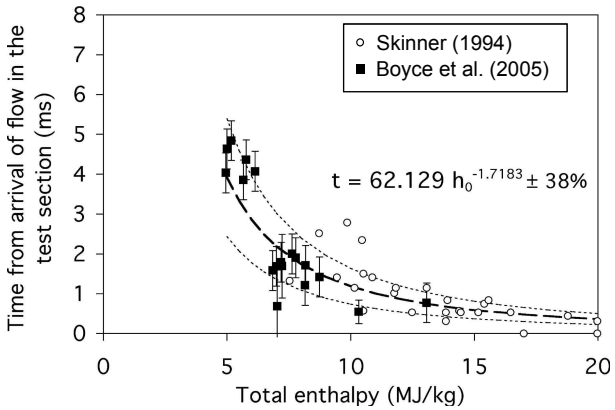

Figure 3.20: Time for 10% driver gas contamination to occur in the T4 Stalker Tube (Figure sourced from Boyce et al. (2005)).

3.4.1.4 Tuning

The second mechanism by which the test time can be terminated is by a significant drop in nozzle supply pressure. The accepted criterion for this mechanism is when the nozzle supply pressure has fallen by 5% (Kirchhartz, 2009). The time of steady nozzle supply pressure is dictated by how well tuned the shot is. Over-tuning is where the nozzle-supply pressure rises significantly over the total flow time and under-tuning the opposite (i.e. pressure fall) (Jacobs et al., 1993). Fortunately, the specific 3 MJ kg^{-1} condition tested was characterised by long periods of steady flow as shown in the nozzle-supply pressure trace in Figure 3.19. For these experiments the test time was terminated by the criterion of a 5% fall in nozzle-supply pressure (as opposed to the driver gas contamination) at 3 ms after the onset of flow.

3.4.2 Uncertainty analysis

As the freestream conditions are not measured directly but computed, there is a degree of uncertainty that derives from the measured parameters on which the calculations are based. Mee (1993) provides a method of estimating these uncertainties for the T4 Stalker Tube. This uncertainty analysis is based on a 95% confidence interval of the value of the measured quantities. The uncertainty analysis of a derive parameter is determined by estimating the sensitivity of that parameter to the perturbation in the measured quantities used to compute it. The results from this uncertainty analysis when applied to the nominal conditions for these experiments and to the fuelling conditions are shown in Tables 3.10 and 3.11 respectively. Further details can be found in Appendix C along with the results demonstrating the repeatability of both the test condition and the flow phenomena being studied.

Table 3.10: uncertainty in the nominal test flow conditions as computed by *ESTCj* & *NENZF*. (Nominal shot: 10816)

Parameter	H_0	p_∞	T_∞	ρ_∞	u_∞	M_∞
Units	MJ/kg	kPa	K	kg/m^3	m/s	-
Nominal Value	3.12	43.6	671	0.226	2331	4.54
Uncertainty	6.6%	12.0%	7.9%	10.5%	2.9%	2.2%

From the uncertainty analysis, the derived parameters of the test flow conditions are most sensitive to the uncertainty in the shock tube speed (u_{ss}) and Pitot pressure

(P_{Pitot}). Due to the large estimate of the fundamental uncertainty in these two measured quantities the resultant uncertainties in the test conditions range from 2% to 12%. For the pressure distributions along the engine shown in Chapter 4, the measured wall pressures are normalised by the derived freestream static pressure in order to account for shot to shot variability. These wall pressure measurements are estimated to have an installed uncertainty of 4%. The uncertainty in the wall pressure measurements and the derived freestream pressure both contribute to the uncertainty in the normalised value. This uncertainty is estimated to be 13% and is depicted as error bars on the plots in Chapter 4.

Table 3.11: Relative uncertainties in the fuelling conditions.

Parameter	Description	Relative Uncertainty (%)
α	Discharge coefficient	6.8
$\dot{m}_{H_2}$	Mass flow rate of hydrogen	7.3
$\dot{m}_{O_2}$	Mass flow rate of oxygen	8.8
ϕ	Equivalence ratio	11.4

For the fuel system, compounding uncertainties in the Ludwieg tube pressure, the integrated plenum pressure and the assumed temperature of the fuel, lead to a large uncertainty in the derived discharge coefficient α. The uncertainty in α is the largest contributor to the uncertainty in the mass flow rate of hydrogen ($\dot{m}_{H_2}$), with the remaining third coming from the uncertainty in the measured plenum pressure. The uncertainty in $\dot{m}_{H_2}$ contributes just under half of the total uncertainty in the equivalence ratio (ϕ) with the other part coming from the uncertainty in the mass flow rate of the test flow air. Together this leads to an uncertainty in ϕ of approximately 11%.

3.4.3 Repeatability

The degree of repeatability of the test flow condition and of the flow phenomenon being studied are presented and discussed in Appendices C.3 and C.4 respectively. Here, Table 3.12 lists the number of shots that were repeated. In general, three repeat shots were performed for each combustor at two to three different fuelling levels. For these shots the time-averaged pressure profiles, a selection of which are presented in Appendix C.4, all show excellent repeatability. Comparisons of the time-histories for the

isolator sensors where separation occurred show reasonably good agreement given the unsteady and sporadic nature of the leading edge of the shock train.

As the successive pressure profiles for each of three combustor configurations all show such a strong relationship with increasing equivalence ratio, and that the difference in pressure between shots at a similar equivalence ratio was smaller than the changes in pressure due to the change in equivalence ratio between specified fuelling conditions, the number of repeat shots were generally restricted to those given in Table 3.12. The full list of shots performed and the corresponding fuelling conditions are listed in Tables D.1 and D.2 respectively.

Table 3.12: Shots used to establish repeatability of flow phenomenon for each of the combustors, most of which are shown in Figures C.1 to C.3. N is the number of shots at a certain fuelling condition.

Combustor	ϕ	N	Shots
Const. area	0.66 ± 0.01	3	10831, 10835, 10839
	0.78 ± 0.02	2	10833, 10838
	1.10 ± 0.03	3	10824, 10826, 10828
1°	0.66 ± 0.02	2	10806, 10813
	0.77 ± 0.01	2	10811, 10812
	1.14 ± 0.01	3	10807, 10808, 10818
2°	0.70 ± 0.05	2	10848, 10849
	1.14 ± 0.02	3	10842 – 10844

Chapter 4

Experimental Results

This chapter presents experimental data acquired from the experiments conducted in the T4 Stalker Tube. The chapter consists of a number of parts. The first part (Section 4.1) presents transient data, in the form of time-history plots, for the pressure measurements taken along the entire engine which are used to determine the time taken for the separated flow to establish. This includes a methodology for determining the establishment time for the formation of a stable shock train and explores correlations between this parameter with other key parameters. For the range of equivalence ratios where flow establishment has been shown, the length of the shock train and how it correlates with fuelling is presented in Section 4.3. Finally, pressure profiles along the isolator and combustor are constructed based on the average pressure over the test time and are presented in Section 4.2.

4.1 Investigation of Separated Flow Establishment

4.1.1 Conventional test time window

In short duration impulse facilities, such as the T4 Stalker Tube, the selection of an appropriate period of time over which to average the data requires a number of fluid phenomena, associated with these types of facilities, to be taken into account. The key effects, as discussed in detail in Chapter 3, are the nozzle start-up time, flow establishment time, supply pressure decay and driver gas contamination. All these effects have implications on the selection of an appropriate test time. However the flow establishment time, marked by (*b*) in Figure 3.19, has been calculated assuming an attached flow. In cases where there is large scale separation then the flow establishment time

(t_{est}) can be much longer (Holden, 1971).

One of the key goals of this research is to determine whether pre-combustion shock trains can be studied in these facilities. This question arises as the large scale separation associated with this phenomenon may lead to such long establishment times that the flow never stabilises in the available test time. As discussed in Chapter 2, Holden (1971) found in the case of a shock boundary layer interaction at the corner of an inclined ramp, that a good measure for the establishment time for that interaction was the time for an acoustic wave to traverse the separated region. This is described by Equation (4.1),

$$t_{est} = \frac{L_{int}}{a_w} \tag{4.1}$$

where t_{est} is the establishment time, L_{int} the length of the interaction and a_w the speed of sound based on the wall temperature. Holden's acoustic criterion is applied next to the nominal conditions entering the isolator, which are given in Chapter 3. The temperature of the flow exiting the diffuser and entering the isolator from the CFD is calculated to be 652 K. Although the temperature would be much higher near the walls where the velocity of the flow is lower, the temperature of the centreline flow is taken to provide a conservative estimate. Assuming a specific heat ratio (γ) of 1.4, a gas constant (R) of 287 J kg^{-1} K^{-1} and a temperature of 652 K, then this results in a speed of sound of 512 m s^{-1}. Now, the maximum size of a contained shock train would be one that occupies the entire isolator (but no more), and in these experiments this would be a length of 137 mm long. Using this length and the speed of sound above, the time taken for an acoustic wave to travel the entire length of isolator would be 268 µs.

Holden (1971) notes that although the acoustic wave method worked well on shock-wave boundary layer interactions on an inclined ramp, these interactions are quite small in comparison with other cases of separated flow, such as the flow behind a bluff body. In the case of sphere mounted on a sting, Holden (1971) found that the time taken for the flow to establish was an order of magnitude longer than that for the inclined ramp experiment. This was due to the large regions of viscous mixing, which took longer to establish than the time it took for an acoustic wave to traverse it. Considering the separation within the isolator may span many duct diameters (4D), and involves viscous mixing, then the latter method may be more applicable. For those experiments Holden found that approximately 30 body lengths were required for establishment. This is represented in the following correlation:

$$\frac{t_{est} \cdot U}{D} = 27.9 \quad \text{(for a sphere)} \tag{4.2}$$

where t_{est} is the establishment time, U the flow velocity and D the diameter of the sphere. Applying this correlation again to the conditions entering the isolator where, the mean velocity of the flow is calculated to be 2275 m/s (again from CFD), and substituting the total length of the isolator ($L_{isolator}$) of 137 mm for D, then t_{est} from Equation (4.2) is 1.68 ms. This value for t_{est} is 6.3 times the length of the time calculated using the acoustic time method.

Applying both approaches from Holden (1971) provide two considerably different estimates of the flow establishment time for these experiments without a clear indication as to which one would be more applicable. The case may be that neither of them are applicable at all. To answer this question of flow establishment, a series of time-history plots (also known as x-t diagrams) are presented next. These plots show the pressure measured by the sensors along the isolator over the flow time. These plots include on them the labels of each of the sensors. To aid the reader in the visualisation of these plots, the sensor labels and their location along the engine model are shown in Figure 4.1 for each of the three combustors. Filled circles identify sensors which were installed and were working for the majority of the tests. Non-filled circles identify pressure taps in which a sensor was not installed or for a sensor which did not work for a majority of the tests (due to causes such as poor electrical connection and loss of thermal protection).

4.1.2 Isolator pressure traces for non-separated cases

The first of the time-history plots of the pressure measurements along the isolator is shown in Figure 4.2. In this plot the trace for each sensor is offset by 100 kPa. As the spacing (7.5 mm) between each sensor tap is the same throughout the isolator, this offset means that the zero pressure level for each trace corresponds directly to an axial distance along the engine. This distance is shown on the right hand side axis of time-history plots and the datum is taken as the location of the fuel injectors. Sensors are stacked from the bottom to the top of figure starting with the sensor furthest upstream of injection (DT1 at 139.5 mm). This style of plot illustrates the state of the flow as it travels down the duct. Displayed on the figure are three vertical lines representing, in order, the conventional start time, a 5% decay in supply pressure and the 10% driver gas contamination.

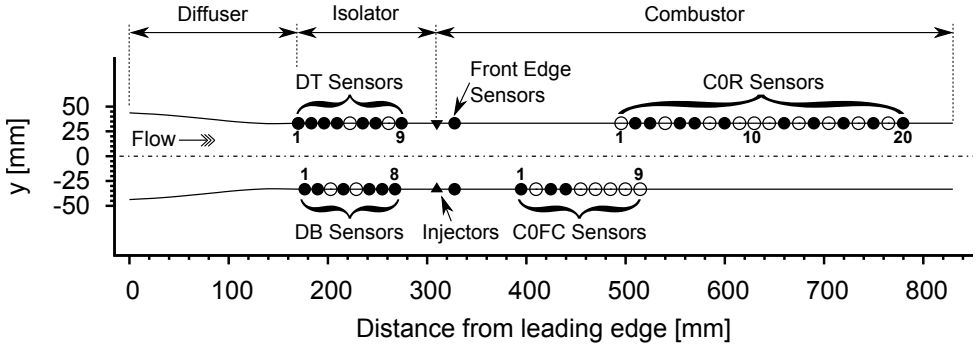

(a) Constant area combustor configuration

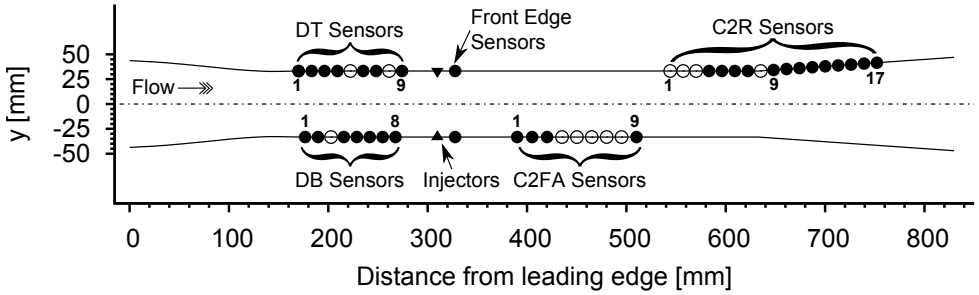

(b) 2° divergent combustor configuration

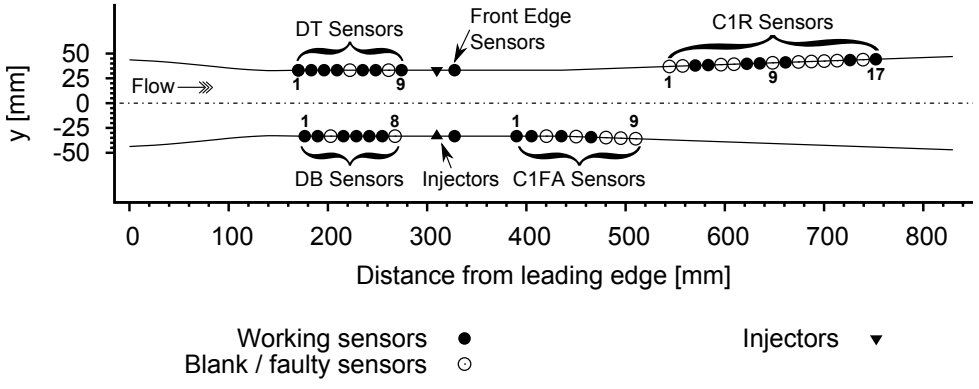

(c) 1° divergent combustor configuration

Figure 4.1: Sensor labels and locations along the engine for all three combustor configurations

The first of these, the conventional start of the test time, includes the time it takes for a hypersonic flow to establish to a steady state over the entire length of the model using the convention laid out by Davies and Bernstein (1969) and Jacobs et al. (1992). The more conservative number of flow lengths is taken, which is 3 for the case of a laminar boundary layer. The calculations of the other two lines (i.e. the 5% decay in supply pressure and 10% driver gas contamination), take into account the time it takes for the flow to travel from the stagnation region to the first pressure sensor along the model. The more conservative line, representing the 5% decay in supply pressure, is selected as the end of the test time, which terminates the period over which the pressure measurements are averaged.

The traces for all the isolator sensors in Figure 4.2 show fairly steady pressure levels over the test time as bounded by either of the two upper limits to the test time with the majority of traces remaining within $\pm 4\%$ of the mean values[1]. There are some moderate to high frequency pressure fluctuations on a number of sensors occurring before the start of the test time (e.g. DT7, DB3 and DB1) with the greatest amplitude occurring on DB3.

The next figure presented, Figure 4.3, is for a fuelled case of the constant area combustor where there is no evidence of separation ahead of the injectors. Here the traces are very similar to those in the previous unfuelled case as expected. The only real difference to note is the initial pressure rise at the point of flow onset (i.e. at 0 ms). In this case the pressure rise is quite sharp whereas for the previous case (Figure 4.2) the initial pressure rise is comparably more gradual. This difference in the gradient of the pressure rise is attributed to the presence of hydrogen within the duct before the test flow arrives as fuelling is commenced several milliseconds before the arrival of the test flow. (The presence of the pre-test fuel can also be seen, although just barely, in that the traces commence slightly above zero (≈ 6 kPa)). So for the fuel-off shots the pilot holes of the transducer mounts are completely evacuated prior to the onset of the test flow and so the shock front of the test gas must first fill these holes. For the fuelled shots the presence of the pre-test fuel pre-fills these pilot holes and so the shock front of the test gas is transmitted more strongly through that fluid of fuel to the sensor face.

[1]This is after a 100 kHz filter has been applied to these traces to remove the very high frequency fluctuations considered to be mechanical vibration conducted through the model.

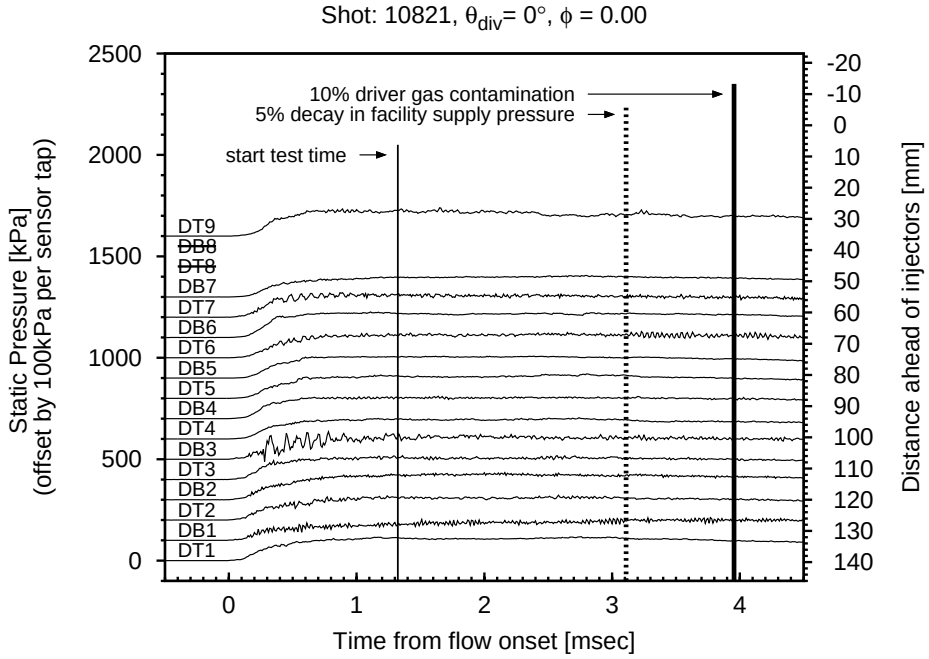

Figure 4.2: Time-history of the isolator pressures sensors (DT1–DT9 and DB1–DB8) for the constant area combustor where no separation is evident in the isolator for the fuel-off case. Each sensor is offset by 100 kPa to distinguish the traces from each other and this corresponds to an axial distance from the leading edge (shown on the right hand side axis). Sensors DB8 and DT8 were inoperative during the test. Vertical lines indicate the following in order: conventional start test time, 5% decay in facility supply pressure and 10% driver gas contamination level.

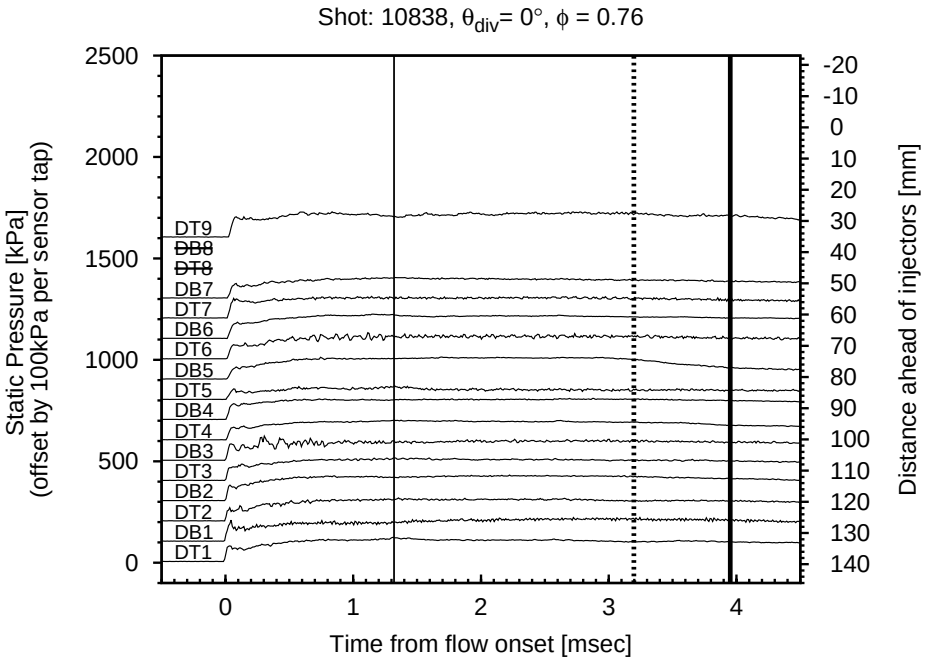

Figure 4.3: Time-history of the isolator pressures sensors (DT1–DT9 and DB1–DB8) for the constant area combustor where no separation is evident in the isolator for a mid-range fuelling case. Each sensor is offset by 100 kPa to distinguish the traces from each other and this corresponds to an axial distance from the leading edge (shown on the right hand side axis). Sensors DB8 and DT8 were inoperative during the test.

4.1.3 Combustion chamber pressure traces for non-separated cases

The next time-history plot presented is of the sensors downstream of injection (i.e. in the combustor). Figure 4.4 shows the time-history of a single front edge (FE) sensor and the two sets of combustor pressures sensors (C0FC and C0R) for the same fuelled case presented in Figure 4.3 in which there was no separation evident in the isolator. Due to the irregular spacing of the sensors (due to gaps in the sensor array from omission and from the loss of sensors over the course of the test campaign) the pressure offset applied to each successive trace does not correspond directly to an axial distance along the combustor. The reader is referred to Figure 4.1a for a detailed map of the sensor locations; however it is briefly stated here that the selected FE sensor (FE1) is approximately 0.6 of a duct diameter (D_{iso}) or 20.3 mm downstream of injection and the first of the forward combustion sensors (C0FC1) and the first of the rear combustion sensors (C0R1) are 85 mm ($2.6D_{iso}$) and 185 mm ($5.6D_{iso}$) downstream of injection respectively.

In Figure 4.4 the pressure for the majority of sensors along the combustor is fairly constant over the conventional test time from 1.3 ms to 3.2 ms. There are some traces which show a constant decline in pressure (for example sensors C0R5 and C0R12) which is contrary to the general trend in the majority of sensors. For the set of C0R traces which do not show this decline, the pressure measured over the test time fluctuates between $\pm 7\%$ and $\pm 11\%$ of the mean value.

Traces which show a very slow rise time and do not exhibit any moderate to high frequency pressure fluctuations are suspected to have a blocked pilot line. The purpose of this pilot line is to provide a flow path from the sensor face to the wall of the combustion chamber, and so for these sensors their measurements have been excluded from these time-history plots and the subsequent pressure profiles presented in Section 4.2.

For these attached cases the pressure profile plots for the combustion chamber pressures, which are presented in Section 4.2, are time averaged over the conventional test time – as was done so for the isolator measurements.

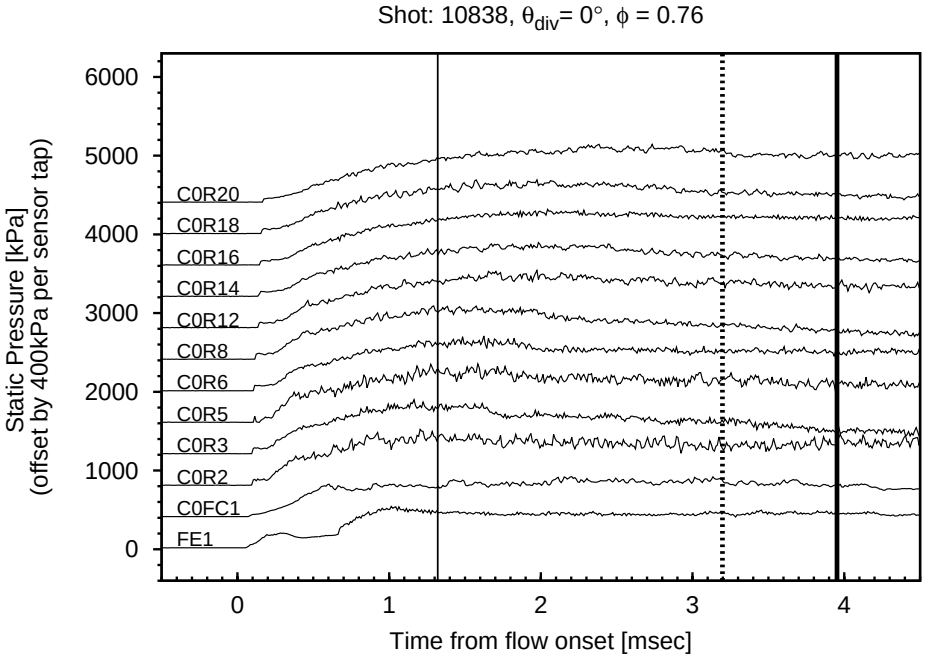

Figure 4.4: Time-history of a single front edge (FE) sensor and the two sets of combustor pressures sensors (C0FC and C0R) for a fuelled case where no separation is evident in the isolator. Each sensor is offset by 100kPa to distinguish the traces from each other and are in the order they are located along the model. (Though, unlike the previous figure, there is no direct relationship of the pressure offset to distance. Refer to Figure 4.1a for sensor locations.) Traces commence on average 12 kPa above zero due to the presence of the pre-test fuel.

4.1.4 Isolator pressure traces for separated cases at moderate ϕ

An increase in the pressure above the fuel-into-nitrogen level at the pressure taps upstream of the injection point is taken in this study to be an indication of flow separation. Figure 4.5 shows the time histories of the isolator pressure sensors for the constant area combustor configuration at the lowest equivalence ratio where separation was detected by these sensors. To aid in the illustration of the behaviour of the shock train, the 'start test time' line has been omitted as a new criterion for the establishment time of this separated flow is introduced and discussed in Section 4.1.8. The separation for this case is evident at the rear of the isolator by the step increase in pressures for sensors DT9 and DB7 at 1 ms and 1.6 ms respectively. The measurement by the DT9 sensor shows that the pressure in the rear of the separated region is fairly steady with the measured pressure remaining within $\pm 8.6\%$ of the mean value over the conventional test window from 1.3 ms to 3.2 ms.

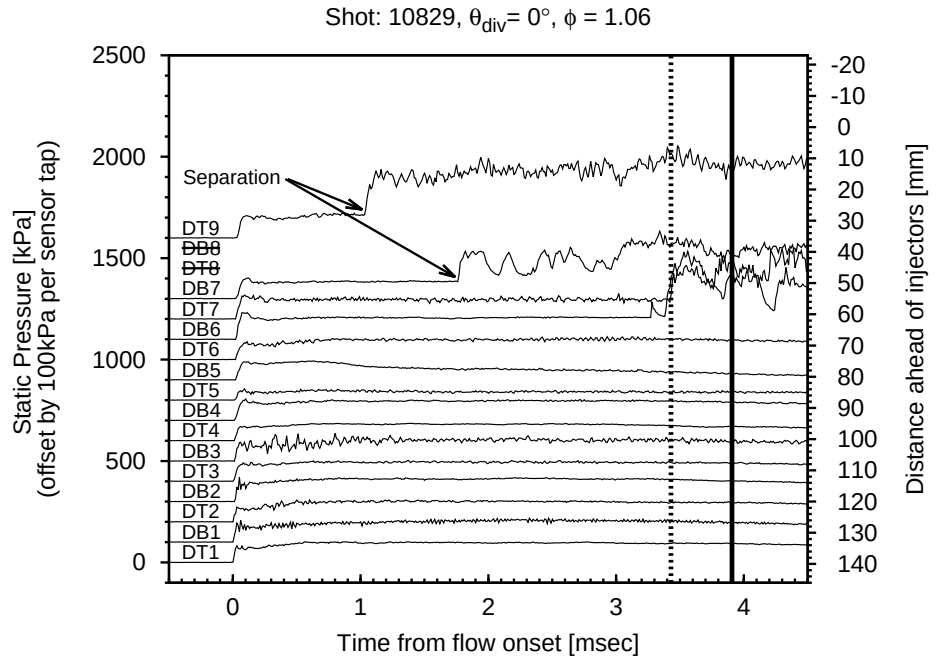

Figure 4.5: Time-history of the pressures sensors along the isolator (DT1–DT9 and DB1–DB8) for the constant area combustor for a fuelled case where some separation is evident in the isolator. Arrows mark where separation occurs for traces DB7 and DT9 only.

It can be observed in the trace of DB7 that, compared with the trace of DT9, there is both a longer delay from flow onset to separation and a greater amplitude in the pressure fluctuation after separation has occurred. This unsteadiness on this trace during the test is attributed to the leading edge of the shock train occurring somewhere in vicinity of this sensor. The fluctuations in this single signal are due to the oscillatory nature of shock train as the first shock moves backwards and forwards over that sensor.

Another two aspects to note are the time it takes for (a) the flow to first separate at the rear of the isolator on trace DT9 after the time of flow onset and (b) the time it takes for the separation to feed forward to the next sensor as shown on trace DB7. For Figure 4.5 the separation covers only two sensors (partly due to loss of DB8 and DT8), however on subsequent plots these aspects are more evident.

Finally, towards the end of available test time where the supply pressure has fallen by 5%, the separation moves forward and is detected by sensors DT7 and DB6. This is attributed to an increase in the equivalence ratio. The fuel rate is constant within $\pm 0.8\%$ during the test time but the static pressure of the freestream falls towards the end of the test time. A 5% reduction in pressure, assuming no change in temperature

and velocity, would result in a corresponding decrease in the density of the freestream and therefore an increase of 5% in the equivalence ratio. However the effect of this increase in equivalence ratio towards the end of the test time is not readily apparent in the time-histories of the combustion chamber pressures, which are presented in Section 4.1.5. This is due to the fact that whilst the equivalence ratio is increasing, this is brought about from a decreasing incoming pressure and so there may not be much change in the overall combustion pressures. However this would still result in a greater effective blockage from combustion as the pressure rise required across the isolator, as a ratio of freestream pressure, has increased. In addition to this increase in the pressure ratio across the isolator, a small change in incoming pressure may result in a large change in the position of the leading edge of the shock train due to the unsteady nature of a shock boundary layer interaction. This is because, as the nozzle supply pressure decreases towards the end of the test time so does the Reynolds number. This could have an additional effect on shock train position as, from Equation (2.1), the length of the shock train is a function of the Reynolds number.

Figure 4.6 shows another case for the constant area combustor where there is flow separation in the isolator but at a slightly higher equivalence ratio. There are two interesting features in the traces of Figure 4.6. The first feature to note is that there is an intermittent pressure rise on DB7 at 1.05 ms before the sustained pressure rise associated with the separated flow at 1.6 ms. The second feature to note is the behaviour evident on DB6 where it appears that the leading edge of the shock train has momentarily surged forward and then settled back again by the end of the test time. These features could be attributed to a number of causes, which are not readily identifiable, such as fluctuations in the test flow itself. Again in Figure 4.6, as with the previous cases, as the supply pressure falls the shock train extends further upstream after the end of the test time window.

In summary, for cases at moderate ϕ, where there is separation within the isolator, the flow takes longer to establish compared with non-separated cases at lower ϕ. However despite this longer establishment time the flow in the isolator appears to be fully established well before the end of the available test time. This is indicated by the steady pressures of the majority of raised isolator sensors, notwithstanding the highly unsteady pressures around the leading edge.

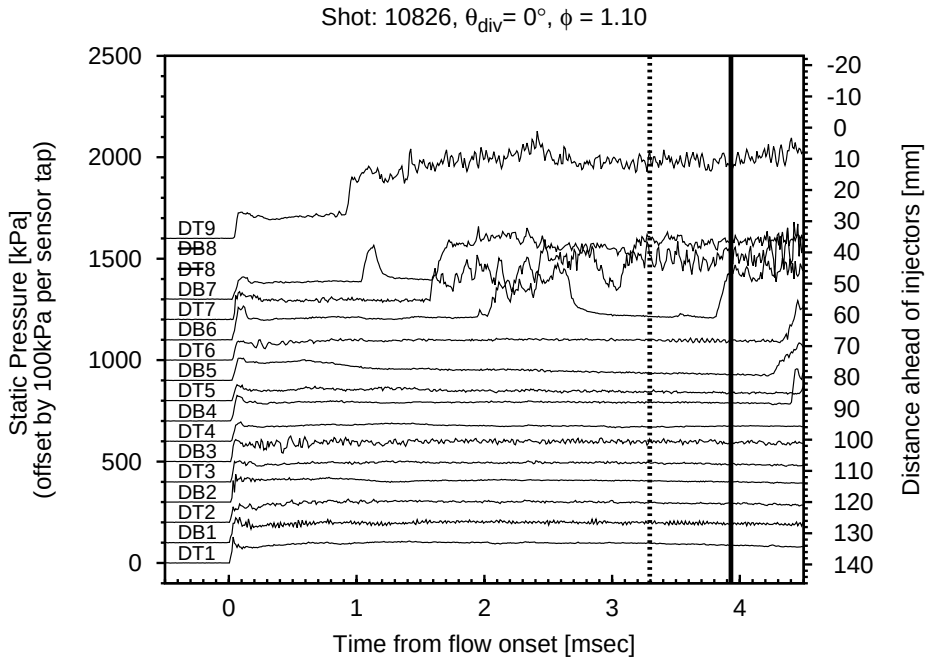

Figure 4.6: A second example showing the time-history of the isolator pressures sensors (DT1–DT9 and DB1–DB8) for the constant area combustor for a fuelled case where some separation is evident in the isolator.

4.1.5 Combustion chamber pressure traces for separated cases at moderate ϕ

Figure 4.7 shows the time histories of the combustion chamber pressure sensors for the constant area combustor for the second of the two previous cases where separation was evident in the isolator. Despite some fluctuations in the isolator pressure sensors near the leading edge of the shock train, the pressures towards the end of combustion chamber remain constant to within $\pm 6\%$ to $\pm 11\%$ during the test time. Again some sensors show a decline in pressures which is not consistent with the majority of the other sensors. This is attributed to either leakage past the o-ring seal used as part of the sensor mounting system or to erosion of the cellophane used as thermal protection. The pressure at the front edge sensor rises at a higher rate than do the combustion chamber pressures. This is attributed to the large scale separation around the injectors which extends downstream to at least the FE sensors. It is this separation which causes the rapid pressure rise, whereas the pressure further down the combustor rises due to combustion. The pressure rise associated with typical port-hole injection is considered to be a small contribution to the total pressure rise for the FE sensors seen in Figure 4.7

as this rapid pressure rise was not observed in the non-separated fuelled case presented in Figure 4.4.

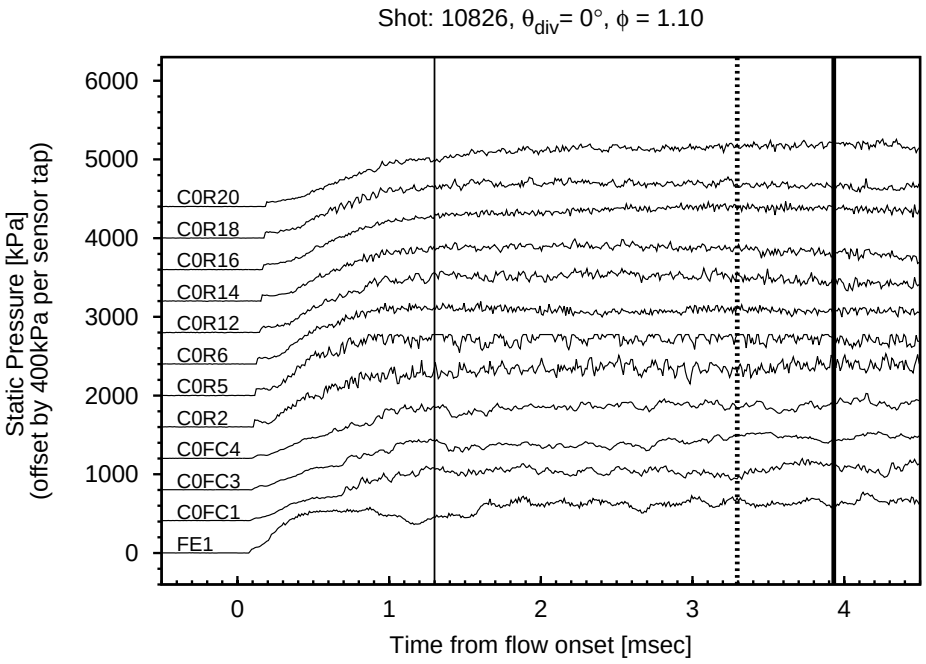

Figure 4.7: Time-history of a single front edge (FE) sensor and the two sets of combustor pressures sensors (C0FC and C0R) for a fuelled case where no separation is evident in the isolator. Each sensor is offset by 100kPa to distinguish the traces from each other and are in the order they are located along the model. (Though, unlike the plots for the isolator time histories, there is no direct relationship of the pressure offset to distance. Refer to Figure 4.1a for sensor locations.)

4.1.6 Isolator pressure traces for cases at high ϕ

There are cases above a certain fuelling rate where the flow in the isolator does not stabilise within the available test time. Figure 4.8 is given as an example, where it can be seen that for trace DT9 the pressure constantly increases and never reaches a steady level. From this increasing back pressure the shock train responds by generally moving forward throughout the test time. From an inspection of the traces DB4 and DT4, the leading edge of the shock train surges forward momentarily before retreating and then it recommences its forward direction to a point where the shock train is finally driven right up to the furthest upstream isolator sensors. This behaviour is consistent with the concept of an increasing back pressure coupled with pressure fluctuations in the incoming test flow.

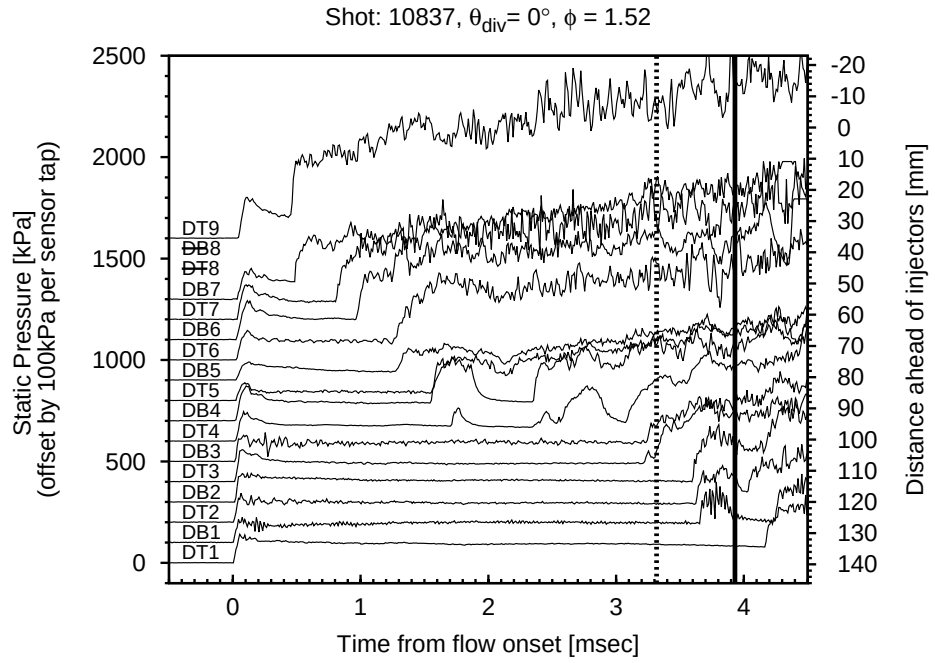

Figure 4.8: Time-history of the isolator pressures sensors (DT1–DT9 and DB1–DB8) for the constant area combustor for a fuelled case where the separation does not reach steady state as indicated by the rising pressure of sensor DT9.

4.1.7 Combustion pressure traces for cases at high ϕ

Figure 4.9 shows the time histories for the combustor pressure sensors for the previous high ϕ case for the isolator traces for the constant area combustor. Although there is a general pressure rise at the beginning of the available test time, this pressure rise tapers off reaching a steady level by half way through the available test time (i.e. around 2 ms). The pressure at the front edge sensor FE1 has reached such a level that it has exceeded the range of this sensor. This is evident by the 'clipping' of the trace at around 1.9 ms. This suggests that the strengthening shock train in the isolator also increases the pressure of the flow entering the combustion chamber, as indicated by FE sensors, though the pressure level further down the combustor does not exhibit this same continued pressure rise. This indicates that generally the combustion process is stable and insensitive to the changes in the condition of the flow entering the combustor from a developing shock train. The implication which follows is that the isolator may not be able to contain the shock train and what is observed is the beginnings of an engine unstart. An alternative explanation is that, given the long shock train length, the test time is not long enough for the separated flow to stabilise.

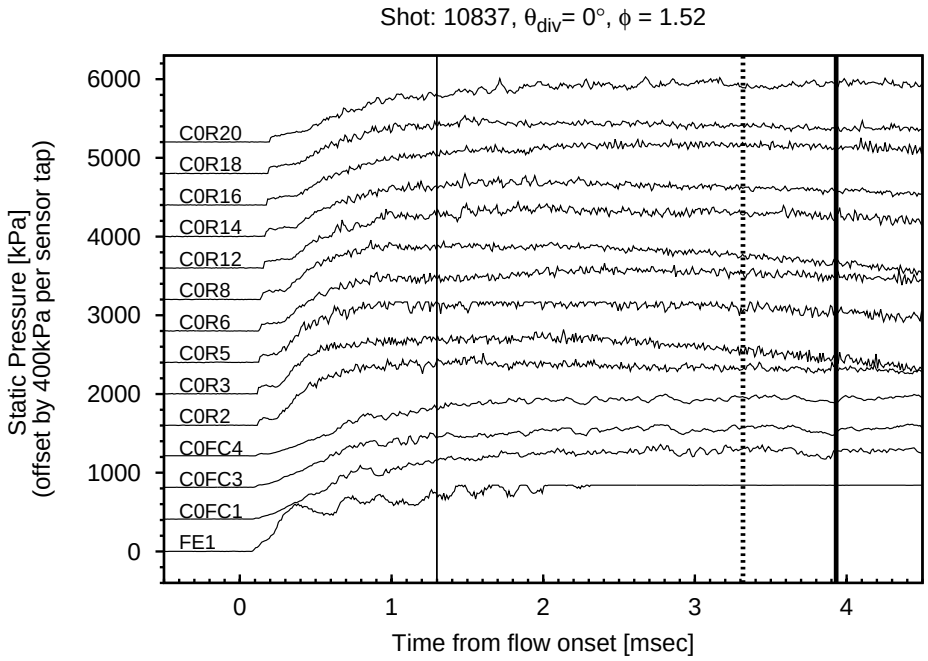

Figure 4.9: Time-history of a single front edge (FE) sensor and the two sets of combustor pressures sensors (C0FC and C0R) for a fuelled case for the constant area combustor at an equivalence ratio (ϕ) of 1.52 where the flow does not reach steady state in the isolator. Each sensor is offset by 100 kPa to distinguish the traces from each other and are in the order they are located along the model. (Though, unlike the previous figure, there is no direct relationship of the pressure offset to distance. Refer to Figure 4.1a for sensor locations.)

The types of flow observed in the tests can be categorised into three types which are: attached, separated and cases where the flow does not establish. The flow type for each combustor over the full range of equivalence ratios are presented in Figure 4.10. Apart from some minor differences in the delineation there are no significant differences between the three combustors geometries. The minor differences are mainly due to fact that each test was performed at discrete equivalence ratios (rather than over a continuum) and as such, the same equivalence ratio was not always able to be reproduced exactly for each combustor due to variations in the inflow conditions. The cases where the flow does not establish are excluded from the data set used to form the pressure profiles presented in Section 4.2.

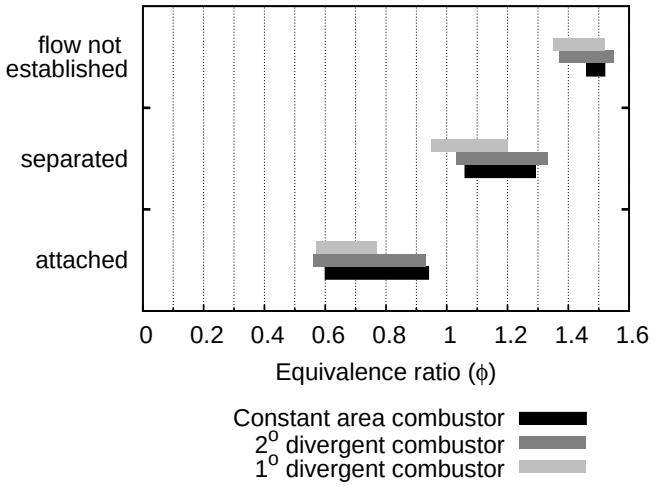

Figure 4.10: Chart showing the type of flow over the full range of equivalence ratios for all three combustors.

4.1.8 Methodology for determining establishment time of separated flow

This section discusses the methodology used to select a time when the shock train has established in the isolator, which marks the commencement of the test time for these separated cases. As with the conventional methodology, the available test time is terminated when the nozzle supply pressure has reduced in pressure by 5% (taking into account the time taken for the test gas to traverse from the supply region to the model). To illustrate the methodology of selecting the point in time when the separated flow is considered to have established itself, a number of cases at different fuelling rates are presented in Figure 4.11. These cases are all for the constant area combustor configur-

ation. In Figure 4.11, the time at which the flow is considered to have established is denoted by the first vertical line, which was selected based on the following rule:

> **Rule 4.1:** *The leading edge of the shock train is assumed to lie close to the most upstream pressure transducer whose traces goes from low to high and remains high until the end of the available test time. The establishment time is chosen as the point in time at which the transition from low to high occurs.*

In the above rule, 'low' pressure is the pressure measured immediately after flow onset and before separation (see the markings in Figure 4.5) and this low pressure would be similar to the pressure measured for a combustion-suppressed case over the conventional test time window. This rule was chosen as it was found that the steady raised pressures of the isolator sensors (typically downstream of the leading edge of the shock train) were a more reliable method of determining the flow establishment time than the fluctuating and highly sporadic pressure traces at the leading edge of the shock train. These fluctuations are attributed to the oncoming flow unsteadiness and not to flow establishment. How the rule is applied to each of the examples given in Figure 4.11 is discussed next.

Beginning with the last case presented, Figure 4.11d, Rule 4.1 is invoked when trace DB6 goes from low to high at 1.95 ms and remains high till the end of the test time at 3.3 ms. The earlier rise, above the low state, on this trace around 1.3 ms does not invoke the rule as it is not sustained. The traces for DB4, DB5 and DT6, which are all further upstream of DB6, all show pressure rises above their low states between 1.95 ms and the end of the test time, however none of these are sustained and so these traces do not invoke the rule.

A similar situation occurs in the case for Figure 4.11b, where again for the furthest upstream traces which show elevated pressures (DT7 and DB6), these elevated pressures are not sustained. As such the rule is instead invoked by a trace which is further downstream, in this case trace DB7 at 1.8 ms, which does show a sustained elevated pressure. For trace DB7 in this figure, like with trace DB6 in Figure 4.11d, there is a small, yet unsustained, rise in pressure (at 1.55 ms) which proceeds the period of sustained elevated pressure.

For the other cases, Figures 4.11a and 4.11c, these are a little more interesting. The case in Figure 4.11c is interesting in that it contains a trace, DB6, which is at an elevated pressure for the majority, but not all, of what has become the typical test time window for these separated cases. In this case, DB6's trace is mostly high over the period from 1.5 ms to 3.4 ms, however the pressure falls back to its low state momentarily at 2.8 ms. As such, the neighbouring trace DT7 is instead considered to invoke the rule at 1.6 ms when it reaches its sustained elevated pressure. For the case in Figure 4.11a, the leading trace which shows an elevated pressure (DB7) exhibits a large degree of fluctuation after its initial rise at 1.8 ms. Normally this trace would be disregarded, however as DB8 and DT8 are unfortunately inoperative and that DB7's pressure never fully returns to the low state, it is selected as invoking the rule.

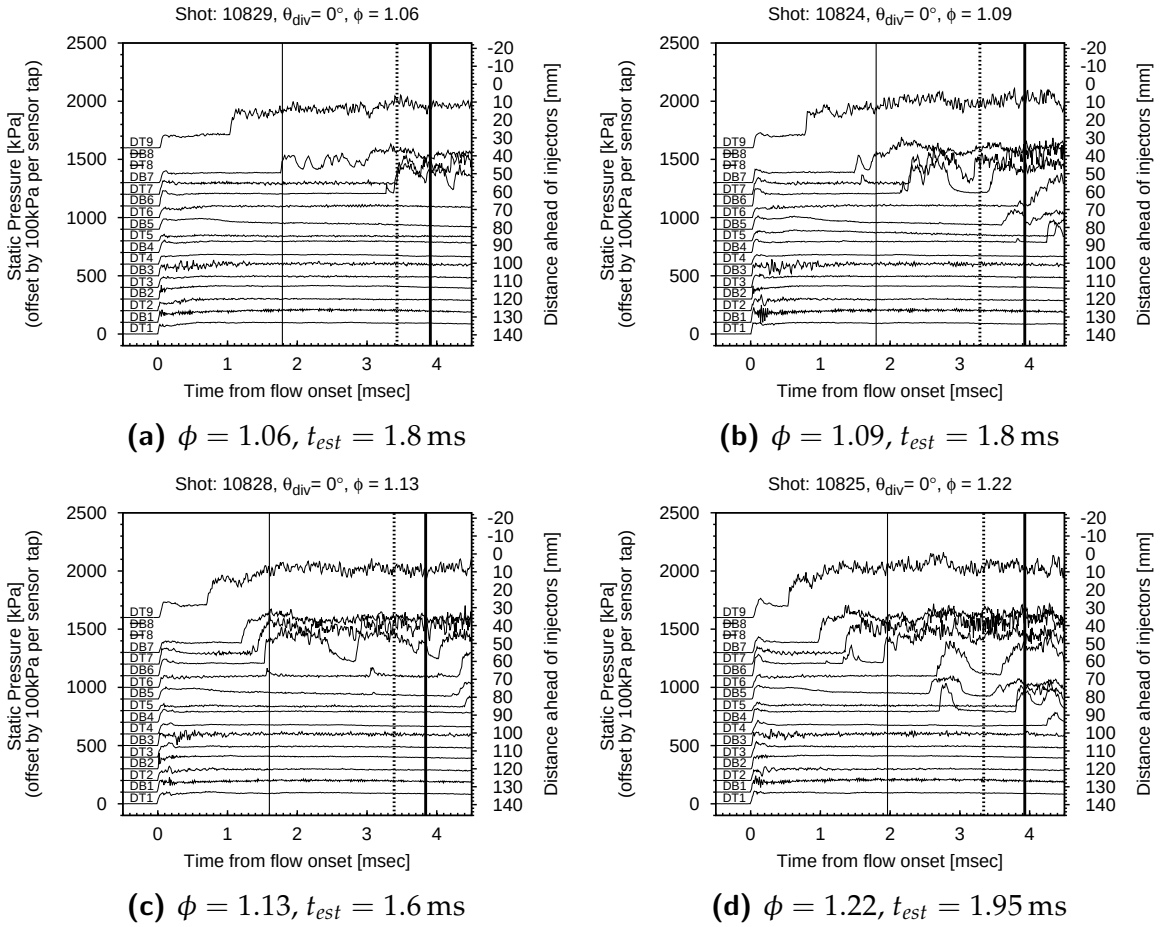

(a) $\phi = 1.06$, $t_{est} = 1.8\,\text{ms}$ **(b)** $\phi = 1.09$, $t_{est} = 1.8\,\text{ms}$

(c) $\phi = 1.13$, $t_{est} = 1.6\,\text{ms}$ **(d)** $\phi = 1.22$, $t_{est} = 1.95\,\text{ms}$

Figure 4.11: Examples of tests for the constant area combustor configuration of how flow establishment time was determined for the separated cases.

These examples above show how the establishment time was determined and hence when the commencement of the test time occurs for separated cases. (For separated

cases the end of the test time is unchanged from convention.) The pressure profiles along the engine presented in Section 4.2 are based on the average pressure over this test time. The unsteady pressures typical of the leading edge of the shock train are included in this averaging and this results in a slightly raised pressure compared with the 'low' level outside these fluctuations. This has a minor influence on the overall pressure profiles and the general character of the shock train can still be gleaned.

4.1.9 Establishment time versus shock train length

This section discuss the relationship, or lack there of, between the establishment time and the shock train length. The characteristic length of the shock train which is of importance in this study is the portion which extends ahead of the injectors. This length is denoted by the term S_o and is referred to in this chapter simply as the "shock train length". This length S_o was determined to be the distance from the injectors to the location of the sensor whose trace satisfied Rule 4.1. The S_o lengths for all the separated cases for all three combustors are catalogued in Appendix A.5.1.

Figure 4.12a is a plot of the establishment times for the isolator plotted as a function of shock train length (S_o) for the constant area combustor. In this plot, there is no clear correlation between S_o and the time it takes for the flow to establish. As indicated in Figures 4.12b and 4.12c, the same is true for the two divergent combustors.

4.1.10 Establishment time versus equivalence ratio

Figure 4.13 shows the establishment times for the isolator plotted as a function of the fuel equivalence ratio for the constant area combustor. Again, there is no clear correlation between ϕ and the time it takes for the flow to establish in the isolator (t_{est}). This lack of correlation is consistent for the other two combustors (see Appendix A.5.2).

4.1.11 Separation time for the furthest downstream isolator sensor

Although in Section 4.1.9 no clear correlation was observed between flow establishment time and S_o, such a correlation may exist but it is not discernible due to the chaotic nature of the leading edge of the shock train. However, from a review of the

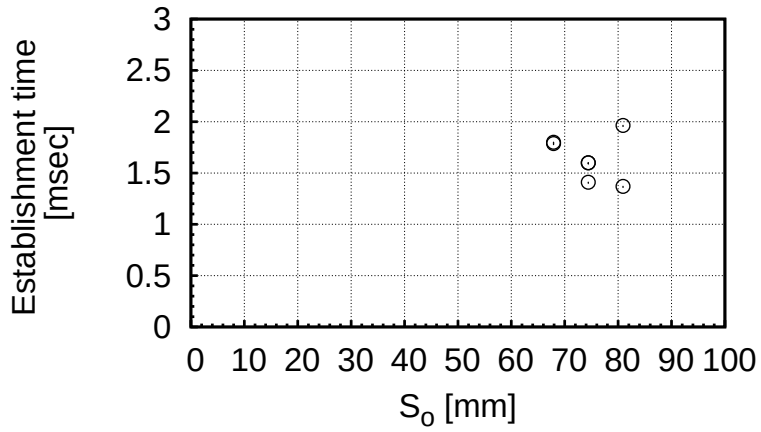

(a) Constant area combustor

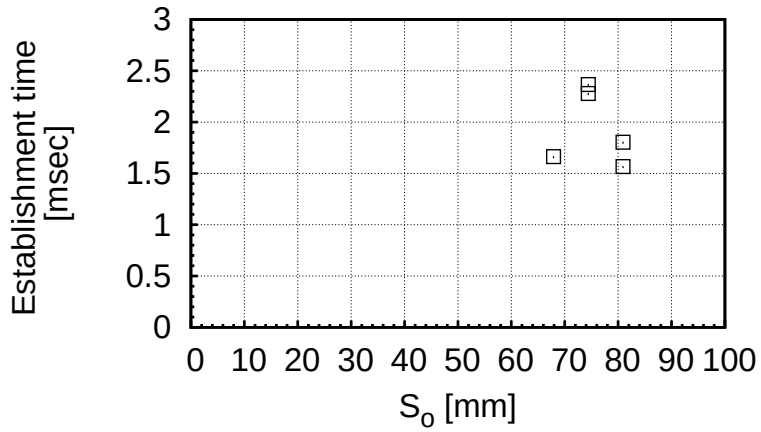

(b) 2° divergent combustor

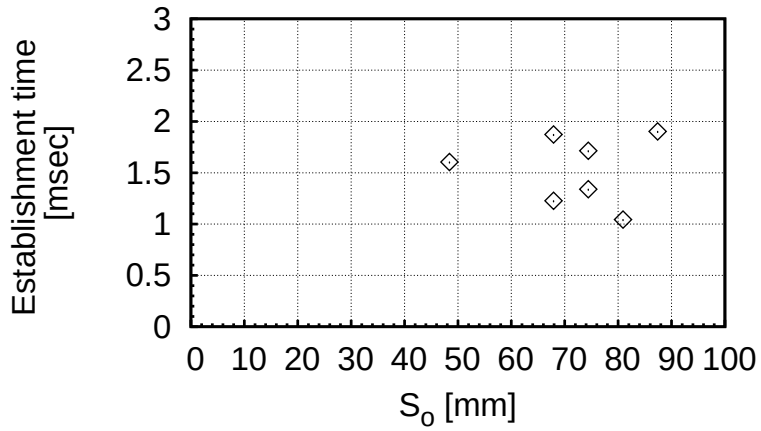

(c) 1° divergent combustor

Figure 4.12: Plots showing flow establishment time (t_{est}) for the isolator versus shock train length (S_o) for all three combustors.

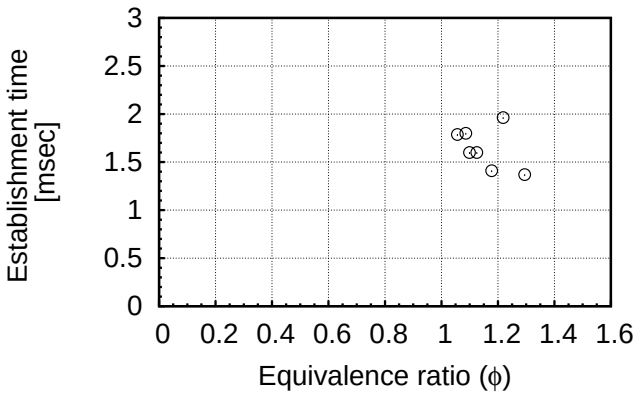

Figure 4.13: Establishment times (t_{est}) for the isolator plotted against the fuel equivalence ratio (ϕ) for the constant area combustor.

separated cases it appears that the time it takes for the flow at the furthest downstream sensor (DT9) to separate after flow-onset does scale with shock train length (S_o), isolator exit pressure (P_{DT9}) and equivalence ratio (ϕ).

The time it takes for the flow at DT9 to separate time is termed $t_{sep_{DT9}}$ and is defined by Equation (4.3) where $t_{flow\,onset_{DT9}}$ is the time of the first pressure rise at the onset of the test flow and $t_{2nd\,rise}$ is the time of the second rapid rise in pressure. An illustration of this delay time is shown in Figure 4.14 which depicts $t_{sep_{DT9}}$. In this figure the datum for the time axis is $t_{flow\,onset_{DT9}}$.

$$t_{sep_{DT9}} = (t_{2nd\,rise} - t_{flow\,onset})_{DT9} \tag{4.3}$$

Separation time for sensor DT9 versus shock train length

Figure 4.15 plots $t_{sep_{DT9}}$ versus shock train length for all three combustors. Whereas no correlation was identified for the establishment time for the entire isolator, there is a trend of a decreasing $t_{sep_{DT9}}$ with increasing S_o. This can be seen in the plots for the constant area combustor in Figure 4.15a and for the 1° divergent combustor in Figure 4.15a; whereas this correlation is weak for the 2° divergent combustor (Figure 4.15b). This may be due to the small data set for this combustor resulting in scatter in the data hiding any trend that would be apparent otherwise. These results for the constant area and 1° divergent combustor do provide evidence that the time it takes the downstream end of the shock train to establish has an inverse relationship to the

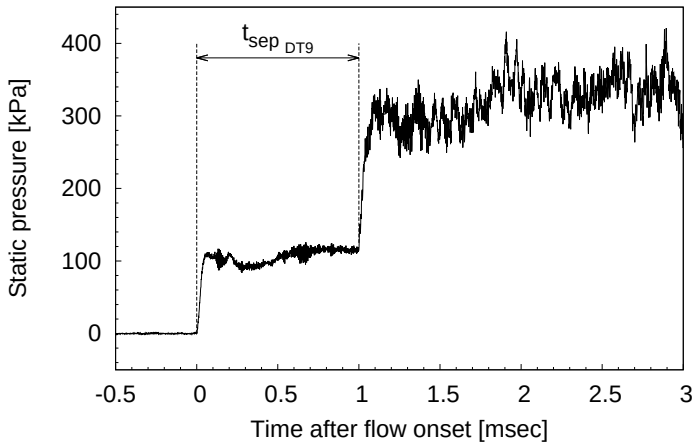

Figure 4.14: Plot illustrating the time it takes for the flow at the furthest downstream isolator sensor (DT9) to separate ($t_{sep_{DT9}}$) after flow onset at that sensor.

size of the shock train.

Separation time for sensor DT9 versus equivalence ratio and isolator exit pressure

Figure 4.16 shows plots of $t_{sep_{DT9}}$ as both a function of the isolator exit pressure normalised by the freestream (P_{DT9}/P_{∞}) in Figure 4.16a and of the equivalence ratio (ϕ) in Figure 4.16b. In Figure 4.16a, apart from the 2° divergent combustor which shows a larger degree of scatter, there is a strong relationship between the $t_{sep_{DT9}}$ and P_{DT9}/P_{∞} and a weaker relationship between $t_{sep_{DT9}}$ and ϕ. The lines of best fit for both these trends which are plotted in Figure 4.16 are based only on the data from the constant area and 1° divergent combustors. These two trends, which are present for at least the constant area and 1° divergent combustors, again show that the time it takes for the separation process to occur at the rear of the isolator scales with key parameters, namely the fuelling rate and the pressure at the end of isolator (which itself scales with ϕ).

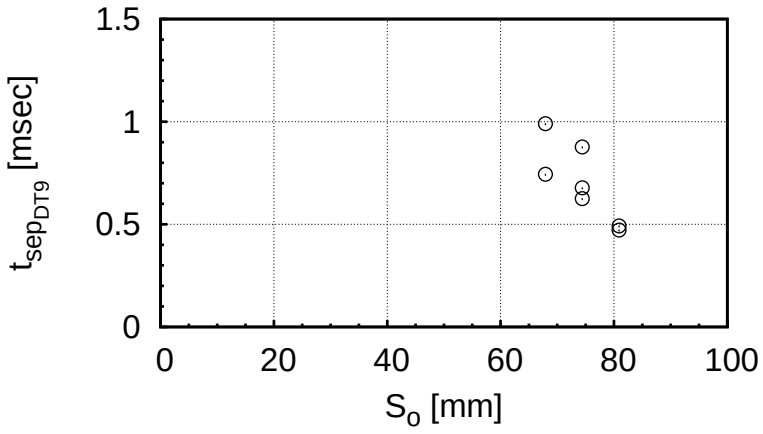

(a) Constant area combustor

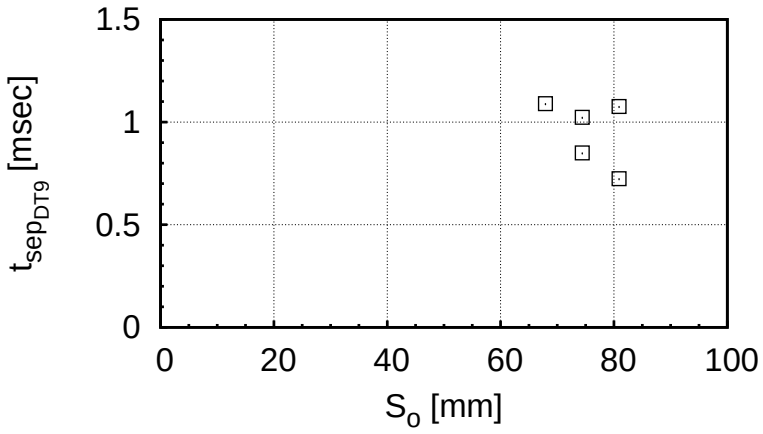

(b) 2° divergent combustor

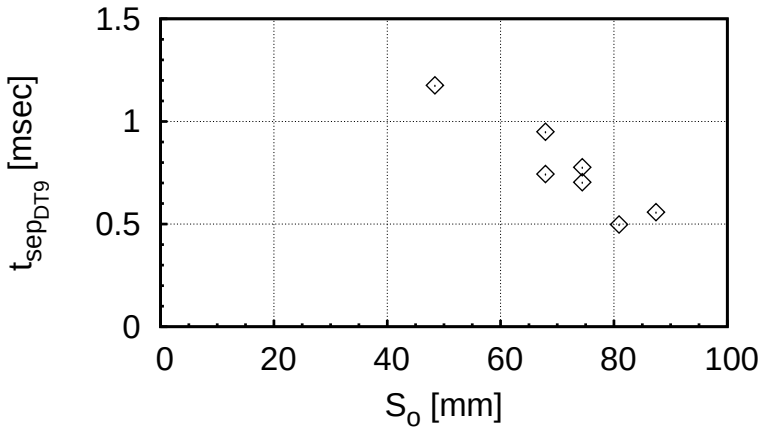

(c) 1° divergent combustor

Figure 4.15: Plots showing flow establishment time for the furthest downstream sensor (DT9) in the isolator ($t_{sep_{DT9}}$) versus pre-injector shock train length (S_o) for all three combustors.

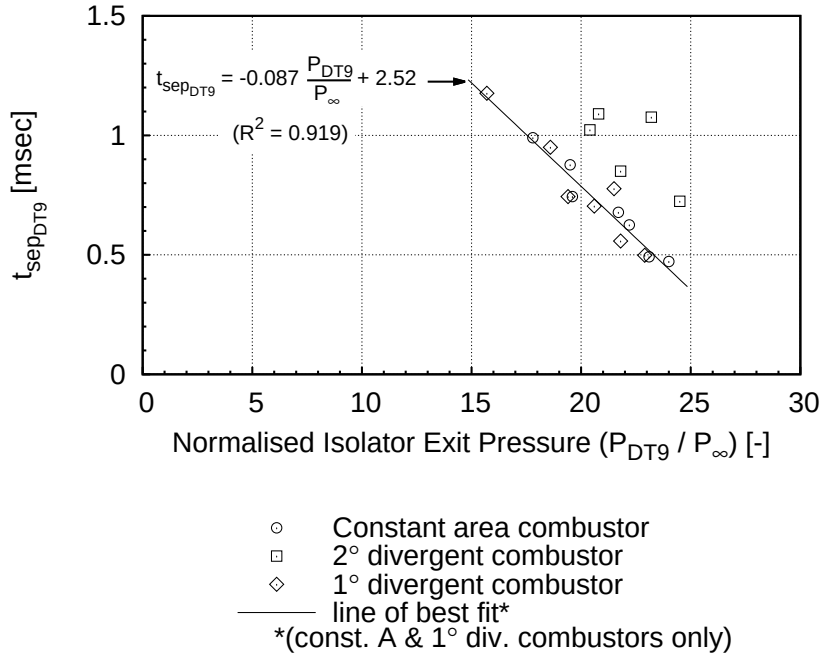

(a) P_{DT9}/P_∞

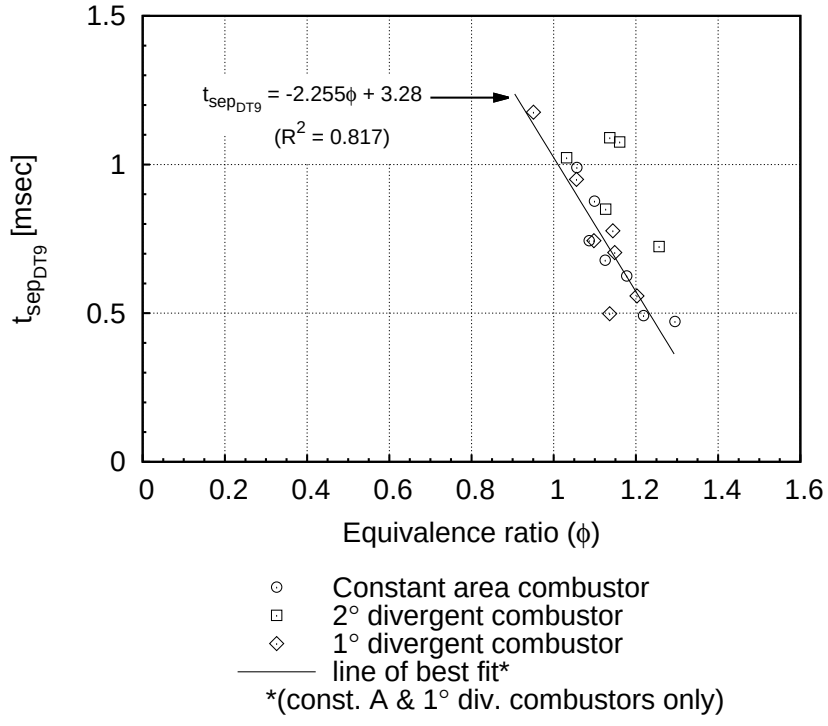

(b) ϕ

Figure 4.16: Plots showing for all three combustors the flow establishment time for the most downstream sensor (DT9) in the isolator ($t_{sep_{DT9}}$) versus the following two variables: (a) normalised isolator exit pressure, P_{DT9}/P_∞ and (b) equivalence ratio, ϕ. Lines of best fit for both plots are based on the data for the constant area and 1° divergent combustors only.

4.1.12 Summary of establishment times

From an investigation into the transient nature of the isolator pressure measurements, a methodology for determining the flow establishment time has been proposed and applied. It is found that the establishment time was longer for separated cases compared with non-separated cases at low ϕ (< 0.95) and that, despite this longer establishment time, for cases up to a ϕ = 1.3 there was sufficient available test time. However for ϕ above 1.3 the flow exiting the isolator did not reach steady state and the establishment time was longer than the available test time. These findings were true for all three combustors.

For those cases where an establishment time could be determined, it was found that the establishment time (t_{est}) did not correlate with shock train length (S_o) nor with equivalence ratio (ϕ) for any of the three different combustors. However it was found, for all three combustors, that the time it took for separation to occur at the rear of the isolator ($t_{sep_{DT9}}$) did have an inverse relationship with S_o, ϕ and the normalised pressure at the isolator exit (P_{DT9}/P_∞).

4.2 Pressure Distributions

The plots presented in this section are of the form of pressure measurements along the isolator and combustor, which have been averaged over the appropriate test time as determined in Section 4.1. The first of the plots is shown in Figure 4.17. In this, and following figures, the horizontal axis represents the distance along the model as measured from the leading edge of the diffuser. The left vertical axis represents the wall pressure measured along the model in the experiment normalised by the freestream pressure computed by *NENZF* for that shot. In the top proportion of the figure, the area profile is shown. This axis of this plot represents the cross-sectional area normalised by the area of the isolator. On this area profile the injection point (as denoted by the symbol ▼) is marked. The error bars in the vertical axis represent the uncertainty in the ratio of pressure measurements as discussed in Chapter 3. For the fuelled shots (the first being Figure 4.18) the results for the fuel-off and the combustion-suppressed cases (fuel into N_2) are plotted as well. The title at the top of each graph contains the shot number, the angle of combustor divergence (0° represents the constant area combustor) and the equivalence ratio (ϕ).

4.2.1 Constant area combustor

Fuel-off and combustion-suppressed cases

Figure 4.17 shows the results from the fuel-off test and the combustion-suppressed test (fuel into N_2) for the constant area combustor. The data from these tests show some scatter about the general trend in pressure along the combustor. Some of this scatter is attributed to the reflected shock waves generated from the leading edge of the diffuser which propagate down the duct. For the fuel-off test the general trend of the pressure along the duct is rising which is due to the growth in the boundary layer and the reflected shock waves. Plotted on this figure is the computed pressure of the diffuser exit flow, which compares favourably with the experimental results.

By overlaying the results from the combustion-suppressed test on the results from the fuel-off test, the effect of mass addition of hydrogen on the pressure profile can be illustrated. Fuel was injected for the combustion-suppressed test at what would be an equivalence ratio (ϕ) of 1.34 for a test with air instead of nitrogen. This ϕ corresponds

approximately to the highest ϕ for the combustion tests in which the flow established along the isolator within the test time (as presented in the time-history plots in Section 4.1).

There is little difference in duct pressure upstream of the injection point between the fuel-off and the combustion-suppressed cases. Past the injection point, the pressure in duct is higher for the combustion-suppressed case than for the fuel-off case. The effects of the hydrogen on the pressure in the duct can be seen first at the front edge (FE) pressure sensors located at 0.32 m where the pressure has risen from $2.6P_\infty$ for the fuel-off test to $4.0P_\infty$ for combustion-suppressed case. By the end of the combustor, the exit pressure has risen to around $3P_\infty$ and $6.0P_\infty$ for the fuel-off and combustion-suppressed cases respectively.

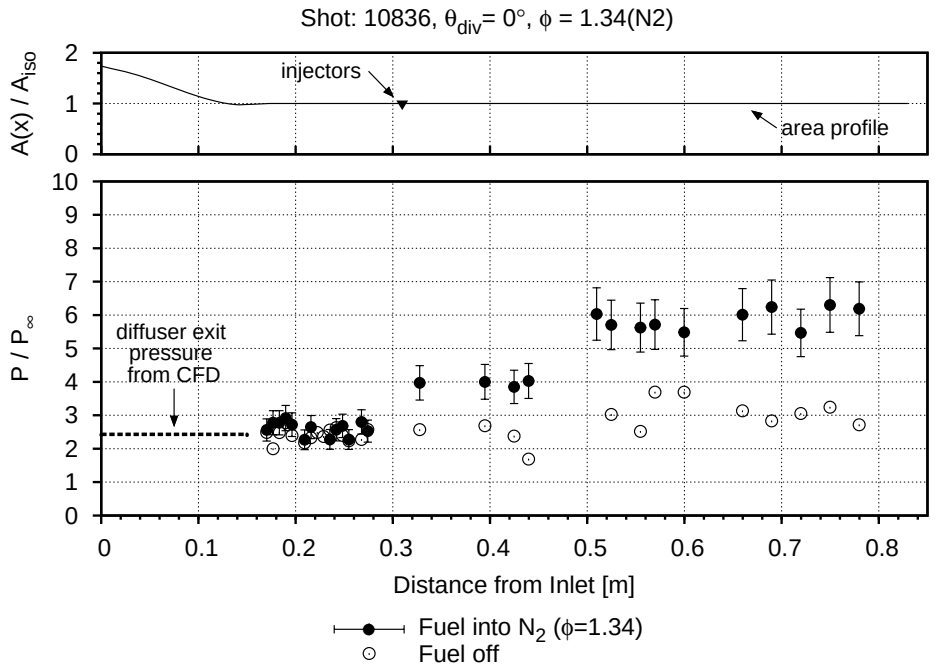

Figure 4.17: Pressure and area profiles for the fuel-off and the combustion-suppressed tests for the constant area combustor. The location of the injection point is denoted by the symbol ▼ in the top plot showing the area profile. Area is normalised by the cross sectional area of the isolator. The bottom plot shows the pressure distribution where the pressure measurements are normalised by the computed freestream pressure. The fuel-off results are depicted by the symbol ○ and the combustion-suppressed (fuel into N_2) are depicted by the symbol ●. Error bars are based on the uncertainty analysis presented in Appendix C.

Non-separated cases

The first of the fuel-into-air results for the constant area combustor is shown in Figure 4.18. (Note the change in range of the vertical axis; previously 10 now 25). Also plotted on this figure are the fuel-off and combustion-suppressed results for this combustor. For this fuel-into-air condition there is on average over a 100% increase above the combustion-suppressed case in the pressure downstream of the injectors. This illustrates that the majority of the pressure rise can be attributed to combustion and a minor proportion to the effects of mass addition from the injection of a fluid (i.e. the fuel) into the main stream. At this equivalence ratio of 0.6, the constant area combustor produces a pressure of $12.3P_\infty$ (determined as an average of the last three sensors). This exit pressure is 4.8 times the pressure at the entrance of the isolator (P_{DT1}). The maximum pressure occurs at the end of the combustor, which is consistent with attached heated supersonic flow. Upstream of the fuel injectors there is no change in the pressure levels compared with fuel-off case. The small variation about the general trend in pressure, which is rising down the duct, is attributed to the reflected shock waves which originate from the leading edge of the diffuser and from the bow shocks around the fuel jets which propagate down the duct.

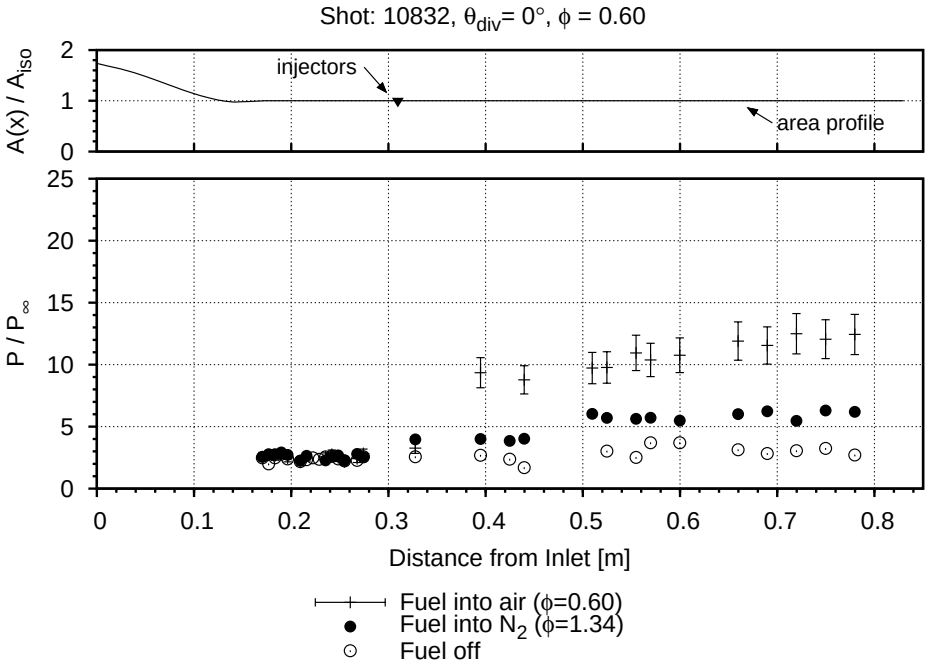

Figure 4.18: Pressure profile for a non-separated case for the constant area combustor (ϕ = 0.6).

For this combustor, this case is the highest equivalence ratio at which no separation is observed near the injectors as indicated by the front edge (FE) pressure sensors (which are 13 mm downstream of the injectors). The front edge pressure is a key measure that is of interest in the subsequent plots as it is the first sensor location at which separation is first observed.

Moderately separated cases

At an equivalence ratio of 0.76 there is a jump in the pressure at the front edge of combustion chamber as shown in Figure 4.19. This large pressure rise is attributed to the separation of the boundary layer due to the pressure rise from combustion. The scale of this separation however is not large enough for it to be detected by the sensors in the isolator. This case is labelled 'moderately separated' as some separation is evident but is localised around the injection point.

The pressure profile for $\phi = 0.94$ (Figure 4.20) is quite similar in nature to that for $\phi = 0.76$, shown in Figure 4.19, in that the front edge pressure shows separation but the separation has not reached as far forward as the most downstream sensor of the isolator. The exit combustor pressures for the cases where $\phi = 0.76$ and $\phi = 0.94$ are $14.8P_\infty$ and $16.1P_\infty$ respectively. For $\phi = 0.76$ the exit pressure was the highest pressure recorded for the duct, whereas for the $\phi = 0.94$ case the highest pressure recorded, which was $16.9P_\infty$, was located just upstream from the exit at $X = 0.72$ m.

Highly separated cases

At an equivalence ratio of 1.06 (Figure 4.21) the first sign of the separation moving into the isolator appears as elevated pressures for the sensors at the downstream end of isolator. From this increase in fuelling the separation has strengthened and moved further forward into the isolator. This is indicated by the elevated pressure measurements in the isolator which are at a much higher pressure than the fuel-off and combustion-suppressed cases. Along with an increase in the isolator pressures there is an increase in the pressure at the front edge ($12.6P_\infty$) and an increase in the combustor exit pressure ($17.3P_\infty$).

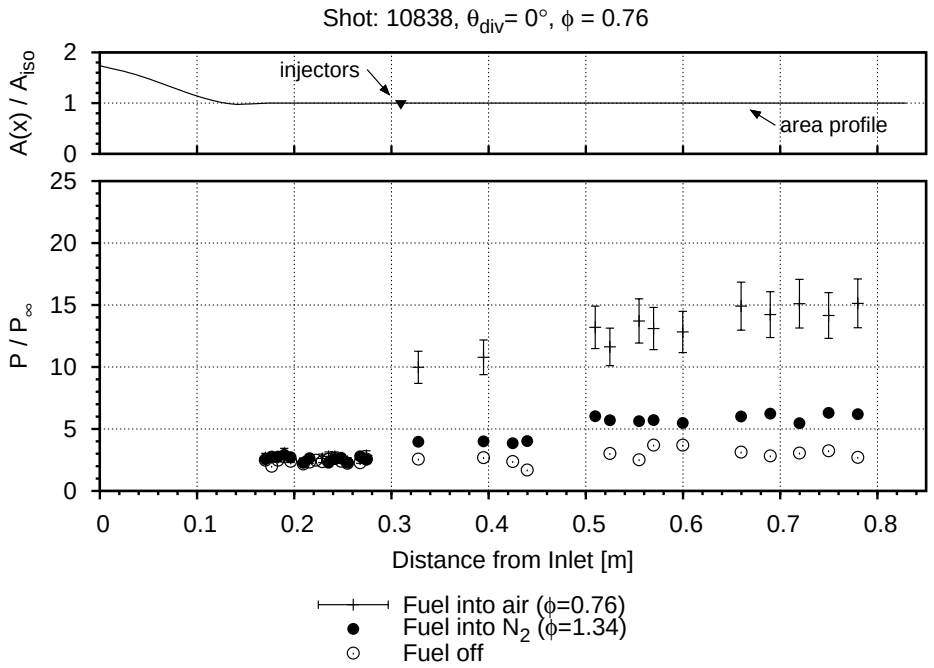

Figure 4.19: Pressure profile for a moderately separated case for the constant area combustor ($\phi = 0.76$).

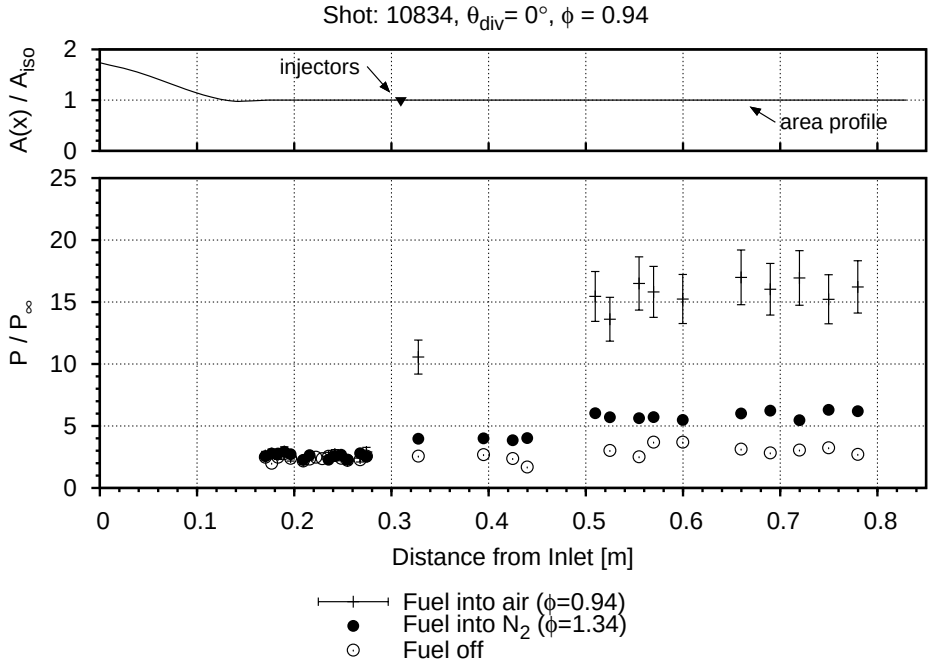

Figure 4.20: Pressure profile for a second example of a moderately separated case for the constant area combustor ($\phi = 0.94$).

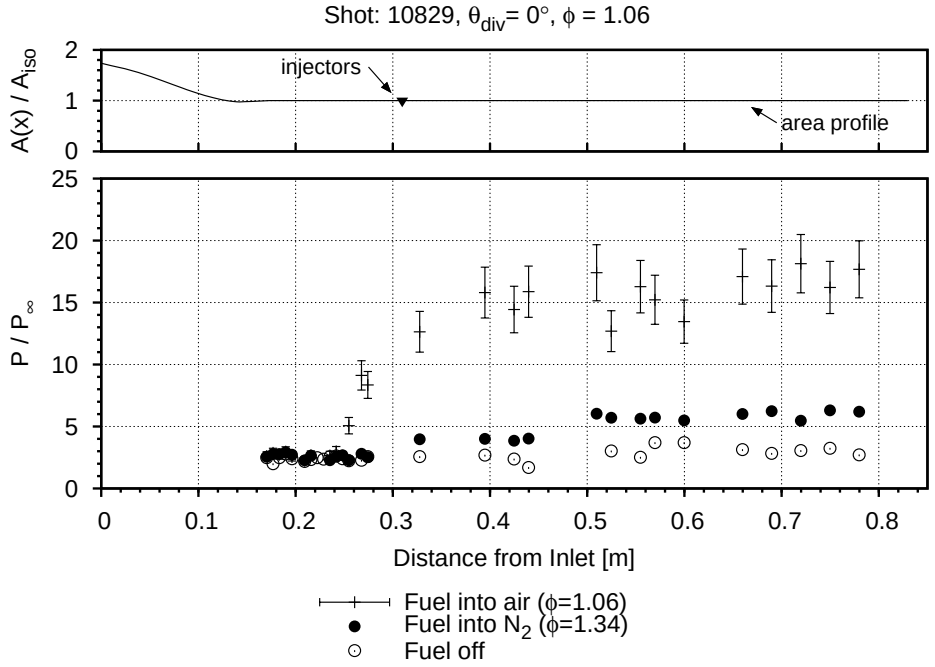

Figure 4.21: Pressure profile for a highly separated case for the constant area combustor (ϕ = 1.06).

As the equivalence ratio increases from 1.06 to 1.22 (Figure 4.22) there is a small increase in the exit pressure of the combustor, it increases from $17.3P_\infty$ to $18.0P_\infty$. There is a greater increase in the pressure at the front edge which rises from $12.7P_\infty$ to $15.6P_\infty$. The separation consequently strengthens and moves further forward into the isolator as evidenced by the increase in the isolator pressures. This front edge pressure is approximately 80% of the peak pressure ($19.5P_\infty$) generated by the combustor which shows that the shock train provides a significant portion of the total pressure rise along the engine. The rapid pressure rise at the front edge sensors might also be due to the possibility that some fuel has been entrained in the recirculation zone in the separated flow around the injectors and that ignition is occurring here due to the high residence time of the fuel in that zone.

As the equivalence ratio increases from 1.22 (Figure 4.22) to 1.29 (Figure 4.23), the pressure increases further for those sensors in the isolator which already showed an elevated pressure. However no additional sensors further upstream show a change in pressure above the combustion-suppressed case. This is a curious result as the shock train has evidently strengthened but has not moved further forward. One explanation is that the leading point of the shock train has 'anchored' on a shock boundary layer interaction from the reflected shocks generated by the diffuser.

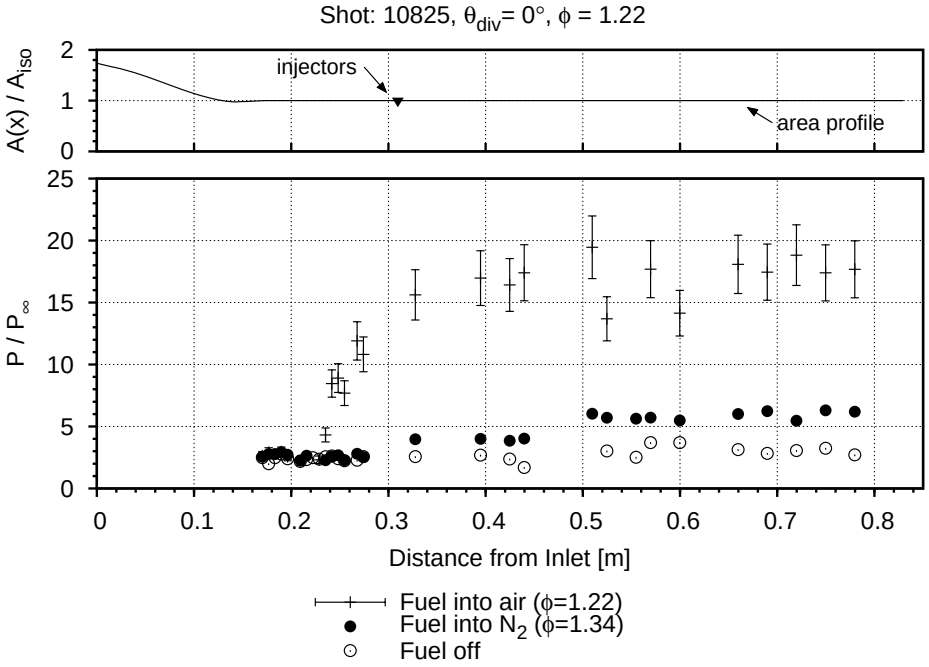

Figure 4.22: Pressure profile for a second example of a highly separated case for the constant area combustor (ϕ = 1.22).

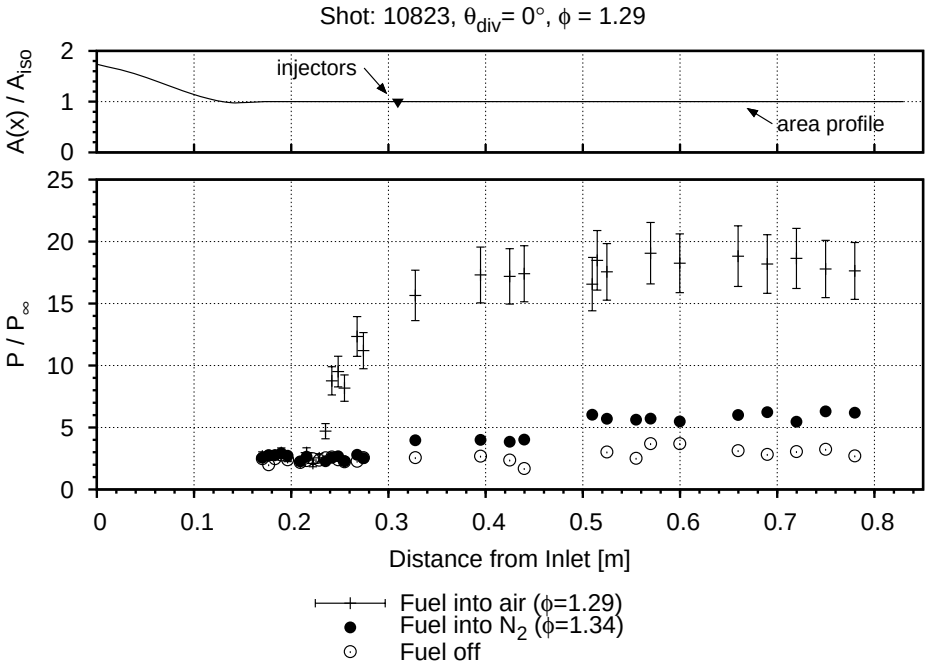

Figure 4.23: Pressure profile for a third example of a highly separated case for the constant area combustor (ϕ = 1.29).

In terms of the overall change in performance of this combustor, there is a marginal increase in the pressure levels at the end of the combustor between this fuelling level and the previous one (Figure 4.22). This suggests that the combustion has now reached the maximum fuelling limit such that no additional amount of fuel will mix and burn with the remaining air and that any additional pressure rise is primarily from the displacement effect of the additional fuel.

Summary of findings from the constant area combustor series:

From this series of pressure profiles for the constant area combustor in which the flow established within the test time the following findings are made:

1. At $\phi = 0.6$ the flow remained attached through the isolator and around the injectors.
2. At and above $\phi = 0.75$, separation was observed around the front edge of the combustor as indicated by the raised pressure above that of the combustion-suppressed case.
3. From $\phi = 0.75$ to $\phi = 1.22$ the separation increases in scale with an increase in fuelling.
4. At $\phi = 1.22$ the separation reaches it furthest most forward position at $2.4D_{iso}$ upstream of the injectors.
5. For a further increase in fuelling, where $\phi = 1.3$, the separation did not move any further forward, however there was only a marginal increase in the combustion chamber pressures and so the maximum fuelling limit may have been reached.

4.2.2 2° divergent combustor

The next combustor presented is the 2° divergent combustor. This combustor has a constant area section followed by a divergent section starting at 0.63 m from the leading edge of the model. The data from the fuel-off and the combustion-suppressed tests are shown in Figure 4.24 (where the pressure scale has been reduced again to P/P_∞ = 10).

Fuel-off and combustion-suppressed case

The combustion pressures in the straight section of the 2° divergent combustor are similar to those for the constant area combustor, however past the divergent point there is a rapid drop in pressure from $3.8P_\infty$ to around $1.6P_\infty$ by around half way down the divergent section. For the combustion-suppressed case the mass-addition of the fuel raises the peak pressure in the constant area section of the combustor to just above $6P_\infty$, which is similar to the peak pressure in the combustion-suppressed case for the constant area combustor at a similar equivalence ratio ($\approx 6P_\infty$). Past the divergence point there is a rapid drop off in pressure, as seen for the fuel-off shot for this combustor.

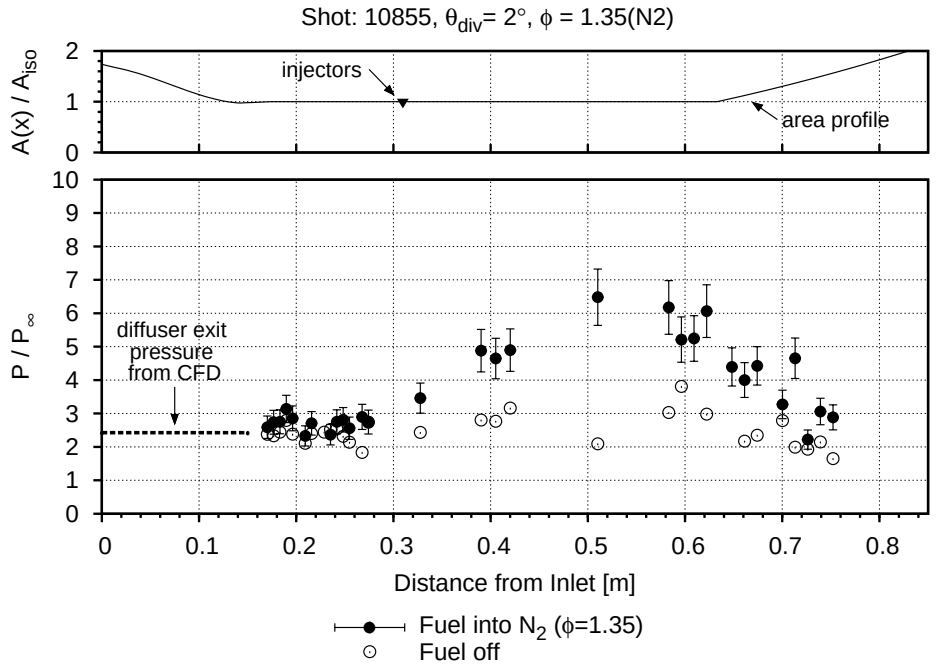

Figure 4.24: Pressure profiles for the fuel-off and combustion-suppressed tests for the 2° divergent combustor.

Non-separated case

The results for the test with the lowest equivalence ratio for the 2° divergent combustor are shown in Figure 4.25. At $\phi = 0.56$ a significant pressure rise is registered at the first sensor in the combustion chamber, which indicates that ignition occurred somewhere between the front-edge pressure sensor and the first combustor sensor. At this equivalence ratio the pressure levels at the front edge of the combustion chamber are still at

fuel-off and combustion-suppressed levels and hence this is defined as a non-separated case. For this case a strong pressure rise above that of combustion-suppressed test is observed with a peak pressure of $12.2P_\infty$ near the end of the constant area section. There is a rapid fall in pressure past this point in the divergence section as is seen in the fuel-off and combustion-suppressed cases, but here it is even more pronounced falling from $12.2P_\infty$ down to as low as $4.1P_\infty$. There also appears to be some wave structure in this divergent section with successive sensors reading alternating pressures above and below the general trend downwards along the divergent section.

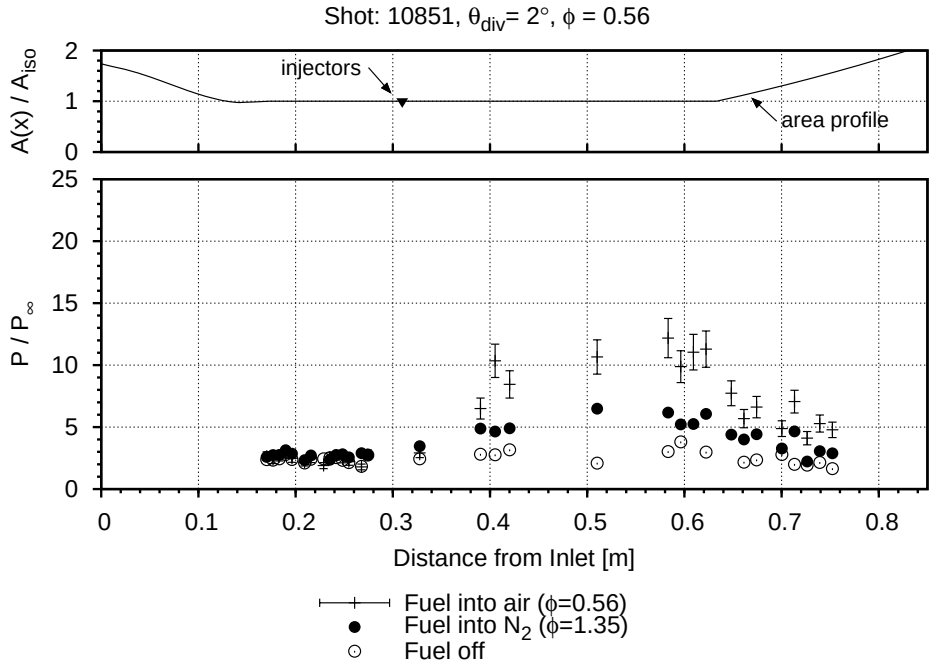

Figure 4.25: Pressure profile for a non-separated case for the 2° divergent combustor ($\phi = 0.56$).

Figure 4.26 shows the key results for the 2° divergent combustor over the full range of equivalence ratios. For $\phi = 0.6$ some separation is observed at front-edge sensors location. For an increase in the fuelling rate to $\phi = 0.93$ the pressure at the front-edge of the combustor also increases, though the separation has not reached as far forward as the instrumented section of the isolator. At $\phi = 1.03$ the separation is now detected by the isolator sensors. As fuelling is increased from $\phi = 1.03$ through to $\phi = 1.26$ the separation strengthens, as indicated by the increase in pressure levels in the isolator sensors. Between these last two cases, the maximum fuelling case ($\phi = 1.26$) and the next lowest ($\phi = 1.03$) fuelling rate, there is only a marginal increase in the peak pressure in the combustor and little change in the most forward position of the separation.

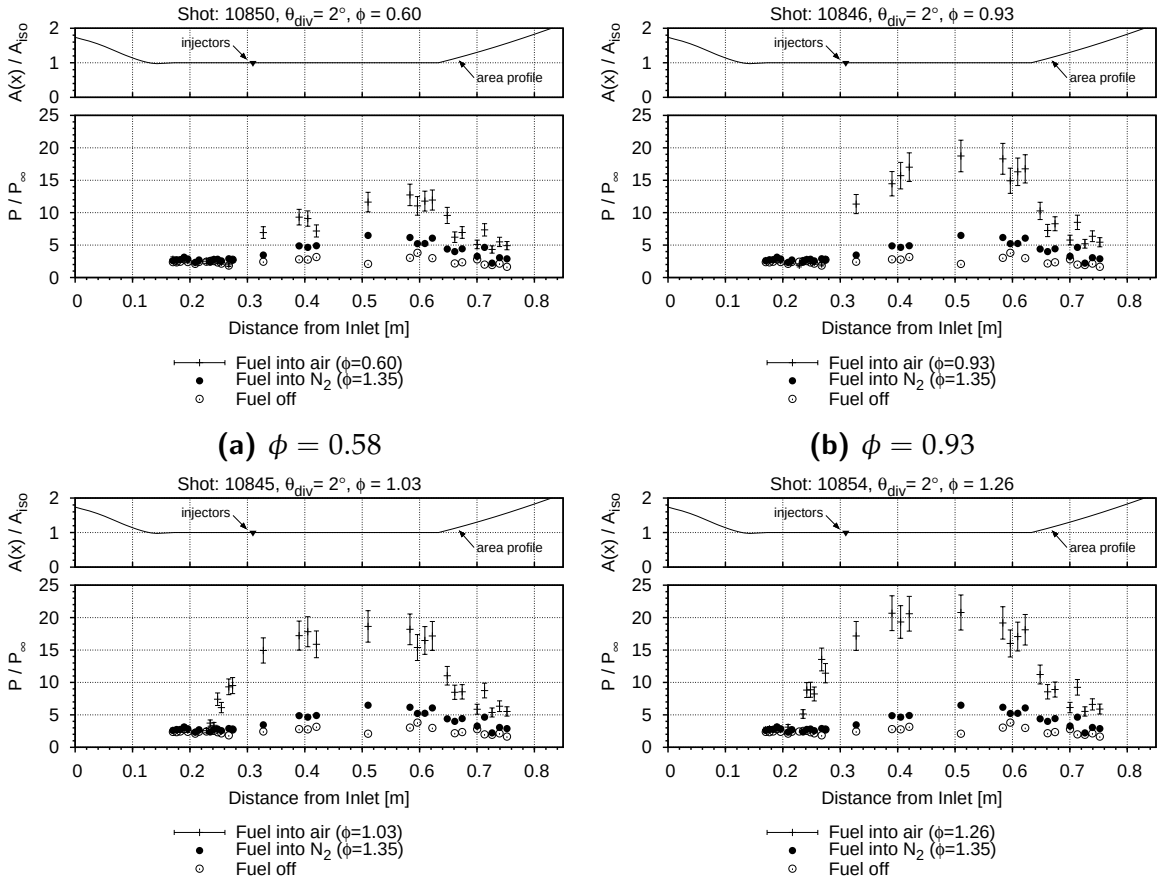

(a) $\phi = 0.58$ **(b)** $\phi = 0.93$

(c) $\phi = 1.03$ **(d)** $\phi = 1.26$

Figure 4.26: Pressure profiles for the key results of the 2° divergent combustor.

Comparison between the constant-area and 2° divergent combustors

Figure 4.27 compares the results from the 2° divergent combustor with those of the constant area combustor. The first figure, Figure 4.27a, shows a single non-separated flow for each combustor at similar equivalence ratios. It can be seen that the flow between the two combustors for the non-separated cases is quite similar up until the divergence point, after which there is a rapid decrease in the pressure in the divergent section of the 2° divergent combustor.

Figure 4.27b shows the results for the moderately-separated cases at $\phi \approx 0.60$. Again, the pressures in the straight section of divergent combustor are quite similar

to those in the constant area combustor. At the higher equivalence ratio of 0.94 (Figure 4.27c) differences appear between the two combustors, where the pressure between 0.5 m and 0.6 m is lower for the constant area combustor than for the 2° divergent combustor. However both combustors achieve rather similar peak pressures, which are $17.0P_\infty$ for the constant area combustor and $18.7P_\infty$ for the 2° divergent combustor. This explains why the front edge pressures are nearly identical as it is the peak pressure which drives the strength of the separation. This discrepancy between the two combustors disappears in the next test where the equivalence ratio is increased to approximately 1.05 (Figure 4.27d). Here, the flows in the two combustors are again similar up to the divergence point of the 2° divergent combustor and both combustors achieve a similar peak pressure. Considering the consistent results either side of the $\phi \approx 0.94$ case and the random component of the uncertainty associated with ϕ, the discrepancy seen in this case is considered an anomaly.

The similarities between the two flows (i.e. the pressures through the separation) are also present for $\phi \approx 1.17$ case. The interesting aspect to note is that the leading edge of the shock train appears to be at the same location for both combustors at $\phi \approx 1.17$, as well as at $\phi \approx 1.05$. This indicates that the peak pressure in each combustor may in fact be similar but it falls in the large gaps between sensors and is therefore not captured. Nevertheless, based on these data the point of divergence for the 2° divergent combustor was too far downstream to affect the shock train.

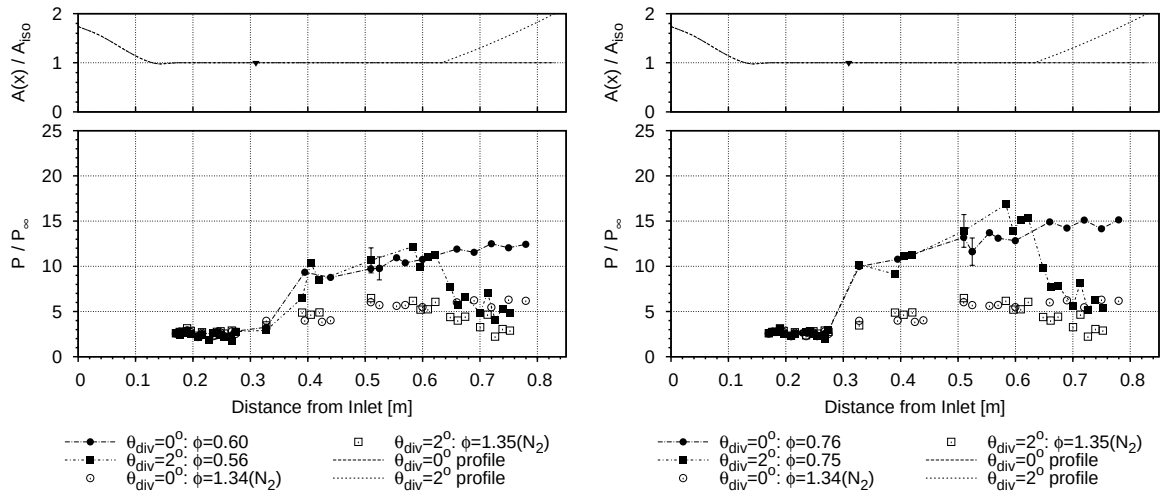

(a) $\phi \approx 0.58$

(b) $\phi \approx 0.76$

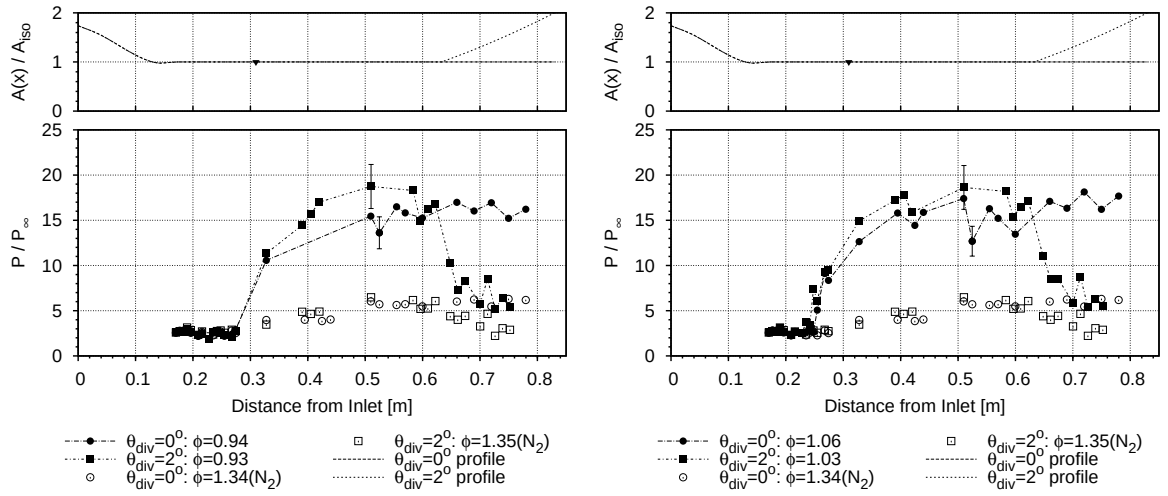

(c) $\phi \approx= 0.94$

(d) $\phi \approx 1.05$

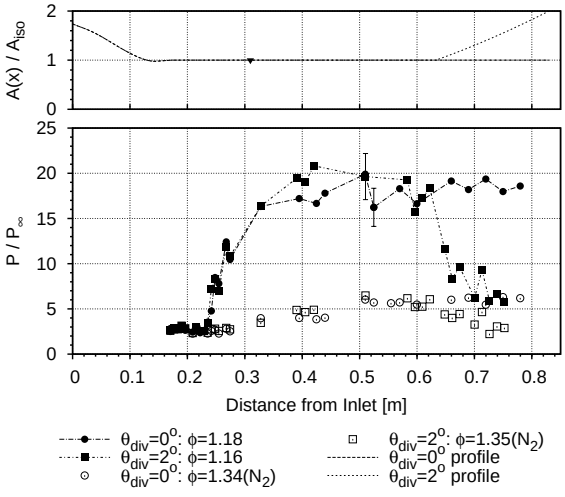

(e) $\phi \approx 1.17$

Figure 4.27: Comparison of the pressure profiles for the constant area and 2° divergent combustors. Error bars represent the uncertainty in the normalised measured pressures.

4.2.3 1° divergent combustor

In this section the data from the from the 1° divergent combustor are presented. Figure 4.28 shows the fuel-off results for this combustor. As for the constant area and 2° divergent combustors, there is a slight increase in pressure along the constant area section of the duct. Past the point of divergence the pressure decreases but not as rapidly as for the 2° divergent combustor. The final exit pressure of around $1.5P_\infty$ is similar to the exit pressure for the 2° divergent combustor, which was $1.6P_\infty$.

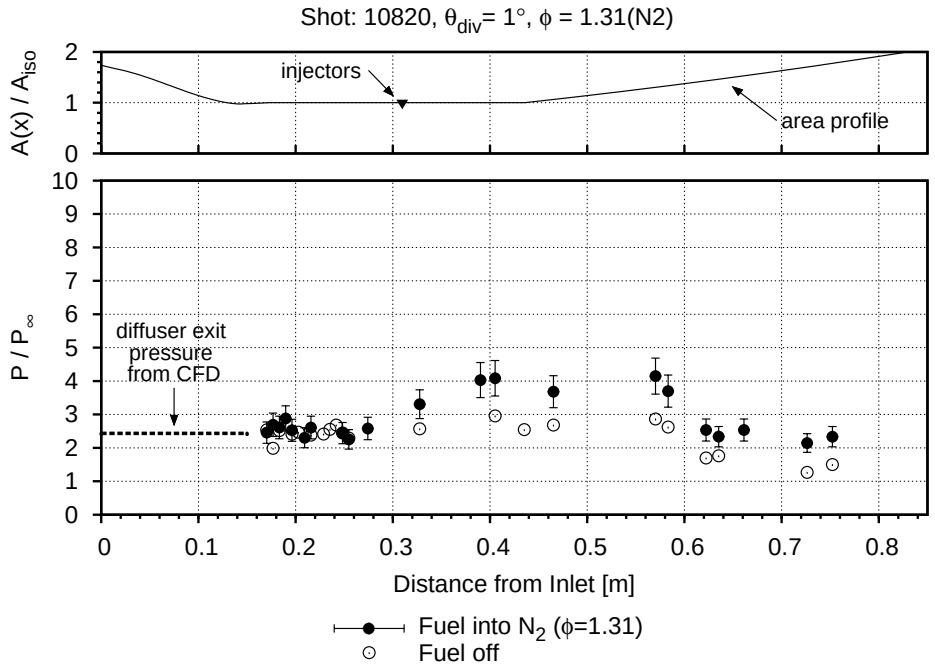

Figure 4.28: Pressure profiles for the fuel-off and combustion-suppressed tests for the 1° divergent combustor

Non-separated cases

The result for the lowest equivalence ratio tested ($\phi = 0.57$) for this combustor is shown in Figure 4.29. Consistent with the constant area and 2° divergent combustors, there is a large pressure rise in the section of constant area of the combustor above that for the fuel-into-nitrogen shot, which confirms robust combustion of the fuel. At this equivalence ratio however separation around the fuel injector is not detected at the front edge pressure sensors ($X = 0.33$ m).

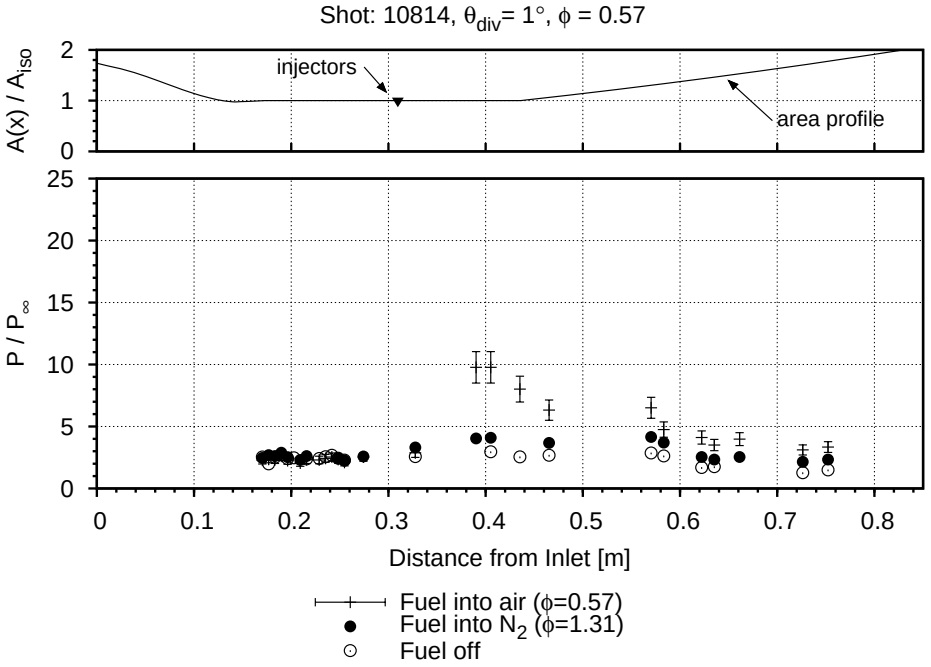

Figure 4.29: Pressure profile for a non-separated case for the 1° divergent combustor

Moderately Separated cases

The results for the 1° divergent combustor for equivalence ratios ranging from 0.68 to 1.52 are presented in Figure 4.30. Similar characteristics are seen in the 1° divergent combustor as are seen in the constant area and 2° divergent combustors; that is separation is observed, as evident by the raised pressure at the front edge of the combustor, for equivalence ratios up to a value of 0.77 (Figure 4.30b). At an equivalence ratio near unity ($\phi = 0.95$, Figure 4.30c), the separation has reached the two most downstream sensors in the isolator. With increasing fuelling this separation continues to be pushed further forward (Figure 4.30e).

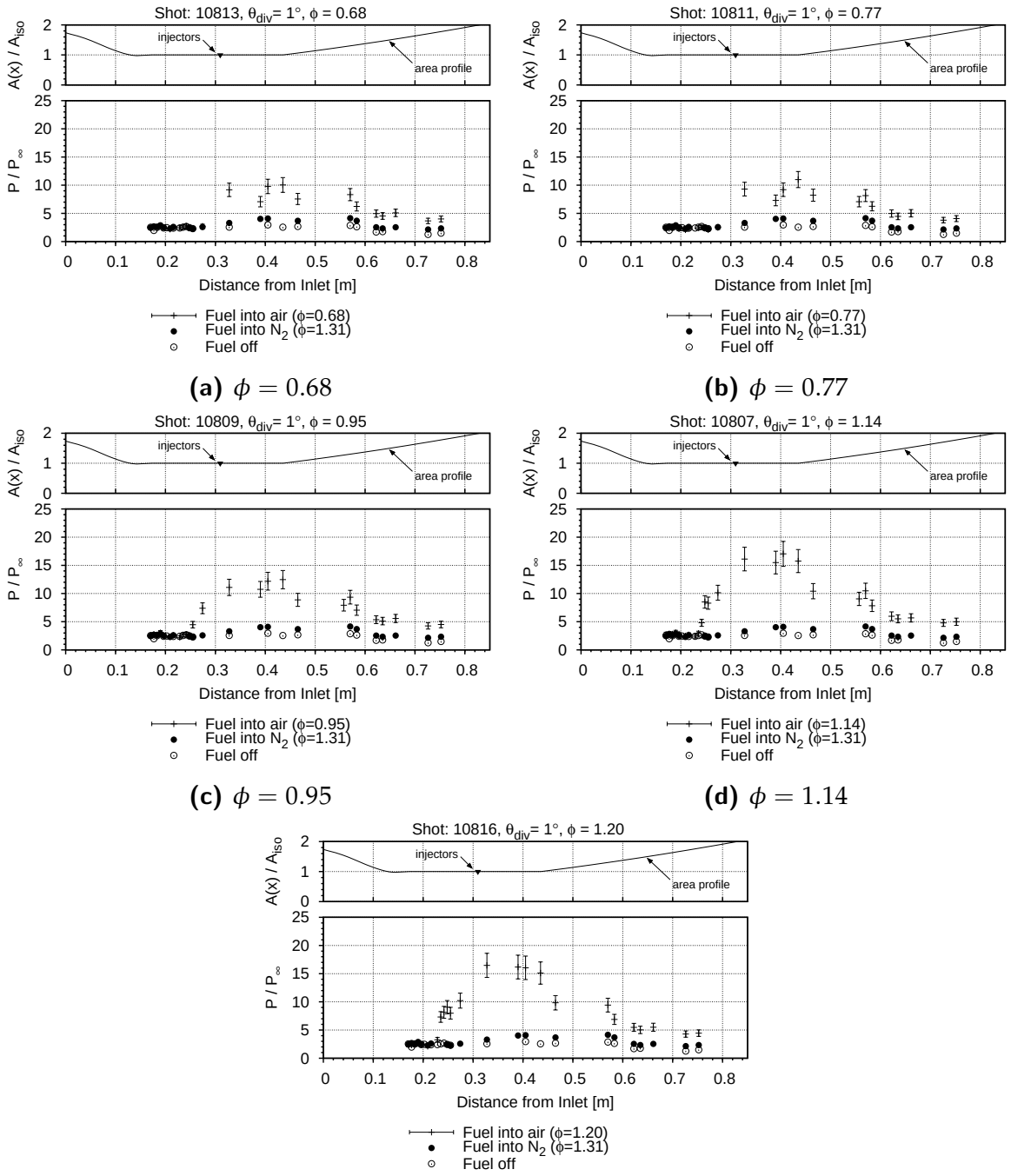

(a) $\phi = 0.68$ **(b)** $\phi = 0.77$

(c) $\phi = 0.95$ **(d)** $\phi = 1.14$

(e) $\phi = 1.20$

Figure 4.30: Pressure profiles for the key results of the 1° divergent combustor. Error bars represent the uncertainty in the normalised measured pressures.

Comparison between the 1° and 2° divergent combustors

The results from the 1° divergent combustor are best compared with the results from the 2° divergent combustor to highlight the effect that shifting the divergence point forward has on the pre-combustion shock train. Figure 4.31 shows these comparisons.

For the non-separated cases (Figure 4.31a) the two divergent combustors have similar flows up to divergence point of the 1° divergent combustor. For both divergent combustors the pressure decreases from the divergence point onwards. For the 1° divergent combustor this decrease commences further upstream and is more gradual than for the 2° divergent combustor, as is expected. However by the exit the 1° divergent combustor has a lower pressure ($3.3P_\infty$) than the 2° divergent combustor ($4.8P_\infty$). As the exit diameter of both divergent combustors is the same, this indicates that the streamwise distribution of area ($A(x)$) has affected combustion resulting in higher losses and/or lower mixing-combustion efficiency for the 1° divergent combustor than for the 2° divergent combustor.[2]

When separation is observed at only the front edge pressure sensor (at $\phi \approx 0.76$) the two divergent combustors again produce similar flows up to the divergence point. Interestingly the exit pressures of both combustors are closer to each other for these cases than for $\phi \approx 0.57$ cases.

Moving through equivalence ratios 0.94 to 1.23, both combustors show highly separated flows with the shock train positioned at similar locations for comparable fuelling rates. The peak pressure measured in both the 2° and 1° divergent combustor are listed in Table 4.1.

Apart from the $\phi \approx 1.05$ case, for all the separated cases ($\phi \geq 0.76$) the peak pressure of the 1° divergent combustor are quite low compared with the 2° divergent combustor, particularly for the $\phi \approx 0.94$ case. This is a curious result as the shock train is further forward for the 1° divergent combustor than for the 2° divergent combustor

[2] In a one-dimensional model, all things being equal, the pressure should be slightly higher for the 1° divergent combustor than for the 2° divergent combustor. This was confirmed using the cycle analysis code presented in Chapter 5 by way of a test case (shot 10851) where the inflow and fuelling parameters were held constant and only the geometry was changed. For this test case, the 1° divergent combustor produced 2% more pressure than the 2° divergent combustor at the exit of the engine.

Table 4.1: The peak pressure, normalised by the freestream pressure (P_∞), measured in the 2° and 1° divergent combustors.

$\approx \phi$	2°	1°
0.57	12.2	9.8
0.76	16.8	11.8
0.94	18.7	12.5
1.05	18.6	15.5
1.16	20.8	15.1
1.23	20.8	16.5

despite having a much lower peak pressure. The key aspect to note when reviewing all the separated cases is that the pressure at the front edge sensor near the injection point is almost exactly the same for the two combustors at comparable fuelling rates. There is a possibility that the peak pressure is not adequately captured, for example if the reattachment point lies between a large gaps between the sensors. Notwithstanding that possibility, the main conclusion to draw is that, for these experiments, it is the pressure at the injection point which dictates the shock train length and not the peak pressure in the engine.

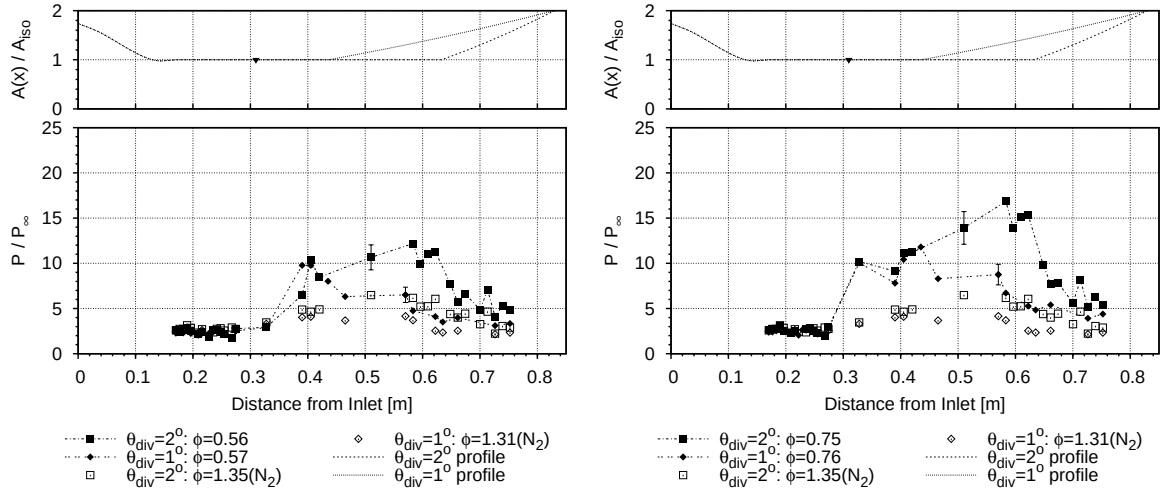

(a) $\phi \approx 0.57$

(b) $\phi \approx 0.76$

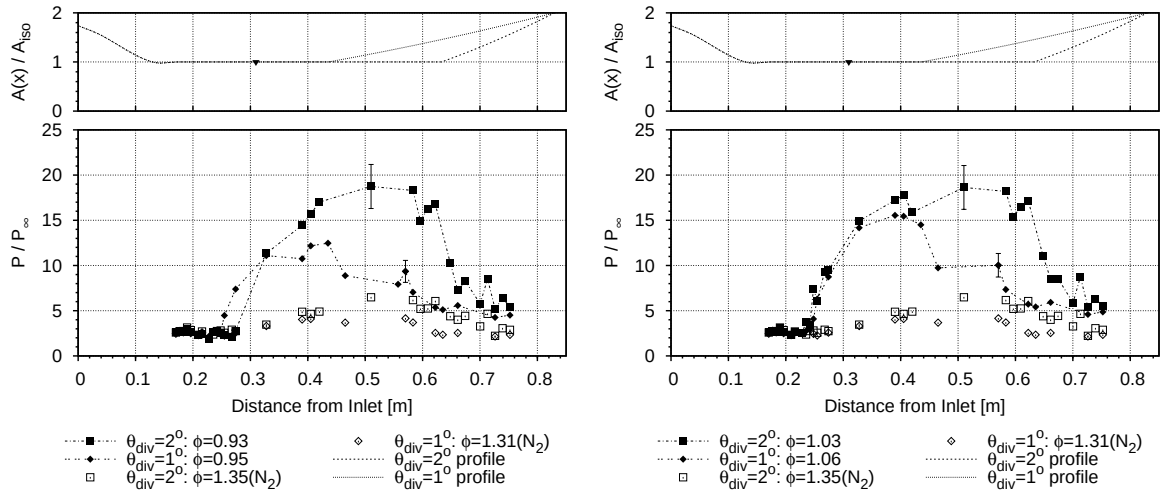

(c) $\phi \approx 0.94$

(d) $\phi \approx 1.05$

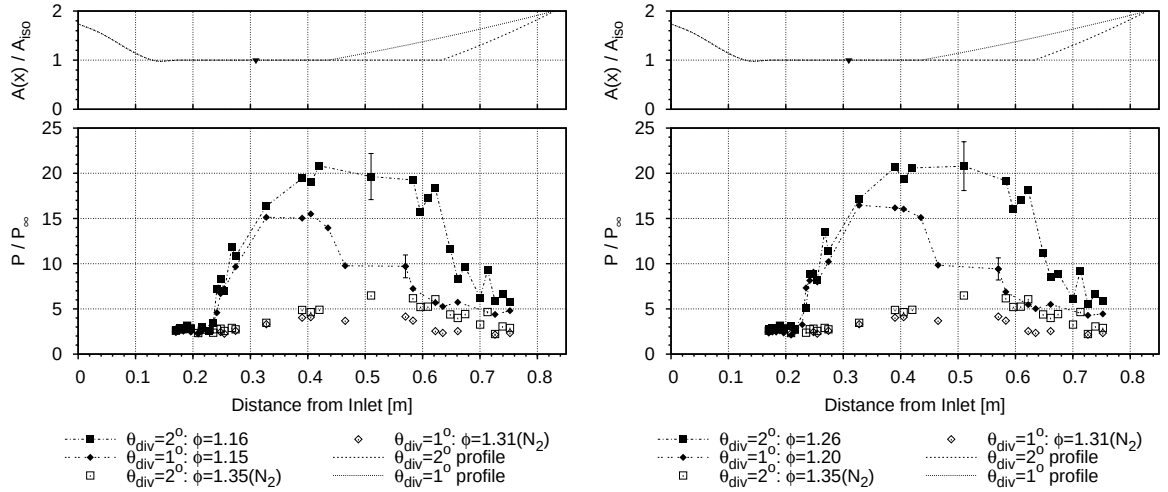

(e) $\phi \approx 1.16$

(f) $\phi \approx 1.23$

Figure 4.31: Comparison of the pressure profiles for the 2° and 1° divergent combustors. Error bars represent the uncertainty in the normalised measured pressures.

Comparison of all three combustors

The results from all three combustors are compared at similar ϕ in Figure 4.32. Similar conclusions can be drawn from these comparisons of all three combustors as are drawn from the comparison of the 2° and 1° divergent combustors, which are:

1. Initial separation, as indicated by an elevated pressure at the front edge (FE) sensors, occurs at a similar equivalence ratio for all three combustors (0°: $\phi = 0.76$, 2°: $\phi = 0.75$ & 1°: $\phi = 0.76$).
2. The separation moves into the isolator to the furthest downstream isolator sensors at approximately the same equivalence ratio ($\phi = 0.94$).
3. For similar equivalence ratios the shock train position and strength (indicated by the slope of the pressure rise) is similar for all three combustors, demonstrating that divergence in the divergent combustors had no effect on the shock train characteristics.
4. There is some discrepancy between the peak pressures for the 1° divergent combustor and the other two combustors at comparable ϕ. (There is also a single case ($\phi \approx 0.94$) where the shock train in the 1° divergent combustor is fore of the other two combustors.) However despite the discrepancy in peak pressures, there is little difference in the pressures near the injection point. This indicates that, for these experiments, it is the pressure at the injection point (i.e. end of the isolator) which dictates the shock train position, not the peak pressure in the duct. This explains the observation that the shock train position was similar for all three combustors at comparable ϕ as the divergence point for both divergent combustors was downstream of the injection point.

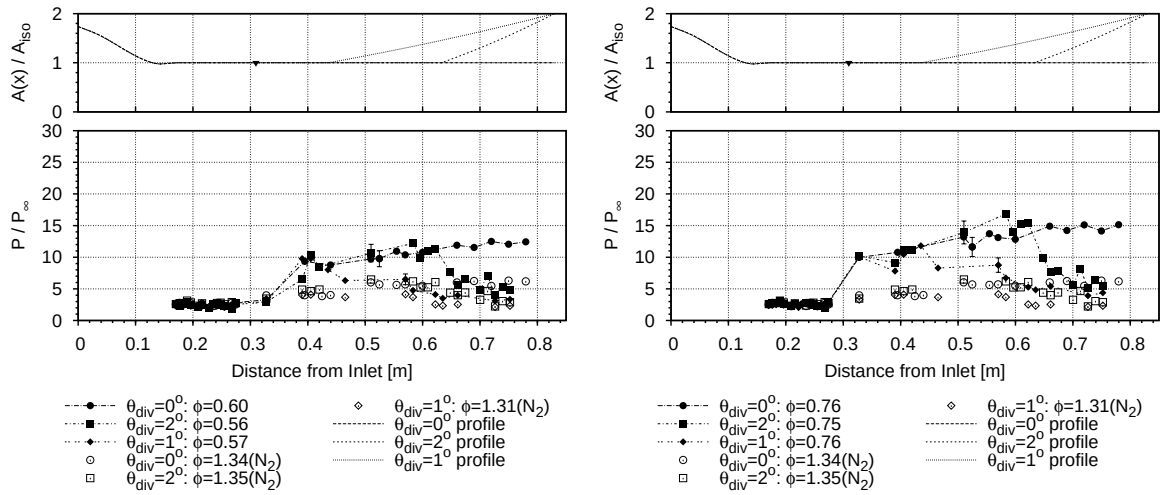

(a) $\phi \approx 0.58$

(b) $\phi \approx 0.76$

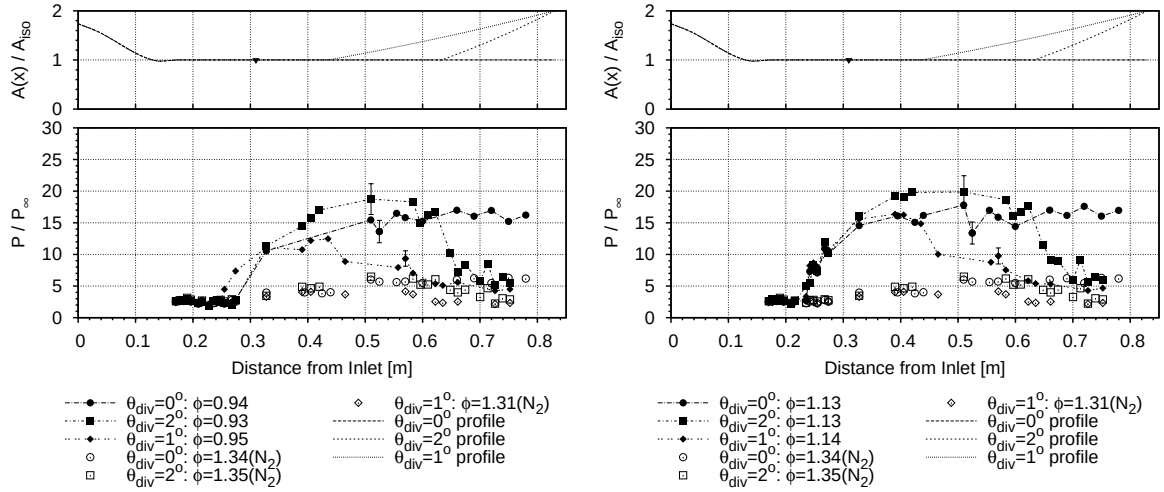

(c) $\phi \approx 0.94$

(d) $\phi \approx 1.13$

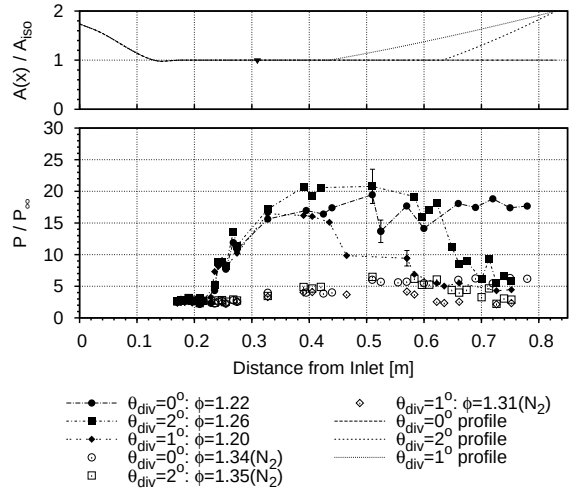

(e) $\phi \approx 1.23$

Figure 4.32: Comparison of the pressure profiles for all three combustors. Error bars represent the uncertainty in the normalised measured pressures.

4.3 Shock Train Characteristics

The results presented in Section 4.1 demonstrate that a stable shock train can form in the isolator within a specific range of equivalence ratio. The shock train characteristics are explored in this section vis-à-vis the relationships between shock train length (S_o), isolator exit pressure (P_{DT9}) and equivalence ratio (ϕ).

4.3.1 Shock train length versus isolator exit pressure

Figure 4.33 shows, for all three combustors, how S_o varies with P_{DT9}/P_∞, which is the normalised static pressure measured at the furthest downstream sensor (DT9) in the isolator. The static pressure is normalised by the computed freestream static pressure. This figure shows that the shock train length, as determined using Rule 4.1, increases with the exit pressure of the isolator (as expected from Waltrup and Billig (1973)) and this provides confidence that the methodology of selecting S_o was appropriate.

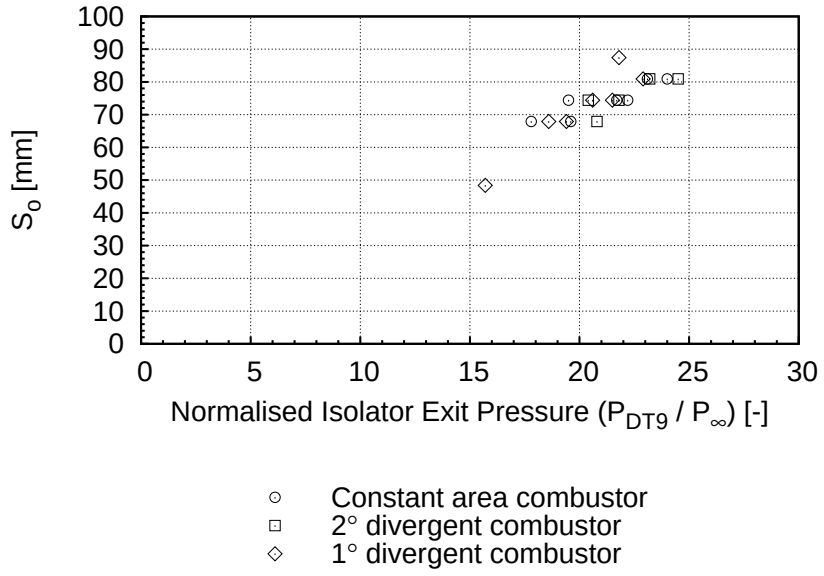

Figure 4.33: Plots showing normalised isolator exit pressure (P_{DT9}/P_∞) versus pre-injector shock train length (S_o) for all three combustors.

4.3.2 Isolator exit pressure versus equivalence ratio

Figure 4.34 shows the normalised pressure at the isolator exit (P_{DT9}/P_∞) versus the equivalence ratio (ϕ) for all three combustors. It can be seen for highly separated cases,

which occur for equivalence ratios greater than 0.92, that there is a strong correlation between ϕ and P_{DT9}/P_{∞}. The pressure at the isolator exit increases linearly with equivalence ratio. This shows that the back pressure at the isolator exit, which drives the shock train, scales with fuelling rate.

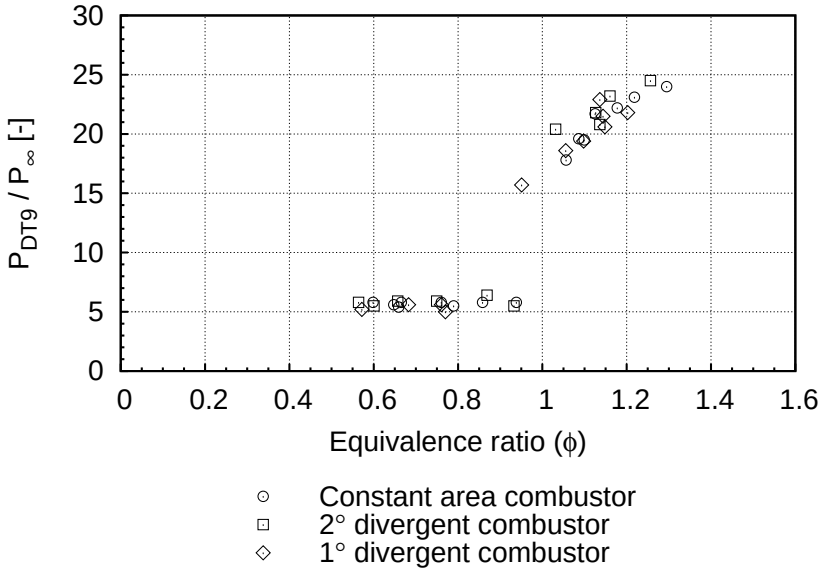

Figure 4.34: Plots showing normalised isolator exit pressure (P_{DT9}/P_{∞}) versus equivalence ratio (ϕ) for all three combustors.

4.3.3 Shock train length versus equivalence ratio

In Sections 4.3.2 and 4.3.2 it is shown that, for all three combustors, the shock train length (S_o) scales with isolator exit pressure (which itself scales with equivalence ratio). Here in Figure 4.35 it is shown, as expected, that the shock train length scales with equivalence ratio. In this plot it can be seen that there is a positive relationship between S_o and ϕ for all three combustors, though there is some scatter about the line of best fit. Due to the limited number of established separated cases and the challenges in the methodology of determining the leading edge of the shock train, it is difficult to determine from these data whether there are substantial differences between the three combustors. The pressure profiles, which are presented in Section 4.2, provide a better insight into the length of the shock train as one can trace the pressure profile forward through the shock train to see where the leading edge is likely to be. From these profiles, it is shown that at comparable equivalence ratios there is no clear difference in shock train length between the combustors.

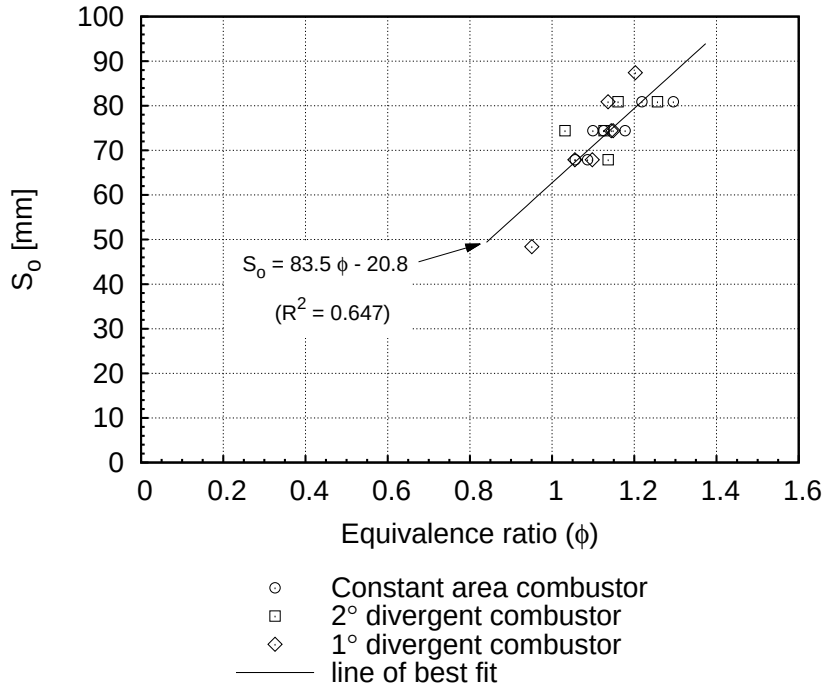

Figure 4.35: Plots showing shock train length (S_o) versus equivalence ratio (ϕ) for all three combustors. R^2 is the coefficient of determination.

4.3.4 Summary of shock train characteristics

The results shown in Figure 4.33 and Figure 4.34 together show that, although establishment time (t_{est}) does not correlate with any key parameter, the characteristics of an established shock train do scale with conditions such as fuelling. Additionally, no discernible difference was found between the three combustor configurations in terms of both the critical ϕ at which separation occurred and the shock train length as a function of ϕ.

4.4 Summary and Conclusions

This chapter presents data from the experiments conducted in the T4 Stalker Tube using the model described in Chapter 3. From an investigation of the transient data (time-history plots) a methodology for determining the establishment time was proposed and applied to the data. From this, no discernible correlation was identified between the flow establishment time of the entire isolator (t_{est}) and the pre-injector shock train length (S_o), nor between t_{est} and the equivalence ratio (ϕ); however the time it took for the flow to separate at the rear of the isolator ($t_{sep_{DT9}}$) does correlate with both S_o and ϕ. This indicates that the mechanism for separation does depend directly on changes in the fuelling.

Some conclusions can also be drawn about the shock train characteristics. S_o scales with both ϕ and the isolator back pressure (P_{DT9}/P_∞). These findings are consistent for all three combustor configurations (i.e. the constant area and the 2° and 1° divergent combustors) where no discernible differences were found. The parameters t_{est}, $t_{sep_{DT9}}$ and S_o also all responded to changes in ϕ and P_{DT9}/P_∞ similarly for all three combustors. A similar trend was found in the pressure profiles. For these pressure profiles there is little difference between the shock train profiles for the three combustors. This is attributed to the following: although the divergence had resulted in much lower exit pressures, the peak pressures were not much lower. (This is because the majority of pressure rise along the combustor occurs before either of the divergence points in the divergent combustors.) Even then, at comparable ϕ, differences in the peak pressure did not translate into differences in the pressure at the rear of the isolator. As such, it is concluded, that for these experiments it is the pressure at the isolator exit which dictates the shock train length and not the peak pressure in the engine.

Chapter 5

Cycle Analysis Methodology and Results

This chapter presents the finding from the cycle analysis which was employed to determine the following performance parameters from the experimental results: mixing-rate (ϑ), combustion efficiency ($\eta_{c,f}$) and mixing-length (x_{fe_1}). This chapter also investigates how these parameters are affected by the presence of a pre-combustion shock train. An overview of the cycle analysis code is presented first, including both the combustion and the shock-train models. The results from the constant area combustor are presented and discussed first, followed by the two divergent combustors (2° and 1°) in turn. The results for each combustor are presented in order of increasing fuel flow rate and are categorised into the following cases: fuel-off, non-separated, moderately separated and highly-separated. The last section of the chapter presents summary plots for key parameters over the full range of fuelling conditions for all three combustors.

5.1 Dual-mode Cycle Analysis Methodology

A key questions posed in this thesis is whether the presence of the shock train affects the performance of this scramjet engine. A common approach taken to appraise the performance of scramjet engines is to employ a stream-thrust averaged cycle analysis (Curran and Craig, 1973; d'Incà and Bouchez, 2006; Heiser and Pratt, 1994; Murthy, 2000). This approach allows certain engine performance parameters to be estimated by finding the computed pressure profile from the cycle analysis that best fits the experimental data.

The cycle analysis code used in this research is *Dual Mode Cycle Analysis (DMCycle)*. The development of and application to previous engines are presented in the works of Smart (2007, 2008, 2010, 2012) and Moule and Smart (2012). This code has the capability to model the pressure rise from the shock train which forms in the isolator of heavily back-pressured scramjets. It is based on the classical equations for quasi one-dimensional flow described in Shapiro (1953), with an additional relation to account for the region of separated flow, which is provided by Ortwerth (2000). These equations are presented in Smart (2007).

The flow is modelled as a mixture of thermally perfect gases in thermal equilibrium as described in Auslender and Smart (2000). Gross parameters define the inflow entering the isolator, which are Mach number, static pressure and static temperature. As a set, these parameters also specify the flow entering the combustor in terms of mass flow rate $\dot{m}_2$, stream thrust F_2, and total enthalpy h_{t_2}. The gross parameters associated with the fuel injection are the fuel mass flow rate $\dot{m}_f$, stream thrust of the fuel F_f (which is zero for injection normal to the flow) and total enthalpy of the fuel h_{t_f}. The geometry of the engine is prescribed in terms of the cross-sectional area and perimeter along its length. For the engine analysed in this study, the modelled region spans from the start of the isolator (station 2) to the end of the combustion chamber (station 4). The temperature of the wall of the geometry is specified and the heat exchange between the wall and the flow is accounted for in the model. For shock tunnel experiments, the wall is assumed to be at laboratory conditions of 300 K.

5.1.1 Combustion model

Combustion is modelled in the code via a combustion efficiency curve (Equation 5.1) from Heiser and Pratt (1994) and through calls to thermodynamic subroutines, which provide the state properties of the gas products from combustion.

$$\eta_c(X) = \eta_{c,f}\left[\frac{\vartheta X}{1+(\vartheta-1)\,X}\right] \tag{5.1}$$

with

$$X = \frac{x - x_3}{x_{fe_1} - x_3}$$

In 5.1 the term $\eta_{c,f}$ is the fuel based combustion efficiency reached by the end of the combustor, ϑ is a mixing rate parameter, and X is the non-dimensional length over which combustion occurs with x_3 as the location where the fuel is injected (station 3), and x_{fe_1} as the point at which combustion is deemed complete.

The combustion curve models both the chemical kinetics and mixing effects on the combustion and does not differentiate between the two. The curve essentially describes the proportion of the fuel which reaches complete combustion along the engine. The proportion of the fuel that is not burnt completely is considered to be inert and is retained as unreacted species.

Also, as the code is quasi one-dimensional, the properties at each point along the length of the engine are assume to be uniform across the cross-section at that point. Whilst it has been shown that the real flow in a scramjet combustor is far from uniform, even for a circular combustor (Brown et al., 2011, 2009), useful global performance parameters can still be estimated from this approach (Smart, 2010).

5.1.2 Ortwerth's diffuser model

The compression of the flow by the shock-train is modelled through a change in the area of the core flow. The flow which is entrained in the recirculation portion of the separation is not considered to be part of the flow through the engine. This separation therefore represents effectively a geometric blockage and thus the core flow, where mass, momentum and energy are conserved, undergoes a change in area in addition to any changes in area from the geometry of the engine. This adds an additional parameter, representing the area of the core, to the governing equations, and as such a diffuser model is required to close the equation set. The model employed in this cycle analysis is by Ortwerth (2000), who established an empirical relation (Equation 5.2) where the pressure rise through the shock train ($\frac{dP}{dx}$) is proportional to both the dynamic pressure ($\frac{1}{2}\rho V^2$) and the coefficient of skin friction at the point of separation (c_{f_0}), and inversely proportional to the hydraulic diameter of the duct (D_H).

$$\frac{dP}{dx} \approx \frac{89}{D_H} c_{f_0} \left(\frac{1}{2} \rho V^2 \right) \tag{5.2}$$

5.1.3 Code logic

The logic of the code is as follows. The calculation begins at the start of the geometry and proceeds piece-wise through to the end of the engine making calls to a sub-routine containing the thermodynamic equilibrium model. For each element the incremental area change is known from the area distribution provided and the incremental changes in stream thrust and total enthalpy from combustion, friction forces, pressure forces and heat loss are calculated. From this the state properties of the flow can be determined at all stations along the engine.

Initially the flow path is computed assuming no separation. If the calculated pressure anywhere along the duct is above the separation criterion specified by Equation (5.3), which is from Korkegi (1975), then the code is re-run assuming a separation with an initial estimation of the point of separation. This results in an elliptical mathematical problem and as such the code is run iteratively until the position of the separation produces a flow path, using Ortwerth's (2000) diffuser model, which satisfies the governing one-dimensional equations.

$$\frac{P_{sep}}{P_4} = \begin{cases} 1 + 0.3M^2 & \text{for } M_4 < 4.5 \\ 1 + 0.17M^{2.5} & \text{for } M_4 \geq 4.5 \end{cases} \tag{5.3}$$

5.1.4 Parameter selection and optimisation

The inputs for the code consist of parameters defining the flow entering the isolator and fuel flow specific for each shot. The method of estimating the properties entering the isolator, which uses a combination of numerical and analytical codes, is outlined in detail in Chapter 3. The average skin friction coefficient (c_f) for the duct was set at a value of 0.002 and this is based on values found for previous experiments at similar conditions (Goyne et al., 2003). The skin friction coefficient at the point of separation c_{f_o} was taken as the coefficient of skin friction where the diffuser ends and the isolator begins. This value was estimated using a boundary layer analysis code from Cebeci and Bradshaw (1984) which was applied to the diffuser geometry for the nominal shot and is estimated to be 0.0015 at the end of the diffuser. In regions where the flow was separated the skin friction coefficient was set to zero.

The remaining parameters were the terminal combustion efficiency $\eta_{c,f}$, a mixing curve parameter ϑ and the point of complete combustion x_{fe_1}. These parameters are the focus of this research and were determined through manual optimisation where each parameter was varied in turn through an acceptable range until a good fit of the cycle analysis to the experimental results was found. Details of this parameter optimisation are described in the Appendix E. The cycle analysis results presented next are for the final values for these parameters as determined from that optimisation.

5.2 Dual-mode Cycle Analysis Results

5.2.1 Constant area combustor

The results from the cycle analysis for the constant area combustor are presented first, beginning with the fuel-off and the combustion-suppressed cases, followed by selected cases of increasing fuelling rates. The results are categorised into cases of non-separated, moderately separated, highly separated and maximum fuelling.

Fuel-off and combustion-suppressed cases

The fuel-off and combustion-suppressed cases, shown in Figure 5.1 and Figure 5.2 respectively, provide an important check that the set of parameters governing the inflow are reasonable. Figure 5.1 shows the results of the cycle analysis when applied to a fuel-off case. In the bottom half of the figure, the experimental data are shown with the computed pressure profile from the cycle analysis overlaid. In the top half of the figure the area distribution of the engine is plotted. The area is normalised by the cross-sectional area of the isolator. Also shown in this area distribution is the location of fuel injectors. This portion of the figure will become important for cases where the boundary layer has separated as it will show the area of the core flow as predicted by the cycle analysis.

As shown in Figure 5.1 there is very good agreement between the cycle analysis and the experiment. The general trend of increasing pressure along the duct observed in the experimental results is captured by the cycle analysis. This trend is due to the displacement effect of the increasing thickness of the boundary layer which grows along

the duct. This provides confidence that the value chosen for c_f is reasonable (see Figure E.1d in Appendix E.1.1 for the sensitivity of the results to c_f). For the combustion-suppressed case (Figure 5.2), the cycle analysis matches the pressure through the isolator well, over predicts in the first third of the combustor and then under predicts in the back two thirds. As the cycle analysis is one-dimensional, the three dimensional effects of the fuel injection into the cross flow are not captured and so the pressure rise predicted in this combustion-suppressed case is due to the mass addition of the fuel alone. Considering this limitation, the match between the cycle analysis and the experiment is a reasonably good one.

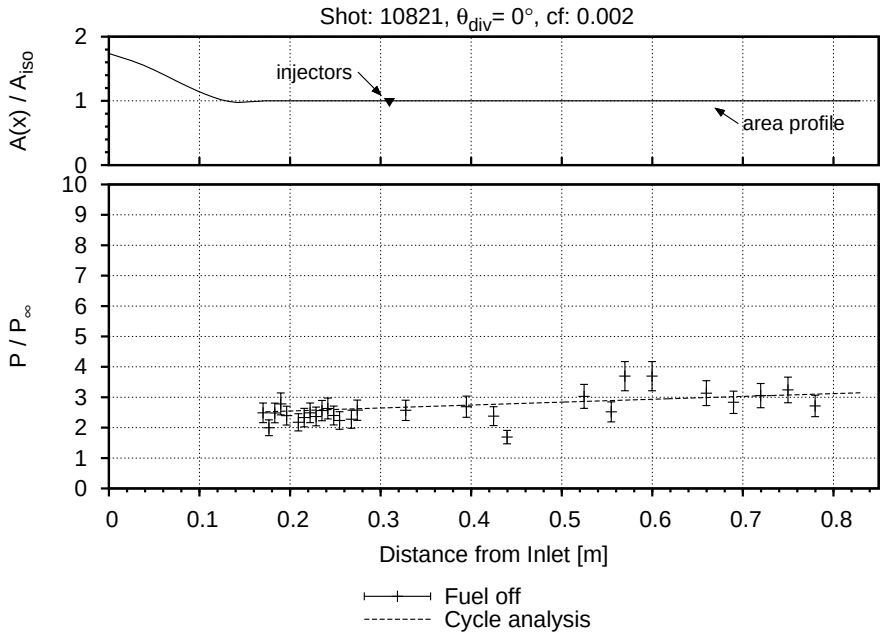

Figure 5.1: Cycle analysis results for the fuel-off case for the constant area combustor. Pressure is normalised by the computed freestream pressure. The top portion of each plot shows the area profile of the engine which is normalised by the cross-sectional area of the isolator. The injection point is marked on the area distribution by ▼.

Non-separated cases

The first of the combustion cases for the constant area combustor presented is the $\phi = 0.6$ case and is shown in Figure 5.3. This is the highest fuelling level where the pressure measured at the front edge (FE) pressure sensors (located at 0.33 m from the leading edge) remains at a level similar to that for the fuel-off and combustion-suppressed shots. As such, for this case an additional constraint was placed when optimising the parameters that no separation occurs in the cycle analysis. For this non-separated case the final values from the cycle analysis give a high mixing rate with

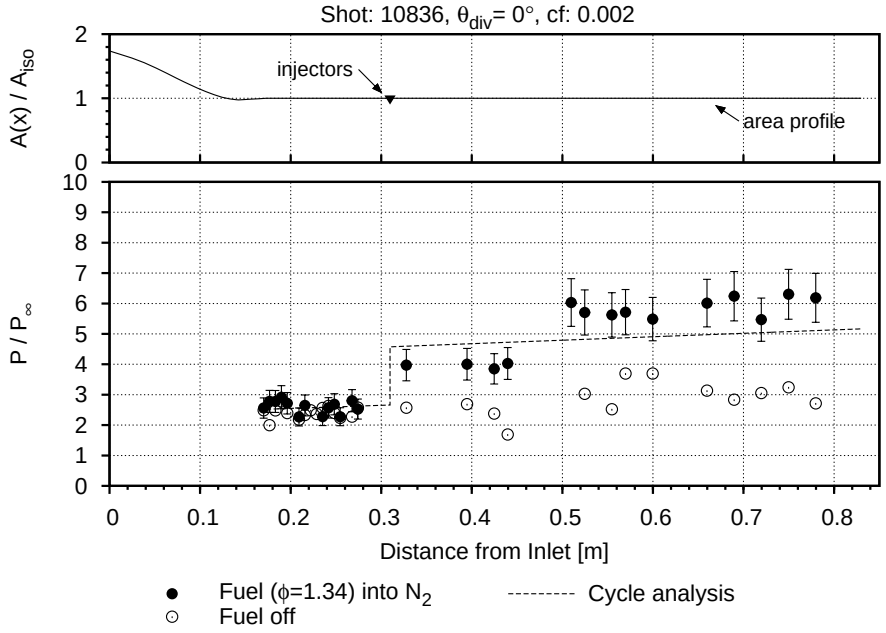

Figure 5.2: Cycle analysis results for the combustion-suppressed case for the constant area combustor.

$\vartheta = 10$, the maximum permissible combustion efficiency with $\eta_{c,f} = 100\%$ and a long mixing-length with $x_{fe_1} = 0.83$.

The high combustion efficiency of 100% is not unexpected considering that the engine has a relatively long combustor with a L/D (500 mm/32 mm) of 15, the injection is via port holes angled perpendicular to the flow which results in strong jet penetration, and that this test was performed at a relatively low ϕ. The high dynamic pressure (q) will also result in strong chemical kinetics. However, even at $\eta_{c,f} = 100\%$ the cycle analysis slightly under predicts the pressures seen in the experiment, but the difference is well within the experimental uncertainty.

For the parameter ϑ, which controls the rate of combustion, the key aspect of the pressure profile from the experiment which was used to determine the value of this parameter was the pressure of the first tap downstream of the injectors where the pressure was above the level for the combustion-suppressed case. In the example given in Figure 5.3, this is the pressure tap located at approximately 0.39 m downstream of the inlet. This first tap downstream of injection which shows a pressure rise from combustion gives an indication of how quickly the fuel mixes and burns with the air. This tap provides a datum to fit the cycle analysis to with respect to the parameter ϑ as this

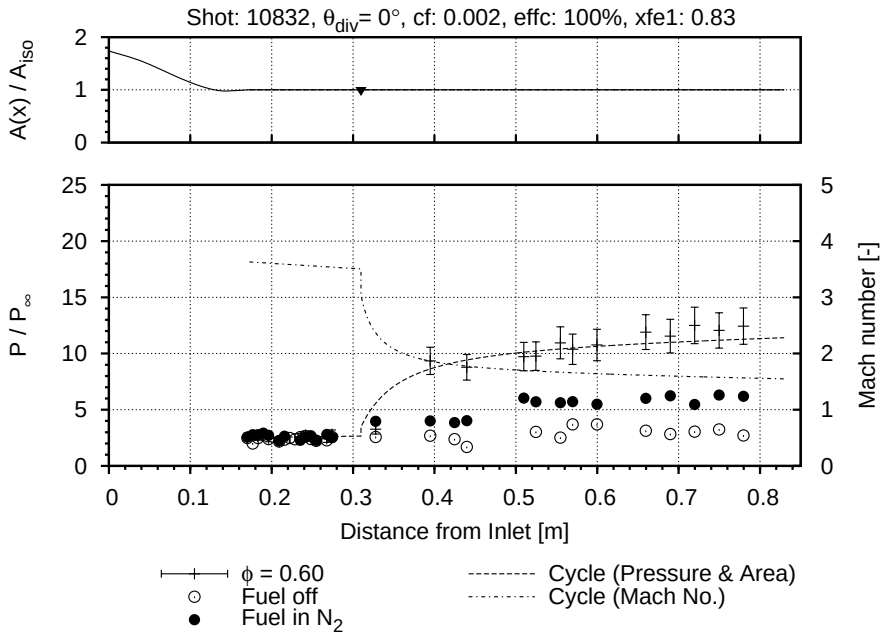

Figure 5.3: Cycle analysis result of a non-separated case for the constant area combustor showing both pressure and Mach number distributions along the isolator and combustion chamber ($\phi = 0.60$).

parameter controls the gradient of the combustion curve prescribed by Equation (5.1). From the optimisation of the cycle analysis for $\phi = 0.6$ case, it was found that a value of 10 for ϑ was required in order for the computed profile to intersect with this pressure measurement. This value of 10 represents robust mixing as this value is at the upper limit of the range given in Heiser and Pratt (1994) for attached scramjet flow.

With regards to the mixing-length, it was found that if x_{fe_1} was brought marginally forward from the end of the duct ($X = 0.83$ m) that separation of the boundary layer was predicted by the code. As no separation is seen in the experiments for this fuel condition it is concluded that, for the non-separated flow cases, the combustion takes the entire length of the combustor to complete and that the engine is operating close to Korkegi's (1985) criterion for separation.

For this case the calculated 1-D Mach number is also shown in Figure 5.3. The cycle analysis calculates that for the constant area combustor at $\phi = 0.6$, for the parameters stated above, that the Mach number of the flow has been driven from 3.63 at the isolator entrance down to 1.55 at the exit of combustion chamber.

Moderately separated cases

Figure 5.4 and Figure 5.5 show the results from the cycle analysis for two cases where separation was observed around the FE pressure sensors in the experiments and these cases are termed "moderately separated" in Chapter 4. The two specific cases which are included here are the $\phi = 0.76$ case (Figure 5.4), as this was the lowest equivalence ratio for which separation was observed in the experiments, and the $\phi = 0.86$ case (Figure 5.5), which is the highest equivalence ratio case where the combustion efficiency remained at 100%.

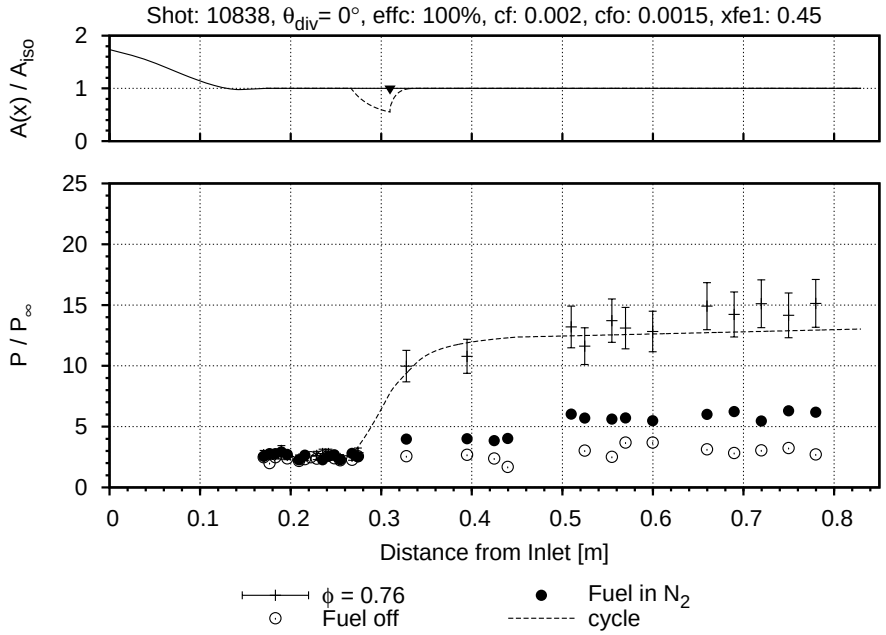

Figure 5.4: Cycle analysis of a separated case for the constant area combustor (ϕ=0.76). The size of the separation as predicted by the cycle analysis (*DMCycle*) is shown in the area distribution in the top portion of the plots.

The pressure distributions for both of these experiments are matched generally well by the cycle analysis, although for both cases the cycle analysis still slightly underpredicts the exit combustor pressure. The key parameter which has changed in value between the non-separated case and these separated cases is the x_{fe_1} parameter. Here there is a large shortening of x_{fe_1} from 0.83 m in the previous non-separated case to 0.45 m for this separated case. The influence which x_{fe_1} has on this cycle analysis result is illustrated in Appendix E as the $\phi = 0.76$ case is given as one of the examples of the optimisation method of this parameter. This large shortening of the region over which the heat from combustion is released indicates that once a shock train forms it is

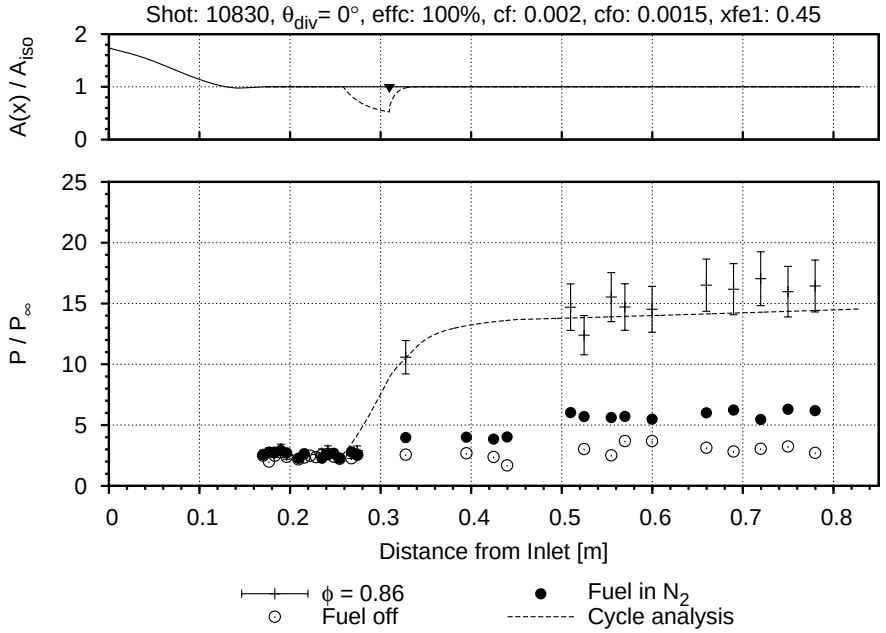

Figure 5.5: Cycle analysis result of a second separated case for the constant area combustor (ϕ = 0.86).

has very strong influence on combustion. This enhancement is due to two effects; one effect is an enhancement in mixing due to injecting fuel into a separated flow and the other effect is an enhancement in kinetics of combustion from the higher temperature and pressure of the flow entering the combustor, which is due to the additional compression from the shock train.

This vigorous combustion also means that the reattachment point predicted by the cycle analysis is not far downstream of the injection point. For this case the reattachment point is 0.344 m downstream from the leading edge or 34 mm ($\approx 1D_{iso}$) downstream of the injection point. This finding, in conjunction with the short combustion length, will be important in relation to the effectiveness of area expansion in the discussion of the divergent combustors.

As separation is now predicted by the cycle analysis, an additional parameter c_{f_o}, which is the skin friction at the point of separation, now becomes an influential parameter as c_{f_o} affects both the shape of the pressure profile through the shock train and the predicted point of separation. For the value for c_{f_o} of 0.0015 (as determined from the boundary layer analysis code) the cycle analysis predicts a shock train that fits the experimental data reasonably well for both the $\phi = 0.76$ and $\phi = 0.86$ cases, consider-

ing the gaps between the sensors. In both cases the computed pressure profile lies very close to the pressure measured at the front edge of the combustor at 0.32 m. The separation points for both these cases are predicted to be just inside the instrumented section of the isolator, with the separation point for the $\phi = 0.86$ case slightly upstream of the $\phi = 0.76$ case. These predicted separation points are both upstream of where separation is actually occurring in the experiments, which for both cases lies somewhere in the un-instrumented region between the sensors in the isolator and the front edge (FE) pressures sensors located at 0.32 m. Considering the limitations of one-dimensional modelling this is a good fit of the experimental data which involves separated flow.

The last of the moderately separated cases presented is the $\phi = 0.94$ case and is shown in Figure 5.6. This is the lowest equivalence ratio at which there was a reduction in the combustion efficiency. Here, as the equivalence ratio is increased from 0.86 to 0.94, the combustion efficiency reduces from 100% for the previous case to 94% for this case. The criterion for finding the combustion efficiency for the constant area combustor in the optimisation procedure was by fitting the computed profile to the pressures measured at the very end of the combustion chamber. One small anomaly to note is the slight increase in the mixing-length parameter x_{fe_1} from 0.45 for the previous case to 0.5 for this case. This change is small and could be attributed to the slight changes in the inflow conditions between the two shots as each case in the cycle analysis uses the computed test flow conditions specific for that shot. The Mach number profile for this case is slightly different than for the attached case of Figure 5.3. Instead of a gradual reduction in Mach number along the isolator followed by a rapid drop as combustion initiates, there is an additional reduction in Mach number through the shock train. This Mach number begins at 3.52 at the leading edge of the shock train but reduces to 2.50 by the injection point. By the end of the duct the Mach number has been driven down to 1.27.

Highly separated cases

As presented in the Chapter 4, for the constant area combustor as the equivalence ratio increases to just above the stoichiometric ratio the separation increases in scale and a pressure rise is now detected by the isolator sensors. These cases are termed 'highly separated'. Figure 5.7 presents the cycle analysis for the lowest equivalence ratio for the set of these cases, which was at an equivalence ratio of 1.06. The initial trend in decreasing combustion efficiency continues as the fuelling rate is increased from lean

to slightly rich. Here the combustion efficiency has fallen from 94% at $\phi = 0.94$ to 87% at $\phi = 1.06$ and x_{fe_1} has reduced from 0.5 to the earlier value of 0.45.

For this case, as the shock train is further forward inside the isolator, there is now more than a single elevated pressure measurement along the shock train. This provides data on the pressure gradient through the initial portion of the shock train, which can be compared with the profile from the cycle analysis. Again, the profile predicted by the cycle analysis fits the experimental data reasonably well.

The computed pressure profile lies very close to the FE measurement and though it under predicts the raised pressures further upstream in the isolator, the separation point is predicted fairly well. The code places the separation point 0.249 m from the leading edge or $1.81D_{iso}$ ahead of the injectors. This is close to the location of the furthest upstream isolator pressure sensor where the pressure is elevated (in this case this is DB7 which is located at 0.255 m from the leading edge).

At the point of separation the predicted pressure gradient is not as large as that indicted by the experimental data. This suggests a higher value for c_{f_o}. However the profile from the cycle analysis represents the one-dimensional averaged pressure across the entire cross section of the engine, and for the experiment such an averaged pressure in the shock train region may be less than that measured at the wall by the pressure sensors.

Shown in the area distribution at the top of the plot is the area of the core flow as predicted by the cycle analysis. For this case the cross-sectional area of the core flow is at its minimum at a distance of 0.310 m from the leading edge and the size of this core area represents 52.8% of the isolator cross-sectional area. This corresponds to a diameter for the core flow of $0.82D_{iso}$ which leaves $0.18D_{iso}$ for the separation. As the separation is in the form of an annulus, the height of the separation is $0.09D_{iso}$ (or $0.18R_{iso}$). This illustrates the additional compressibility of a circular duct, compared with a rectangular duct, where the separation height is approximately 20% of the radius but represents nearly half of the cross-sectional area.

A second highly separated case is presented in Figure 5.8. As the fuelling rate is further increased the separation moves further forward into the isolator as observed in the experiments. For this case, which has a larger separation region than the previous

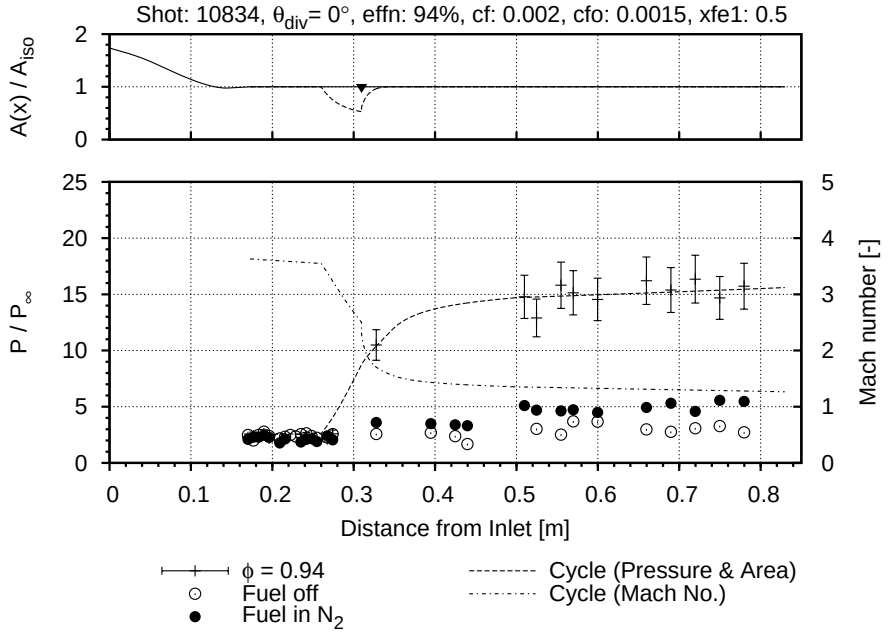

Figure 5.6: Cycle analysis result of a third separated case for the constant area combustor (ϕ = 0.94).

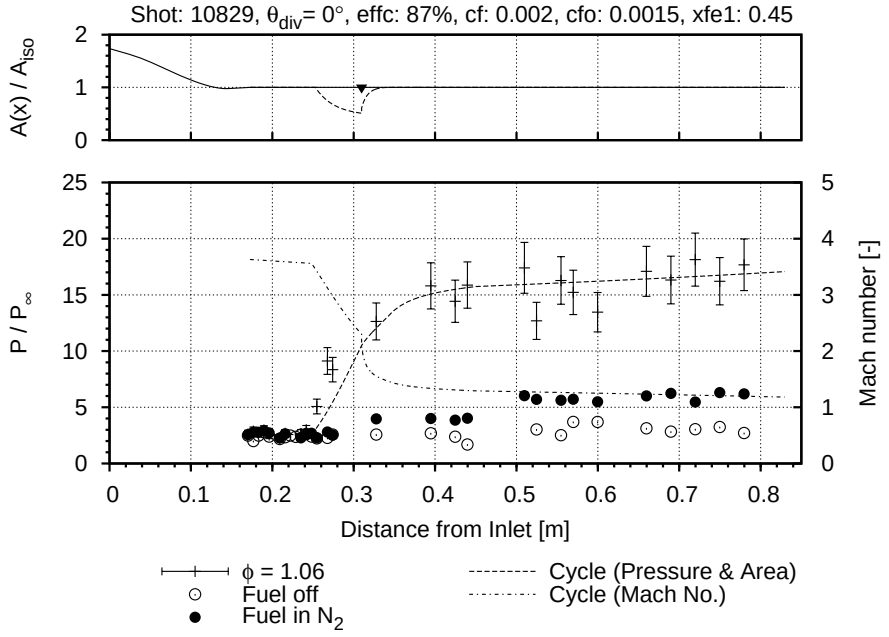

Figure 5.7: Cycle analysis result of a highly separated case for the constant area combustor (ϕ = 1.06).

case, there is a further reduction in the value for x_{fe_1} from 0.45 to 0.4 indicating further enhancement in combustion from the longer shock train. Again, the general pressure profile of the shock train from the cycle analysis compares well with the measurements from the experiment, although the pressures are again underpredicted through the initial portion of the shock train. This is despite the separation point being predicted just 3 mm downstream of the point indicated by the experimental result. As previously mentioned, these discrepancies are attributed to the one-dimensional nature of analysis.

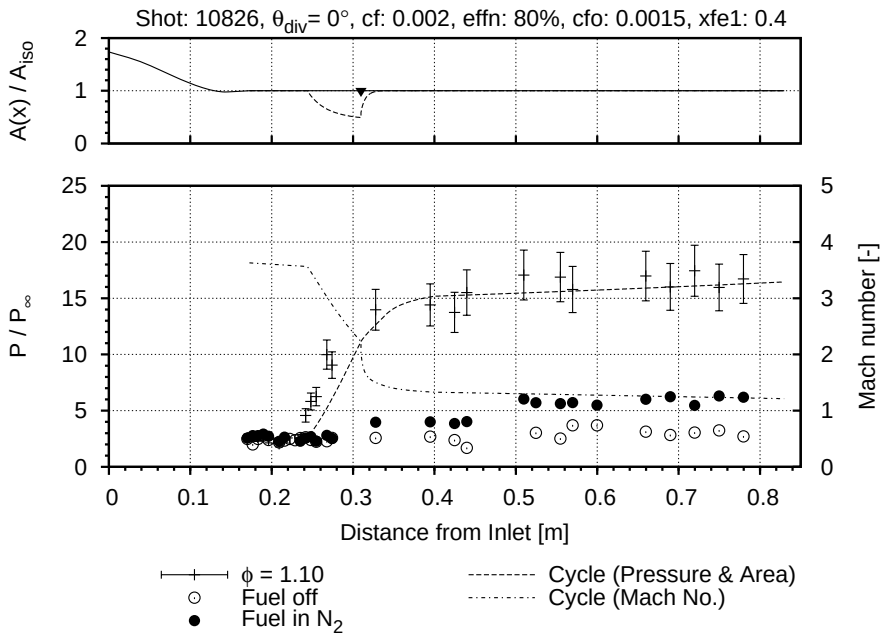

Figure 5.8: Cycle analysis result of a highly separated case for the constant area combustor (ϕ = 1.1).

Maximum fuelling rate

The result from the highest fuelling case for the constant area combustor is presented in Figure 5.9. The exit pressures are matched well by the cycle analysis giving a combustion efficiency of 60%. However for the pressures through the shock train, the discrepancy between the experiment and the cycle analysis as to the location of the separation has grown from the previous case. This adds to the growing trend of underprediction by the cycle analysis of the pressures through the shock train. As can be seen in the Mach number distribution for this case, the combustor exit Mach number is 1.16 which highlights that the engine is operating with little margin from the choked condition.

The exacerbation of the discrepancy between the cycle analysis and the experiment at this maximum fuelling case may be due to an increased sensitivity of the cycle analysis to the inflow conditions now that the engine is operating very close to the choked condition. Thus any differences between the computed and true freestream properties would have a greater influence on the result. This is supported by the results from the optimisation (Appendix E.1.4) where it is found that, for certain cases, the modelling of the shock train is very sensitive to inflow conditions when the separation is large and the Mach number is close to unity at the exit. At these conditions a small change in the Mach number of the inflow of only a few percent results in a large change in the shock train size and position. This is also true of $\eta_{c,f}$ where only a fractional change of a percentage point ($\approx$ 0.2%) results in a large change in the shock train position. Considering the uncertainties in the inflow conditions, the accurate prediction of the shock train size and position of these highly separated cases close to the choke limit may be outside the capabilities of current quasi one-dimensional modelling methods.

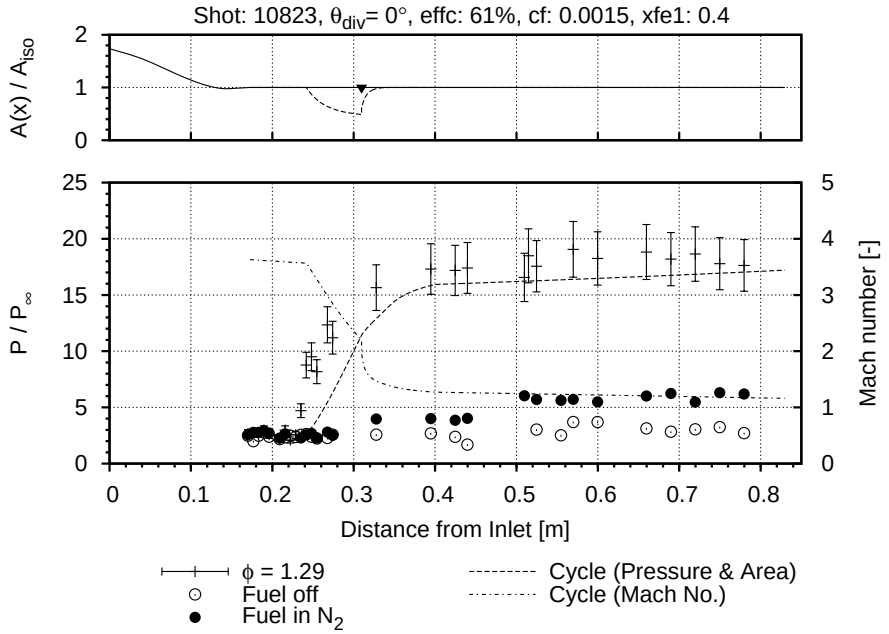

Figure 5.9: Cycle analysis result for the maximum fuelling of an established flow for the constant area combustor (ϕ = 1.29).

5.2.2 2° divergent combustor

The results from the cycle analysis of the 2° divergent combustor are presented next. Example results for each category (fuel-off, combustion-suppressed, non-separated, separated, highly separated and maximum fuelling case) are presented together in Figure 5.10. For the combustion cases, the similarities and differences between the constant area combustor and 2° divergent combustor for the parameters of interest (ϑ, $\eta_{c,f}$ and x_{fe_1}) are identified and discussed.

Fuel-off and combustion-suppressed cases

As with the constant area combustor, the results from the cycle analysis match the measured pressures for the fuel-off and combustion-suppressed cases well (see Figures 5.10a and 5.10b). There is a reasonable fit of the computed pressure profile to the pressure measurements along the constant area section of this combustor for both the fuel-off and combustion-suppressed cases. Importantly, the pressures in the divergent section are also predicted well, for both the fuel-off (Figure 5.10a) and combustion-suppressed cases (Figure 5.10b), with the pressure measurements in the divergent section scattered either side of the cycle analysis result.

Mixing rate parameter (ϑ)

No difference was found between the constant area combustor and the 2° divergent combustor for ϑ with a value of 10 again giving the best fit for the non-separated combustion cases. This is expected as the fuel injection system is the same for all engine configurations and the initial mixing rate, for the non-separated cases, is dominated by the fuel jet interaction with main flow. With $\vartheta = 10$, the combustion efficiency reaches 90% of its final value by the mid point of the combustion chamber. As the mixing and combustion is mostly complete by the divergence point, the downstream divergence is expected to have little to no affect on ϑ.

Combustion efficiency ($\eta_{c,f}$)

Similar performance in combustion efficiency was found for the 2° divergent combustor as for the constant area combustor at comparable ϕ. Again, there is complete consumption of the fuel at low ϕ with $\eta_{c,f} = 100\%$ and $\eta_{c,f}$ reduces as ϕ increases through and above the stoichiometric ratio.

The combustion efficiency was determined for the divergent combustors in a similar method to the constant area combustor. For this combustor, the combustion efficiency was first adjusted until the peak pressure along the constant area section, upstream of the divergence, matched well with the measurements. However, the two divergent combustors impose an additional constraint on the cycle analysis in relation to the combustion efficiency than does the constant area combustor. This constraint is that the measurements in the divergent section of a divergent combustor also provides a bound to the upper limit for $\eta_{c,f}$ such that the computed pressure profile also needs to fit the measurements taken along that section.

The first fuelled case presented, shown in Figure 5.10c, is for a non-separated case where $\eta_{c,f} = 100\%$. Overall there is a good match of the pressures along the constant area section between the results from the cycle analysis and the experiment. However the predicted pressures in the divergent section are towards the higher measurements taken in the experiment. For fuelling rates up to $\phi = 0.93$ (Figure 5.10d) the combustion efficiency remains at 100%, however even at this maximum permissible value for $\eta_{c,f}$ the cycle analysis underpredicts the pressures in the constant area section. This same issue was encountered for the constant area combustor at similar ϕ's. For the case of this divergent combustor, this underprediction in the constant area section still results in a general overprediction in the divergent section. For higher values of ϕ at and above the stoichiometric ratio the combustion efficiency begins to fall for this divergent combustor as it did for the constant area combustor; for example $\eta_{c,f} = 85\%$ for the $\phi = 1.03$ case, which is the highly separated case (Figure 5.10e) and $\eta_{c,f} = 65\%$ for the $\phi = 1.26$ case, which is the maximum fuelling case (Figure 5.10f). For this last case, the competing constraints imposed on fitting the cycle analysis result to the experimental measurements are most evident. In Figure 5.10e, the pressure profile predicted by the cycle analysis is below the measured pressure through the constant area section of the combustor and above the measured pressure in the divergent section.

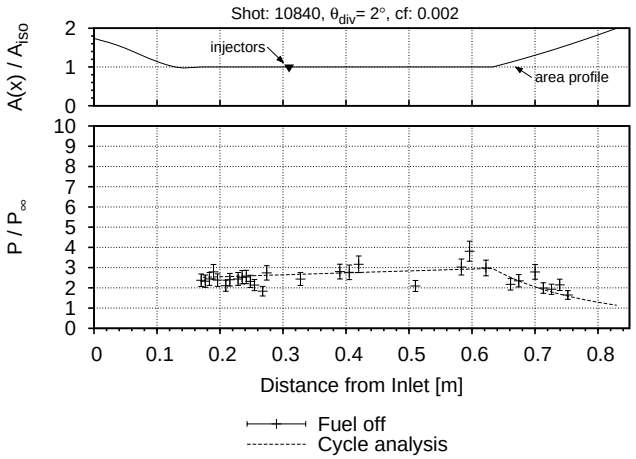

(a) Fuel-off case

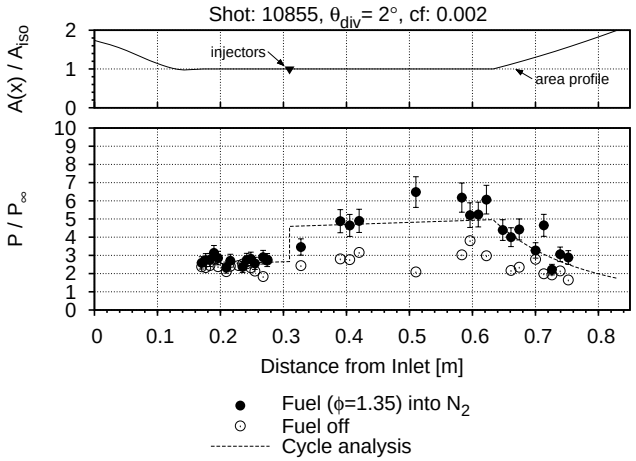

(b) Combustion-suppressed case

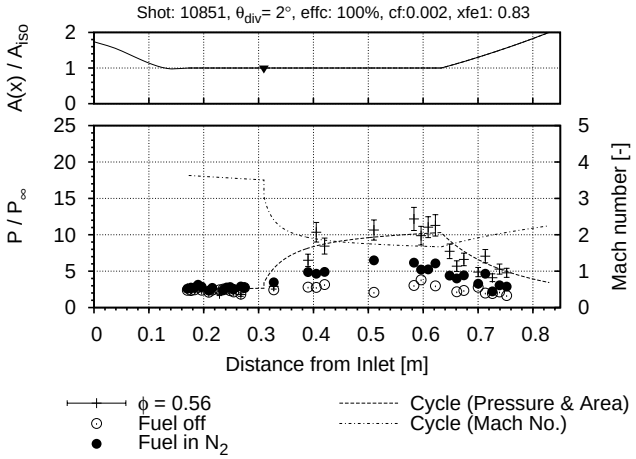

(c) Non-separated case

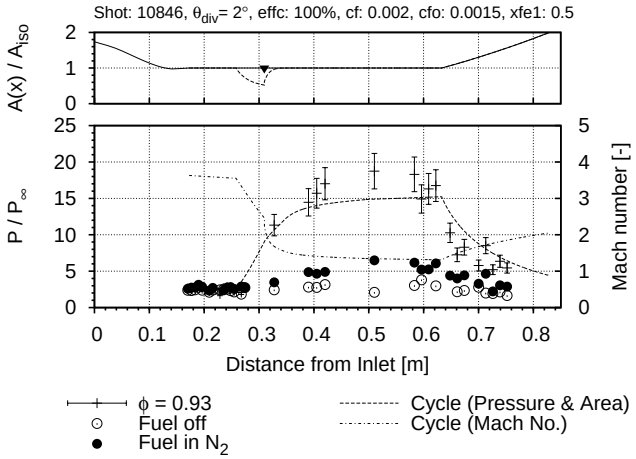

(d) Moderately separated case

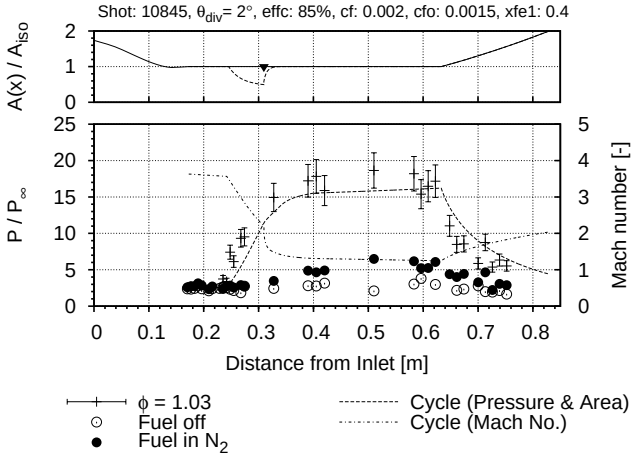

(e) Highly separated case

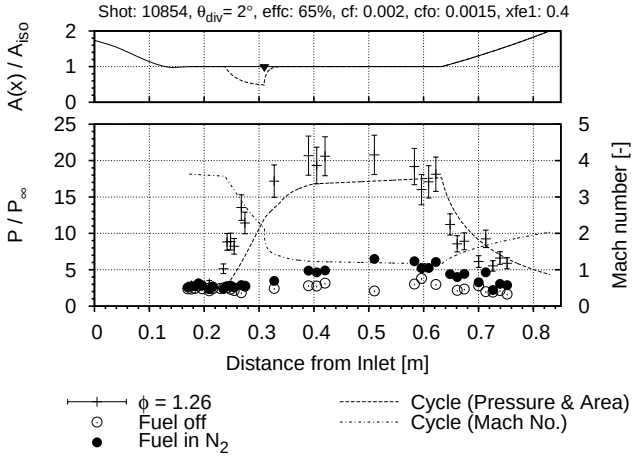

(f) Maximum fuelling case

Figure 5.10: Cycle analysis results of key cases for the 2° divergent combustor

For all the fuelled cases, this general over prediction of the pressure trend in the divergent section of this combustor is consistent with findings by others. Razzaqi (2011) found when employing one-dimensional analysis to expansion surfaces of a scramjet engine, namely the exhaust nozzle, that cycle analysis tends to overpredict the pressures in those sections. This discrepancy between the results from the cycle analysis and the experiment was attributed to a limitation of the one-dimensional analysis, that it is not able to model the multi-dimensional features and their specific effects, as opposed to an over-estimation of the combustion efficiency (Razzaqi, 2011, pg. 105-106).

Point of combustion completion (x_{fe_1})

For the combustion length, very similar trends in x_{fe_1} which are found for the constant area combustor are also found for the 2° divergent combustor. For the non-separated cases (Figure 5.10c) the combustion length ($x_{fe_1} = 0.83$) is long. For the separated cases (Figure 5.10d) there is a large shortening of the combustion length ($x_{fe_1} = 0.5$). For the separated cases there is a further shortening of the combustion length ($x_{fe_1} = 0.4$) as the shock train increases in scale with increasing ϕ (Figure 5.10f). These findings indicate that the mixing characteristics between these two combustors are similar and also that the pressure relief from the area expansion for this divergent combustor has little effect on the critical pressure for separation.

Separation characteristics

Similar characteristics of the separation are found for the 2° divergent combustor as are found for the constant area combustor. For the first of the separated cases, Figure 5.10d, the separation point predicted by the cycle analysis is located at $X = 0.243\,\text{m}$. Again, this is ahead of the point of separation indicated in the experiment which lies between the last sensor in the isolator ($X = 0.274\,\text{m}$) and the FE sensors ($X = 0.327\,\text{m}$).

For the first of the highly separated cases (Figure 5.10e) again there is a reasonable fit, however for the other highly separated case (Figure 5.10f), which is at the highest fuelling rate and where the separation observed in the experiment is the largest, the fit between the result from cycle analysis and the experiment deteriorates. In this case the pressure through the shock train is well underpredicted by the cycle analysis.

The similarity of the shock train characteristics between these two combustors is reflected in the dimensions of the separation region. For the better match of the two highly separated cases presented (Figure 5.10e), where $\phi = 1.03$, the separation point is predicted at $X = 0.243$ m. This is quite close to the separation point predicted for the constant area combustor at a similar fuelling rate, which for $\phi = 1.06$ is at $X = 0.249$ m. For the 2° divergent combustor the core area is smallest at $X = 0.310$ m at a value of $0.523A_{iso}$. Again, these values are close to those found for the constant area combustor at $\phi = 1.06$ where the core flow was smallest at a value of $0.528A_{iso}$ located at 0.310 m from the leading edge.

The size of the shock train predicted by the cycle analysis for the 2° divergent combustor is similar to that predicted for the constant area combustor at similar ϕ. This is consistent with the observations from the experiments. The results from the cycle analysis gives some indication as to why this is the case. For the separated cases of the 2° divergent combustor, the cycle analysis calculates the reattachment point to be located just downstream of the injection point. For example, the cycle analysis calculates the location of the reattachment point to be at 0.335 m for the moderately separated case ($\phi = 0.93$) and to be at 0.338 m for both the highly separated and maximum fuelling cases. These reattachment points are less than $0.9D_{iso}$ downstream of the injectors which are located at 0.310 m and they are also far upstream ($\approx 9D_{iso}$) of the divergent point for this combustor, which is located at 0.633 m. For the separated cases the point at which combustion has completed is also far upstream of the divergent point. For these cases x_{fe_1} is located between 0.4 m to 0.5 m. This explains why there is a no appreciable effect on the shock train from the area divergence. For the constant area combustor the peak pressure is at the very end of the combustor, as expected for supersonic combustion. However the majority of the pressure rise from combustion occurs between 0.310 m (the injectors) and 0.5 m (x_{fe_1}). The additional pressure rise from this point onwards is from the displacement effect of the growing boundary layer. For the 2° divergent combustor, as the divergent point is located downstream of x_{fe_1}, the pressure relief which comes from the expansion in area reduces the peak pressure for that combustor by only the amount that the growth in the boundary layer would have added if the area were held constant. As this is a small contribution to the total pressure rise across the combustor, the difference in peak pressure between the 2° divergent combustor and the constant area combustor is minor. Additionally, as the shock train length is driven by the peak pressure (Waltrup and Billig, 1973), then the small reduction in peak pressure due to the area expansion for the 2° divergent combustor has

only a minor effect on the shock train length. Consequently, there will be a narrow band of ϕ where separation would occur in the constant area duct but not in the 2° divergent combustor. This is possibly not captured in the experimental results given the increments of ϕ at which these experiments were conducted. Additionally, variations between the flow conditions between shots, independent of the corollary change in ϕ, may dominate the critical conditions for separation over any controlled changes in ϕ.

In summary, the values for ϑ, x_{fe_1} and $\eta_{c,f}$ for the 2° divergent combustor were found to be similar to those found for the constant area combustor. For ϑ, which controls the rate of mixing, the value of 10 was found to be same for both the constant area and 2° divergent combustors. This suggests that the mixing/combustion characteristics through initial portion of combustion curve are similar for these combustors. As the injection system is common for all three combustor configurations, the same or very similar values for ϑ are expected. This is because ϑ is determined from the non-separated cases and in these cases the interaction of the fuel jet with the main flow will dominate the initial mixing rate. For the 2° divergent combustor, again there was a large reduction in x_{fe_1} from the non-separated cases to the separated cases. The values for x_{fe_1} for both the non-separated and separated cases were similar for the 2° divergent combustor to those for the constant area combustor. The cycle analysis also reveals that the area expansion for this divergent combustor has no appreciable effect on the $\eta_{c,f}$. In general, the results from the cycle analysis through the separated region fitted reasonably well to the experimental results. As was found for the constant area combustor, the cycle analysis for the 2° divergent combustor, predicted the separation point reasonably close to the experiment but underpredicted the pressure through the separation. The characteristics of the separation from the cycle analysis, in terms of size and position, were again similar between the 2° divergent and the constant area combustors at similar ϕ. This is not all that surprising as the predicted reattachment point, as well as the point where combustion had completed (x_{fe_1}), were both far upstream of the divergence point for all the separated cases.

5.2.3 1° divergent combustor

The results from the cycle analysis for key cases of the 1° divergent combustor are presented together Figure 5.11. The specific findings for the performance parameters for this combustor are presented briefly below, with an in-depth discussion of the findings for all three combustors left to Section 5.2.5.

Fuel-off and combustion-suppressed cases

The fuel-off and combustion-suppressed cases for the 1° divergent combustor are shown in Figure 5.11a and Figure 5.11b respectively. As before for the previous combustors, for both these test cases there is a reasonable match between the results from experiment to those from the cycle analysis. For the 1° divergent combustor the divergence commences further upstream than for the 2° divergent combustor, although this divergence is more gradual and both these aspects are captured in the pressure profile from the cycle analysis.

Mixing rate parameter (ϑ), combustion efficiency ($\eta_{c,f}$) and mixing-length (x_{fe_1})

The same methodology used to determine the parameters ϑ, $\eta_{c,f}$ and x_{fe_1} for the 2° divergent combustor was used for the 1° divergent combustor. The non-separation case (Figure 5.11c) was used again to find the value for ϑ which is unchanged from the previous two combustors at a value of 10.

As was found for the 2° divergent combustor, the measured pressures at the front edge and in the constant area section of this combustor imposes a lower bound on the $\eta_{c,f}$ whereas the pressure in the divergent section imposes an upper bound; the final value for $\eta_{c,f}$ is the compromise between these two bounds. For the 1° divergent combustor, the trends found in $\eta_{c,f}$ for an increasing ϕ follow closely those trends found for the previous two combustors. For lean mixtures where ϕ is below 0.9 the combustion efficiency is 100%. At and above $\phi = 0.9$, the combustion efficiency declines with increasing ϕ. For example, the result shown in Figure 5.11e, $\eta_{c,f}$ is down to 90% when $\phi = 0.95$. Again, this is similar to the values found for $\eta_{c,f}$ for the previous two combustors at similar ϕ's, which were 94% at $\phi = 0.94$ for the constant area combustor and 100% at $\phi = 0.93$ for the 2° divergent combustor. This favourable agreement

between the three combustors continues up to the maximum fuelling case shown in Figure 5.11f. For the 1° divergent combustor $\eta_{c,f} = 65\%$ at $\phi = 1.2$, which compares well with 65% for the 2° divergent combustor at $\phi = 1.26$ and 61% for the constant area combustor at $\phi = 1.29$.

Very similar values for x_{fe_1} are found for this combustor for the key cases to those found for the previous two combustors with $x_{fe_1} = 0.83$ m for the non-separated cases, followed by a step change to between 0.4 m to 0.5 m for the separated cases.

5.2.3.1 Separation Characteristics

Similar characteristics relating to the separation are found the 1° divergent combustor as are found for the constant area and 2° divergent combustors. For the moderately separated case (Figure 5.11d) the separated point predicted by the cycle analysis, which lies inside the instrumented section of the isolator, is again slightly fore of the point indicated by the pressure profile from the experiment, which is between the last sensor in the isolator and the next set of sensors around the front edge of the combustor. For the two highly separated cases (Figure 5.11e and Figure 5.11f), which includes the maximum fuelling case, the separation predicted by the cycle analysis matches the separation point indicated by the experimental result reasonably well. However the pressures through the separation are again underpredicted.

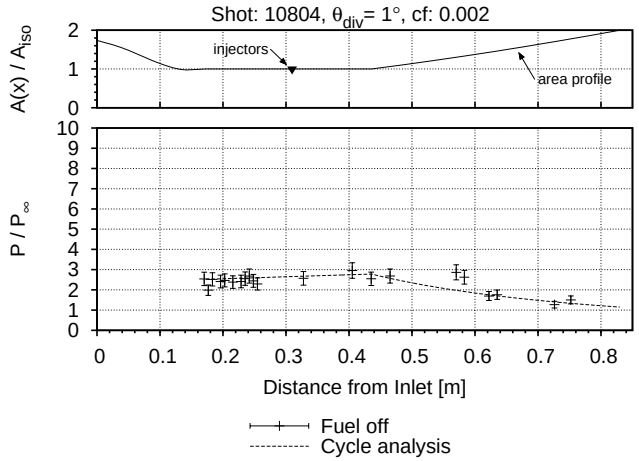

(a) Fuel-off case

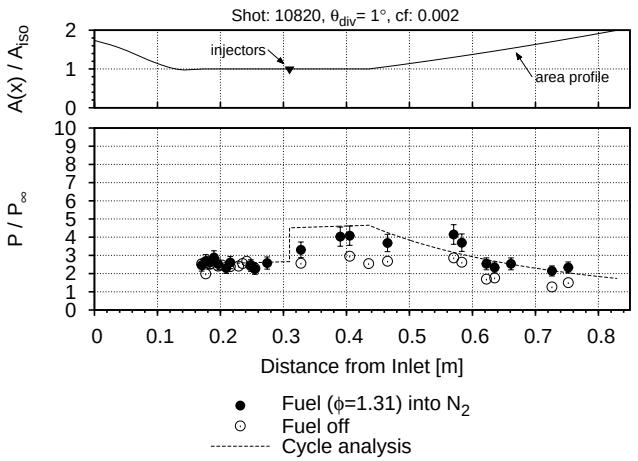

(b) Combustion-suppressed case

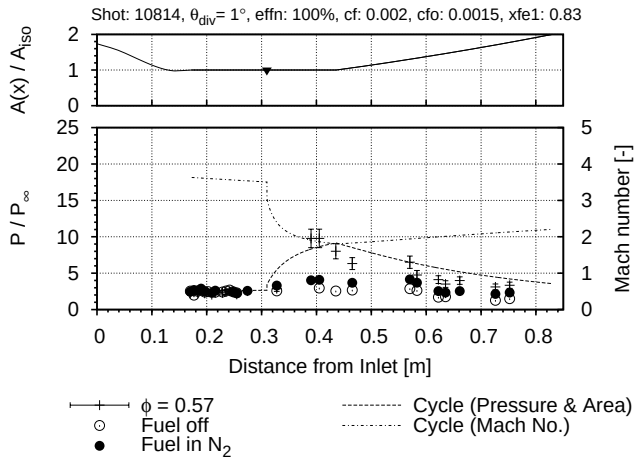

(c) Non-separated case

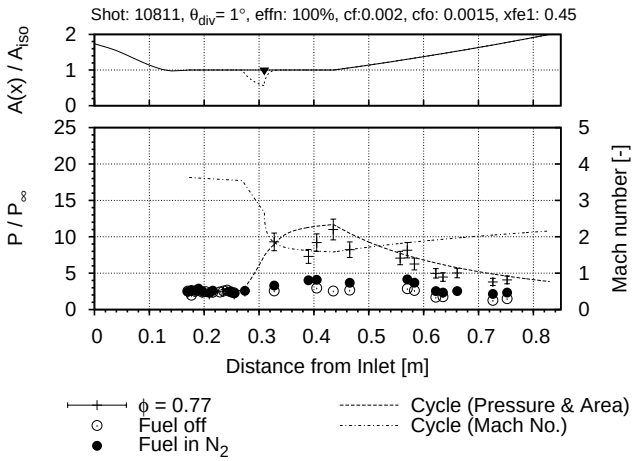

(d) Separated case

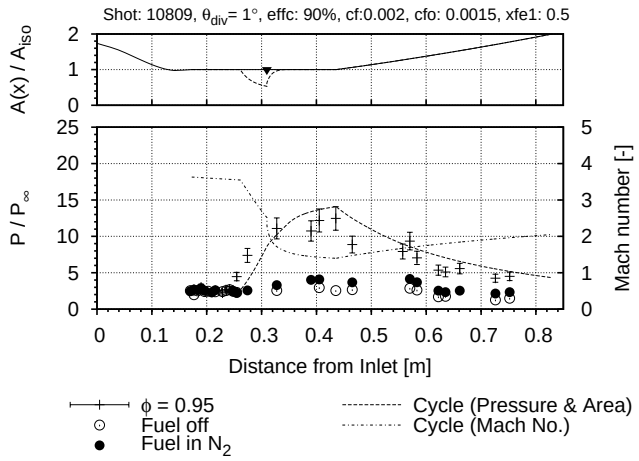

(e) Highly separated case

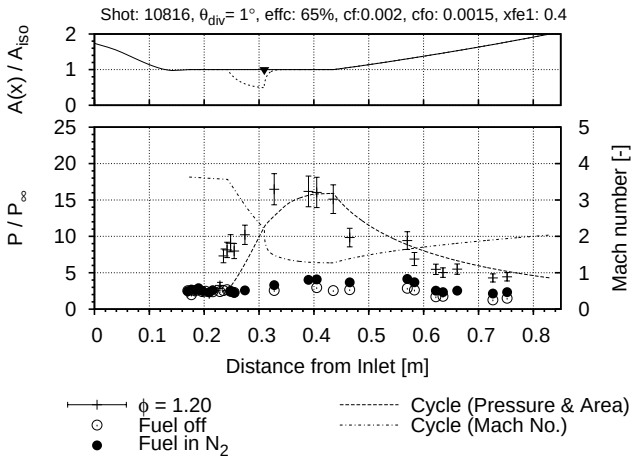

(f) Maximum fuelling case

Figure 5.11: Cycle analysis results of key cases for the 1° divergent combustor

5.2.4 Separation characteristics and key Mach numbers

Tables 5.1 and 5.2 lists the values from the cycle analysis relating to the separation and to the key Mach numbers respectively for each of the three combustors at $\phi = 0.94 \pm 0.01$. Despite some variation of the combustion efficiencies for the three cases selected, the separation is quite similar for all three combustors in terms of both the separation point and of the size of the core flow at its minimum value. The reattachment point is slightly upstream for the constant area combustor than for the two divergent combustors. This parameter is key as it is located well upstream of the divergent point for both the 2° and 1° divergent combustors, which respectively are 0.633 m and 0.436 m.

As expected, the longer the constant area section of the combustor the lower the minimum Mach number. For the constant area combustor the minimum Mach number is at the combustor exit whereas for the divergent combustors the minimum Mach numbers occurs at the divergence point. The exit Mach number for the two divergent combustors are quite similar being within ± 0.02, with the 1° slightly higher. Similar exit Mach numbers for the divergent combustors are expected as the combustion is completed within the constant area section of both these combustors and so the combustion part of the thermodynamic cycle is the same for each combustor. As such the flow entering the divergent section of both combustors is similar in state and, as both combustors have the same exit area, the non-combusting flow is expanded up to a similar Mach number in the 1-D code.

Table 5.1: Key values relating to the separation from the cycle analysis for the three combustors at similar equivalence ratios. Stream-wise distances are referenced from the leading edge of the model. N.B. The location of the injectors were at 0.309 m and the location of the divergent points for the 2° and 1° divergent combustors were 0.633 m and 0.436 m respectively.

Combustor	ϕ	$\eta_{c,f}$	x_{fe_1}	Separation point	Reattachment point	Core flow area (min.)	Core flow diameter (min.)	Separation height (max.)
	-	-	[m]	[m]	[m]	$[A_{iso}]$	$[D_{iso}]$	$[D_{iso}]$
Const. A.	0.94	94%	0.50	0.261	0.334	0.528	0.820	0.0899
2°	0.93	100%	0.50	0.259	0.344	0.523	0.816	0.0921
1°	0.95	90%	0.50	0.262	0.344	0.532	0.823	0.0886

Table 5.2: Key Mach numbers from the cycle analysis for all three combustors at similar equivalence ratios.

Combustor	ϕ	$\eta_{c,f}$	x_{fe_1}	Min. Mach number	Exit Mach number
	-	-	[m]	-	-
Const. A.	0.94	94%	0.50	1.27	1.27
2°	0.93	100%	0.50	1.31	2.05
1°	0.95	90%	0.50	1.40	2.09

5.2.5 Trends in combustion efficiency, air-based combustion efficiency and mixing-length

The key performance parameters from all of the cycle analysis results for the three combustors are plotted in Figures 5.12 to 5.14. The first plot, Figure 5.12, shows $\eta_{c,f}$ versus ϕ which illustrates the trends observed in reviewing the individual plots successively in Sections 5.2.1 to 5.2.3. Figure 5.12 shows that $\eta_{c,f}$ is 100% for lean mixtures up to around $\phi = 0.85$ for all combustors, after which there is a steady decline as ϕ increases through and above unity. From this plot it is also clear that little to no difference exists between the three combustors for this performance parameter.

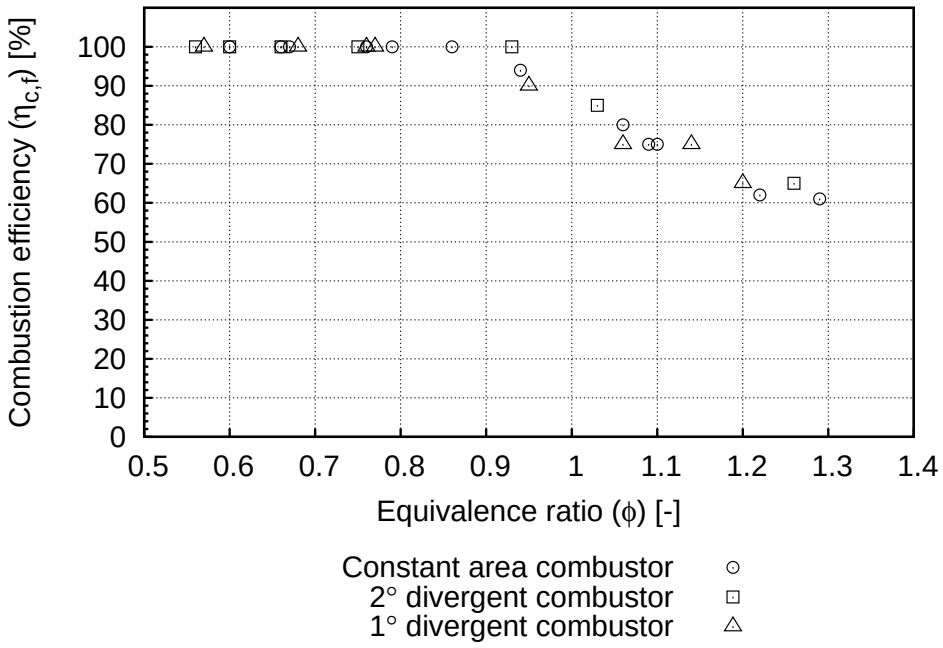

Figure 5.12: Combustion efficiency ($\eta_{c,f}$) versus equivalence ratio (ϕ) for all three combustors.

Whereas ϕ is the quantity of fuel injected as a fraction (or multiple) of the stoichiometric quantity, not all of this fuel is consumed if $\eta_{c,f}$ is less 100%. To determine the fraction of the stoichiometric quantity of fuel which was actually consumed, the term $\eta_{c,tot}$ is multiplied by the equivalence ratio ϕ to give the parameter η_{air}. This is referred to as the 'air-based combustion efficiency', however it is also sometimes referred to as the 'effective combustion efficiency' (ϕ_{eff}) (Kirchhartz, 2009). This parameter represents the fraction of the air that was consumed in combustion by the end of the combustor. While the injected equivalence ratio ϕ can be higher than one, the air-based combustion efficiency η_{air} must be less than or equal to one.

The parameter η_{air} is calculated across the full range of fuelling conditions for all three combustors and is presented in Figure 5.13. Obviously, for values of ϕ where $\eta_{c,f}$ is 100% there will be a direct relationship between η_{air} and ϕ, as is the case in Figure 5.13 for ϕ between 0.5 and 0.9 for all three combustors. For ϕ above 0.9, at around stoichiometric levels, the trend in η_{air} reaches an upper limit of around 80-85% for all three combustors. Beyond this point, for rich fuelling, there is a levelling off, if not a decline, as combustion becomes limited by mixing. These trends appear due to the following reasoning. At low ϕ the combustion efficiency will not be significantly limited by mixing as a small quantity of fuel can mix readily with the air around the circumference where it is injected. However as ϕ increases then $\eta_{c,f}$ begins to decline at fuelling rates near stoichiometric levels as the fuel is unable to penetrate and mix sufficiently with the remaining unconsumed air at the very centre of the duct. In these circumstances the combustion is considered to have reached the limit to which the fuel can adequately mix with the air. Above stoichiometric levels, any additional fuel actually becomes a hindrance to performance as large regions exist where the mixture is too rich for combustion to occur and this prevents the air in those regions from being consumed. This is evident in the slight decline in η_{air} for $\phi \geq 1$.

The third of these summary plots, Figure 5.14, shows the mixing length (x_{fe_1}) versus ϕ. It is clear in Figure 5.14 that the behaviour of x_{fe_1} is very similar for all three combustors, which supports the general finding from the review of the individual cycle analysis results. At the lower fuelling conditions, for ϕ between 0.55 and 0.65, x_{fe_1} is at the very end of the combustor at 0.83 m. Beyond this point, for ϕ between 0.65 to 0.95, there is step reduction in the x_{fe_1} from 0.83 m to 0.45 m as the mode switches from attached flow throughout to separated flow. As fuelling is further increased from lean to rich, x_{fe_1} reaches an asymptote of 0.4 m for all cases.

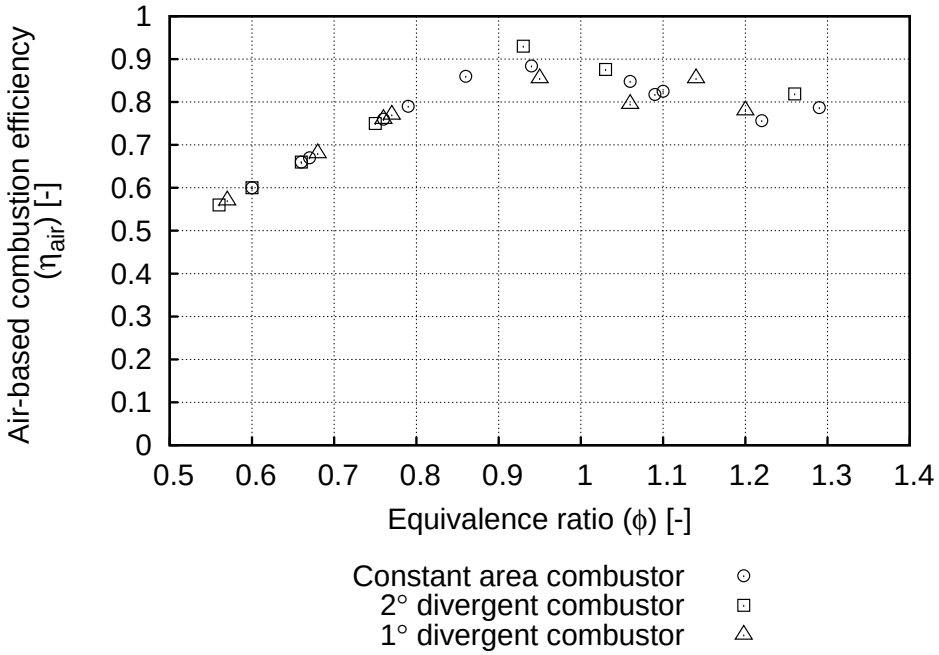

Figure 5.13: Air-based combustion efficiency (η_{air}) versus equivalence ratio (ϕ) for all three combustors.

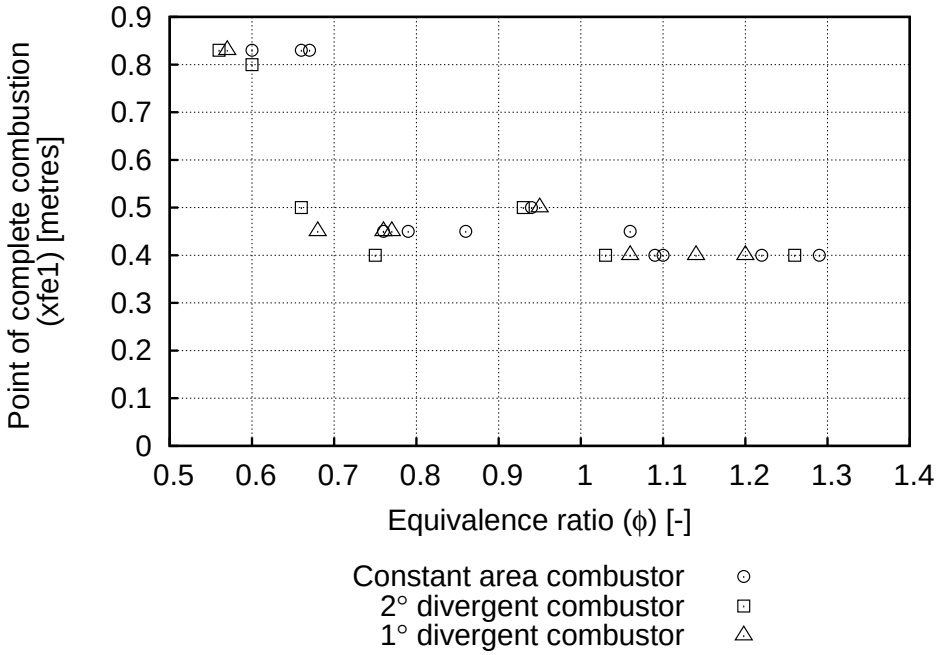

Figure 5.14: Point of complete mixing (x_{fe_1}) versus equivalence ratio (ϕ) for all three combustors.

It should also be noted that adjusting the parameter x_{fe_1} also changes the 'effective' ϑ as $\eta_c(X, \vartheta)$ is a function of X which has x_{fe_1} as a variable. Shortening the mixing-length means that mixing is occurring over a shorter length and this results in a higher mixing rate (mixing per unit length) for a given ϑ. Although the decision has been taken to manipulate the parameter x_{fe_1} the parameter ϑ could have equally been chosen. In fact, it was found that by fixing x_{fe_1} at the end of the combustor and adjusting ϑ above 10, the conventional limit for scramjets, that this had a similar effect on the scale of the predicted separation as did reducing x_{fe_1} (see Figure E.2d in Appendix E.1.1). Using values above 10 for ϑ is not unreasonable given that the source of the conventional range of ϑ of 1 to 10 for scramjets (Heiser and Pratt, 1994, p.348) notes that for ramjets higher values for ϑ of 40 to 50 are applicable. Considering that dual-mode scramjets operate with a mixture of supersonic and subsonic flow, then it could be argued that the value of ϑ may be higher than the value accepted for conventional scramjets (i.e. a scramjet operating in pure scramjet mode). A comparison of the effects of these two parameters ϑ and x_{fe_1} on combustion efficiency curves is presented in Appendix E.2. Nonetheless, regardless of the parameter varied, x_{fe_1} or ϑ, the general conclusion is the same. That is, for separated flow more rapid combustion through a higher rate of mixing is required in the 1-D analysis in order to predict a separation of the same scale and position as observed in the experiments. As such, for the purposes of the analysis in this research x_{fe_1} is selected as the single parameter relating to mixing which is to be manipulated and ϑ is fixed at a value of 10.

The relationship between x_{fe_1} and ϕ suggests that once separation occurs it has a substantial effect on mixing and combustion, which could almost be characterised as acting like a switch (on/off). In truth, the adjusting of the parameter x_{fe_1} in the cycle analysis is manipulating the region over which the heat released from combustion is distributed along the engine. This enhancement is most likely from enhanced mixing due to the presence of the shock train. Additionally, the kinetics of combustion would also be enhanced as the shock train provides additional compression which would raise the pressure and temperature of the incoming flow to the combustor. From this finding it can be concluded that for the accurate prediction of the position and scale of a pre-combustion shock train, in addition to determining the proportion of the fuel that is burnt, the distribution of the heat release also has an important role. For a given η_{air}, burning that occurs more rapidly and further upstream in a combustor causes a larger shock train. This suggests that in order for shock trains to be predicted accurately it necessary to model well the coupling between the mixing and the pre-combustion shock train.

Although a large degree of uncertainty accompanies any specific value determined using the approach presented in this chapter for the parameters investigated here, namely $\eta_{c,f}$, η_{air} and x_{fe_1}, which is due to the compounding uncertainties from the experiment and from the assumptions of the one-dimensional model, these uncertainties are largely systematic, which apply to all cases fairly equally and as such general trends can still be drawn from these results.

5.3 Summary and Conclusions

This chapter presents results from the cycle analysis code *DMCycle* as applied to the experimental results in Chapter 4. This code is based on the classical quasi-one-dimensional flow equations from Shapiro (1953) with a separated flow model from Ortwerth (2000). For each case examined the isolator inflow conditions were calculated using a combination of analytical and numerical methods namely *ESTCj*, *NENZF* and *CFD++*. These isolator entrance conditions, along with fuelling conditions for the experiments, form the flow inputs for the cycle analysis code. Estimations for the parameters relating to skin friction coefficients, c_f and c_{f_o}, were based on measurements from an experiment at a similar condition and calculations from a boundary layer code respectively. The following parameters were selected as the parameters of interest: combustion efficiency $\eta_{c,f}$, mixing profile parameter ϑ and point of complete combustion x_{fe_1}. These parameters were varied manually through a reasonable range until an optimal fit was found.

From the lean cases, where there was no separation of flow, the value for ϑ is equal to 10 for all three combustors, indicating that the size and 90° angle of the porthole injectors produced rapid initial mixing and combustion.

For lean mixtures, where $\phi < 0.9$, the combustion efficiency is at the maximum of 100% for all combustors. As ϕ is increased above 0.9 through unity, there was a corresponding, almost linear, reduction in $\eta_{c,f}$. A similar trend was found for both the 2° and 1° divergent combustors with no discernible difference in $\eta_{c,f}$ between the three combustors at similar ϕ, demonstrating that the area expansion of the divergent combustors does not degrade overall engine performance.

The air-based combustion efficiency (η_{air}) was calculated for all cases from the product of ϕ and $\eta_{c,f}$. It was found that η_{air} scales directly with ϕ up to a $\phi \approx 0.9$ for all combustors where it reaches a maximum itself of ≈ 0.9 (as $\eta_{c,f} = 100\%$ up to this point). For $\phi > 0.9$, η_{air} deteriorated slightly for mixtures which were increasingly rich. This indicates that combustion has become mixing limited near stoichiometric levels.

The separation characteristics as modelled by the cycle analysis were similar for all three combustors at similar ϕ. For the constant area combustor, separation was first seen in the experimental results, at $\phi = 0.76$, around the FE sensors at the front edge of the combustor. When the cycle analysis was matched to this result, the x_{fe_1} parameter reduces from a value of 0.83 m for the non-separated cases to 0.45 m. For the highly separated case at $\phi = 1.10$ and the maximum fuelling case at $\phi = 1.29$, where the separation in both cases has been driven up into the instrumented section of the isolator, there was a corresponding further reduction of x_{fe_1} to 0.4. Similar trends are found for the two divergent combustors. For all three combustors, this dramatic reduction of x_{fe_1} indicates that the presence of the shock train has a substantial effect on combustion. This effect is via both an enhancement of the mixing of the fuel with the air and an enhancement of the combustion from the higher pressure and temperature of the flow entering the combustion chamber. The further reduction of x_{fe_1} from the moderately to the highly separated cases indicates further enhancement of the mixing and combustion from the longer shock train.

For the separated cases the pressure through the shock train is modelled fairly well by Ortwerth's (2000) diffuser model. The value for c_{f_o} of 0.0015 from the boundary layer analysis gave the best fit to the separation, which was a compromise of fitting both the separation point and the gradient of the pressure rise through the separation. Of these two constraints, the separation point is better matched by the cycle analysis to the experiment than the pressure through separation, which is generally under-predicted by the code. This was attributed to the nature of the 1-D analysis which can not resolve multi-dimensional features of the real flow. At similar ϕ, the predicted shock train position and length is found to be similar for the divergent combustors as for the constant area combustor. This finding is in agreement with the findings from the experiments, with the cycle analysis providing the explanation that the area expansion has little effect on the shock train as the divergent point for both divergent combustors is downstream of the predicted reattachment point and the point where combustion has completed for all the separated cases.

Chapter 6

Conclusions

This thesis investigates a particular mode of scramjet operation known as dual-mode combustion. This investigation has consisted of two approaches: one experimental and one analytical. The experimental approach consisted of testing an axi-symmetric circular combustion chamber in the T4 Stalker Tube in a semi-direct connect configuration. The analytical approach applied cycle analysis to the results from the experiment to assess the effect the presence of the pre-combustion shock train had on the performance of the different combustors.

All experiments were performed at a test condition representative of Mach 8 flight where the total enthalpy of the flow was $\sim 3.1\,\mathrm{MJ/kg}$. The freestream flow entering the diffuser was at a pressure of $\sim 44\,\mathrm{kPa}$, a temperature of $\sim 670\,\mathrm{K}$ and a Mach number of 4.5. The calculated properties of the flow entering the isolator in terms of pressure, temperature and Mach number were: $\sim 119\,\mathrm{kPa}$, $\sim 905\,\mathrm{K}$ and 3.65 respectively. Hydrogen was used as the fuel and was injected via six portholes at the end of the isolator. A total of three combustors of equal length were tested: one constant area and two divergent combustors with a half-cone angle of 1° and 2°.

Cycle analyses were performed using the code *Dual-Mode Cycle Analysis* from Smart (2007). This code is based on the classic gas dynamic equations from Shapiro (1953) and uses a diffusion model based from Ortwerth (2000) to close the equation set. The code incorporates a equilibrium chemistry model (Auslender and Smart, 2000) to simulate combustion.

Freestream properties were determined for each individual shot using a combination of established shock tunnel computer programs, *ESTCj* (Gordon and McBride,

1994; McIntosh, 1968) and *NENZF* (Lordi et al., 1966), to determine freestream properties for each shot. A nominal condition was selected as the basis of a CFD solution of the diffuser (using the code *VULCAN*) to establish a set of nominal ratios for the conditions of the flow exiting the diffuser. This set of ratios was then applied to the freestream conditions for each individual shot to arrive at a set of isolator entrance conditions. These isolator conditions were then used as the inflow conditions for the dual-mode cycle analysis.

The cycle analysis code was run for all shots and parameters adjusted to get the best fit. The key parameters were the combustion efficiency ($\eta_{c,f}$), point of complete combustion (x_{fe_1}), mixing profile (ϑ) and the coefficient of skin friction at the point of separation (c_{f_0}).

The conclusions from the experimental and analytical results are summarised in this section and each of the research questions posed in Section 1.2 is discussed below. Recommendations for future studies are discussed in Section 6.1.

1. Can dual-mode operation of a scramjet be studied experimentally in a shock tunnel and if so, what is the establishment time of this phenomenon?

Dual-mode combustion can be established at conditions representative of flight at Mach 8 in the T4 Stalker Tube
Above a certain equivalence ratio ($\phi > 0.9$) separation of the boundary occurs forming a pre-combustion shock train. From a review of the transient data (time-history plots) for $0.9 < \phi < 1.3$ this separation is stable as indicated by the steady pressure at the rear of the isolator. Importantly, for this range in ϕ the establishment time of the flow (approximately 1.5 ms to 2.0 ms) is sufficiently shorter than the available test time of the facility, showing that such phenomena can be studied in such facilities. Above $\phi > 1.3$ steady flow is not achieved during the available test time which is attributed to either a longer establishment time due to the longer shock train or that engine is beginning to unstart.

2. How does the pre-combustion shock train affect mixing and thereby combustion efficiency of a scramjet?

The establishment of a shock train enhances mixing (or reduces the mixing-length)
From both the pressure profiles from the experiments and from the dual-mode cycle analysis, mixing is enhanced by the presence of a shock train. From the cycle analysis, in order to fit to the pressure measured nearest the injector, and the pressure profile through isolator, the heat release from combustion needs to occur over a shorter distance for the separated cases than for the non-separated cases. This indicates that mixing and combustion is enhanced from the presence of the shock train.

All three combustors are mixing-limited at the highest fuelling rates despite the enhanced mixing from the shock train
At fuelling rates where the equivalence ratios is above 1.4 any further increase in the fuelling rate does not result in any increase in the pressures in the combustion chambers. Therefore, it is concluded that the combustion is mixing-limited at that point.

3. Considering that scramjet engine designs are likely to incorporate an area expansion in the combustion chamber, how does area expansion in the combustion chamber affect the pre-combustion shock train and in turn the mixing and combustion efficiency of a scramjet?

The position of the shock-train is not affected by the point of divergence
The fore position of the shock train (i.e. the separation point) is similar for all three combustors at similar equivalences ratios. This is supported by the results from the cycle analysis, presented in Chapter 5, where the point of complete combustion is modelled to be upstream of the divergent point for both divergent combustors, and so the area expansion has little influence on the shock train position.

Initial boundary layer separation occurs at similar equivalence ratios for all three combustors
The measurements taken at the front edge of the combustor give the first sign of separation, as indicated by a large pressure rise above the fuel-off and combustion-suppressed cases. This increase in pressure occurs at an equivalence ratio approxim-

ately equal to 0.7 for all three combustors. This again shows that the area divergence for either divergent combustor has little to no effect on the separation characteristics.

Other findings from this research which are considered important but not directly related to the main research questions posed are:

The divergence point in the combustor needs to be located upstream of the point of complete combustion for the divergence to affect the size and position of the shock train.
If area divergence is to be incorporated into a dual-mode scramjet design, with the aim to increase the operational range, then the divergence point will need to be located upstream of the point of where combustion completes in order for the area expansion to have its desired effect. The estimation of this combustion length will need to take into account the enhancement in mixing from the shock train.

The accurate modelling of dual-mode scramjets requires the coupling between the shock train and mixing to be well understood.
Based on the conclusions that the establishment of a shock train enhances mixing, it is important for the design of dual-mode scramjet engines that the coupling between the fuel mixing and the shock train be well understood in order to predict the position and length of the shock train satisfactorily. This is also important for the previous finding relating to the positioning of the divergence point, where an estimate of the point of complete combustion is required.

Heavily back-pressured dual-mode scramjets require an accurate estimation of the inflow conditions
From the parametric study of the highly separated cases using the cycle analysis it is found that these cases are highly sensitive to inflow conditions. For a small change in freestream mass flow rate, momentum or Mach number the characteristics of the separation are significantly altered, along with a corresponding change in combustion efficiency. In order to model dual-mode engines with a long shock train, accurate and precise knowledge of the inflow conditions is required.

6.1 Recommendations for Future Studies

Investigation using visual diagnostics
One of the biggest limitations to this investigation was that the engine was axi-symmetric and this restricted the diagnostics which could be used. By switching to a two-dimensional planar geometry then windows could be used, which would allow high-speed visualisation techniques to be employed. This would provide a much better understanding of the shock train physics, particularly the transient nature, and better estimates of the shock train length.

Investigation into enthalpy effects
The main advantage of using a shock tunnel over other hypersonic facilities is the high total enthalpies which can be achieved and this allows combustion to be studied at high flight Mach numbers. The experiments in this investigation were all conducted at a single condition to conserve the number of shots. As there are only a few shock-train studies involving combustion at comparable enthalpies, there would be value in conducting experiments over a range of enthalpies to ascertain the sensitivity of this phenomena to changes in enthalpy.

Further exploration of the effect of the divergence point and angle
It is clear from the cycle analysis that the divergence point for both divergent combustors tested was too far downstream to affect the shock train. Additional divergent combustors should be tested which have a shorter constant area section so that the divergence point is further upstream. Additionally, one of the limitations of the design of the experiment was that maintaining a common combustor length for all three combustors meant that the change in the divergence angle also resulted in a change in the position of the point of divergence (i.e. the section of constant area before the divergence section of the combustor chamber). Further modularising of the combustion chambers would allow for the testing of changes in the divergence angle independent of the point of divergence.

Investigation using isolators of different lengths
One question which arose in this investigation that remains unanswered is whether the tests for ϕ above approximately 1.3 were the beginnings of an engine unstart or whether the test time was not sufficient for the separation to establish. Repeating these

experiments with a longer isolator would answer this question. It would also be interesting to compare such results with those from the HEG shock tunnel by Laurence et al. (2013) and to Laurence et al.'s quasi-unsteady one-dimensional model. A shorter isolator would allow engine unstart, caused by combustion induced separation, to be further investigated.

Effect of novel cross section shape

There is little work in the literature on the effect that the cross-section shape has on the flow through the isolator (Bagaveyev et al., 2010; Grendell et al., 2003; Grendell, 2004). Considering the interest in rectangular-to-elliptical transition (REST) engines (Smart, 1999; Suraweera and Smart, 2008; Turner and Smart, 2008), in which the cross-sectional shape from the isolator to the nozzle is elliptical, a fundamental study of pre-combustion shock trains in these novel cross-sectional shapes would be of interest to such engine designers.

Include heat transfer measurements along isolator walls

A measurement of heat transfer along the isolator walls would provide further insight into the boundary layer state along the wall of the isolator. These measurements would also provide a secondary independent measurement, to that of pressure sensors, of the flow establishment time for the region of separated flow. These heat transfer measurements may also provide (in conjunction with or following a similar approach to Le et al. (2008b)) an indication of imminent separation prior to that detected by the pressure measurements, which would reveal further information about the transient nature of this phenomenon.

Investigation into heat transfer measurements along combustor walls
Recent flight experiments (Walker et al., 2008) have highlighted the severity of the heating loads on hypersonic vehicles. Additional information of the temperatures and heating loads inside the combustion chambers of scramjets would be of great benefit. Additionally, if the heating loads in the combustor are higher than what materials can withstand then the greatest benefit of divergent combustors may be in the reduction of the combustion temperature.

Investigation into the effect the entropy layer has on shock trains
Kirchhartz (2009) investigated the effects of the entropy layer on boundary layer combustion, by varying the bluntness of the leading edge, with promising results. The motivation for that study was that blunt leading edges are a common design feature of hypersonic vehicles and are used to minimise the aerodynamic heating loads (Anderson, 1989). From Waltrup and Billig (1973), Carroll and Dutton (1990) and Matsuo et al. (1999), it is known that the state of the boundary layer influences the size of a shock train. Following a similar approach to Kirchhartz (2009), the effect of the state of the boundary layer on the pre-combustion shock train in a shock tunnel facility could be investigated.

Frequency analysis of shock train oscillations
Shock trains can have an oscillatory nature (Ikui et al., 1974b). Whilst some low frequency oscillations were noticed in a few of the signals (i.e. a shock moving forward or backwards over a sensor during the test time), a power spectral analysis of these signals may yield high frequency oscillations. This may require further testing if there is a need to characterise the oscillation in the test flow itself. This might be achieved by instrumenting the nozzle or through the inclusion of miniature Pitot probes to capture the variations in the freestream pressure over the test time.

References

Anderson, Jr., J.D. (**1989**). *Hypersonic and High Temperature Gas Dynamics*. Aeronautical and Aerospace Engineering Series, McGraw-Hill. ISBN 0-07-001671-2.

Anderson, Jr., J.D. (**2001**). *Fundamentals of Aerodynamics*. Aeronautical and Aerospace Engineering, McGraw-Hill, New York, 3rd ed. ISBN 0-07-237335-0.

Andreadis, D. (**2004**). "Scramjets Integrate Air and Space". *Industrial Physicist*, **vol. 10, no. 4**, pp. 24–27.

Auslender, A. and **Smart, M.** (**2000**). "Comparison of Ramjet Isolator Performance with Emphasis on Non-Constant Area Processes". In *Joint Army-Navy-NASA-Air Force (JANNAF) Meeting, Monterey, CA, United States of America*.

Bagaveyev, N.T.; **Engblom, W.A.** and **Bhagwandin, V.A.** (**2010**). "Parametric Investigation of Racetrack-to-Circular Cross-Section Transition of a Dual-Mode Ramjet Isolator". In *48th AIAA Aerospace Sciences Meeting including the New Horizons Forum and Aerospace Exposition, Orlanda, FL, United States of America*. American Institute of Aeronautics and Astronautics. AIAA-2010-942.

Bateup, M.L. (**2004**). "Supersonic Hydrocarbon Combustion Measurements in T4". In *9th International Workshop on Shock Tube Technologies, Woomera, SA, Australia*.

Baurle, R.A. and **Eklund, D.R.** (**2001**). "Analysis of Dual-Mode Hydrocarbon Scramjet Operation at Mach 4-6.5". In *37th AIAA/ASME/SAE/ASEE Joint Propulsion Conference and Exhibit, Salt Lake City, UT, United States of America*. American Institute of Aeronautics and Astronautics. AIAA-2001-3299.

Bement, D.; **Stevens, J.** and **Thompson, M.** (**1990**). "Measured Operating Characteristics of a Rectangular Combustor/Inlet Isolator". In *26th AIAA, SAE, ASME Joint Propulsion Conference, Orlando, FL, United States of America*. American Institute of Aeronautics and Astronautics. AIAA-1990-2221.

Billig, F.S.; **Waltrup, P.J.** and **Stockbridge, R.D.** (**1979**). "The Integral-Rocket, Dual-Combustion Ramjet - A New Propulsion Concept". In *4th International Symposium on Air Breathing Engines, Orlando, FL, United States of America*, (pp. 433–444). American Institute of Aeronautics and Astronautics. AIAA-1979-7044.

Billig, F.S.; **Waltrup, P.J.** and **Stockbridge, R.D.** (**1980**). "Integral-Rocket Dual-Combustion Ramjets: A New Propulsion Concept". *Journal of Spacecraft and Rockets*, **vol. 17, no. 5**, pp. 416–424.

Billig, F. (**1993**). "Research on Supersonic Combustion". *Journal of Propulsion and Power*, **vol. 9, no. 4**, pp. 499–514.

Billig, F. and **Dugger, G.** (**1969**). "The Interaction of Shock Waves and Heat Addition in the Design of Supersonic Combustors". In *12th Symposium (International) on Combustio, The Combustion Institute, Pittsburgh, PA, United States of America*, vol. 12, (pp. 1125–1139).

Billig, F.; **Dugger, G.** and **Waltrup, P.** (**1972**). "Inlet-Combustor Interface Problems in Scramjet Engines". In *1st International Symposium on Air Breathing Engines, Institut de Mecanique des Fluides, Marseille, France*.

Billig, F.; **Orth, R.C.** and **Funk, J.A.** (**1971**). "Direct-Connect Test of a Hydrogen Fuelled Supersonic Combustor". NASA Contractor Report, Applied Physics Laboratory, John Hopkins University for Langley Research Center, National Aeronautics and Space Administration (NASA), Washington, DC, United States of America. NASA-CR-1904.

Boyce, R.; **Paull, A.**; **Stalker, R.**; **Wendt, M.**; **Chinzei, N.** and **Miyajima, H.** (**2000**). "Comparison of Supersonic Combustion between Impulse and Vitiation-Heated Facilities". *Journal of Propulsion and Power*, **vol. 16**, pp. 709–717.

Boyce, R.; **Takahashi, M.** and **Stalker, R.** (**2005**). "Mass Spectrometric Measurements of Driver Gas Arrival in the T4 Free-Piston Shock-Tunnel". *Shock Waves*, **vol. 14**, pp. 371–378.

Brown, L.; **Boyce, R.** and **Tirtey, S.** (**2011**). "Numerical Simulation of SCRAMSPACE I Flight Experiment". In *17th AIAA International Space Planes and Hypersonic Systems and Technologies Conference, San Francisco, CA, United States of America*. American Institute of Aeronautics and Astronautics. AIAA-2011-2367.

Brown, L.M.; **Boyce, R.R.**; **Mudford, N.** and **OByrne, S.** (**2009**). "Intrinsic Three-dimensionality of Laminar Hypersonic Shock Wave/Boundary Layer Interactions". In *Proceeding of the 16th AIAA/DLR/DGLR International Space Planes and Hypersonic Systems and Technologies Conference, Bremen, Germany*. American Institute of Aeronautics and Astronautics. AIAA-2009-7205.

Brun, R. and **Dumitrescu, L.Z.** (Eds.) (**1993**). *Shock Waves @ Marseille I, Hypersonics, Shock Tube & Shock Tunnel Flow, Proceedings of the 19th International Symposium on Shock Waves, Marseille, France*. Springer. ISN 3-540-57710-6.

Carroll, B. and **Dutton, J.C.** (**1990**). "Characteristics of Multiple Shock Wave/Turbulent Boundary-Layer Interactions in Rectangular Ducts". *Journal of Propulsion and Power*, **vol. 6, no. 2**, pp. 186–193.

Carroll, B.F. and **Dutton, J.C.** (**1992**). "Multiple Normal Shock Wave/Turbulent Boundary-Layer Interactions". *Journal of Propulsion and Power*, **vol. 8, no. 2**, pp. 441–448.

Cebeci, T. and **Bradshaw, P.** (**1984**). *Physical and Computational Aspects of Convective Heat Transfer*. Springer-Verlag, New York.

Chan, Y.K.W. (**2012**). *Effects of Flow Non-Uniformities on the Drag Reduction by Boundary Layer Combustion*. Ph.D. thesis, School of Mechanical and Mining Engineering, The University of Queensland, Brisbane, QLD, Australia.

Choi, J.Y.; **Ma, F.** and **Yang, V.** (**2005**). "Combustion Oscillations in a Scramjet Engine Combustor with Transverse Fuel Injection". *Proceedings of the Combustion Institute*, **vol. 30, no. 2**, pp. 2851–2858.

Crocco, L. (**1958**). "One-Dimensional Treatment of Steady Gas Dynamics". In Emmons (1958), chap. B, (pp. 64–349).

Cuffel, R. and **Back, L.** (**1976**). "Flow and Heat Transfer Measurements in a Pseudo-Shock Region with Surface Cooling". *AIAA Journal*, **vol. 14, no. 12**, pp. 1716–1722.

Curran, E.T.; **Heiser, W.H.** and **Pratt, D.T.** (**1996**). "Fluid Phenomena in Scramjet Combustion Systems". *Annual Review of Fluid Mechanics*, **vol. 28**, pp. 323–360.

Curran, E.T. and **Murthy, S.N.B.** (Eds.) (**2000**). *Scramjet Propulsion*, vol. 189 of *Progress in Astronautics and Aeronautics*. American Institute of Aeronautics and Astronautics, Reston, VA, United States of America.

Curran, E.T. and **Craig, R.R.** (**1973**). "The Use of Stream Thrust Concepts for the Approximate Evaluation of Hypersonic Ramjet Engine Performance". Tech. rep., United States Air Force (USAF) Aero Propulsion Laboratory, Wright-Patterson Air Force Base, OH, United States of America. AFAPL-TR-73-38.

Curran, E.T. and **Stull, F.D.** (**1964**). "The Utilization of Supersonic Combustion Ramjet Systems at Low Mach Numbers". Tech. rep., United States Air Force (USAF) Aero Propulsion Laboratory, Wright-Patterson Air Force Base, OH, United States of America. RTD-TDR-63-4097, AD-348073.

Davies, W.R. and **Bernstein, L.** (**1969**). "Heat Transfer and Transition to Turbulence in the Shock-Induced Boundary Layer on a Semi-Infinite Flat Plate". *Journal of Fluid Mechanics*, **vol. 36, no. 1**, pp. 87–112.

Denis, S.R.; **Brandstetter, A.** and **Kau, H.P.** (**2003**). "Experimental Study on Transition between Ramjet and Scramjet Modes in a Dual-Mode Combustor". In *12th AIAA International Space Planes and Hypersonic Systems and Technologies, Norfolk, VA, United States of America*. American Institute of Aeronautics and Astronautics.

d'Incà, R. and **Bouchez, M.** (**2006**). "Use of the SCHOLAR Supersonic Combustion Data - 1D Analysis of the SCHOLAR Experiment". In *Technologies for Propelled Hypersonic Flight*, vol. 2, chap. 8. Research and Technology Organisation (RTO), North Atlantic Treaty Organization (NATO). NATO TR-AVT-007.

Diskin, G.S. and **Northam, G.B.** (**1987**). "Effects of Scale on Supersonic Combustor Performance". In *23rd AIAA/SAE/ASME/ASEE Joint Propulsion Conference, San Diego, CA*. American Institute of Aeronautics and Astronautics. AIAA-1987-2164.

Do, H.; **Im, S.k.**; **Mungal, M.G.** and **Cappelli, M.A.** (**2011**). "The Influence of Boundary Layers on Supersonic Inlet Flow Unstart Induced by Mass Injection". *Experiments in Fluids*, **vol. 51, no. 3**, pp. 679–691.

Doherty, L. (**2007**). *Flowpath Design for a Dual Mode Mach 5 Scramjet*. Undergraduate thesis, Division of Mechanical Engineering, School of Engineering, The University of Queensland, Brisbane, QLD, Australia.

Dutton, J.C. and **Carroll, B.F.** (**1988**). "Numerical and Experimental Investigation of Multiple Shock Wave/Turbulent Boundary Layer Interactions in a Rectangular Duct". Tech. rep., Department of Mechanical and Industrial Engineering, University of Illinois at Urbana-Champaign, Urbana, IL, United States of America. UILU-ENG-88-4001.

East, R.A.; **Stalker, R.J.** and **Baird, J.P.** (**1980**). "Measurements of Heat Transfer to a Flat Plate in a Dissociated High-Enthalpy Laminar Air-Flow". *Journal of Fluid Mechanics*, **vol. 97, no. 4**, pp. 673–699.

Edelman, R.B. and **Spadaccini, L.J.** (**1969**). "Theoretical Effects of Vitiated Air Contamination on Ground Testing of Hypersonic Airbreathing Engines". *Journal of Spacecraft and Rockets*, **vol. 6, no. 12**, pp. 1442–1447. AIAA-1969-338.

Emami, S.; **Trexler, C.A.**; **Auslender, A.H.** and **Weidner, J.P.** (**1995**). "Experimental Investigation of Inlet-Combustor Isolators for a Dual-Mode Scramjet at a Mach Number of 4". NASA technical paper, National Aeronautics and Space Administration (NASA), Washington, DC, United States of America. NASA-TP-3502.

Emmons, H. (Ed.) (**1958**). *Fundamentals of Gas Dynamics*, vol. 3 of *High Speed Aerodynamics and Jet Propulsion*. Oxford University Press, copyright by Princeton University Press.

Fejer, A.A.; **Heath, G.L.** and **Driftmyer, R.T.** (**1964**). "An Investigation of Constant Area Supersonic Flow Diffusion". Tech. rep., Aero Propulsion Laboratory (APL), United States Air Force (USAF), Wright-Patterson Air Force Base, OH, United States of America. ARL 64-81.

Fotia, M.L. and **Driscoll, J.F.** (**2012**). "Isolator-Combustor Interactions in a Direct-Connect Ramjet-Scramjet Experiment". *Journal of Propulsion and Power*, **vol. 28, no. 1**, pp. 83–95.

Fotia, M.L. and **Driscoll, J.F.** (**2013**). "Ram-Scram Transition and Flame/Shock-Train Interactions in a Model Scramjet Experiment". *Journal of Propulsion and Power*, **vol. 29**, pp. 1–13.

Freebairn, G.S. (**2010**). *The Phyiscs of Transitional Jet Interactions*. Ph.D. thesis, The University of New South Wales, Canberra, ACT, Australia.

Frost, M.A.; **Gangurde, D.Y.**; **Paull, A.** and **Me, D.J.** (**2009**). "Boundary-Layer Separation Due to Combustion-Induced Pressure Rise in a Supersonic Flow". *AIAA Journal*, **vol. 47, no. 4**, pp. 1050–1053.

Gangurde, D.Y. (**2007**). "L1d Simulation of Ludwieg Tube Fuel System for T4". Project report, The University of Queensland, Brisbane, QLD, Australia. ENGG 7240.

Gildfind, D.E. (**2012**). *Development of High Total Pressure Scramjet Flow Conditions Using the X2 Expansion Tube*. Ph.D. thesis, School of Mechanical and Mining Engineering, The University of Queensland, Brisbane, QLD, Australia.

Goldberg, U.; **Batten, P.**; **Palaniswamy, S.**; **Chakravarthy, S.** and **Peroomian, O.** (**2000**). "Hypersonic Flow Predictions Using Linear and Nonlinear Turbulence Closures". *Journal of Aircraft*, **vol. 37, no. 4**, pp. 671–675.

Goldberg, U.; **Peroovian, O.**; **Chakravarthy, S.** and **Sekar, B.** (**1997**). "Validation of CFD++ Code Capability for Supersonic Combustor Flowfields". In *33rd Joint Propulsion Conference and Exhibit, Seattle, WA, United States of America*. American Institute of Aeronautics and Astronautics. AIAA-1997-3271.

Gordon, S. and **McBride, B.J.** (**1994**). "Computer Program for Calculation of Complex Chemical Equilibrium Compositions and Applications: I. Analysis". NASA Reference Report, Lewis Research Center, National Aeronautics and Space Administration (NASA), Cleveland, OH, United States of America. NASA RP-1311.

Goyne, C.P.; **Jr., J.C.M.**; **Krauss, R.H.** and **Whitehurst, W.B.** (**2007**). "Test Gas Vitiation Effects in a Dual-Mode Scramjet Combustor". *Journal of Propulsion and Power*, **vol. 23, no. 3**, pp. 559–565.

Goyne, C.P.; **McDaniel, J.C.**; **Quagliaroli, T.M.** and **Krauss, R.H.** (**1999**). "Dual-Mode Combustion of Hydrogen in a Mach 5 Enthalpy, Clean-Air, Continuous-Flow Facility". In *14th International Symposium on Air Breathing Engines (ISABE), Florence, Italy*. American Institute of Aeronautics and Astronautics. ISABE-Paper-1999-7138.

Goyne, C.P.; **McDaniel, J.C.**; **Quagliaroli, T.M.**; **Krauss, R.H.** and **Day, S.W.** (**2001**). "Dual-Mode Combustion of Hydrogen in a Mach 5, Continuous-Flow Facility". *Journal of Propulsion and Power*, **vol. 17, no. 6**, pp. 1313–1318.

Goyne, C.P.; **Stalker, R.J.** and **Paull, A.** (**2003**). "Skin-Friction Measurements in High-Enthalpy Hypersonic Boundary Layers". *Journal of Fluid Mechanics*, **vol. 485**, pp. 1–32.

Grendell, K.M.; **Hagenmaier, M.A.** and **Orkwis, P.D.** (**2003**). "Numerical Design Study of Scramjet Isolator Cross-Sectional Shape Transition with Varied Divergence Angle". In *16th International Symposium on Air Breathing Engines, August 31-September 5, 2003, Renaissance Cleveland Hotel, Cleveland, OH, United States of America*. International Society of Air Breathing Engines (ISABE). ISABE-2003-1174.

Grendell, K.M. (**2004**). "A Comparison Study of Rectangular and Chamfered Isolator Cross-Sectional Shape with Varied Divergence". In *42nd AIAA Aerospace Sciences Meeting and Exhibit, Reno, NV, United States of America*. American Institute of Aeronautics and Astronautics. AIAA-2004-129.

Haw, W.L.; **Goyne, C.P.**; **Rockwell, R.D.**; **Krauss, R.H.** and **McDaniel, J.C.** (**2011**). "Experimental Study of Vitiation Effects on Scramjet Mode Transition". *Journal of Propulsion and Power*, **vol. 27, no. 2**, pp. 506–508.

Hayne, M.; **Mee, D.**; **Gai, S.**; **Stewart, B.** and **Morgan, R.** (**2005**). "Flow Establishment over Rearward-Facing Steps in High Enthalpy Flows". *Shock Waves*, **vol. 1**, pp. 173–178.

He, Y. and **Morgan, R.** (**1994**). "Transition of Compressible High Enthalpy Boundary Layer Flow over a Flat Plate". *The Aeronautical Journal of the Royal Aeronautical Society*, **vol. 98, no. 972**, pp. 25–34.

Heiser, W.H. and **Pratt, D.T.** (**1994**). *Hypersonic Airbreathing Propulsion*. AIAA Education Series, American Institute of Aeronautics and Astronautics, Washington, 370 L'Enfant Promenade, Washington, DC, United States of America. ISBN 1-56347-035-7.

Heiser, W.H. and **Pratt, D.T.** (**2000**). "Aerothermodynamics of the Dual-Mode Combustion System". In Curran and Murthy (2000), chap. 9, (pp. 569–596).

Holden, M.; **Harvey, J.**; **Boyd, I.**; **George, J.** and **Horvath, T.** (**1997**). "Experimental and Computational Studies of the Flow over a Sting Mounted Planetary Probe Configuration". In *35th Aerospace Sciences Meeting and Exhibit*, vol. 768. American Institute of Aeronautics and Astronautics.

Holden, M.S. (**1971**). "Establishment Time of Laminar Separated Flows". *AIAA Journal*, **vol. 9, no. 11**, pp. 2296–2298.

Hunt, J.L. and **Martin, J.G.** (**2000**). "Rudiments and Methodology for Design and Analysis of Hypersonic Air-Breathing Vehicles". In Curran and Murthy (2000), chap. 15, (pp. 939–978).

Ikui, T. and **Matsuo, K.** (**1969**). "Researches of Supersonic Flow with the Shock Wave as Main Subject". *Journal of the Japanesse Society of Mechanical Engineering (JSME)*, **vol. 72, no. 609**, pp. 1306–1312.

Ikui, T.; **Matsuo, K.**; **Mochizuki, H.** and **Somekawa, K.** (**1980**). "Pseudo-Shock Waves in a Divergent Channel". *Bullentin of the Japanesse Society of Mechanical Engineering (JSME)*, **vol. 23, no. 175**, pp. 20–25.

Ikui, T.; **Matsuo, K.** and **Nagai, M.** (**1974**a). "The Mechanism of Pseudo-Shock Waves". *Bullentin of the Japanesse Society of Mechanical Engineering (JSME)*, **vol. 17, no. 108**, pp. 731–739.

Ikui, T.; **Matsuo, K.**; **Nagai, M.** and **Honjo, M.** (**1974**b). "Oscillation Phenomena of Pseudo-Shock Waves". *JSME International Journal Series B*, **vol. 17, no. 112**, pp. 1278–1285.

Ikui, T.; **Matsuo, K.** and **Sasaguchi, K.** (**1981**). "Modified Diffusion Model of Pseudo-Shock Waves Considering Upstream Boundary Layers". *Bullentin of the Japanesse Society of Mechanical Engineering (JSME)*, **vol. 24, no. 197**, pp. 1920–1927.

Jacobs, P.A. (**1988**). "An Interactive Graphics Program for Computer Assisted Calculations of Isentropic Flows." Department of Mechanical Engineering Report 7-88, University of Queensland, Brisbane, QLD, Australia.

Jacobs, P.A.; **Morgan, R.G.**; **Stalker, R.J.** and **Mee, D.J.** (**1993**). "Use of Argon-Helium Driver-Gas Mixtures in the T4 Shock Tunnel". In Brun and Dumitrescu (1993), (pp. 263–268). ISN 3-540-57710-6.

Jacobs, P.; **Rogers, R.**; **Weidner, E.** and **Bittner, R.** (**1992**). "Flow Establishment in a Generic Scramjet Combustor". *Journal of Propulsion and Power*, **vol. 8, no. 4**, pp. 890–899.

Jacobs, P. and **Stalker, R.** (**1991**). "Mach 4 and Mach 8 Axisymmetric Nozzle for a High-Enthalpy Shock Tunnel". *The Aeronautical Journal of the Royal Aeronautical Society*, **vol. 95, no. 949**, pp. 324–334.

Jacobs, P.A. (**1989**). "A Mach 4 Nozzle for Hypervelocity Flow". Departmental Report 9-1989, Department of Mechanical Engineering, The University of Queensland, Brisbane, QLD, Australia.

Kanda, T.; **Chinzei, N.**; **Kudo, K.** and **Murakami, A.** (**2001**). "Dual-Mode Operation in a Scramjet Combustor". In *10th AIAA/NAL-NASDA-ISAS International Space Planes and Hypersonic Systems and Technologies Conference, Kyoto, Japan*. American Institute of Aeronautics and Astronautics. AIAA-2001-1816.

Kanda, T. and **Tani, K.** (**2005**). "Momentum Balance Model of Flow Field with Pseudo-Shock". In *43rd AIAA Aerospace Sciences Meeting and Exhibit, Reno, NV, United States of America*. American Institute of Aeronautics and Astronautics. AIAA-2005-1045.

Kato, K.; **Kanda, T.**; **Kobayashi, K.**; **Kudo, K.** and **Murakami, A.** (**2006**). "Downstream Ramjet-Mode Combustion in a Dual-Mode Scramjet Engine". *Journal of Propulsion and Power*, **vol. 22, no. 3**, pp. 511–517.

Kawatsu, K.; **Koike, S.**; **Kumasaka, T.**; **Masuya, G.** and **Takita, K.** (**2005**). "Pseudo-Shock Wave Produced by Backpressure in Straight and Diverging Rectangular Ducts". In *13th AIAA/CIRA International Space Planes and Hypersonics Systems and Technologies Conference, Capua, Italy*. American Institute of Aeronautics and Astronautics. AIAA-2005-3285.

Kay, I.; **Peschke, W.** and **Guile, R.** (**1992**a). "Hydrocarbon-Fueled Scramjet Combustor Investigation". *Journal of Propulsion and Power*, **vol. 8, no. 2**, pp. 507–512.

Kay, I.; **Peschke, W.** and **Guile, R.** (**1992**b). "Hydrocarbon-Fueled Scramjet Combustor Investigation". In *26th SAE, ASME, and ASEE Joint Propulsion Conference, Orlando, FL, United States of America*. American Institute of Aeronautics and Astronautics. AIAA-1990-2337.

Kirchhartz, R.M. (**2009**). *Upstream Wall Layer Effects on Drag Reduction with Boundary Layer Combustion*. Ph.D. thesis, The University of Queensland, Brisbane, QLD, Australia.

Kobayashi, K.; **Kanda, T.**; **Tomioka, S.**; **Tani, K.**; **Sakuranaka, N.** and **Mitani, T.** (**2007**). "Suppression of Combustor-Inlet Interaction in a Scramjet Engine Under Mach 4 Flight Conditions". *Transactions of the Japan Society for Aeronautical and Space Sciences*, **vol. 49, no. 166**, pp. 246–253.

Kobayashi, K.; **Tomioka, S.**; **Kato, K.**; **Murakami, A.** and **Kudo, K.** (**2006**). "Performance of a Dual-Mode Combustor with Multistaged Fuel Injection". *Journal of Propulsion and Power*, **vol. 22, no. 3**, pp. 518–526.

Korkegi, R.H. (**1975**). "Comparison of Shock Induced Two- And Three-Dimensional Incipient Turbulent Separation". *AIAA Journal*, **vol. 13, no. 4**, pp. 534–535.

Korkegi, R.H. (**1985**). "A Lower Bound for Three-Dimensional Turbulent Separation in Supersonic Flow". *AIAA Journal*, **vol. 23**, pp. 475–476.

Laurence, S.; **Karl, S.**; **Schramm, J.M.** and **Hannemann, K.** (**2013**). "Transient Fluid-Combustion Phenomena in a Model Scramjet". *Journal of Fluid Mechanics*, **vol. 722**, pp. 85–120.

Le, D.B.; **Goyne, C.P.**; **Krauss, R.H.** and **McDaniel, J.C.** (**2008**a). "Experimental Study of a Dual-Mode Scramjet Isolator". *Journal of Propulsion and Power*, **vol. 24, no. 5**, pp. 1050–1057.

Le, D.; **Goyne, C.** and **Krauss, R.** (**2008**b). "Shock Train Leading-Edge Detection in a Dual-Mode Scramjet". *Journal of Propulsion and Power*, **vol. 24, no. 5**, pp. 1035–1041.

Le, D.; **Goyne, C.**; **Krauss, R.** and **McDaniel, J.** (**2006**). "Shock Train Leading-Edge Detection in a Dual-Mode Scramjet". In *44th AIAA Aerospace Sciences Meeting and Exhibit, Reno, NV, United States of America*. American Institute of Aeronautics and Astronautics. AIAA-2006-815.

Le, D.; **Goyne, C.**; **Krauss, R.** and **McDaniel, J.** (**2005**). "Experimental Study of a Dual-Mode Scramjet Isolator". In *43rd AIAA Aerospace Sciences Meeting and Exhibit, Reno, NV, United States of America*. American Institute of Aeronautics and Astronautics. AIAA-2005-23.

Li, J.; **Ma, F.**; **Yang, V.**; **Lin, K.C.** and **Jackson, T.A.** (**2007**). "A Comprehensive Study of Combustion Oscillations in a Hydrocarbon-Fueled Scramjet Engine". In *45th AIAA Aerospace Sciences Meeting and Exhibit, Reno, NV, United States of America*. American Institute of Aeronautics and Astronautics. AIAA-2007-836.

Lin, K.C.; **Tam, C.J.**; **Jackson, K.**; **Eklund, D.R.** and **Jackson, T.A.** (**2006**). "Characterization of Shock Train Structures Inside Constant-Area Isolators of Model Scramjet Combustors". In *44th AIAA Aerospace Sciences Meeting and Exhibit, Reno, NV, United States of America*. American Institute of Aeronautics and Astronautics.

Lin, P. (**1993**). "Geometric Effects on Precombustion Shock Train in Constant Area Isolators". In *29th AIAA/SAE/ASME/ASEE Joint Propulsion Conference and Exhibit, Monterey, CA, United States of America*. American Institute of Aeronautics and Astronautics. AIAA-1993-1838.

Lordi, J.A.; **Mates, R.E.** and **Moselle, J.R.** (**1966**). "Computer Program for the Numerical Simulation of Non-Equilibrium Expansions of Reaction Gas Mixtures". Nasa contractor report, Cornell Aeronautical Laboratory, Buffalo, NY for the National Aeronautics and Space Administration (NASA), Washington, DC, United States of America. NASA-CR-472.

Lorrain, P.; **S. Brieschenk, B.R.Capra, R.B.**; **Lorrain, P.**; **Brieschenk, S.**; **Capra, B.** and **Boyce, R.** (**2012**). "A Detailed Investigation of Nominally 2-D Radical-Farming Scramjet Combustion". In *18th AIAA/3AF International Space Planes and Hypersonic Systems and Technologies Conference, Tours, France*. American Institute of Aeronautics and Astronautics. AIAA-2012-5812.

Lorrain, P. and **Boyce, R.R.** (**2011**). "Supersonic Fin-Body Interactions in an Internal Scramjet Flow". *Journal of Propulsion and Power*, **vol. 27, no. 2**, pp. 319–329.

Lu, F.K. and **Marren, D.E.** (Eds.) (**2002**a). *Advanced Hypersonic Test Facilities*, vol. 198 of *Progress in Astronautics and Aeronautics*. American Institute of Aeronautics and Astronautics, Washington, Reston, VA, United States of America.

Lu, F.K. and **Marren, D.E.** (**2002**b). "Principles of Hypersonic Test Facility Development". In Lu and Marren (2002a), chap. 2, (pp. 17–28).

Lustwerk, F. (**1950**). "The Influence of Boundary Layer on the 'Normal' Shock Configuration". Meteor Report 61, Guided Missiles Program, Massachusetts Institute of Technology, Cambridge, MA, United States of America.

Mager, A. (**1956**). "On the Model of the Free, Shock-Separated, Turbulent Boundary Layer". *Journal of the Aeronautical Sciences*, **vol. 23**, pp. 181–184.

Masumoto, R.; **Tomioka, S.** and **Yamasaki, H.** (**2009**). "Study on Transition of Combustion Modes in a Dual-Mode Combustor". In *16th AIAA/DLR/DGLR International Space Planes and Hypersonic Systems and Technologies Conference, Bremen, Germany*. American Institute of Aeronautics and Astronautics. AIAA-2009-7364.

Mateer, G. and **Viegas, J.R.** (**1980**). "Mach and Reynolds Number Effects on a Shock-Wave/Boundary-Layer". *AIAA Journal*, **vol. 18, no. 8**, pp. 1016–1018.

Matsuo, K.; **Kage, K.** and **Kawagoe, S.** (**1975**). "The Interaction of a Reflected Shock Wave with the Contact Region in a Shock Tube". *Bullentin of the Japanesse Society of Mechanical Engineering (JSME)*, **vol. 18, no. 121**, pp. 681–688.

Matsuo, K.; **Miyazato, Y.** and **Kim, H.D.** (**1999**). "Shock Train and Pseudo-Shock Phenomena in Internal Gas Flows". *Progress in Aerospace Sciences*, **vol. 35, no. 1**, pp. 33–100.

McBride, B.J.; **Zehe, M.J.** and **Gordon, S.** (**2002**). "NASA Glenn Coefficients for Calculating Thermodynamic Properties of Individual Species". NASA Technical Pa-

per, John H. Glenn Research Center, National Aeronautics and Space Administration NASA, Cleveland, OH, United States of America. NASA-TP-2002-211556.

McGuire, J. (**2007**). *Ignition Enhancement for Scramjet Combustion*. Ph.D. thesis, The University of New South Wales, Kensington, NSW, Australia.

McIntosh, M.K. (**1968**). "Computer Program for the Numerical Calculation of Frozen and Equilibrium Conditions in Shock Tunnels". Tech. rep., Department of Physics, Australian National University, Canberra, ACT, Australia.

McLafferty, G. (**1953**). "Theoretical Pressure Recovery Through a Normal Shock in a Duct with Initial Boundary Layer". *Journal of the Aeronautical Sciences*, **vol. 30, no. 3**, pp. 169–174.

Mee, D.J. (**1993**). "Uncertainty Analysis of Conditions in the Test Section of the T4 Shock Tunnel." Research Report 4/93, Department of Mechanical Engineering, The University of Queensland, Australia.

Mee, D. (**2002**). "Boundary-Layer Transition Measurements in Hypervelocity Flows in a Shock Tunnel". *AIAA Journal*, **vol. 40, no. 8**, pp. 1542–1548.

Mehta, U.B. and **Bowles, J.V.** (**2001**). "Two-Stage-to-Orbit Spaceplane Concept with Growth Potential". *Journal of Propulsion and Power*, **vol. 17, no. 6**, pp. 1149–1161.

Merkli, P. (**1976**). "Pressure Recovery in Rectangular Constant Area Supersonic Diffusers". *AIAA Journal*, **vol. 14, no. 2**, pp. 168–172.

Micka, D.J. and **Driscoll, J.F.** (**2009**). "Combustion Characteristics of a Dual-Mode Scramjet Combustor with Cavity Flameholder". *Proceedings of the Combustion Institute*, **vol. 32**, pp. 2397–2404.

Mitani, T.; **Hiraiwa, T.**; **Sato, S.**; **Tomioka, S.**; **Kanda, T.** and **Tani, K.** (**1997**). "Comparison of Scramjet Engine Performance in Mach 6 Vitiated and Storage-Heated Air". *Journal of Propulsion and Power*, **vol. 13, no. 5**, pp. 635–642.

Moule, Y. and **Smart, M.** (**2012**). "Performance Analysis of a Mach 12 Scramjet at Off-Design Conditions". *Journal of Propulsion and Power*, **vol. 29, no. 1**, pp. 282–285.

Murthy, S.N.B. (**2000**). "Basic Performance Assessment of Scram Combustors". In Curran and Murthy (2000), chap. 10, (pp. 597–695).

Murthy, S. and **Curran, E.** (Eds.) (**1991**). *High-Speed Flight Propulsion Systems*, vol. 137 of *Progress in Astronautics and Aeronautics*. American Institute of Aeronautics and Astronautics, Reston, VA, United States of America.

Muylaert, J. and **Kumar, A.** (Eds.) (**2006**). *Technologies for Propelled Hypersonic Flight*. Research and Technology Organisation (RTO), North Atlantic Treaty Organisation (NATO). RTO Technical Report TR-AVT-007.

Nagel, A. (**1968**). "Analysis of the Unit Reynolds Number Effect in Hypersonic Flat Plate Boundary Layer Transition". In *Proceedings of the 1968 Heat Transfer and Fluid Mechanics Institute*, (pp. 51–64). Stanford University Press.

National Instruments (**2005**). "NI 6132/6133 Specifications". Website, accessed 14th August 2009. 371231C-01.
URL `www.ni.com`

Nedungadi, A. and **Van Wie, D.** (**2004**). "Understanding Isolator Performance Operating in the Separation-Shock Mode". In *40th AIAA Joint Propulsion Conference, Fort Lauderdal, FL, United States of America*. American Institute of Aeronautics and Astronautics. AIAA-004-3832.

Neumann, E.P. and **Lustwerk, F.** (**1949**). "Supersonic Diffusers for Wind Tunnels". *Journal of Applied Mechanics*, **vol. 16, no. 2**, pp. 195–202.

Neumann, E. and **Lustwerk, F.** (**1951**). "High-Efficiency Supersonic Diffusers". *Journal of the Aeronautical Sciences*, **vol. 18, no. 6**, pp. 369–374.

Noda, J.; **Masuya, G.**; **Tomioka, S.**; **Izumikawa, M.**; **Rockwell, R.** and **Goyne, C.** (**2011**a). "Comparison of Dual-Mode Combustor Performance with Various Heating Methods". In *47th AIAA/ASME/SAE/ASEE Joint Propulsion Conference and Exhibit, San Diego, CA, United States of America*. American Institute of Aeronautics and Astronautics. AIAA-2011-6087.

Noda, J.; **Tomioka, S.**; **Izumikawa, M.**; **Goyne, C.P.**; **Rockwell, R.D.** and **Masuya, G.** (**2011**b). "Estimation of Enthalpy Effects in Direct-Connect Dual-Mode Combustor". *Journal of Thermal Science And Technology*, **vol. 6, no. 2**, pp. 289–296.

Nussdorfer, T.J. (**1954**). "Some Observations of Shock-Induced Turbulent Separation on Supersonic Diffusers". NACA research memorandum, Lewis Flight Propulsion Laboratory, Cleveland OH for National Advisory Committee for Aeronautics (NACA), Washington, DC, United States of America. NACA-RM-E51L26.

Odam, J. (**2004**). *Scramjet Experiments Using Radical Farming*. Ph.D. thesis, Department of Mechanical Engineering, The University of Queensland, Brisbane, QLD, Australia.

Ortwerth, P.J. (**2000**). "Scramjet Flowpath Integration". In Curran and Murthy (2000), chap. 17, (pp. 1105–1293).

Ostras, V. and **Penzin, V.** (**1975**). "Experimental Study of Friction in a Channel with a Pseudoshock". *Fluid Mechanics-Soviet Research*, **vol. 4, no. 6**, pp. 32–38.

Park, C. (**1985**). "On Convergence of Computation of Chemically Reacting Flows". In *AIAA 23rd Aerospace Sciences Meeting, Reno, NV, United States of America*. American Institute of Aeronautics and Astronautics. AIAA-1985-0247.

Paull, A. (**1996**). "A Simple Shock Tunnel Driver Gas Detector". *Shock Waves*, **vol. 6, no. 5**, pp. 309–312.

Paull, A. and **King, M.D.** (**1995**). "A Driver Gas Detection Device for Shock Tunnels". *Shock Waves*, **vol. 4, no. 5**, pp. 289–291.

Paull, A.; **Stalker, R.J.** and **Mee, D.J.** (**1995**). "Scramjet Thrust Measurement in a Shock Tunnel". *Aeronautical Journal*, **vol. 99**, pp. 161–163.

Pellett, G.L.; **Bruno, C.** and **Chinitz, W.** (**2006**). "Air Vitiation Effects on Scramjet Combustion Tests". In Muylaert and Kumar (2006), chap. 4. RTO-TR-AVT-007-V2.

Penzin, V. (**1995**). "Experimental Investigation of Supersonic Flows with Separated Regions in Ducts." Technical report, Central Aerodynamic Institution (TSAGI), Moscow, Russia for Department of Defence, United States of America. DTIC-Document-ADA319719.

Pergament, H.S. (**1963**). "Theoretical Analysis of Non-Equilibrium Hydrogen-Air Reactions in Flow Systems". In *AIAA-ASME Hypersonic Ramjet Conference, Naval Ordnance Laboratory, White Oak, MD, United States of America*. American Institute of Aeronautics and Astronautics. AIAA-1963-113.

Portwood, T.W. (**2006**). *Enhancement of Hydrocarbon Supersonic Combustion by Radical Farming and Oxygen Enrichment*. Master's thesis, Department of Mechanical Engineering, The University of Queensland, Brisbane, QLD, Australia.

Portz, R. and **Segal, C.** (**2006**). "Penetration of Gaseous Jets in Supersonic Flows". *AIAA Journal*, **vol. 44**, pp. 2426–2429.

Pratt, D.T. and **Heiser, W.H.** (**1993**). "Isolator-Combustor Interaction in a Dual-Mode Scramjet Engine". In *31st Aerospace Sciences Meeting & Exhibit, Reno, NV, United States of America*. American Institute of Aeronautics and Astronautics. AIAA-1993-358.

Razzaqi, S.A. (**2011**). *Oxygen Enrichment in a Hyrdogen Fuelled Scramjet*. Ph.D. thesis, School of Mechanical and Mining Engineering, The University of Queensland, Brisbane, QLD, Australia.

Reinartz, B.; **Ballmann, J.**; **Brown, L.**; **Fischer, C.** and **Boyce, R.** (**2007**). "Shock Wave/Boundary Layer Interactions in Hypersonic Intake Flows". In *2nd European Conference for Aerospace Sciences, Brussels, Belgium*. European Conference for AeroSpace Sciences (*EUCASS*).

Ridings, A. (**2012**). "UQ's T4 Shock Tunnel Data Acquisition System". In *2012 National Instruments Technical Symposium, Brisbane, QLD, Australia*.

Robinson, M.J.; **Rowan, S.A.** and **Odam, J.** (**2003**). "T4 Free Piston Shock Tunnel Operator's Manual". Research Report 2003-1, Department of Mechanical Engineering , The University of Queensland, Brisbane, QLD, Australia.

Rockwell, R.J.; **Goyne, C.**; **Haw, W.**; **Krauss, R.**; **Mcdaniel, J.** and **Trefny, C.** (**2010**). "Experimental Study of Test Medium Vitiation Effects on Dual-Mode Scramjet Mode Transition". In *48th AIAA Aerospace Sciences Meeting including the New Horizons Forum and Aerospace Exposition, Orlanda, FL, United States of America*. American Institute of Aeronautics and Astronautics.

Rockwell, R.D.J.; **Goyne, C.P.**; **Haw, W.**; **Krauss, R.H.**; **McDaniel, J.C.** and **Trefny, C.J.** (**2011**). "Experimental Study of Test-Medium Vitiation Effects on Dual-Mode Scramjet Performance". *Journal of Propulsion and Power*, **vol. 27, no. 5**, pp. 1135–1142.

Rowan, S.A. (**2003**). *Viscous Drag Reduction in a Scramjet Combustor*. Ph.D. thesis, Division of Mechanical Engineering, The University of Queensland, Brisbane, QLD, Australia.

Settles, G.S. (**2001**). *Schlieren and Shadowgraph Techniques: Visualizing Phenomena in Transparent Media*. Springer. ISBN 978-3-642-56640-0.

Shapiro, A.H. (**1953**). *The Dynamics and Thermodynamics of Compressible Fluid Flow*. John Wiley and Sons, New York.

Skinner, K.A. (**1994**). *Mass Spectrometry in Shock Tunnel Experiments of Hypersonic Combustion*. Ph.D. thesis, School of Mechanical Engineering, The University of Queensland, Brisbane, QLD, Australia.

Smart, M.K. (**1999**). "Design of Three-Dimensional Hypersonic Inlets with Rectangular-to-Elliptical Shape Transition". *Journal of Propulsion and Power*, **vol. 15, no. 3**, pp. 408–416.

Smart, M.K. (**2007**). "Scramjets". *The Aeronautical Journal of the Royal Aeronautical Society*, **vol. 111, no. 1124**, pp. 605–619.

Smart, M.K. (**2008**). "Scramjets". In *Advances on Propulsion Technology for High-Speed Aircraft*, (pp. 9–1–9–38). 9, Research and Technology Organisation (RTO), North Atlantic Treaty Organization (NATO) ,Neuilly-sur-Seine, France. Educational Notes RTO-EN-AVT-150.

Smart, M.K. (**2010**). "Scramjet Isolators". In *High Speed Propulsion: Engine Design - Integration and Thermal Management*. VKI Lecture Series, von Karman Institute for Fluid Dynamics. RTO-EN-AVT-185.

Smart, M.K. (**2012**). "How Much Compression Should a Scramjet Inlet Do?" *AIAA Journal*, **vol. 50, no. 3**, pp. 610–619.

Smith, A.L. (**1999**). *Multiple Component Force Measurement in Short Duration Test Flows*. Ph.D. thesis, The University of Queensland, Brisbane, QLD, Australia.

Smith, C.E. (**1966**). "The Starting Process in a Hypersonic Nozzle". *Journal of Fluid Mechanics*, **vol. 24, no. 2**, pp. 625–640.

Stalker, R.J. (**1966**). "The Free-Piston Shock Tube". *The Aeronautical Quarterly*, **vol. 17**, pp. 351–369.

Stalker, R.J. (**1990**). "Recent Developments with Free Piston Drivers". In Y.W. Kim (Ed.), *17th International Symposium on Shock Waves and Shock Tubes, Bethlehem, PA, United States of America*, vol. 208 of *Current Topics in Shock Waves*, (pp. 96–107). American Institute of Physics, Melville, NY, United States of America.

Stalker, R.J. (**2006**). "Modern Developments in Hypersonic Wind Tunnels". *The Aeronautical Journal of the Royal Aeronautical Society*, **vol. 110, no. 1103**, pp. 21–39.

Stalker, R.J.; **Paull, A.**; **Mee, D.J.**; **Morgan, R.G.** and **Jacobs, P.A.** (**2005**). "Scramjets and Shock Tunnels - The Queensland Experience". *Progress in Aerospace Sciences*, **vol. 41**, pp. 471–453.

Stalker, R.J. (**1987**). "Shock Tunnels for Real Gas Hypersonics". In *Aerodynamis of Hypersonic Lifting Vehicles, Proceedings of the Fluid Dynamics Panel Symposium in Bristol, United Kingdom*, (pp. 4–1–4–10). Advisory Group for Aerospace Research & Development (AGARD), North Atlantic Treaty Organization (NATO). AGARD-CP-428.

Stalker, R. (**1967**). "A Study of the Free-Piston Shock Tunnel". *AIAA Journal*, **vol. 5, no. 12**, pp. 2160–2165.

Stalker, R. and **Crane, K.** (**1978**). "Driver Gas Contamination in a High-Enthalpy Reflected Shock Tunnel". *AIAA Journal*, **vol. 16, no. 3**, pp. 277–279.

Stalker, R. and **Morgan, R.** (**1984**). "Supersonic Hydrogen Combustion with a Short Thrust Nozzle". *Combustion and flame*, **vol. 57, no. 1**, pp. 55–70.

Stalker, R. and **Morgan, R.** (**1988**). "The University of Queensland Free Piston Shock Tunnel T4 - Initial Operation and Preliminary Calibration". In *4th National Space Engineering Symposium, Adelaide, SA, Australia*. Institute of Engineers Australia (IEAust).

Sugiyama, H.; **Takeda**; **Sugiyama, H.**; **Takeda, H.**; **Zhang, J.**; **Okuda, K.** and **Yamagishi, H.** (**1988**). "Locations and Oscillation Phenomena of Pseudo-Shock Waves in a Straight Rectangular Duct". *JSME International Journal Series 2*, **vol. 31, no. 1**, pp. 9–15.

Sugiyama, H.; **Minato, R.**; **Mizobata, K.**; **Tojo, A.** and **Muto, Y.** (**2006**). "Study on Shock Wave and Turbulent Boundary Layer Interactions in a Square Duct at Mach 2 and 4". *Journal of Thermal Science*, **vol. 15, no. 1**, pp. 37–42.

Sullins, G. (**1993**). "Demonstration of Mode Transition in a Scramjet Combustor". *Journal of Propulsion and Power*, **vol. 9, no. 4**, pp. 515–520.

Sullins, G. and **McLafferty, G.** (**1992**). "Experimental Results of Shock Trains in Rectangular Ducts". In *4th AIAA International Aerospace Planes Conference, Orlando, FL, United States of America*. American Institute of Aeronautics and Astronautics. AIAA-1992-5103.

Suraweera, M.V. (**2006**). "Application of Mounting Configuration for Kulite Pressure Transducers in T4 Shock Tunnel". Tech. rep., Centre for Hypersonics, The University of Queensland, Brisbane, (QLD), Australia.

Suraweera, M.V. and **Smart, M.K.** (**2008**). "Shock Tunnel Experiments with a Mach 12 REST Scramjet at Off-Design Conditions". In *46th AIAA Aerospace Sciences Meeting*

and Exhibit, Reno, NV, United Sates of America. American Institute of Aeronautics and Astronautics.

Tamaki, T.; **Tomita, Y.** and **Yamane, R.** (**1970**). "A Study of Pseudo-Shock, 1st Report, λ-type Pseudo-Shock." *Bullentin of the Japanesse Society of Mechanical Engineering (JSME)*, **vol. 13, no. 55**, pp. 51–58.

Tamaki, T.; **Tomita, Y.** and **Yamane, R.** (**1971**). "A Study of Pseudo-Shock, 2nd Report, X-type Pseudo-Shock". *Bullentin of the Japanesse Society of Mechanical Engineering (JSME)*, **vol. 14, no. 74**, pp. 807–817.

Tan, H.j.; **Sun, S.** and **Yin, Z.l.** (**2009**). "Oscillatory Flows of Rectangular Hypersonic Inlet Unstart Caused by Downstream Mass-Flow Choking". *Journal of Propulsion and Power*, **vol. 25, no. 1**, pp. 138–147.

Tanimizu, K. (**2008**). *Nozzle Optimization Study and Measurements for a Quasi-Axisymmetric Scramjet Model*. Ph.D. thesis, Division of Mechanical Engineering, School of Engineering, The University of Queensland, Brisbane, QLD, Australia.

Tanno, H.; **Paull, A.** and **Stalker, R.** (**2001**). "Skin-Friction Measurements in a Supersonic Combustor with Crossflow Fuel Injection". *Journal of Propulsion and Power*, **vol. 17, no. 6**, pp. 1333–1338.

Tomioka, S.; **Kobayashi, K.**; **Kudo, K.**; **Murakami, A.** and **Kanda, T.** (**2006**). "Performance of Supersonic Combustors with Fuel Injection in Diverging Section". *Journal of Propulsion and Power*, **vol. 22, no. 1**, pp. 111–119.

Tu, Q. and **Segal, C.** (**2010**). "Isolator/Combustion Chamber Interactions During Supersonic Combustion". *Journal of Propulsion and Power*, **vol. 26, no. 1**, pp. 182–185.

Turner, J. and **Smart, M.** (**2008**). "Application of Radical Farming to a 3-D Scramjet at Mach 8". In *46th AIAA Aerospace Sciences Meeting and Exhibit, Reno, NV, United Sates of America*. American Institute of Aeronautics and Astronautics. AIAA-2008-101.

Turner, J.C. and **Smart, M.K.** (**2010**). "Application of Inlet Injection to a Three-Dimensional Scramjet at Mach 8". *AIAA Journal*, **vol. 48, no. 4**, pp. 829–838.

Turner, J.C.T. (**2010**). *An Experimental Investigation of Inlet Fuel Injection in a Three-Dimensional Scramjet Engine*. Ph.D. thesis, Division of Mechanical Engineering, The University of Queensland, Brisbane, QLD, Australia.

Turner, J. and **Smart, M.** (**2009**). "Experimental Investigation of Inlet Injection in a Scramjet with Rectangular to Elliptical Shape Transition". *Shock Waves*, (pp. 1117–1122).

Vinogradov, V.; **Grachev, V.**; **Petrov, M.** and **Sheechman, J.** (**1990**). "Experimental Investigation of 2-D Dual Mode Scramjet with Hydrogen Fuel at Mach 4...6". In *AIAA 2nd International Aerospace Planes Conference, Orlando, FL, United States of America*. American Institute of Aeronautics and Astronautics. AIAA-1990-5269.

von Kármán, T. (**1921**). "On Laminar and Turbulent Friction". *Z. Angew. Math. Mech*, **vol. 1**, pp. 235–236.

Wagner, J.; **Yuceil, K.** and **Clemens, N.** (**2009**). "PIVmeasurements of Unstart of an Inlet-Isolator Model in a Mach 5 Flow". In *39th AIAA Fluid Dynamics Conference, San Antonio, TX, United states*. American Institute of Aeronautics and Astronautics. AIAA-2009-4209.

Walker, S.; **Rodgers, F.**; **Paull, A.** and **Van Wie, D.M.** (**2008**). "HyCAUSE Flight Test Program". In *15th AIAA International Space Planes and Hypersonic Systems and Technologies Conference, Dayton, OH, United States of America*. American Institute of Aeronautics and Astronautics. AIAA-2008-2580.

Waltrup, P.J. and **Billig, F.S.** (**1973**). "Structure of Shock Waves in Cylindrical Ducts". *AIAA Journal*, **vol. 11, no. 10**, pp. 1404–1408.

Waltrup, P.J. and **Billig, F.** (**1972**). "Precombustion Shock Structure in Scramjet Engines." In *8th AIAA and SAE, Joint Propulsion Specialist Conference, New Orleans, LA, United States of America*. American Institute of Aeronautics and Astronautics. AIAA-1972-1181.

Waltrup, P.J. and **Cameron, J.M.** (**1974**). "Wall Shear and Boundary-Layer Measurements in Shock Separated Flow". *AIAA Journal*, **vol. 12, no. 6**, pp. 878–880.

Weber, R.J. and **MacKay, J.S.** (**1958**). "An Analysis of Ramjet Engines Using Supersonic Combustion". NACA Technical Note 4386, Lewis Flight Propulsion Laboratory for National Advisory Committee for Aeronautics NACA, Cleveland, OH, United States of America. NACA-TN-4386.

White, J.A. and **Morrison, J.H.** (**1999**). "A Pseudo-temporal multi-grid relaxation scheme for solving the parabolized Navier-Stokes equations". In *14th Computational Fluid Dynamics Conference*. American Institute of Aeronautics and Astronautics. AIAA-1999-3360.

White, M.E.; **Stevens, J.R.**; **Van Wie, D.M.**; **Mattes, L.A.** and **Keirsey, J.** (**1988**). "Investigation of Cowl Vent Slots for Stability Enhancement in MITS Scramjet Inlets". In *24th AIAA/ASME/SAE/ASEE Joint Propulsion Conference, Boston, MA, United States of America*. American Institute of Aeronautics and Astronautics. AIAA-1988-2956.

Wise, D.J. and **Smart, M.K.** (**2012**). "Forced Transition of Hypervelocity Boundary Layers". In *18th AIAA/3AF International Space Planes and Hypersonic Systems and Technologies Conference, Tours, France*. American Institute of Aeronautics and Astronautics. AIAA-2012-5866.

Zimont, V. and **Ostras, V.** (**1976**). "Calculation of Pseudo-Shocks in a Cylindrical Duct". *Fluid Mechanics-Soviet Research*, **vol. 5, no. 2**, pp. 78–87.

Appendix A

Additional Theory and Results

A.1 Aerothermodynamics of Dual Mode Scramjets

It is worth discussing the aerothermodynamics of ramjets and scramjets first to gain an appreciation of the flow processes that are involved. From this discussion the role of the dual-mode scramjet can be illustrated. The flow that passes through ramjets and scramjets undergo several different types of thermodynamic processes. To aid in the presentation of such processes, Pratt and Heiser (1993) introduced the dimensionless enthalpy-kinetic energy coordinates system referred to as H–K diagrams. A generic plot is given in Figure A.1 which serves as a legend plot for the subsequent H–K plots. The authors promote that an attractive feature of this diagram is that a number of processes appear as straight lines. The constant impulse function (Φ) used in the plots is defined by Equation (A.1). Its value is specific for an engine based on the operational parameters M and $\tau = T_t/T_{t0}$.

$$\Phi = \frac{I}{\dot{m}\sqrt{C_p T_{t0}}} = \left(\frac{\gamma - 1}{\gamma}\right)\frac{H}{\sqrt{2K}} + \sqrt{2K} = constant \tag{A.1}$$

A full discussion of these figures and the underlying equations can be found in the original texts of Pratt and Heiser (1993) and Curran et al. (1996), however it worth noting some key aspects here. Firstly, two of the isolines represent loci of states: diagonal lines of constant enthalpy (τ) represent states of adiabatic flow and lines of constant impulse (Φ) represent states of diabatic, frictionless flows for a constant area duct (i.e.

Rayleigh flow). Secondly, certain intersections represent important gas dynamic effects. The intersection of lines of constant τ and Φ represent the states of either side of a normal shock wave (Rankine-Hugoniot conditions). The intersection of constant Φ and Mach 1 isoline represents sonic or choked flow (denoted by c) and represents the maximum heat that can be added along a given impulse curve.

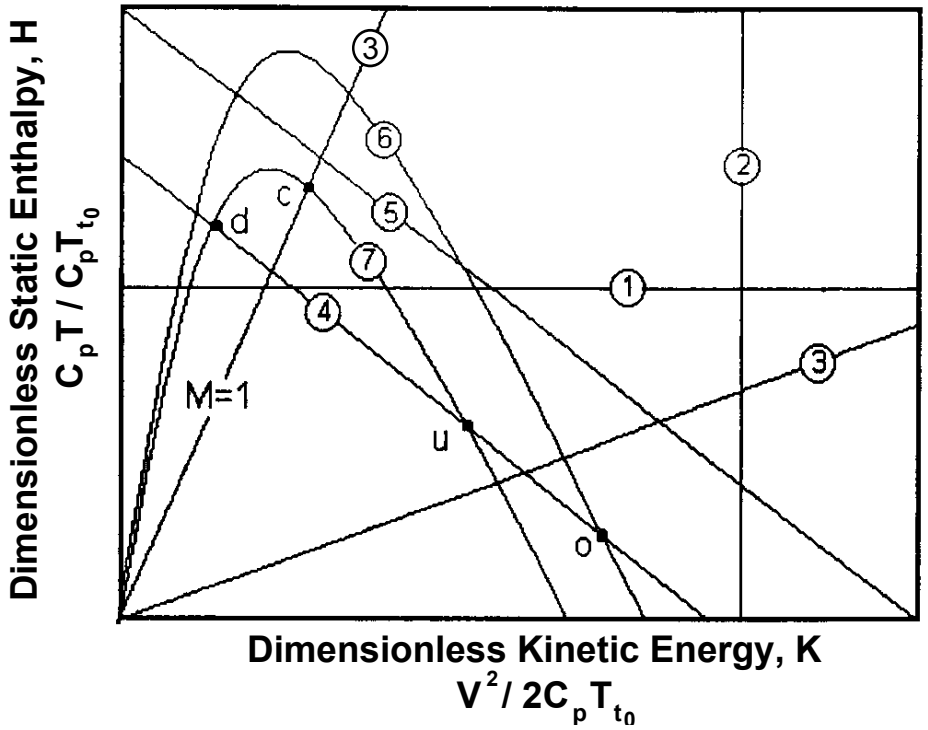

Figure A.1: Dimensionless kinetic energy versus dimensionless static enthalpy (H-K diagram) depicting constant property isolines and idealised compressible flow. Point 0 = freestream reference state. Point c = choked condition at constant impulse. Points u and d denote end states of normal shock. circled numbers denote isolines of constant: 1 static enthalpy, static temperature; 2 kinetic energy, velocity, pressure (for frictionless flow); 3 Mach number; 4 total enthalpy, total temperature, T_t/T_{t0} = 1.5; post heat release adiabatic, $T_t/T_{t0} > 1$; 6 impulse function/stream thrust, area (frictionless flow), $I = I_0$; 7 impulse function, $I < I_0$. 4 and 5 represent Fanno flow; 6 and 7 represent Rayleigh flow. (Figure and caption reproduced from Pratt and Heiser (1993)).

The next two figures reproduced here from Pratt and Heiser's 1993 analyses are the plots for the conventional ramjet and pure scramjet. These figures illustrate the significant difference between these two types of engines. In both cases the vehicle fore-body and inlet compress the flow initially from freestream conditions (point 0) to point u in the case of a ramjet or point 1 for the scramjet. For the ramjet, the flow is further compressed via a normal shock to arrive at point 1. Path d–1 represents addi-

tional subsonic diffusion in the ramjet prior to the combustion chamber. In both cases combustion is modelled either by heating at constant pressure (path 1–3) or at constant area (path 1–2); though these are just two of many different possible combustor designs.

The small operating margin for the ramjet scenario presented can be identified by noticing that if the additional subsonic diffusion did not take place (path 1–d) then the engine would quickly reach a choke point (near τ-isoline = 1.20) well before the desired amount heat had been added to the flow. (The additional diffusion places the subsequent constant area heating on a different Rayleigh curve, i.e. Φ is increased from 1.10 to 1.30). Whereas the scramjet in the scenario presented is far from choking for neither constant-pressure nor constant-area heat addition.

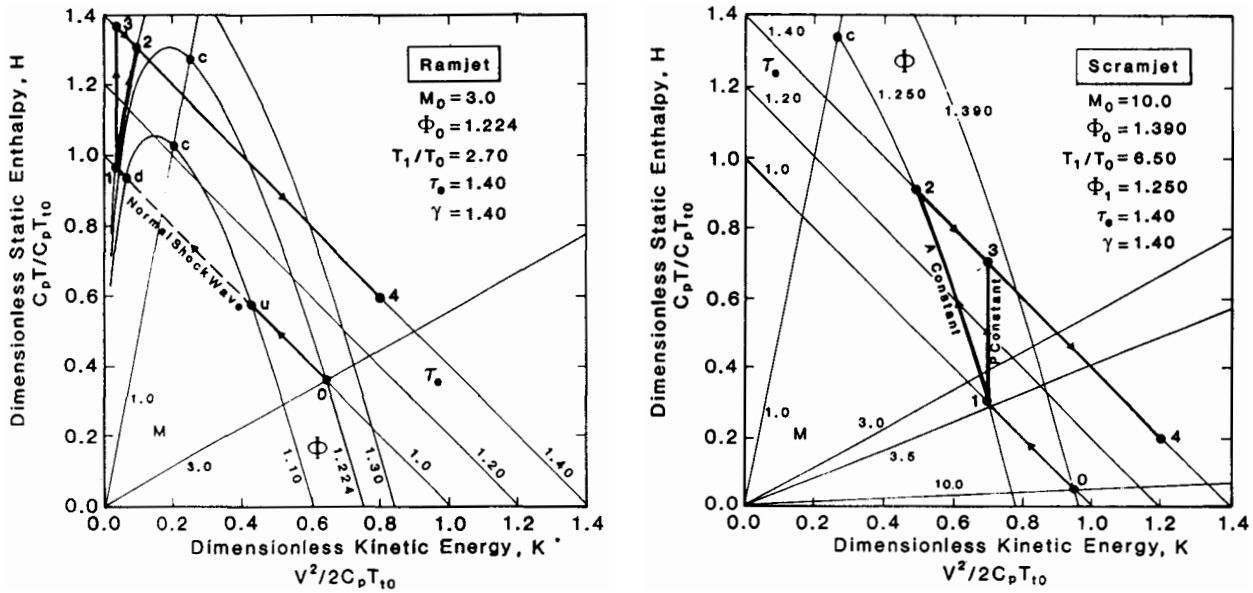

(a) Ramjet **(b)** Scramjet

Figure A.2: H-K diagrams for a ramjet and scramjet. (0–1) inlet compression, including normal shock for ramjet from u-d; (1–2) constant-area heat addition; (1–3) constant-pressure heat addition; (2–4, 3–4) thrust nozzle expansion. (c) choke point. (Figure reproduced from Curran et al. (1996))

Figure A.3 is a compilation of the separated processes described in Pratt and Heiser (1993) pertaining to the processes through a scramjet with a pre-combustion shock train. The engine being considered in this example has a constant area combustor and isolator. For normal scramjet operation combustion occurs along Path A with a total

temperature change across the engine of 1.2. However, if a adverse pressure gradient exists in the combustor this can feed forward ahead of the injection point and a pre-combustion shock train will develop. The start and end of this shock train is represented by the points u_B and d_B. The flow now undergoes additional compression before entering the combustor from points 2 to 3_B. Combustion now occurs predominately at constant pressure designated by B from 3_B to 4_B.

With increasing fuelling rates, the increase in pressure in the combustion chamber will extend the shock train forward up through a series of intermediate points up to point d_C where the subsequent combustion drives the flow to a choke point at 4_C. At this point the engine is operating at the limit of the scramjet mode.

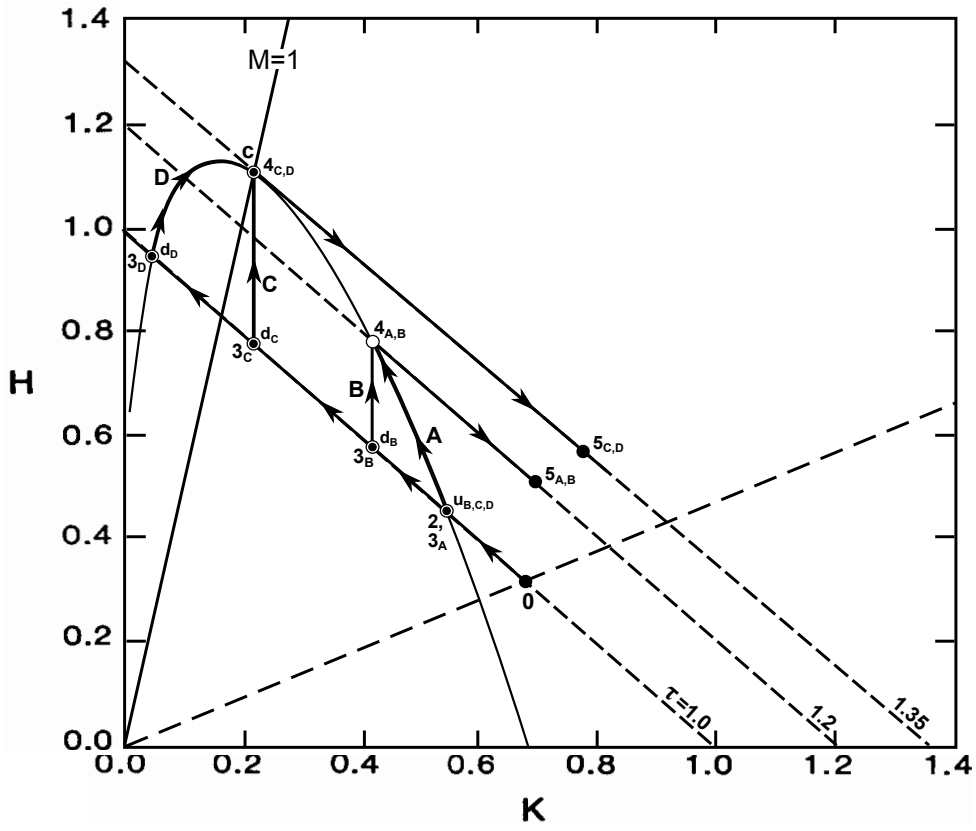

Figure A.3: H-K diagram for a dual-mode scramjet engine with a constant area isolator and constant area combustor. Paths: 0–2 forebody and inlet compression, 3–4 heat addition; 4–5 thrust nozzle expansion. Points: u and d represent start and end of a shock train respectively, c choke point. Paths A the engine operating in pure scramjet mode, B represents a the scramjet operating with a pre-combustion shock train with C being the upper limit of that mode and D represents the engine operating in ramjet mode. (Compiled from figures from Pratt and Heiser (1993))

Any further increase in the pressure rise in the combustor will cause the pre-combustion shock train to strengthen such that the outflow from the isolator is equivalent to a normal-shock (u_D to d_D) and as such would be considered a pseudo-normal-shock (Matsuo et al., 1999). Combustion now occurs along the left hand side of the Rayleigh curve (path $3_D - 4_D$). For the engine presented, this would be the operating limit as any further increase in heat release would cause an inlet unstart. This is the case as point 2 designates the end of the compression by the inlet and thereby determines the maximum pressure rise that can exist in the downstream constant area duct (i.e. the isolator) as the pressure rise across a normal shock. Any further increase in pressure across the isolator would result in a change in the inflow conditions.

Regarding these plots a few caveats must be made. Firstly, the cases C and D presented may in fact not be possible in a particular engine as it would depend largely on the length of the isolator. If the isolator is too short then it would not be possible to reach point d_C or d_D before un-starting the inlet. It should be noted that the shock train and combustion processes are highly simplified on these types of plots. A number of physical and chemical effects, such as mixing and chemical kinetics, would affect the profile of the combustion curves. Additionally, in the case of a scramjet with constant area combustor but with a pre-combustion shock train, burning could be considered to be occurring in a combustor where the area of the core flow varies along the length and as such would not necessarily follow a Rayleigh curve.

Despite the assumptions and simplifications involved these H–K diagrams are useful in visualising the dynamics of such complicated flow and highlight the potential operational boundaries. In both the C and D cases, the dual-mode scramjet can operate as a conventional ramjet by using a thermal throat where otherwise a physical one would be required. The literature on the pre-combustion shock train, the key phenomenon that permits the dual-mode operation of a fixed geometry scramjet engine, will be discussed in the following section.

A.2 Chemical Reaction Kinetics

In the combustion model used in the cycle analysis code (described in Section 5.1), it is assumed that the chemical reactions occur instantaneously and are controlled only by the mixing rate of the fuel with the air. However, in reality reaction rates are finite and are a function of the properties of test flow (Razzaqi, 2011).

Of the various chemical reaction schemes used to model the hydrogen-air reaction, the scheme often used in scramjet combustion is the one by Pergament (1963). This scheme, which is listed in Table A.2, consists of eight reactions. The reactions form two categorises: radical (and water) forming reactions and recombination reactions. The first four equations of the scheme are the bimolecular equations which produce the radicals OH, O, H in addition to forming H_2O and proceed in the forward direction. The majority of the heat release comes from the latter recombination reactions. In the reaction scheme it is assumed that nitrogen acts as a diluent and is ignored and only the hydrogen-oxygen reaction is analysed.

Using this scheme, Pergament (1963) performed a series of calculations over a range of conditions relevant to scramjet combustion and from these calculations established the following two correlations for ignition and reaction times based on the pressure and temperature of the flow.

$$t_i = \frac{8 \times 10^{-9}}{p} e^{(\frac{9600}{T})} \tag{A.2}$$

$$t_r = \frac{105 \times 10^{-6}}{p^{1.7}} e^{(\frac{-1.2T}{1000})} \tag{A.3}$$

These equations are valid for the following ranges: Pressure between 0.2 and 5 atm and temperatures between 1000 K to 2000 K. The equivalence ratio limits differ for the ignition and reaction processes. For ignition the range is $0.4 \leq \phi \leq 2$ and for reaction the range is $0.8 \leq \phi \leq 1.2$. For flows where the global equivalence ratio is outside these regions, the relations are still applicable as there will be regions within the flow where the local equivalence ratio falls between these limits.

To illustrate the effects of temperature and pressure on both ignition and reaction times, these equations are plotted in the following Figure A.4. As temperature has a greater effect than pressure on ignition and vice versa for reaction, the dominant parameter for each function is the abscissa of the relevant plot. Several curves are plotted at varying values of the less dominant parameter. On both these figures, the right hand side axis represents the corresponding ignition and reaction lengths based on the flow velocity entering the isolator. The precise condition of the flow entering the isolator of these experiments are marked on these plots and the corresponding values are listed in Table A.1.

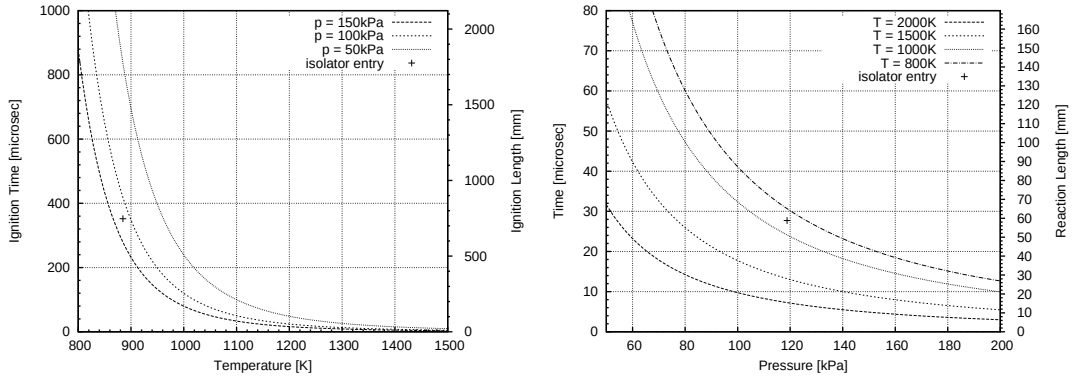

(a) Ignition time and length **(b)** Reaction time and length

Figure A.4: Ignition and reaction times with corresponding lengths for a flow speed of 2122 m s^{-1}

Table A.1: Ignition and reaction times based on the properties of flow entering the isolator (P_2=118 kPa, T_2=885 K, u_2=2122 m s^{-1})

Ignition Time µs	Ignition Length mm	Reaction Time µs	Reaction Length mm
352	747	27.7	59

The long ignition length predicted using this scheme is troubling. At an ignition length of 747 mm the point of ignition would be well past the exit of the combustion chamber; however as demonstrated in the experiments (presented in Chapter 4) ignition and near complete combustion was observed at this test condition for all three combustors. Unfortunately, due to space restrictions imposed by the fuelling system, measurements in the area where ignition was likely to have occurred were not obtained.

There are two possible explanations for this discrepancy between the predicted ignition length and what was observed in the experiment. The first is that the mean temperature of 885 K is outside the valid range of this scheme (and that the exponential increase in ignition time as temperature is reduced may not be as steep in this extrapolated region of the curve. Pergament (1963) noted that "determination of the rate constants for all reactions in the chain can be found in the literature but the accuracy of the published results, when applied to flow systems which cover a wide range of temperature, pressure, and fuel/air ratio, is certainly questionable." Pergament (1963) highlights this specific issue when cautioning on the interpretation of the results from his numerical approach when he states "Extrapolation of the empirical curve to lower temperatures [below 1000 K] can be misleading since a sharp increase in delay time is expected as the auto-ignition temperature is approached."

The second explanation is that there could be regions within the flow where the local temperature is much higher than the mean temperature across the flow and would provide a region where the ignition process is accelerated. This is akin, but different, to the idea of radical farming investigated by Odam (2004). An example of such an area would be behind the bow shock that would form around each injector porthole. Another would be where a shock impinges on the boundary layer cause an interaction of localised flow with higher temperatures than the main flow.

In the absence of a reaction scheme with a lower boundary for temperature and a detailed CFD solution of the flow around and downstream of the fuel jets, this estimation for ignition length should not be taken as a firm prediction of where ignition should be occurring. Rather it should be taken as an indication that considering a long ignition length is predicted and this is in conflict with what was observed in the experiment, that ignition must be accelerated by some additional process which is not readily identifiable.

A.3 Hydrogen-Oxygen Reaction Scheme

Reaction No.	Reaction	Rate Constant
1	$H + O_2 \longrightarrow OH + O$	$3 \times 10^{14}\, e^{\frac{-8810}{T}}$
2	$O + H_2 \longrightarrow OH + H$	$3 \times 10^{14}\, e^{\frac{-4030}{T}}$
3	$OH + H_2 \longrightarrow H_2O + H$	$3 \times 10^{14}\, e^{\frac{-3020}{T}}$
4	$2\,OH + H_2 \longrightarrow H_2O + H$	$3 \times 10^{14}\, e^{\frac{-3020}{T}}$
5	$H_2 + M \longrightarrow 2\,H + M$	$\frac{9.25 \times 10^{19}}{T}\, e^{\frac{-54000}{T}}$
6	$H_2O + M \longrightarrow H + OH + M$	$\frac{9.66 \times 10^{21}}{T}\, e^{\frac{-62200}{T}}$
7	$OH + M \longrightarrow H + O + M$	$\frac{8.0 \times 10^{19}}{T}\, e^{\frac{-52000}{T}}$
8	$O_2 + M \longrightarrow O_2 + M$	$\frac{2.9 \times 10^{19}}{T}\, e^{\frac{-60600}{T}}$

Table A.2: Hydrogen-oxygen chemical reaction scheme used by Pergament (1963)

A.4 CFD of Mach 4 nozzle

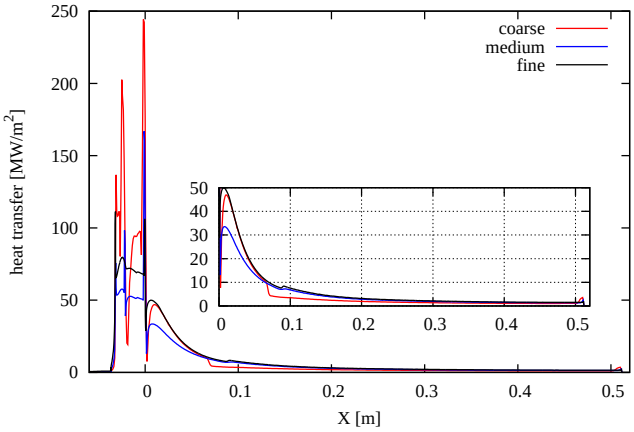

(a) Mesh sensitivity of heat transfer along nozzle wall (with insert covering region $0 \leq X \leq 0.5$).

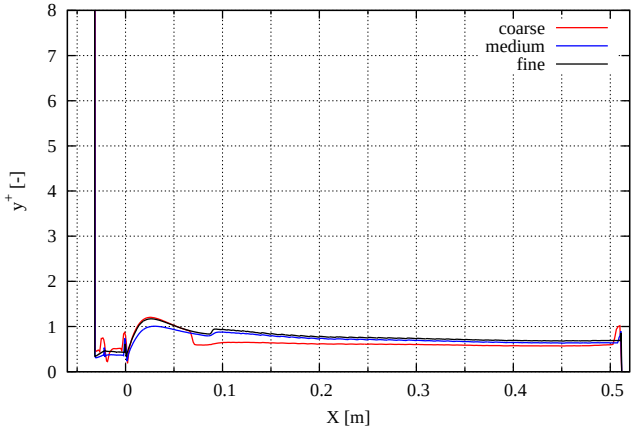

(b) Mech sensitivity of $y+$ distribution along nozzle wall

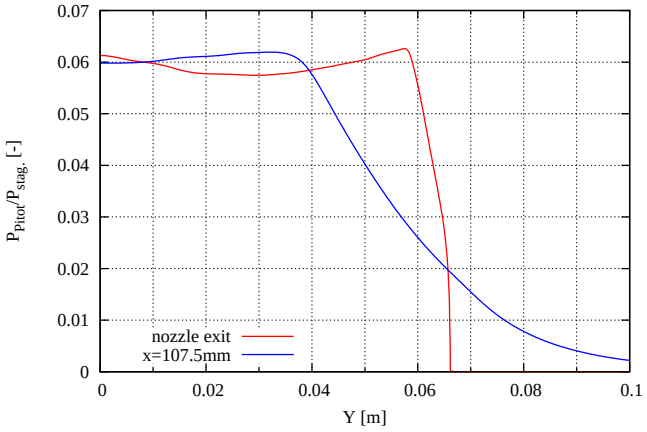

(c) Comparison of Pitot to stagnation pressure ratio at nozzle exit and at model leading edge

Figure A.5: Key results from the CFD simulation of the Mach 4 nozzle flow.

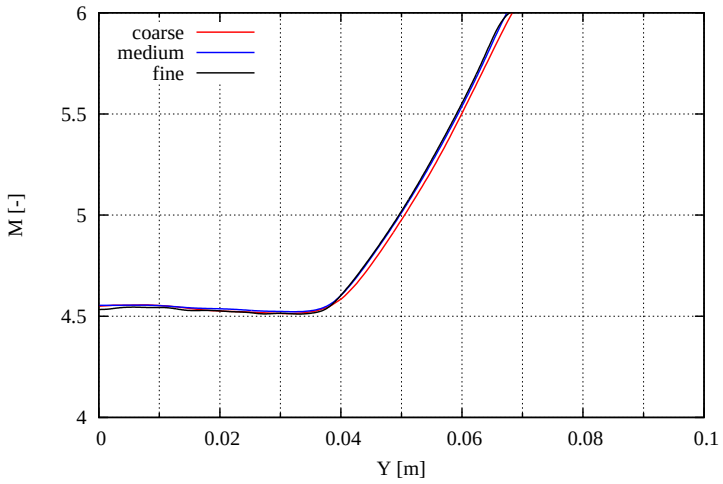

(a) Mesh sensitivity of Mach number across a plane located at the model leading edge

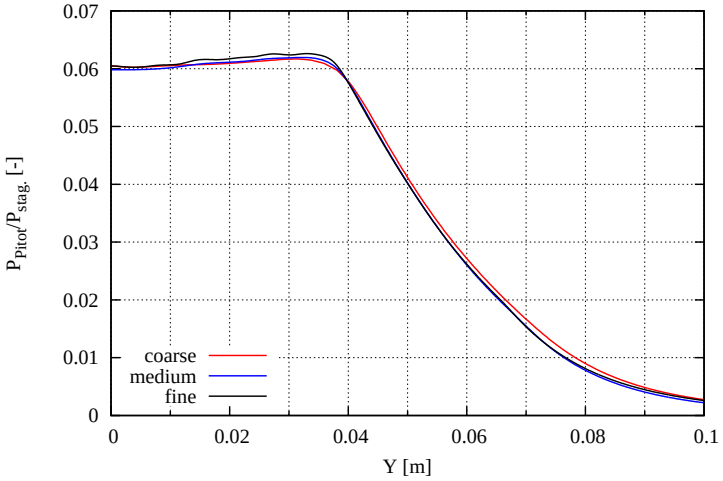

(b) Mesh sensitivity of Pitot-to-stagnation pressure ratio across a plane located at the model leading edge

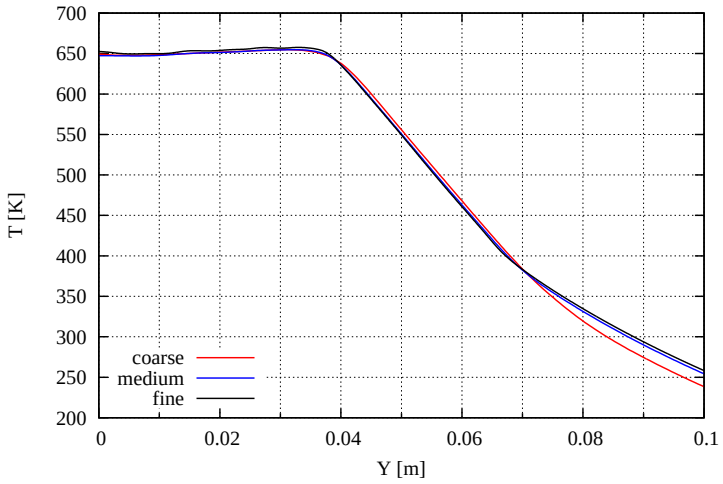

(c) Mesh sensitivity of static temperature across a plane located at the model leading edge

Figure A.6: The CFD solution sensitivity to mesh refinement for various key flow parameters

A.5 Shock Train Characteristics

A.5.1 Location of the leading edge of the shock train

The lengths of the shock trains for the separated cases for the three combustors are listed in Tables A.3 to A.5. The length S_o was determined to be the distance from the injectors to the location of the sensor which the trace satisfied Rule 4.1 in Chapter 4.

Table A.3: Location of furthest upstream sensor in the isolator where flow separated and remained separated over the test time for the constant area combustor. Distance from this point to the injectors is termed S_o

Shot No.	ϕ	Sensor Label	S_o (mm)	(D_{iso})
10829	1.06	DB7	67.9	2.0
10824	1.09	DB7	67.9	2.0
10826	1.10	DT7	74.4	2.2
10828	1.13	DT7	74.4	2.2
10827	1.18	DT7	74.4	2.2
10825	1.22	DB6	80.9	2.4
10823	1.29	DB6	80.9	2.4

Table A.4: Location of furthest upstream sensor in the isolator where flow separated and remained separated over the test time for the 2° divergent combustor. Distance from this point to the injectors is termed S_o

Shot No.	ϕ	Sensor Label	S_o (mm)	(D_{iso})
10845	1.03	DT7	74.4	2.2
10844	1.13	DT7	74.4	2.2
10843	1.14	DB7	67.9	2.0
10842	1.16	DB6	80.9	2.4
10854	1.26	DB6	80.9	2.4

Table A.5: Location of furthest upstream sensor in the isolator where flow separated and remained separated over the test time for the 1° divergent combustor. Distance from this point to the injectors is termed S_o

Shot No.	ϕ	Sensor Label	S_o (mm)	(D_{iso})
10809	0.95	DT9	48.4	1.5
10817	1.06	DB7	67.9	2.0
10819	1.10	DB7	67.9	2.0
10808	1.14	DB6	80.9	2.4
10807	1.14	DT7	74.4	2.2
10818	1.15	DT7	74.4	2.2
10816	1.20	DT6	87.4	2.6

A.5.2 Shock train establishment time versus equivalence ratio for the divergent combustors

The following figures, Figures A.7 and A.8, present the results for the divergent combustors which plot the establishment times for the isolator flow as a function of the fuel equivalence ratio. As presented and discussed before for the constant area combustor in Section 4.1.10, there is again no clear correlation between ϕ and t_{est}, the time it takes for the flow to establish in the isolator.

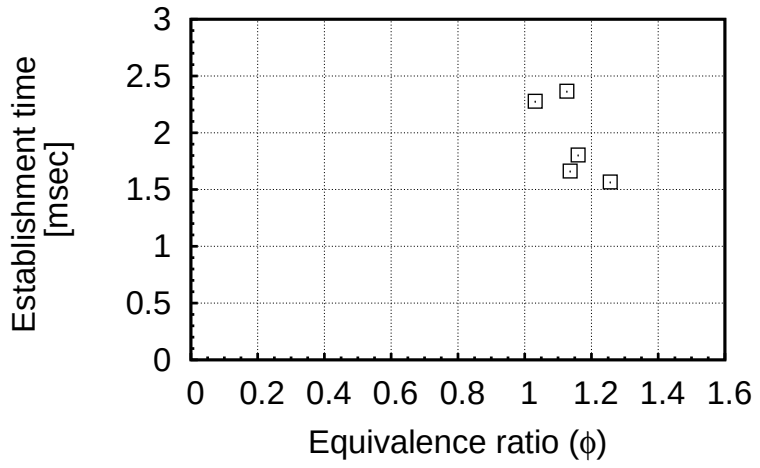

Figure A.7: Establishment times (t_{est}) for the isolator plotted versus the fuel equivalence ratio (ϕ) for the 2° divergent combustor

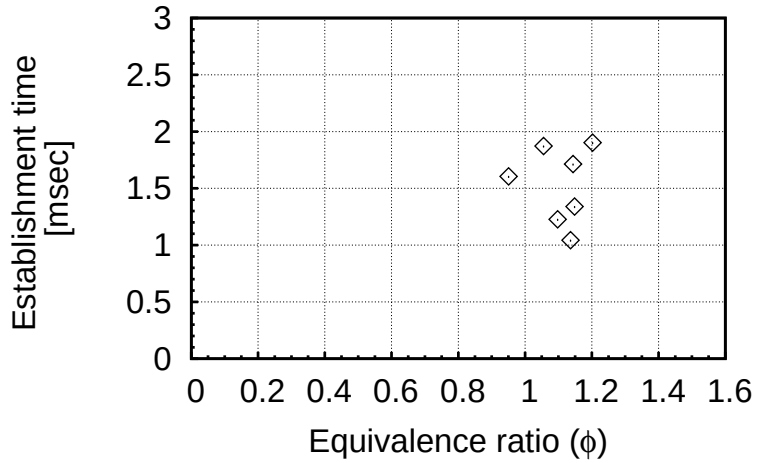

Figure A.8: Establishment times (t_{est}) for the isolator plotted versus the fuel equivalence ratio (ϕ) for the 1° divergent combustor

A.5.3 Isolator exit pressure versus equivalence ratio

In Section 4.3.2, the plots for P_{DT9}/P_∞ versus equivalence ratio were again plotted for all combustors on a single figure (Figure 4.34). Here in Figures A.9 to A.11 the data has been separated for each combustor.

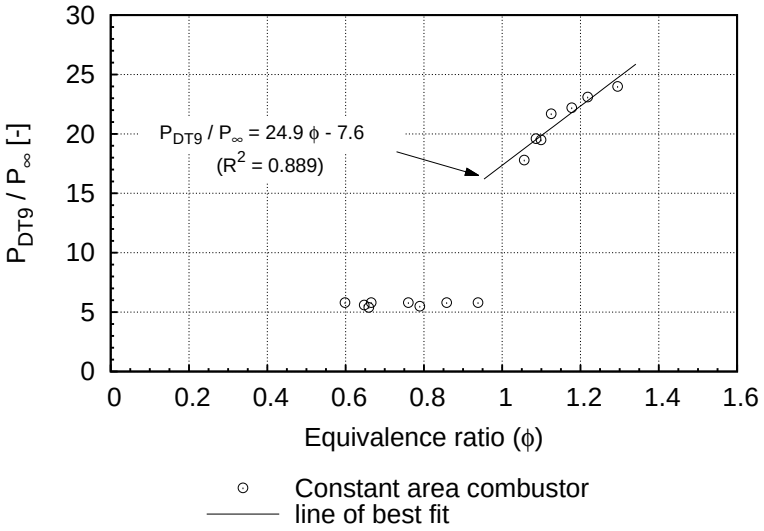

Figure A.9: Plots showing the normalised isolator exit pressure (P_{DT9}/P_∞) versus equivalence ratio (ϕ) for the constant area combustor. Line of best fit is through data only for the separated cases. R^2 is the coefficient of determination.

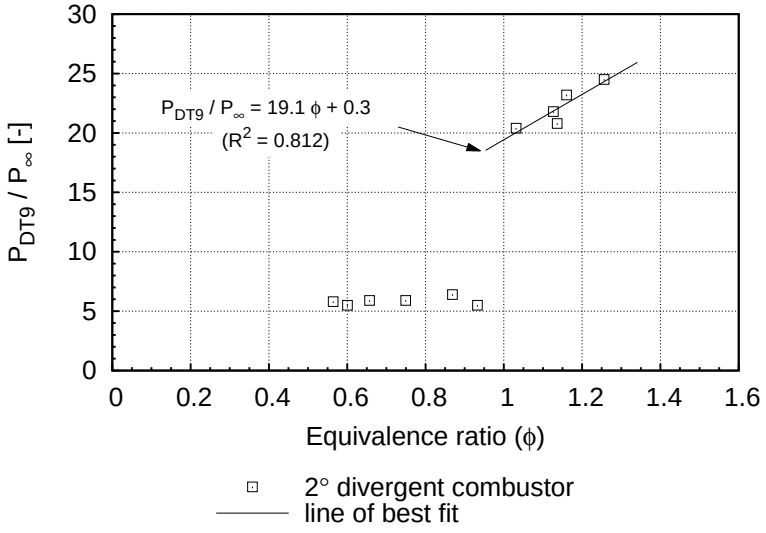

Figure A.10: Plots showing the normalised isolator exit pressure (P_{DT9}/P_∞) versus equivalence ratio (ϕ) for the 2° divergent combustor. Line of best fit is through data only for the separated cases. R^2 is the coefficient of determination.

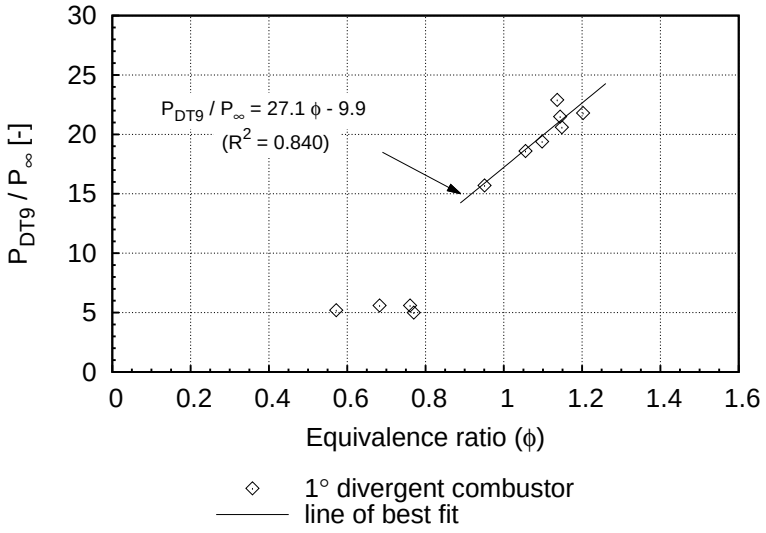

Figure A.11: Plots showing the normalised isolator exit pressure (P_{DT9}/P_∞) versus equivalence ratio (ϕ) for the 1° divergent combustor. Line of best fit is through data only for the separated cases. R^2 is the coefficient of determination.

A.5.4 Shock train length versus isolator exit pressure

In Section 4.3.1, the plots for shock train length (S_o) versus P_{DT9}/P_∞ were plotted for all combustors on a single figure (Figure 4.33). Here, in Figures A.12 to A.14 the data has been separated for each combustor.

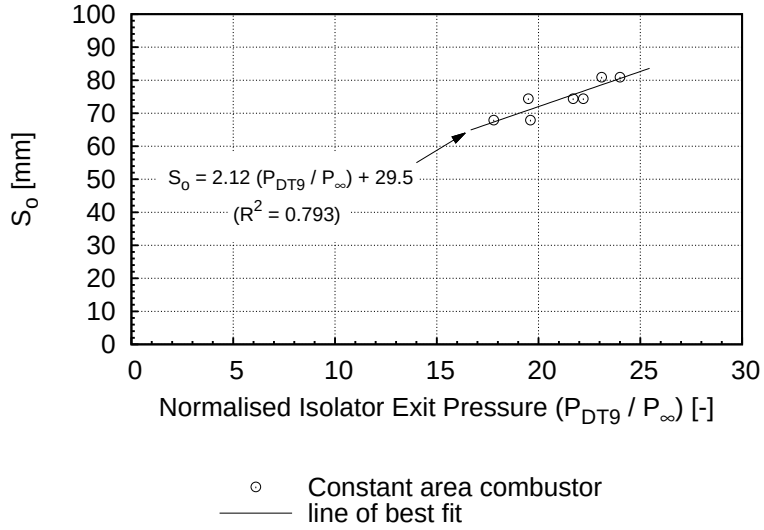

Figure A.12: Plots showing the shock train length (S_o) versus normalised isolator exit pressure (P_{DT9}/P_∞) for the constant area combustor. R^2 is the coefficient of determination.

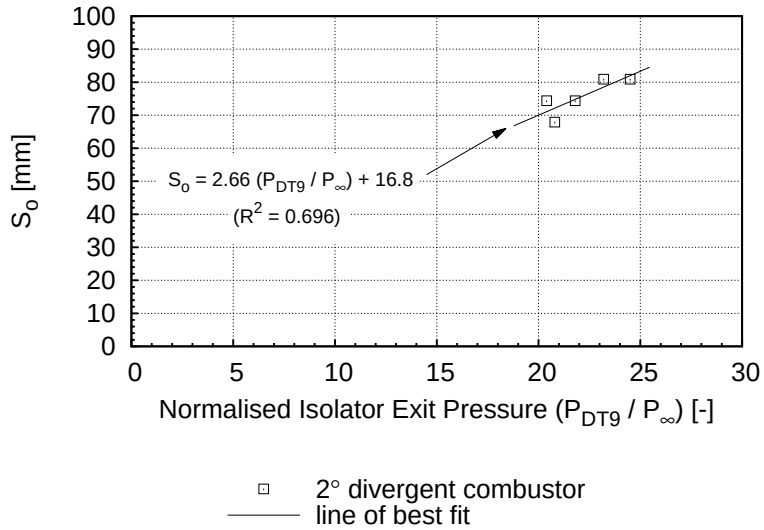

Figure A.13: Plots showing the shock train length (S_o) versus normalised isolator exit pressure (P_{DT9}/P_∞) for the 2° divergent combustor. R^2 is the coefficient of determination.

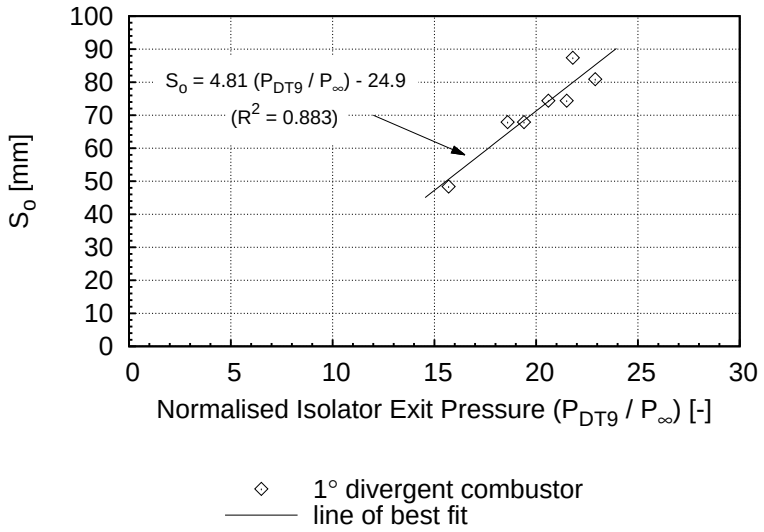

Figure A.14: Plots showing the shock train length (S_o) versus normalised isolator exit pressure (P_{DT9}/P_∞) for the 1° divergent combustor. R^2 is the coefficient of determination.

A.5.5 Shock train length versus equivalence ratio

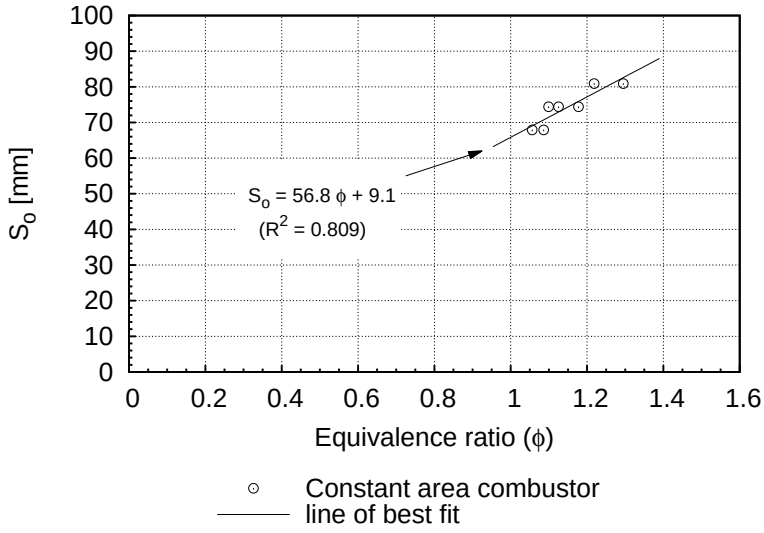

Figure A.15: Plot showing shock train length (S_o) versus equivalence ratio (ϕ) for the constant area combustor. R^2 is the coefficient of determination.

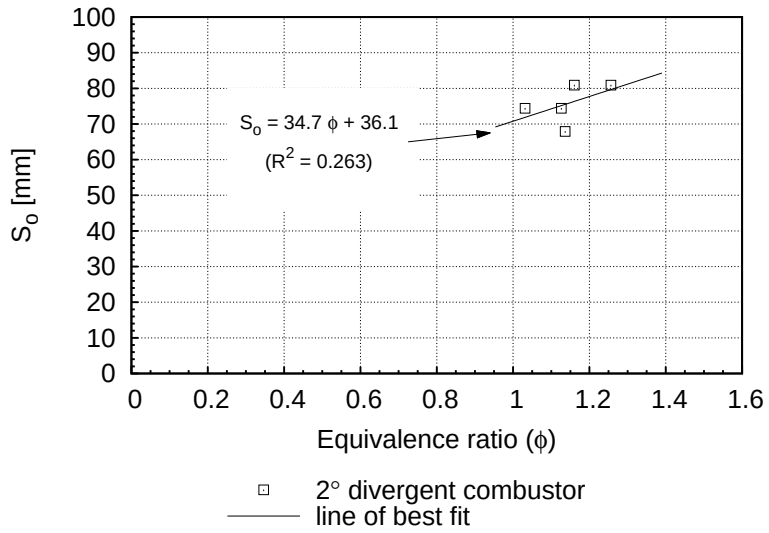

Figure A.16: Plot showing shock train length (S_o) versus equivalence ratio (ϕ) for the 2° divergent combustor. R^2 is the coefficient of determination.

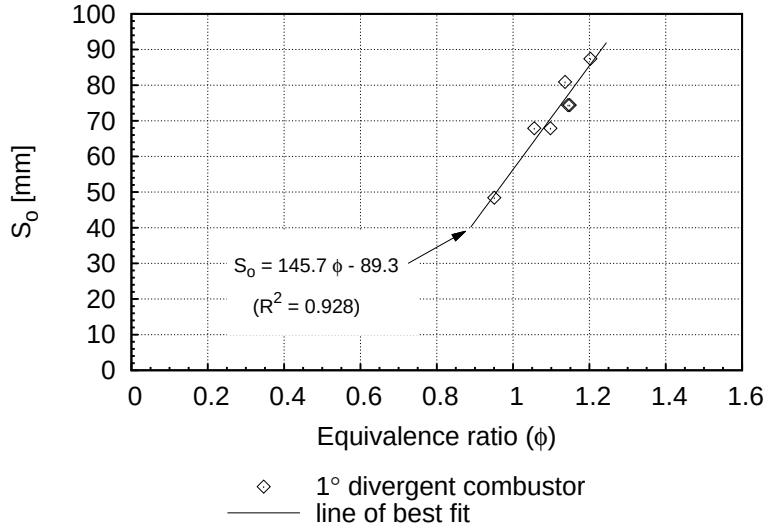

Figure A.17: Plot showing shock train length (S_o) versus equivalence ratio (ϕ) for the 1° divergent combustor. R^2 is the coefficient of determination.

A.6 Propagation Rate of Separation

The following figures, Figures A.18 to A.20, are the same time-history plots presented in Chapter 4 however a line of best fit has been plotted on each plot which intersects the points where the separation occurs. This separation is indicated by the second rapid rise in pressure for each sensor. The first figure, Figure A.18, is for a highly separated case for the constant area combustor where the isolator flow did stabilise as indicated by the constant pressure at sensor DT9. The propagation speed for this case is estimated to be 49.5 m/s. This falls in between the propagation speeds for the next two cases, Figures A.19 and A.20, for the constant area combustor which are cases for which the flow did not stabilise in the isolator within the test time. The propagation speed for these two cases are 43.6 m/s and 53.2 m/s respectively. The similar propagation speeds for these three cases indicates that the propagation speed is not dependent on the pressure at rear of the isolator. These propagation speeds are also similar in magnitude to the speeds recorded by Laurence et al. (2013) who found propagation speeds of 93 m/s for the Hyshott II engine tested in HEG.

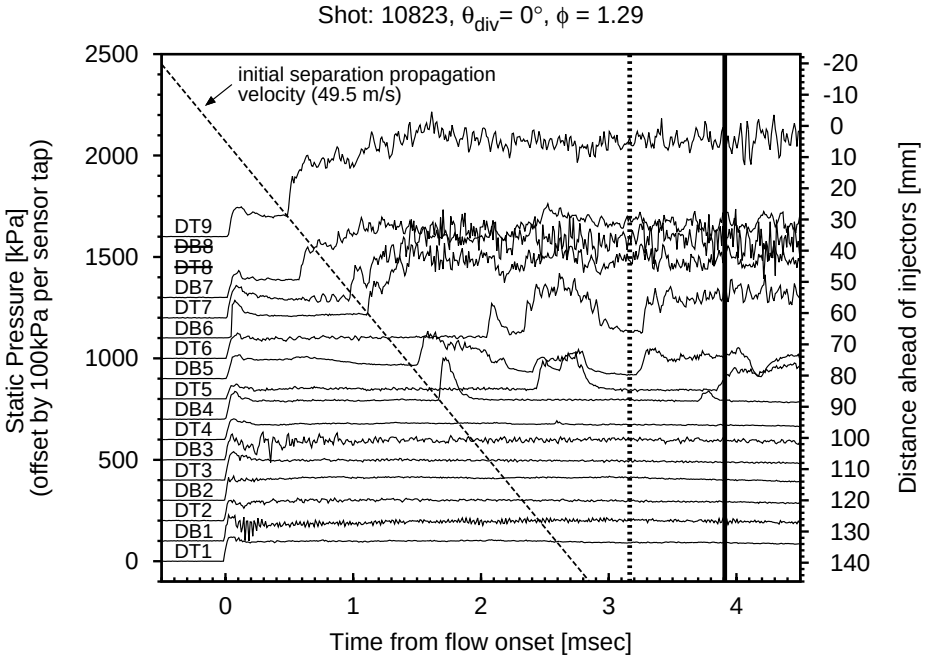

Figure A.18: Time history of the pressures sensors (DT1–DT9 and DB1–DB8) along the isolator for a highly separated case of the constant area combustor at $\phi = 1.29$ where the flow did stabilise within the test time. The diagonal line illustrates the propagation speed of the separation and is a line of best fit through the second pressure rise of the sensors along the isolator.

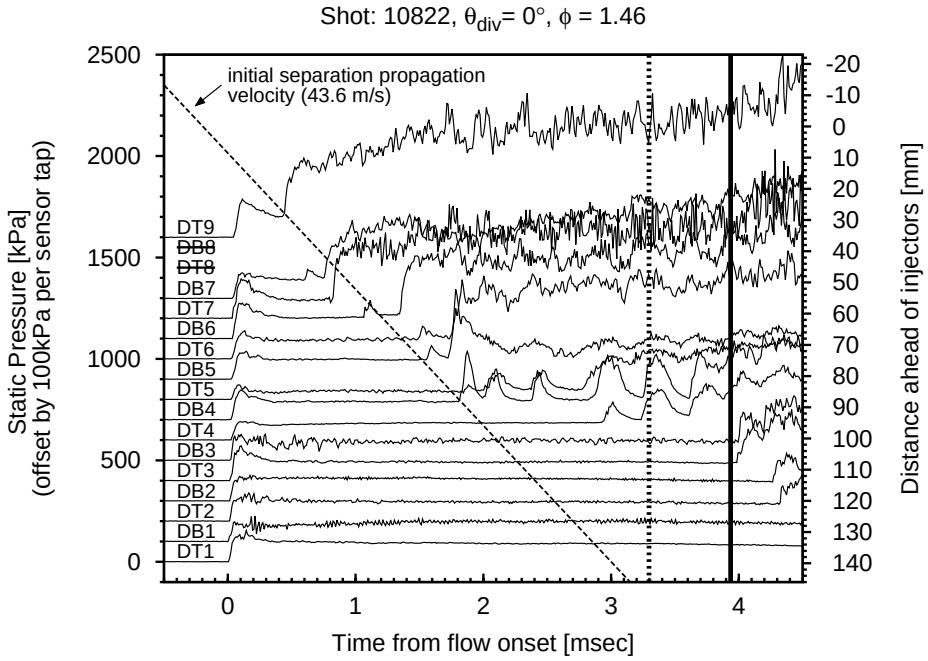

Figure A.19: Time history of the pressures sensors (DT1–DT9 and DB1–DB8) along the isolator for a highly separated case of the constant area combustor at $\phi = 1.46$ where the flow did stabilise within the test time. The diagonal line illustrates the propagation speed of the separation and is a line of best fit through the second pressure rise of the sensors along the isolator.

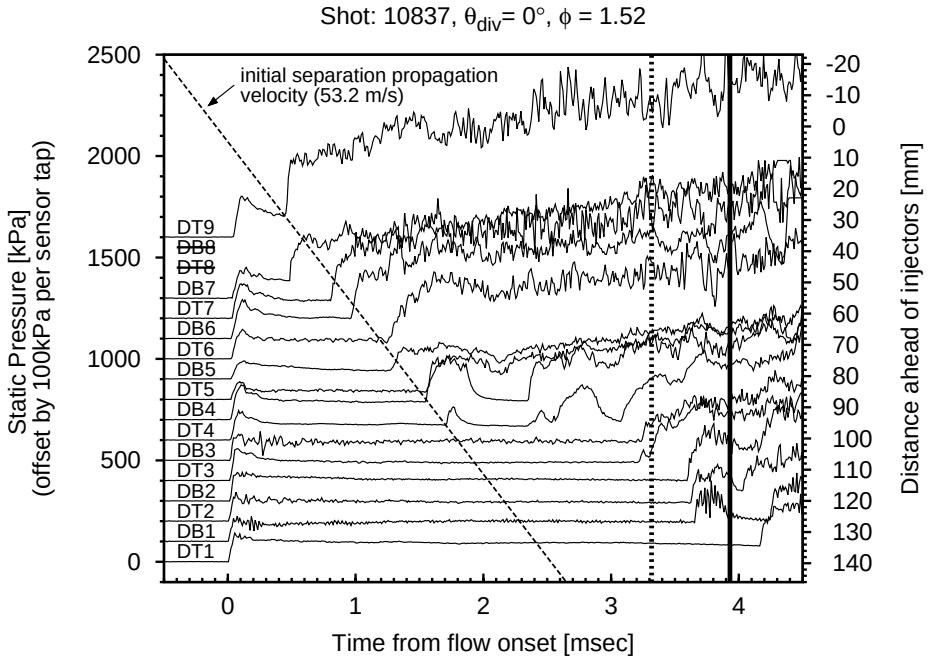

Figure A.20: Time history of the pressures sensors (DT1–DT9 and DB1–DB8) along the isolator for a highly separated case of the constant area combustor at $\phi = 1.52$ where the flow did stabilise within the test time. The diagonal line illustrates the propagation speed of the separation and is a line of best fit through the second pressure rise of the sensors along the isolator.

Appendix B

Fuel System

B.1 Calculation of Fuel Mass Flow Rate

The fuel mass flow rate as a function of the plenum chamber pressure was determined over a range of fuelling conditions using a calibration procedure outlined in the T4 Operator's Manual (Robinson et al., 2003). As the effective sonic throat area cannot be measured directly, an effective discharge coefficient, termed α, was determined experimentally. This is achieved by performing a series of fuel calibrations over the range of fuelling rates/Ludwieg fill pressures. The fuel calibration consists of filling the Ludwieg tube to the desired pressure and triggering the valve to open for 40-50ms. The pressure levels in Ludwieg tube and plenum chamber are recorded over the entire calibration test time. From the initial and final pressures of the Ludwieg tube the total volume of fuel that passed through the injectors over the test can be be determined. By integrating across the time history of the plenum pressures the discharge rate can be characterised in the form of the parameter α. Once α is known, to calculate mass flow rate over the tunnel test time, one only needs the following variables: Ludwieg tube initial pressure and plenum pressure history over the tunnel test time.

$$\alpha = \frac{\left(p_{L,f} - p_{L,i}\right) V_L}{R\, T_{L,i}\, p_{L,i}^{\frac{\gamma-1}{2\gamma}} \int_{t,i}^{t,f} p_{\text{plenum}}^{\frac{\gamma+1}{2\gamma}} dt}. \tag{B.1}$$

The mass flow rate of the fuel can then be given by:

$$\dot{m}_{\text{H}} = \alpha\, p_{L,i}^{\frac{\gamma-1}{2\gamma}}\, p_{plenum}^{\frac{\gamma+1}{2\gamma}}\,. \tag{B.2}$$

where $\dot{m}_{\mathrm{H}}$ is the instantaneous mass flow rate of fuel, α is an experimentally determined calibration constant, $p_{L,i}$ and $p_{L,f}$ are the initial and final pressures measured in the Ludwieg tube reservoir respectively, p_{plenum} is the pressure measured in the injector reservoir at flow arrival and γ is the ratio of specific heats for hydrogen.

The equivalence ratio can be determined from the following chemical equations:

$$H_2 + O_2 + 3.76N_2 \rightarrow 2H_2O + 3.76N_2 \tag{B.3}$$

$$2\,\mathrm{H_2} \;+\; \mathrm{O_2} \quad \longrightarrow \quad 2\,\mathrm{H_2O} \;+\; \Delta H\;.$$

$$\phi = 8\frac{\dot{m}_{\mathrm{H}}}{\dot{m}_{\mathrm{O}}}\;.$$

The mass flow rate of oxygen in the above equation is calculated as follows:

$$\dot{m}_{\mathrm{O}} = Y \cdot \dot{m}_{air} \tag{B.4}$$

$$\dot{m}_{air} = M_c\; A_c\; \rho_1\; u_1 \tag{B.5}$$

where Y is mass fraction of oxygen in air (=0.232), M_c is the mass capture ratio, A_c is the capture area of the diffuser, ρ_∞ and u_∞ are the density and velocity of the freestream flow respectively. For this model it assumed that the mass capture ratio (M_c) is 100% due to the sharp leading edge of the diffuser.

B.2 Effect of Pre-Test Fuel on Data Reduction

The data acquisition system (DAQ) follows the established convention for the T4 Stalker Tube in how it performs the initial post-processing of data. For these experiments, the signals from all the instrumentation for the tunnel and the model are provided as voltages to the DAQ system. For all channels, the recording of the signal commences for a short specified period before the triggering event. Before these voltages are converted into their respective property values (e.g. pressure), an offset is first calculated. This offset is the average voltage of the first 100 samples. The offset voltage is then subtracted from the entire voltage trace. This trace is then converted into its respective values based on the sensitivity of the sensor and the gain of the amplifier. Calculating and removing the offset has the advantage of removing any unwanted bias from the signal due to any electrical noise. For PCB's, as they are piezo-electric, they should be reading zero when the tunnel is fully evacuated. The Kulites on the other hand are piezo-resistive and so they provide an absolute pressure reading. However, they are designed to read zero volts at zero pressure.

Removing this offset for both types of sensors is not an issue for the non-fuelled cases as the test section is at a very low vacuum ($\leq$1 Torr) before the onset of the test flow. As such, all pressure sensors should be reading zero before the triggering event and so any non-zero voltage in the pre-trigger samples is very likely to be a bias from electrical noise which should be removed. For the fuelled-cases this is not necessarily the case. Due to the time it takes for the fuel valve to open fully, the valve is opened approximately 15 ms to 20 ms before the arrival of the test gas from the facility. This means that the initial pressure in the duct immediately before the onset of flow is not zero. To minimise the memory demands on the DAQ, the length of time for pre-trigger portion of the wall pressure measurements of the model, which are sampled at a relatively high frequency (1 MHz), is usually 5 ms. This means any influence of the fuel on the pressure measurements will present in the calculated offset for that sensor. Fortunately the DAQ records the calculated offset which has been removed and saves it to the header of the converted data for each sensor, and so the raw data can be reconstructed.

To account for this influence of fuel on the pressure readings, the offset value for the fuelled shots of these experiments was converted into their respective pressures. The signals from the PCBs simply had this initial pressure added to the post-processed data

from the DAQ. For the majority of these types of sensors, the electrical noise was small (e.g. for the fuel-off shot 10821, the mean equivalent pressure of the offsets for DT & DB sensors was 0.05 ± 0.14 kPa). The signals from the Kulites were treated differently as the offsets were larger for these sensors (e.g. for the fuel-off shot 10821, the equivalent pressures for the offsets of the Kulites ranged from -12.6 kPa to 5.4 kPa). So for the fuelled shots, first the voltage offset for each shot was added back onto the original voltages (essentially as was done for the PCBs sensors). Then the voltage offset from the fuel-off shot for a specific combustor was now assumed for all the fuelled shots for that combustor. This assumed offset was then subsequently subtracted from the entire voltage trace and the pressures were calculated from this new voltage trace. This produced quite a tight spread of the pressures measured by the six Kulites around the front edge of the combustor for the combustion-suppressed cases (e.g. for shot 10855, FE pressure range: ± 1.4 kPa and σ: 1.1 kPa). This tight spread was also true for an example of the fuelled shots (e.g. for shot 10841, FE pressure range: $\pm 1.8\%$ and σ: 1.3%). These results provides confidence that this methodology is quite sound and that the electrical bias on the Kulite signals for the fuel-off shot persisted at a similar level for the other shots for that combustor. The long term solution, however, to this issue for future experiments in the T4 Stalker Tube facility is to record the offset for the Kulites before each shot and/or to test whether the DAQ can handle extending the pre-trigger out to before the commencement of the trigger of the fuel-valve.

B.3 Jet Penetration Parameter Model

$$\frac{P}{D} = A\left(\frac{q_j}{q_a}\right)^B \cdot \left(\frac{x}{D} - C\right)^E \cdot \left(\frac{\delta}{D}\right)^F \cdot \left(\frac{\mathcal{M}_j}{\mathcal{M}_a}\right)^G \tag{B.6}$$

Table B.1: Penetration equation parameters as a function of the air Mach number from Portz and Segal (2006). For this study $M_a = 3.62$

Coefficients	Relation
$A =$	$1.049M_a - 0.192$
$B =$	$-0.08M_a + 0.615$
$C =$	$-2.34/M_a$
$E =$	$0.395M_a + 0.823$
$F =$	$-0.067M_a + 0.325$
$G =$	-0.025

Fast Acting Solenoid Valve

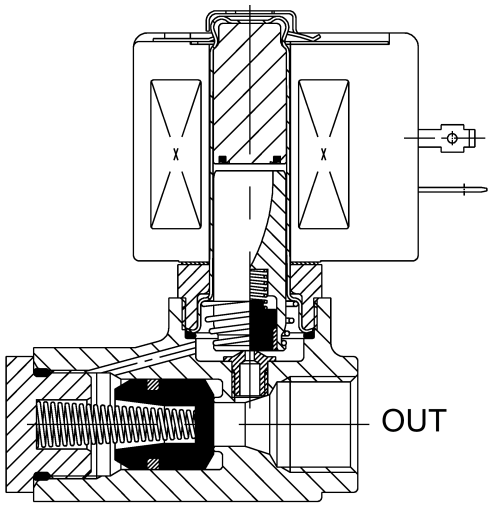

Figure B.1: Schematic of ASCO/JOUCOMATIC® fast-acting solenoid valve (sourced from Portwood (2006)).

Appendix C

Uncertainty and Repeatability

C.1 Uncertainties in the Freestream Test Conditions

A summary of the results from the following uncertainty analysis is presented in Section 3.4.2. The analysis below follows the methodology outlined by Mee (1993).

For a fundamental parameter F which has been derived from a combination of measured quantities $\psi_1 \ldots \psi_n$ can be expressed as a function such as $F = f(\psi_1, \ldots, \psi_n)$, the absolute uncertainty can be expressed as

$$\delta F = \sqrt{\sum_{i=1}^{n} (\delta F)_i^2} \tag{C.1}$$

where

$$(\delta F)_i = \left(\frac{\partial F}{\partial \psi_i} \right) \delta \psi_i \quad , \tag{C.2}$$

and

$$\psi_i = \psi_{i_{\text{true}}} + \delta \psi_i \tag{C.3}$$

The relative uncertainty in the derived quantity F can then be defined as

$$X_F = \sqrt{\sum_{i=1}^{n} (X_F)_i^2} \tag{C.4}$$

where

$$X_F = \frac{\delta F}{F} \quad , \quad (X_F)_i = \left(\frac{\partial X_F}{\partial X_{\psi_i}}\right) X_{\psi_i} \quad , \quad X_{\psi_i} = \frac{\delta \psi_i}{\psi_i}$$

and where

$$\frac{\partial X_F}{\partial X_{\psi_i}} = \frac{\left(\frac{F_{\psi_i^+} - F_{\psi_i^-}}{F_{\psi_i}}\right)}{\left(\frac{\psi_i^+ - \psi_i^-}{\psi_i}\right)}$$

Table C.1: Fundamental relative uncertainties of the measured quantities. Values taken from Mee (1993)

Parameter	Description	Relative Uncertainty (%)
P_{ST}	Shock Tube Fill Pressure	4
T_{ST}	Shock Tube Fill Temperature	2
u_{ss}	Incident Shock Speed	5
P_S	Nozzle-Supply Pressure	4
P_{Pitot}	Pitot Pressure	8

Table C.2: Sensitivity $(\partial X_F / \partial X_{\psi_i})$ of the freestream conditions to the measured quantities.

		$\partial X_F / \partial X_{\psi_i}$								
ψ_i	$F =$	T_S	H_S	T_∞	P_∞	ρ_∞	u_∞	M_∞	$\rho_\infty u_\infty$	q_∞
P_{ST}		−0·17	−0·23	−0·26	−0·06	0·20	−0·10	0·02	0·10	0·00
T_{ST}		0·24	0·27	0·38	0·10	−0·28	0·14	−0·04	−0·14	0·00
U_{ss}		0·89	1·23	1·38	0·34	−1·05	0·52	−0·13	−0·52	0·00
P_S		0·18	0·23	−0·11	−0·43	−0·32	0·16	0·21	−0·16	0·00
P_{Pitot}		0·00	0·00	0·36	1·46	1·10	−0·06	−0·23	1·04	0·98

Table C.3: Components $\left((X_F)_{\psi_i}\right)$ of the total uncertainties (X_F) of the test condition.

		$(X_F)_{\psi_i}$							
ψ_i	$F =$	H_S	T_∞	P_∞	ρ_∞	u_∞	M_∞	$\rho_\infty u_\infty$	q_∞
P_{ST}		1·87	2·09	0·49	1·60	0·79	0·20	0·81	0·01
T_{ST}		0·54	0·76	0·20	0·56	0·28	0·08	0·27	0·01
U_{ss}		6·16	6·92	1·69	5·24	2·62	0·65	2·62	0·00
P_S		1·17	0·55	2·13	1·58	0·79	1·04	0·79	0·01
P_{Pitot}		0·00	2·92	11·68	8·80	0·46	1·85	8·34	7·87
X_F		6·57	7·85	12·01	10·50	2·90	2·23	8·82	7·87

The plots in Section 4.2 are in the form of P_w/P_∞, where P_w is the pressure measured at the wall of the engine and P_∞ is the calculated freestream pressure from *NENZF*. This is a simple fractional relation which can be treated in same manner as the fuel equivalence ratio, which is discussed in Appendix C.2, and is simply the root of the sum of the relatively uncertainties squared. For the ratio based on the PCB sensors, which have an estimated installed uncertainty of 4%, and taking the uncertainty for P_∞ of 12.01% from Table C.3, the total uncertainty for P_w/P_∞ is 12.7%. The uncertainty for P_w/P_∞ based on the Kulites just downstream of injection will be less than for PCBs as this measurement is an average of six independent sensors. If the same uncertainty for a PCB sensor is adopted for an individual Kulite, then the uncertainty for the average of the six Kulites would be 1.6%. This results in a total uncertainty for P_w/P_∞ for the front-edge pressure of 12.1%. However, for simplicity, the larger uncertainty for P_w/P_∞ from the PCB sensors is used for both the PCB and Kulite measurements and is represented by the error bars in the plots in Section 4.2.

C.2 Uncertainties in the Fuelling Conditions

Since the derived quantities of interest relating to the fuelling (the discharge coefficient α, mass flow rate of hydrogen $\dot{m}_{H_2}$, mass flow rate of oxygen $\dot{m}_{O_2}$ and the equivalence ratio ϕ) are in the form $F = \text{constant} \cdot \psi_1^{m_1}\psi_2^{m_2}\ldots\psi_n^{n_1}$, then the relative sensitivity $\frac{\partial F}{\partial \psi_i}$ can be obtained directly analytically by differentiating F with respect to ψ. As such, the perturbation method in Appendix C.1 can be skipped in determining the sensitivity of the derived quantities for the fuelling condition.

$$(X_F)_i = \left(\frac{\partial X_F}{\partial X_{\psi_i}}\right) X_{\psi_i} \quad = \quad m_i \frac{\delta \psi_i}{\psi_i} \tag{C.5}$$

$$X_F = \sqrt{\sum_{i=1}^{n} \left(m_i \frac{\delta \psi_i}{\psi_i}\right)^2} \tag{C.6}$$

Table C.4: Fundamental relative uncertainties of the measured quantities relating to the fuel system. Values taken from Chan (2012)

Parameter	Description	Relative Uncertainty (%)
P_{LT_i}	Ludwieg tube initial fill pressure	2
P_{LT_f}	Ludwieg tube final fill pressure	2
T_{LT_i}	Ludwieg tube initial temperature	3
V_{LT}	Ludwieg tube volume	3
P_{plenum}	Plenum chamber pressure	3

Table C.5: Sensitivity $(\partial X_F / \partial X_{\psi_i})$ of the discharge coefficient (α) due to the measured and calculated quantities.

ψ_i	$\partial X_\alpha / \partial X_{\psi_i}$	$(X_\alpha)_{\psi_i}$
P_{LT_i}	2·205	4·41
P_{LT_f}	−1·348	2·70
T_{LT_i}	−1·000	2·00
V_{LT}	−1·000	3·00
$\int P_{\mathrm{plen}}$	−1·000	2·57
X_F		6·81

where $\int P_{\mathrm{plen}} = \int_{t_i}^{t_f} P_{\mathrm{plen}}^{\frac{\gamma+1}{2\gamma}}$

Table C.6: Sensitivity $(\partial X_F / \partial X_{\psi_i})$ of the fuel mass flow rate $(\dot{m}_F)$ due to the measured quantities

ψ_i	$\partial X_{\dot{m}_F} / \partial X_{\psi_i}$	$(X_{\dot{m}_F})_{\psi_i}$
P_{LT_i}	0·143	0·29
P_{plen}	0·857	2·57
α	1·000	6·81
X_F		7·28

Finally, as the equivalence ratio is a function of only the mass flow rate of hydrogen and the mass flow rate of oxygen, and the mass flow rate is a fraction of the mass flow rate of air, the uncertainty relating to the equivalence ratio comes directly from the root sum square of the relative uncertainties of $\dot{m}_{H_2}$ and $\rho_\infty u_\infty$.

Table C.7: Relative uncertainties of the fuelling conditions.

Parameter	Description	Relative Uncertainty (%)
α	Discharge coefficient	6.8
$\dot{m}_{H_2}$	Mass flow rate of hydrogen	7.3
$\dot{m}_{O_2}$	Mass flow rate of oxygen	8.8
ϕ	Equivalence ratio	11.4

C.3 Repeatability of Test Conditions

There is some variability in the test flow produced by the facility due to a number of factors, including differences in the ambient conditions, the openning characteristics of primary diaphragm, and in the fill pressures due to the tendencies of different operators. The repeatability of the test conditions is evaluated on 95% confidence interval given by

$$I(x) = 1.96\frac{\sigma(x)}{x} \times 100 \tag{C.7}$$

where x the mean value of a parameter and $\sigma(x)$ is the standard deviation about this mean value and $I(x)$ is the 95% confidence interval as percentage of the mean value. Estimates for $I(x)$ are present in Table C.8 for the experiments where air is the test gas.

Table C.8: Repeatability of the test flow conditions (for air as the test gas) expressed as a 95% confidence interval. Shots: 10804–10855 (air only), N = 48

x	U_{ss}	H_0	P_0	T_0	P_∞	T_∞	ρ_∞	u_∞	M_∞
Units	m/s	MJ/kg	MPa	K	kPa	K	kg/m^3	m/s	-
Mean Value	1817	3.12	19.6	2815	43.6	671	0.226	2332	4.54
$I(x)$ [%]	2.1	3.7	7.1	2.7	7.7	4.0	5.8	1.6	0.3

In general there is generally good repeatability for this condition over the set of shots. The largest variability is for the stagnation pressure (P_0) and the calculated freestream static pressure (P_∞), the latter is expected to have a minor effect on the

flow phenomena being studied. To account for this variation, the pressure distributions presented in Chapter 4 are presented as normalised pressures. The flow speed of the freestream and Mach number are of more critical importance and it is reassuring that both these parameters have a low variability under 2% and 0.5% respectively.

C.4 Repeatability of Flow Phenomena

Figures C.1 to C.3 show the repeatability of the tests with combustion at two different fuelling levels for each of the three combustors. The layout and basis for these figures are discussed in detail in Chapter 4. These figures show very good repeatability over both a range of equivalence ratios (ϕ) and for all three combustors.

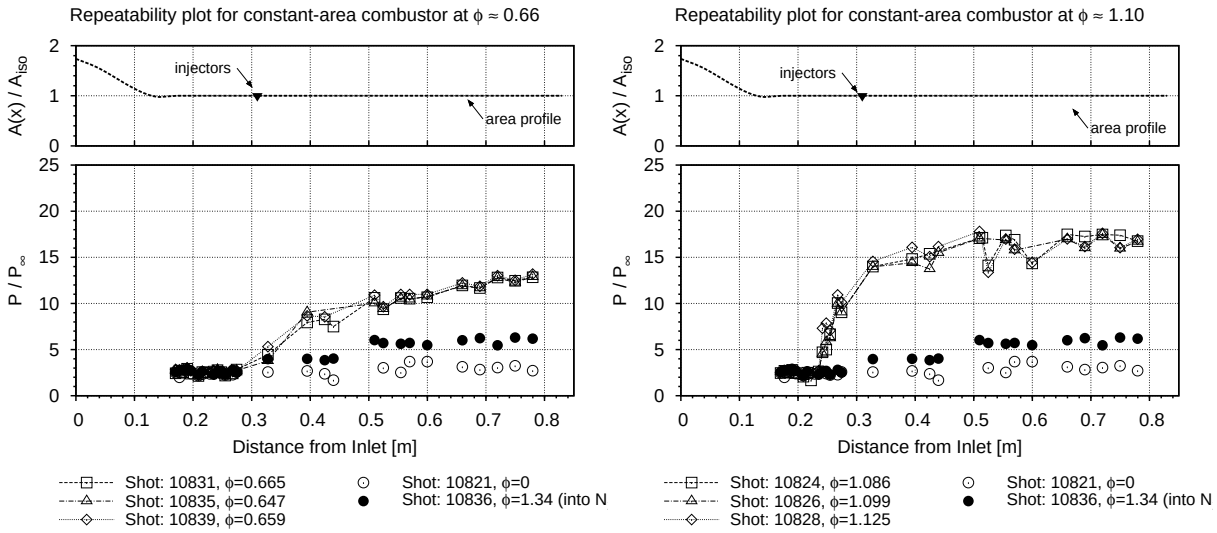

(a) $\phi \approx 0.66$ **(b)** $\phi \approx 1.10$

Figure C.1: Plots showing repeatability of testing with combustion in the constant area combustor at mid and high fuelling levels

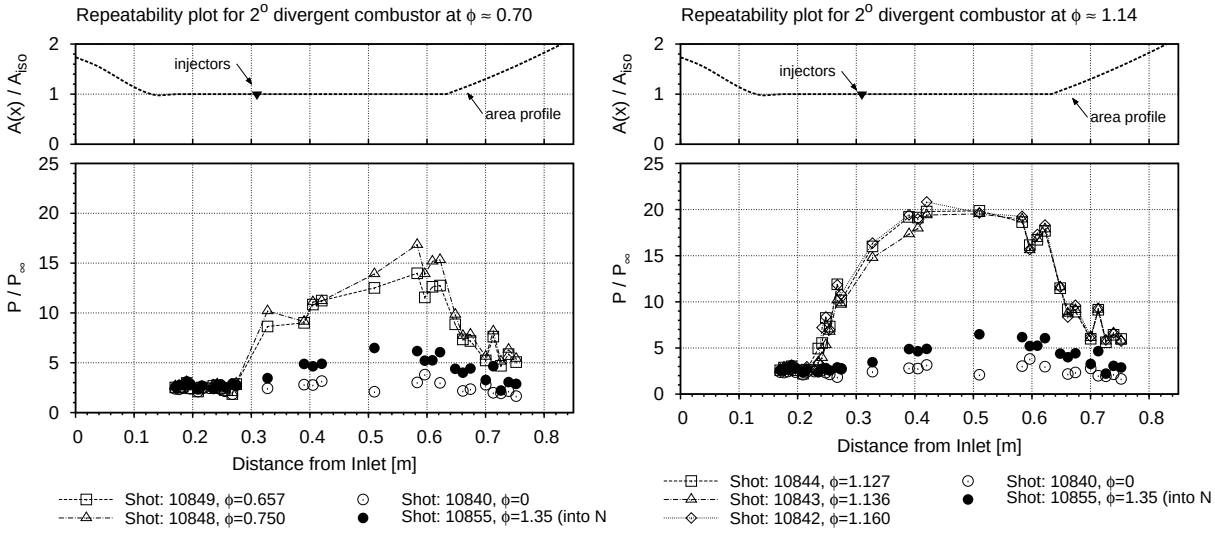

(a) $\phi \approx 0.70$ **(b)** $\phi \approx 1.14$

Figure C.2: Plots showing repeatability of testing with combustion in the 2° divergent combustor at mid and high fuelling levels

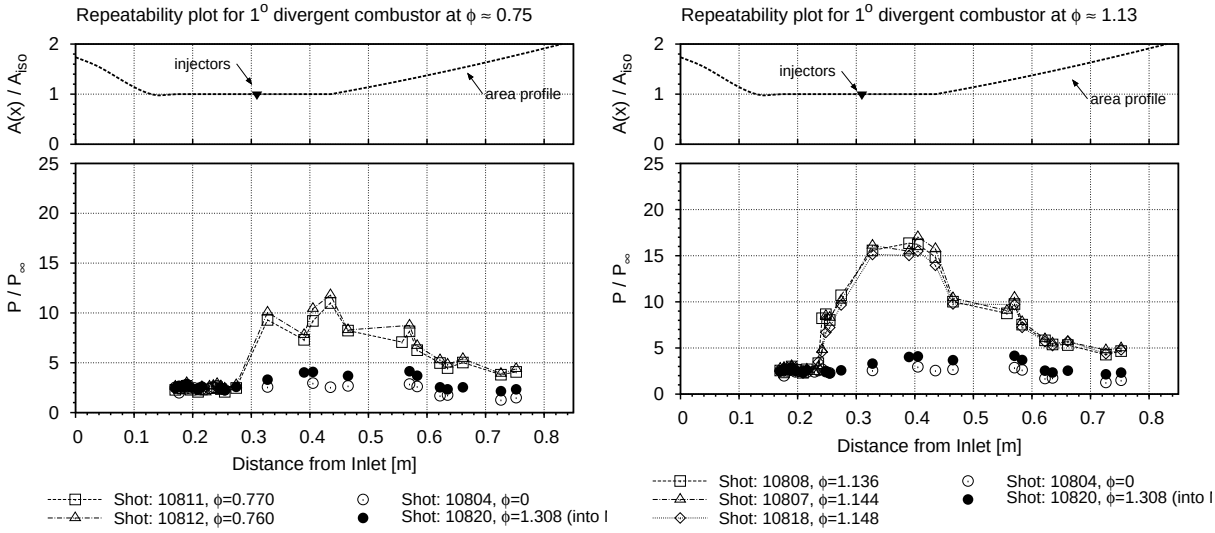

(a) $\phi \approx 0.77$ **(b)** $\phi \approx 1.13$

Figure C.3: Plots showing repeatability of testing with combustion in the 1° divergent combustors at mid and high fuelling levels

Appendix D

Experimental Runs

This Appendix contains the key parameters for each experiment. Table D.1 contains the operational parameters of the T4 Stalker Tube as well as the calculated freestream properties. Table D.2 contains the initial conditions of the fuel system, the measured plenum pressures, the calculated mass flow rates for both the fuel and freestream, and the calculated equivalence ratios.

Notation for the T4 Stalker Tube parameters:

Shot. No	Shot number
P_{Res}	Fill pressure of reservoir
P_{CT}	Fill pressure of compression tube
gas comp.	Volume fraction of Argon in driver gas
diaph.	Primary diaphragm thickness
test gas	Test gas (air or nitrogen) in shock tube
P_{ST}	Fill pressure of shock tube
T_{ST}	Fill temperature of shock tube
u_{ss}	Incident shock speed in shock tube
H_S	Nozzle-supply enthalpy
P_S	Nozzle-supply pressure
T_S	Nozzle-supply temperature
ρ_S	Nozzle-supply density
P_∞	Freestream static pressure
T_∞	Freestream temperature
ρ_∞	Freestream density
u_∞	Freestream flow speed
M_∞	Freestream Mach number

Table D.1: Shock tunnel operational parameters and the resulting free-stream flow properties. All shots performed with the Mach 4 nozzle.

	Reser.	Comp. Tube			Shock Tube				Nozzle Supply				Nozzle Exit				
Shot	P_{Res}	P_{CT}	gas comp.	diaph.	test	P_{ST}	T_{ST}	u_{ss}	H_S	P_S	T_S	ρ_S	P_∞	T_∞	ρ_∞	u_∞	M_∞
No.	MPa	kPa	%Ar	mm		kPa	K	m/s	MJ/kg	MPa	K	kg/m^3	kPa	K	kg/m^3	m/s	-
10804	2.6	40.2	100	3	air	130	300	1786.8	3.04	19.56	2766.6	24.62	43.26	654	0.230	2309	4.55
10805	2.6	40.2	100	3	air	130	300	1841.0	3.22	20.71	2884.9	24.98	46.41	696	0.232	2365	4.53
10806	2.6	40.2	100	3	air	130	300	1812.7	3.13	20.19	2825.2	24.88	44.94	675	0.232	2337	4.54
10807	2.6	40.2	100	3	air	130	300	1799.6	3.05	18.91	2768.6	23.78	41.81	655	0.222	2310	4.55
10808	2.6	40.2	100	3	air	130	300	1791.6	3.09	20.36	2796.0	25.35	45.20	665	0.237	2323	4.54
10809	2.6	40.2	100	3	air	130	300	1820.9	3.14	19.85	2829.1	24.43	44.20	676	0.228	2338	4.54
10811	2.6	40.2	100	3	air	130	300	1852.9	3.29	21.65	2929.1	25.72	48.77	712	0.239	2385	4.52
10812	2.6	40.2	100	3	air	130	300	1841.0	3.17	19.49	2851.3	23.79	43.53	684	0.222	2349	4.54
10813	2.6	40.2	100	3	air	130	300	1846.1	3.22	20.35	2883.2	24.56	45.63	696	0.229	2364	4.53
10814	2.6	40.2	100	3	air	130	300	1782.0	3.10	21.44	2808.5	26.57	47.61	669	0.248	2328	4.54
10815	2.6	40.2	100	3	air	130	300	1791.6	3.04	19.11	2761.6	24.10	42.25	653	0.225	2306	4.55
10816	2.6	40.2	100	3	air	130	300	1782.0	3.10	21.21	2802.7	26.35	47.13	667	0.246	2326	4.54
10817	2.6	40.2	100	3	air	130	300	1799.6	3.07	19.40	2782.3	24.27	42.96	660	0.227	2316	4.55
10818	2.6	40.2	100	3	air	130	300	1819.3	3.11	19.39	2813.6	23.99	43.13	671	0.224	2331	4.54
10819	2.6	40.2	100	3	air	130	300	1775.7	3.04	20.02	2761.1	25.25	44.23	653	0.236	2306	4.55
10820	2.6	40.2	100	3	N_2	130	300	1834.3	3.22	19.77	2932.6	22.72	42.50	652	0.220	2378	4.61
10821	2.6	40.2	100	3	air	130	300	1824.2	3.14	19.86	2834.7	24.38	44.24	678	0.227	2341	4.54
10822	2.6	40.2	100	3	air	130	300	1804.5	3.05	18.76	2771.9	23.56	41.51	656	0.220	2311	4.55
10823	2.6	40.2	100	3	air	130	300	1830.9	3.16	19.85	2845.2	24.29	44.27	682	0.226	2346	4.54
10824	2.6	40.2	100	3	air	130	300	1817.6	3.15	20.39	2838.4	25.00	45.47	680	0.233	2343	4.54
10825	2.6	40.2	100	3	air	130	300	1806.1	3.08	19.44	2794.2	24.23	43.13	664	0.226	2322	4.54
10826	2.6	40.2	100	3	air	130	300	1832.6	3.18	20.29	2859.9	24.70	45.37	687	0.230	2353	4.53
10827	2.6	40.2	100	3	air	130	300	1780.4	2.99	18.62	2729.7	23.75	41.00	642	0.223	2291	4.56
10828	2.6	40.2	100	3	air	130	300	1802.9	3.08	19.58	2792.8	24.41	43.42	664	0.228	2321	4.55
10829	2.6	40.2	100	3	air	130	300	1834.3	3.14	19.21	2832.4	23.61	42.78	678	0.220	2340	4.54

Table D.1: continued.

	Reser.	Comp. Tube			Shock Tube				Nozzle Supply				Nozzle Exit				
Shot No.	P_{Res} MPa	P_{CT} kPa	gas comp. %Ar	diaph. mm	test	P_{ST} kPa	T_{ST} K	u_{ss} m/s	H_S MJ/kg	P_S MPa	T_S K	ρ_S kg/m^3	P_∞ kPa	T_∞ K	ρ_∞ kg/m^3	u_∞ m/s	M_∞ -
10830	2.6	40.2	100	3	air	130	300	1837.6	3.15	19.28	2840.0	23.63	42.99	680	0.220	2344	4.54
10831	2.6	40.2	100	3	air	130	300	1832.6	3.16	19.84	2847.6	24.25	44.30	683	0.226	2347	4.53
10832	2.6	40.2	100	3	air	130	300	1829.2	3.13	19.20	2824.3	23.67	42.73	675	0.221	2336	4.54
10833	2.6	40.2	100	3	air	130	300	1783.6	2.99	18.38	2728.0	23.46	40.46	641	0.220	2291	4.56
10834	2.6	40.2	100	3	air	130	300	1824.2	3.14	19.67	2829.5	24.20	43.83	677	0.226	2339	4.54
10835	2.6	40.2	100	3	air	130	300	1811.0	3.08	18.96	2788.1	23.67	42.02	662	0.221	2319	4.55
10836	2.6	40.2	100	3	N_2	130	300	1832.6	3.19	19.13	2907.9	22.16	40.99	645	0.214	2368	4.61
10837	2.6	40.2	100	3	air	130	300	1786.8	3.02	19.03	2751.7	24.08	42.02	649	0.225	2302	4.55
10838	2.6	40.2	100	3	air	130	300	1835.9	3.16	19.53	2844.2	23.90	43.56	682	0.223	2346	4.54
10839	2.6	40.2	100	3	air	130	300	1822.6	3.08	18.53	2794.1	23.09	41.09	664	0.216	2322	4.55
10840	2.6	40.2	100	3	air	130	300	1830.9	3.16	19.93	2847.4	24.36	44.51	683	0.227	2347	4.53
10841	2.6	40.2	100	3	air	130	300	1832.6	3.14	19.36	2834.0	23.78	43.14	678	0.222	2341	4.54
10842	2.6	40.2	100	3	air	130	300	1819.3	3.09	18.89	2799.4	23.50	41.95	666	0.219	2324	4.54
10843	2.6	40.2	100	3	air	130	300	1847.8	3.19	19.50	2862.3	23.71	43.57	688	0.221	2354	4.53
10844	2.6	40.2	100	3	air	130	300	1830.9	3.15	19.59	2837.9	24.03	43.68	680	0.224	2343	4.54
10845	2.6	40.2	100	3	air	130	300	1807.8	3.09	19.55	2799.6	24.31	43.41	666	0.227	2324	4.54
10846	2.6	40.2	100	3	air	130	300	1829.2	3.15	19.77	2840.1	24.22	44.08	680	0.226	2344	4.54
10847	2.6	40.2	100	3	air	130	300	1820.9	3.09	18.76	2798.2	23.34	41.63	666	0.218	2324	4.54
10848	2.6	40.2	100	3	air	130	300	1829.2	3.14	19.48	2832.2	23.95	43.40	677	0.223	2340	4.54
10849	2.6	40.2	100	3	air	130	300	1830.9	3.15	19.56	2837.2	24.00	43.64	679	0.224	2342	4.54
10850	2.6	40.2	100	3	air	130	300	1812.7	3.08	18.99	2791.8	23.69	42.12	663	0.221	2321	4.55
10851	2.6	40.2	100	3	air	130	300	1822.6	3.13	19.60	2824.6	24.15	43.61	675	0.225	2336	4.54
10852	2.6	40.2	100	3	air	130	300	1817.6	3.13	19.83	2823.2	24.45	44.12	674	0.228	2336	4.54
10853	2.6	40.2	100	3	air	130	300	1807.8	3.05	18.61	2772.7	23.36	41.19	657	0.218	2312	4.55
10854	2.6	40.2	100	3	air	130	300	1825.9	3.10	18.64	2802.4	23.15	41.41	667	0.216	2326	4.54
10855	2.6	40.2	100	3	N_2	130	300	1825.9	3.16	18.90	2887.7	22.05	40.44	640	0.213	2359	4.61

Notation for the fuel system parameters:

Shot. No	Shot number
CC	Combustion chamber type (by the divergence angle)
P_{LT_i}	Fill pressure of the Ludwieg Tube
$P_{F\#}$	Measured plenum pressure for each pressure transducer
$\dot{m}_{H_2}$	Mass flow rate of hydrogen fuel
u_∞	Freestream flow speed
ρ_∞	Freestream density
$\dot{m}_{air}$	Mass flow rate of air through model inlet
$\dot{m}_{O_2}$	Mass flow rate of oxygen through model inlet
ϕ	Equivalence ratio

Table D.2: Measured and calculated key properties of the fuel system. The calculated discharge coefficients, based on calibration data, for each of the fuel sensors were: $\alpha_{F1} = -2.08 \times 10^{-8}$ and $\alpha_{F2} = -1.94 \times 10^{-8}$. Mass flow rate through the engine was calculated based on the area of the diffuser inlet which was $A_1 = 1.504 \times 10^{-3}\,\mathrm{m}^2$. Fuel-off shots for the constant area, 1° divergent and 2° divergent combustors were 10821, 10804 and 10840 respectively and are omitted from this table.

Shot No.	CC deg.	P_{LT_i} kPa	P_{F1} kPa	P_{F2} kPa	$\dot{m}_{H_2}$ kg/s	u_∞ m/s	ρ_∞ kg/m^3	$\dot{m}_{air}$ kg/s	$\dot{m}_{O_2}$ kg/s	ϕ -
10805	1	2800	1486.3	1466.4	0.0323	2365	0.232	0.826	0.191	1.353
10806	1	2300	658.2	649.6	0.0156	2337	0.232	0.815	0.189	0.663
10807	1	2300	1166.9	1152.0	0.0256	2310	0.222	0.772	0.179	1.144
10808	1	2300	1256.4	1237.3	0.0272	2323	0.237	0.827	0.192	1.136
10809	1	1900	1013.7	998.9	0.0220	2338	0.228	0.801	0.185	0.951
10811	1	1628	878.7	866.7	0.0191	2385	0.239	0.856	0.198	0.770
10812	1	1450	795.9	784.3	0.0172	2349	0.222	0.783	0.181	0.760
10813	1	1348	741.5	731.3	0.0160	2364	0.229	0.812	0.188	0.683
10814	1	1199	664.6	655.8	0.0144	2329	0.248	0.868	0.201	0.572
10815	1	2988	1587.8	1562.4	0.0345	2306	0.225	0.782	0.181	1.525
10816	1	2595	1377.5	1356.8	0.0299	2326	0.246	0.861	0.199	1.202
10817	1	2084	1110.2	1093.9	0.0241	2316	0.227	0.790	0.183	1.056
10818	1	2257	1199.4	1182.7	0.0261	2331	0.224	0.785	0.182	1.148
10819	1	2257	1195.5	1179.1	0.0260	2306	0.236	0.819	0.190	1.098
10820	1	2592	1365.1	1345.6	0.0297	2378	0.220	0.785	0.182	1.308
10822	0	2796	1424.1	1522.7	0.0322	2311	0.220	0.766	0.177	1.455
10823	0	2589	1320.5	1412.3	0.0299	2346	0.226	0.798	0.185	1.295
10824	0	2243	1139.0	1219.2	0.0258	2343	0.233	0.821	0.190	1.086
10825	0	2422	1229.7	1314.9	0.0279	2322	0.226	0.790	0.183	1.218
10826	0	2244	1143.4	1222.3	0.0259	2353	0.230	0.814	0.188	1.099
10827	0	2254	1154.0	1236.7	0.0261	2291	0.223	0.767	0.177	1.178
10828	0	2241	1143.9	1225.5	0.0259	2321	0.228	0.796	0.184	1.125
10829	0	2045	1045.1	1118.9	0.0237	2340	0.220	0.774	0.179	1.056

Table D.2: continued.

Shot No.	CC deg.	P_{LT_i} kPa	P_{F1} kPa	P_{F2} kPa	$\dot{m}_{H_2}$ kg/s	u_∞ m/s	ρ_∞ kg/m^3	$\dot{m}_{air}$ kg/s	$\dot{m}_{O_2}$ kg/s	ϕ -
10830	0	1646	852.9	912.9	0.0193	2344	0.220	0.776	0.180	0.858
10831	0	1293	681.4	729.0	0.0154	2347	0.226	0.798	0.185	0.665
10832	0	1112	596.3	639.8	0.0134	2336	0.221	0.775	0.179	0.598
10833	0	1455	768.0	821.2	0.0173	2291	0.220	0.757	0.175	0.790
10834	0	1848	953.7	1019.6	0.0215	2339	0.226	0.794	0.184	0.938
10835	0	1206	640.9	688.1	0.0144	2319	0.221	0.771	0.179	0.647
10836	0	2585	1302.9	1393.1	0.0295	2368	0.214	0.762	0.176	1.339
10837	0	2992	1512.4	1618.3	0.0343	2302	0.225	0.780	0.181	1.519
10838	0	1457	765.8	820.5	0.0173	2346	0.223	0.785	0.182	0.760
10839	0	1202	636.9	683.5	0.0144	2322	0.216	0.753	0.174	0.659
10841	2	2592	1325.1	1417.5	0.0300	2341	0.222	0.780	0.181	1.329
10842	2	2239	1135.3	1217.2	0.0257	2324	0.219	0.767	0.178	1.160
10843	2	2240	1131.1	1213.3	0.0257	2354	0.221	0.781	0.181	1.136
10844	2	2237	1133.7	1215.8	0.0257	2343	0.224	0.789	0.183	1.127
10845	2	2045	1046.5	1120.2	0.0237	2324	0.227	0.794	0.184	1.031
10846	2	1861	947.6	1015.4	0.0215	2344	0.226	0.796	0.184	0.933
10847	2	1644	845.5	907.5	0.0191	2324	0.218	0.762	0.176	0.869
10848	2	1444	753.8	809.0	0.0170	2340	0.223	0.785	0.182	0.750
10849	2	1258	664.1	712.6	0.0150	2342	0.224	0.788	0.182	0.657
10850	2	1113	596.3	639.9	0.0134	2321	0.221	0.772	0.179	0.601
10851	2	1064	574.3	615.9	0.0129	2336	0.225	0.791	0.183	0.564
10852	2	2783	1399.1	1498.6	0.0318	2336	0.228	0.801	0.185	1.371
10853	2	2980	1506.0	1611.1	0.0341	2312	0.218	0.760	0.176	1.553
10854	2	2393	1212.3	1298.9	0.0275	2326	0.216	0.756	0.175	1.256
10855	2	2585	1297.5	1388.9	0.0294	2359	0.213	0.756	0.175	1.346

Appendix E

Cycle Analysis Optimisation

This Appendix contains the results from the parameter optimisation of the cycle analysis inputs. The details of the parameter optimisation process are as follows. An initial estimation was made for each of these parameters based on values from similar scramjet experiments. Each parameter was then varied through a range to optimise the match between the pressure profile predicted from the cycle analysis to the experimental data. After one parameter had been optimised, previously optimised parameters were returned to to see whether there was further improvement.

E.1 Optimisation of Performance Parameters

E.1.1 Constant area combustor

Non-separated cases

The first figure in the parametric study, Figure E.1a, shows the effect the combustion efficiency has on the pressure distribution. As the terminal combustion efficiency ($\eta_{c,f}$) is increased, the pressure at the exit of the combustion chamber increases. In order to match the exit pressure level seen in the experiment, a combustion efficiency of 100% is required. At this low ϕ, with a combustor with a L/D of 15 (500/32) and equally spaced port hole injectors around the circumference, fuel combustion of the fuel is not unexpected. Even at $\eta_{c,f} = 100\%$ the cycle analysis underpredicts the pressures seen in the experiment. This can be attributed to a number of factors such as the real flow effects not captured by the one-dimensional model and also to the uncertainties in the inflow conditions associated with this type of wind tunnel. Although these factors limit the degree of certainty of the value derived for the combustion efficiency the general trend in response to fuelling and also the trend across combustors can still be drawn.

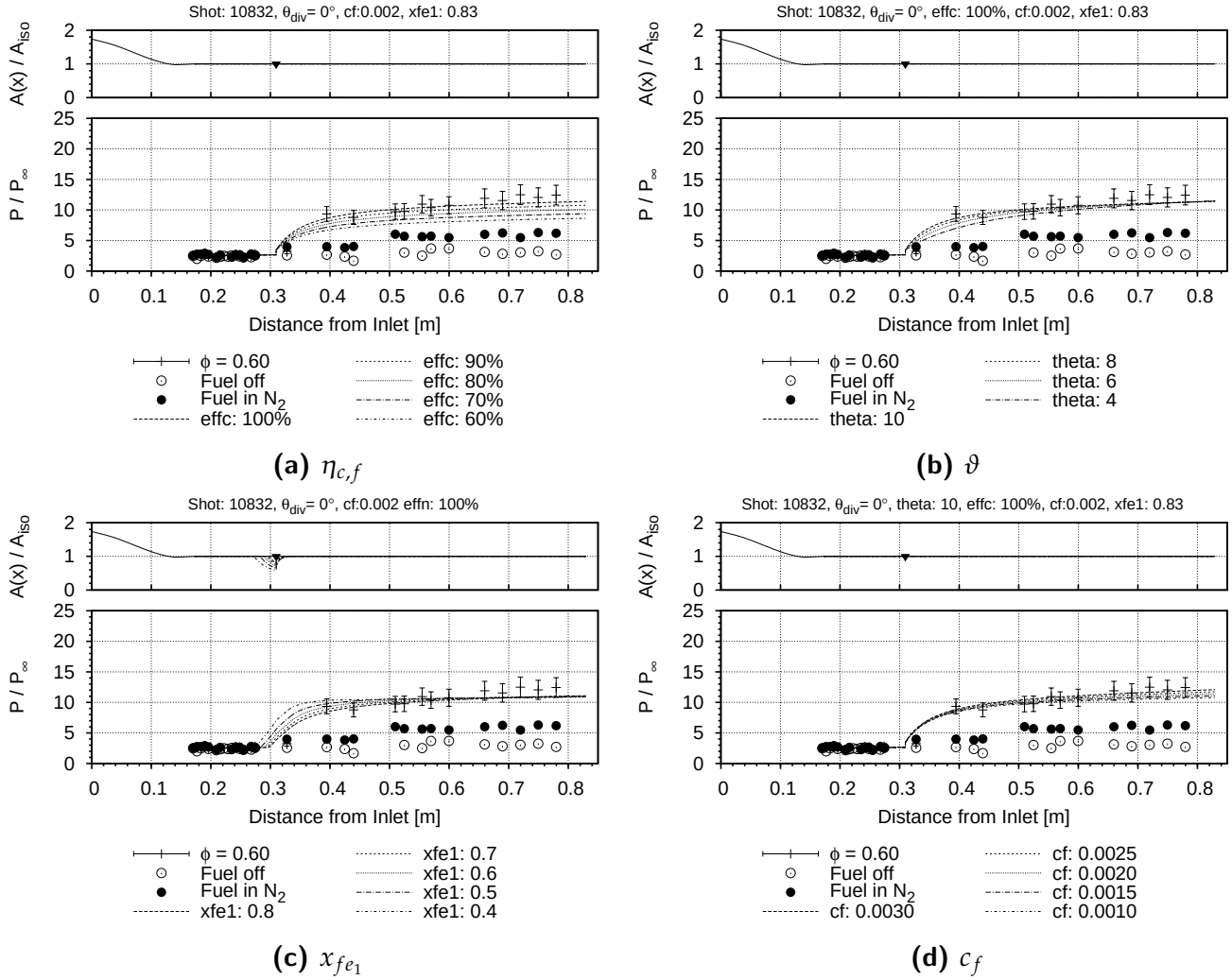

Figure E.1: Parameter study of the cycle analysis result of the non-separated case for the constant area combustor

The next parameter investigated was the mixing parameter ϑ and the results from the study of its effects are shown in Figure E.1b. As ϑ is increased, the mixing rate is increased and there is a higher gradient in the initial portion of the pressure rise from combustion. As this code does not separate the mixing from the kinetics, it is assumed that the portion of the fuel at a given stream wise position is completely mixed and combusts immediately (i.e. the fuel is limited by mixing and not by kinetics). In Figure E.1b it was found that in order to reach the raised pressure levels at station 0.4 m a value of 10 for ϑ was required. This is at the upper bound of the range given in Heiser and Pratt (1994) for attached scramjet flow.

The next parameter examined was x_{fe_1}. This parameter controls the end point of the mixing curve. Moving this point also changes the 'effective' ϑ as the $\eta_c(X, \vartheta)$ is a function of X which has x_{fe_1} as a variable. Reducing the mixing-length means that mixing is occurring over a shorter length and would result in a higher mixing rate (mixing

per unit length) when comparing curves with the same value for ϑ but different values of x_{fe_1}. The adjustment of this parameter controls not only the rate but the point at which mixing has completed. This is important in this research as it was observed in the experimental data that when separation occurred, the combustor reached 90% to 95% of the exit pressure much further upstream than for non-separated cases and indicating that mixing was being enhanced and reaching completion over a shorter distance.

In Figure E.1c x_{fe_1} is plotted between values of 0.4 and 0.8 with all showing separation predicted by the code. It was only for $x_{fe_1} = 0.83$ that resulted in a non-separated case (presented in Chapter 5). As no separation was seen in the experiments for this fuelling condition it is concluded that the mixing takes the entire length of the combustor to come to completion for non-separated flow cases. This indicates that for this fuelling case, this engine is operating close to the critical point for where separation is likely to occur such that only a minor change in the heat distribution from a higher mixing rate causes a greater pressure gradient leading to exceeding a pressure criteria for separation.

The last parameter examined was the skin friction coefficient c_f. In Figure E.1d as the c_f was varied through a range of reasonable values from 0.001 to 0.003, the effect it has on the pressure distribution is minor compared with the other parameters ϑ and x_{fe_1}. It was found that c_f also had a minimal effect on the critical condition for separation and as such was held constant for all cases at a value of 0.002.

Moderately separated cases

The next series of figures relate to the optimisation of parameter set for the moderately separated cases. The first figure in this series, Figure E.2a shows how the value for x_{fe_1} was found for these cases. The criteria for a good fit was based on finding a pressure profile that intersected with the pressure measure by the front edge (FE) pressure sensors at a distance of 0.32 m from the leading edge. The FE pressure measured is chosen as a good measurement to match the cycle analysis as this measurement comprises six sensors equally spaced around the circumference of the combustor and therefore has a lower uncertainty in this measurement compared with an individual measurement further along the combustor. It was found that a value for x_{fe_1} that lies between 0.4 m and 0.5 m was the best fit for this criteria.

Figure E.2b show the effect that varying the skin friction at the point of separation (c_{f_o}). Decreasing c_{f_o} increases the scale of the separation by moving the point of separation forward along the combustor as decreasing c_{f_o} decreases the pressure gradient of the separation that the boundary layer can support. So for a given pressure rise across the shock train, the pressure rise must occur over a larger distance for a lower value of c_{f_o}.

The c_f parameter has minimal effect on the pressure profile as shown in Figure E.2c. As the pressure distribution predicted by the cycle analysis has a low sensitivity to the value of c_f, even for separated cases, this parameter is fixed at a value of 0.002 for the remaining analyses and is no longer considered in any of the following parametric studies.

The last parameter explored in this parametric study of this separated case was ϑ. In Figure E.2d ϑ was adjusted above the standard limit of 10 for scramjets whilst fixing x_{fe_1} at the end of the combustor. It was found that this change in ϑ had a similar effect on the separation as reducing x_{fe_1} did. As argued in Chapter 5, using values above 10 for ϑ is not entirely unreasonable, as reducing x_{fe_1} causes an increase in the 'effective ϑ' as mixing is occurring over a shorter distance and therefore there must be at increased mixing rate. A review of the literature that provided the basis of the upper limit for ϑ of 10 for scramjets (Heiser and Pratt, 1994, p.348) notes that for ramjets a higher values of 40-50 is applicable. Considering that dual-mode scramjets operate with a mixture of supersonic and subsonic flow, then it is not without basis that the value of ϑ may be higher than the value accepted for conventional scramjets (i.e. a scramjet operating in pure scramjet mode). However, regardless of the parameter varied, x_{fe_1} versus ϑ, the general conclusion is the same: for separated flow, a higher rate of mixing is required in the analysis in order to predict a separation of the same scale and position as observed in the experiments.

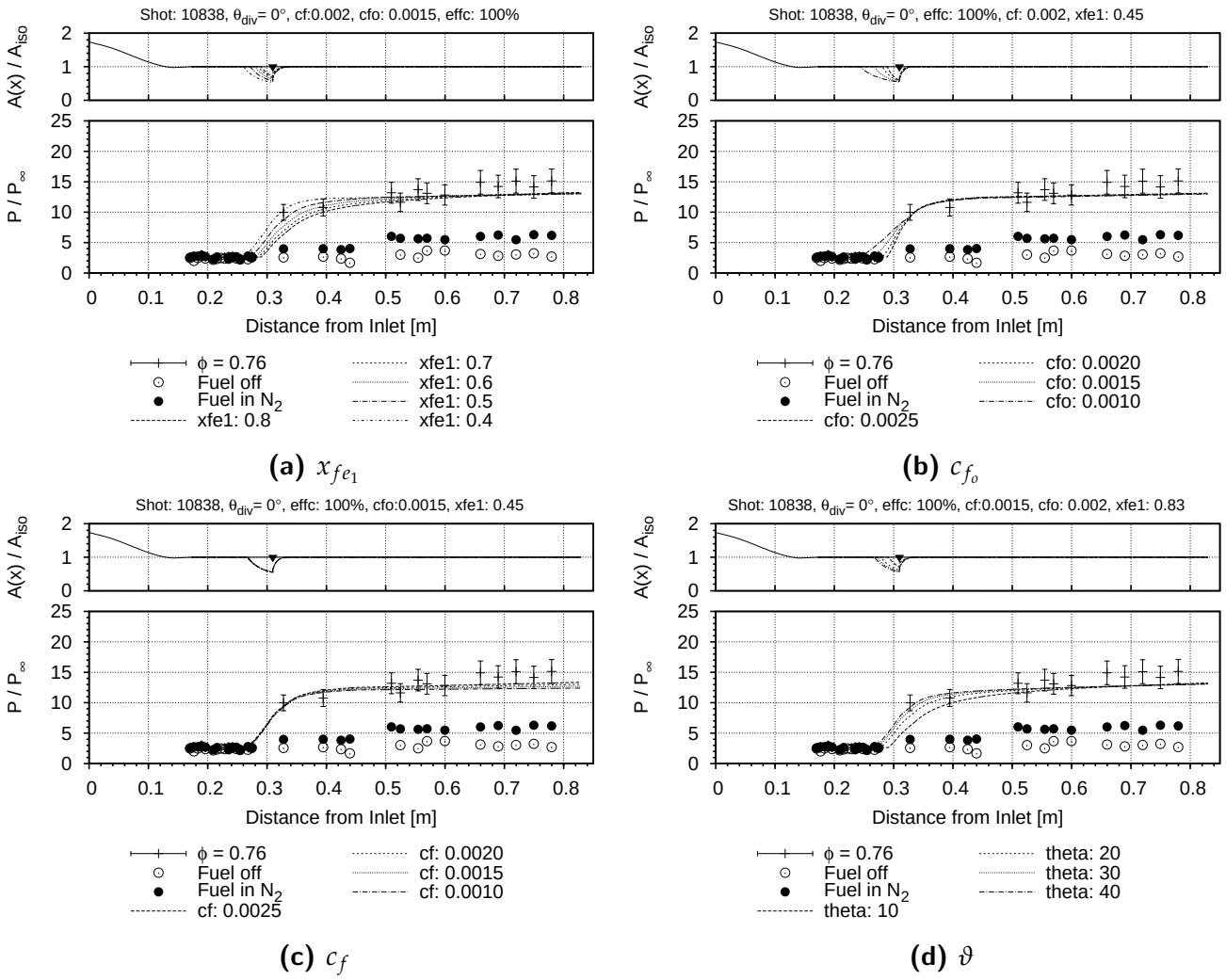

(a) x_{fe_1} **(b)** c_{f_o}

(c) c_f **(d)** ϑ

Figure E.2: Parameter study of the cycle analysis result of a separated case for the constant area combustor

Highly separated cases

The following set of figures in Figure E.3 shows the optimisation of the parameter set for the highly separated cases. Figure E.3a shows that the $\eta_{c,f}$ is around 80% to 90%. Figure E.3b shows that x_{fe_1} is at least as low as 0.4 in order to generate a shock train of sufficient strength to fit the FE measured pressures. Finally in Figure E.3c a value of 0.0015 for c_{f_o} is required to extend the separation point of the shock train in the cycle analysis to around the point observed in the experiments.

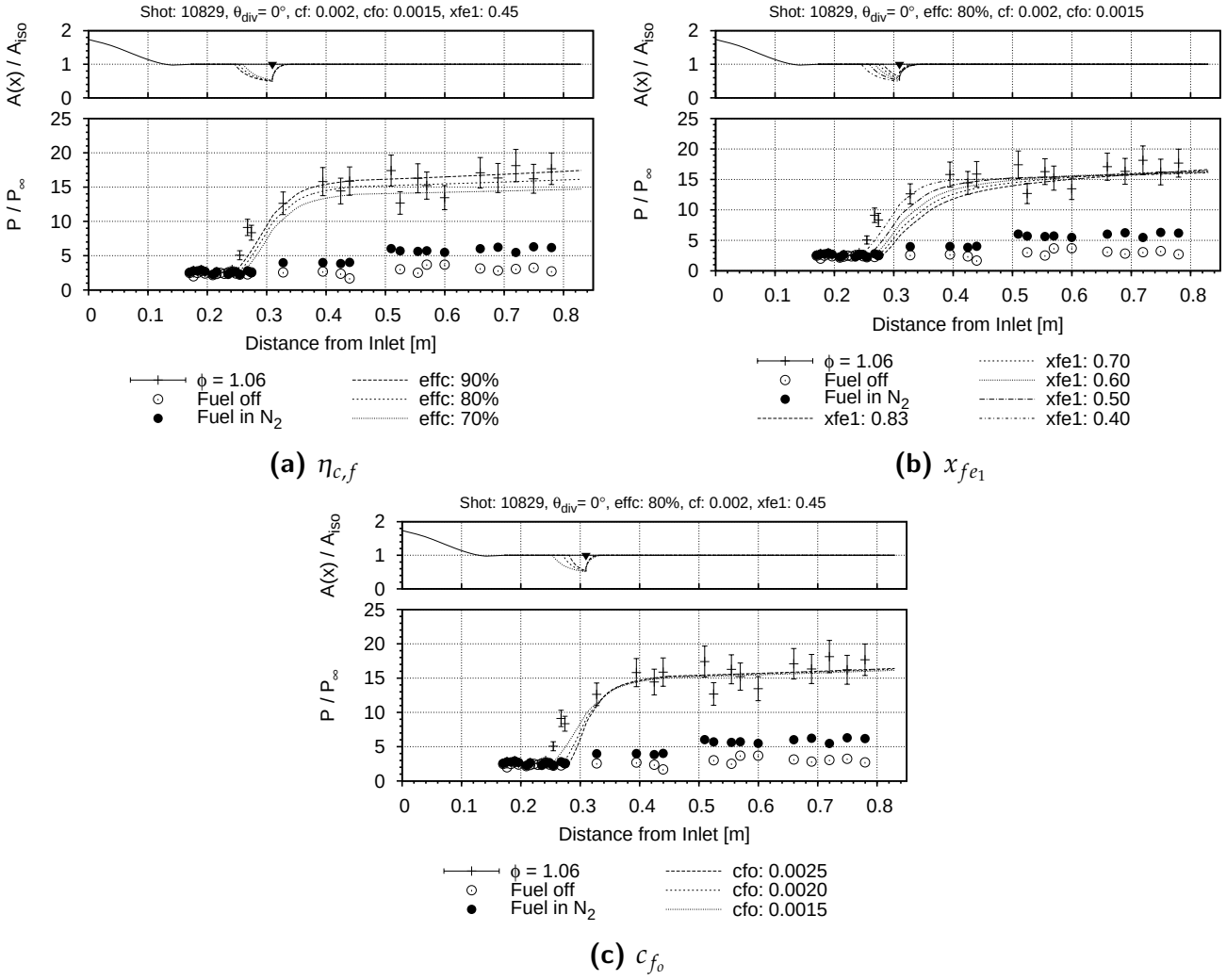

(a) $\eta_{c,f}$ **(b)** x_{fe_1}

(c) c_{f_o}

Figure E.3: Parameter study of the cycle analysis result of a highly separated case for the constant area combustor

E.1.2 2° divergent combustor

Non-separated cases

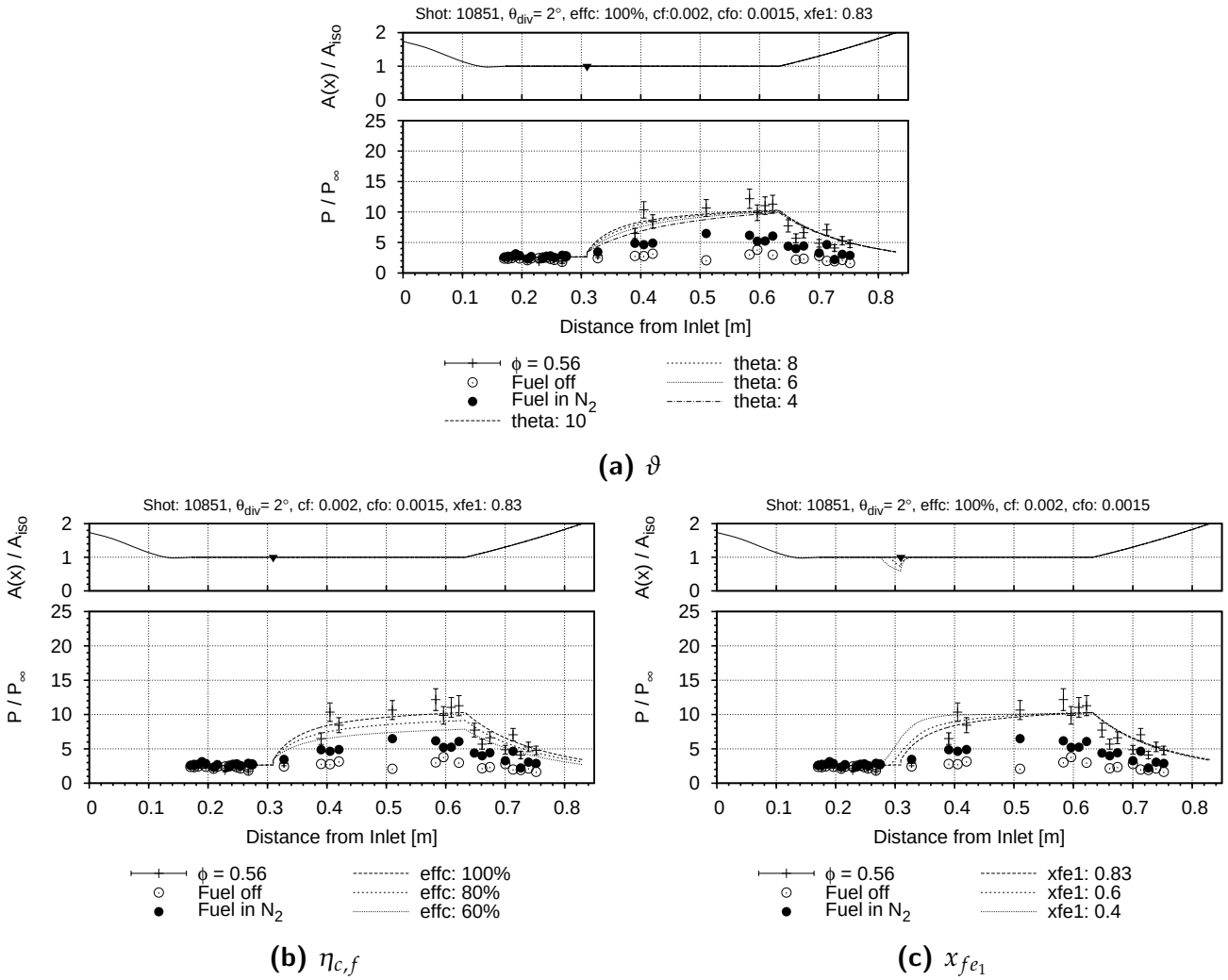

Figure E.4: Parameter study of the cycle analysis result of a non-separated case for the 2° divergent combustor

Moderately separated cases

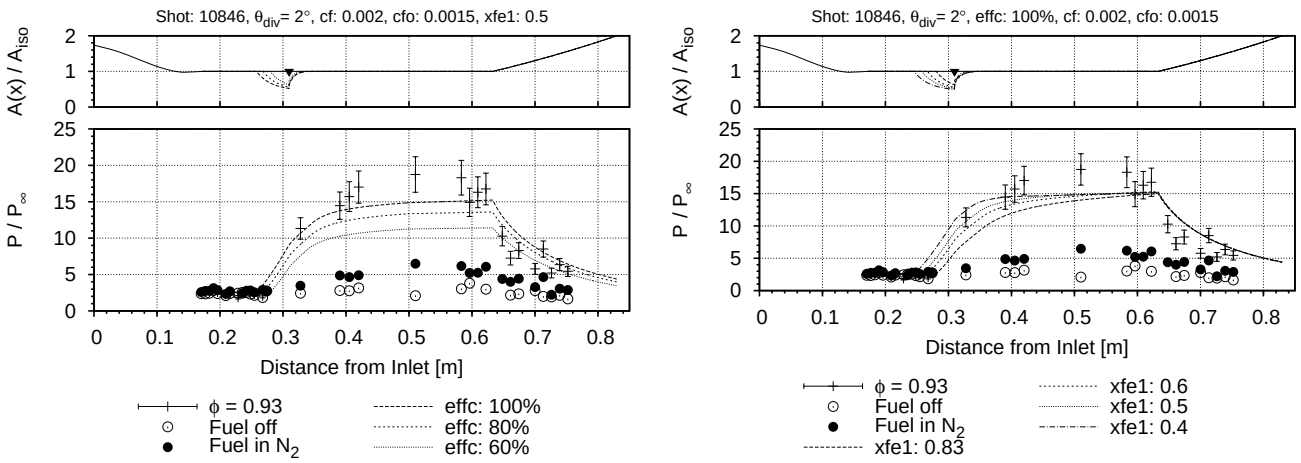

(a) $\eta_{c,f}$ **(b)** x_{fe_1}

Figure E.5: Parameter study of the cycle analysis result of a moderately separated case for the 2° divergent combustor

Highly separated cases

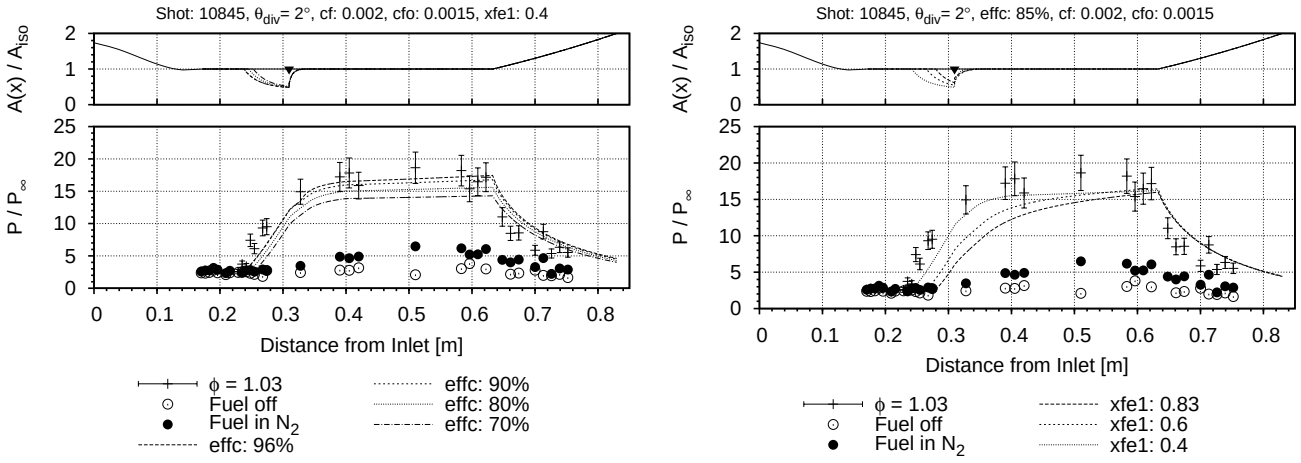

(a) $\eta_{c,f}$ **(b)** x_{fe_1}

Figure E.6: Parameter study of the cycle analysis result of a highly separated case for the 2° divergent combustor

E.1.3 1° divergent combustor

Non-separated cases

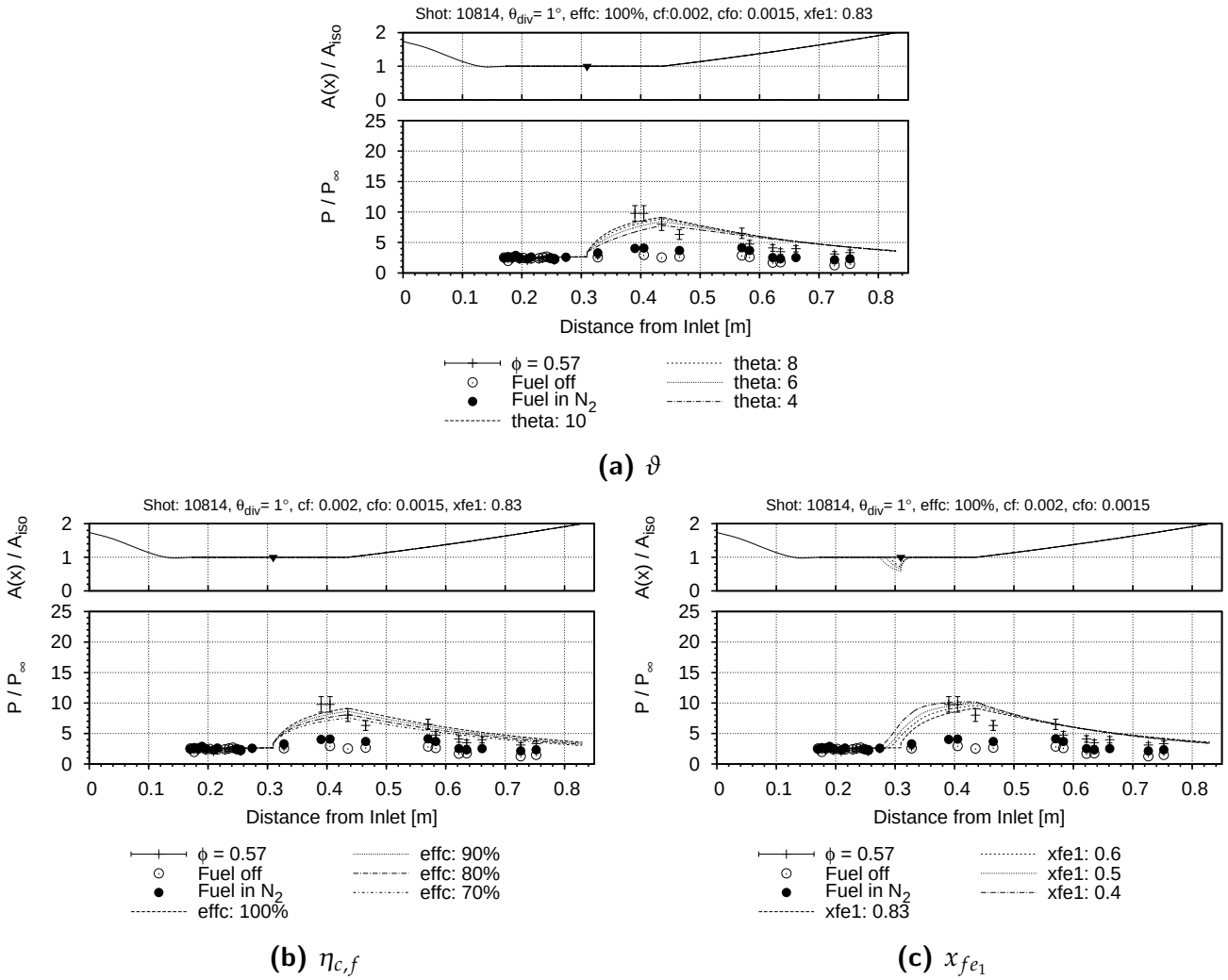

(a) ϑ **(b)** $\eta_{c,f}$ **(c)** x_{fe_1}

Figure E.7: Parameter study of the cycle analysis result of a non-separated case for the 1° divergent combustor

Moderately separated cases

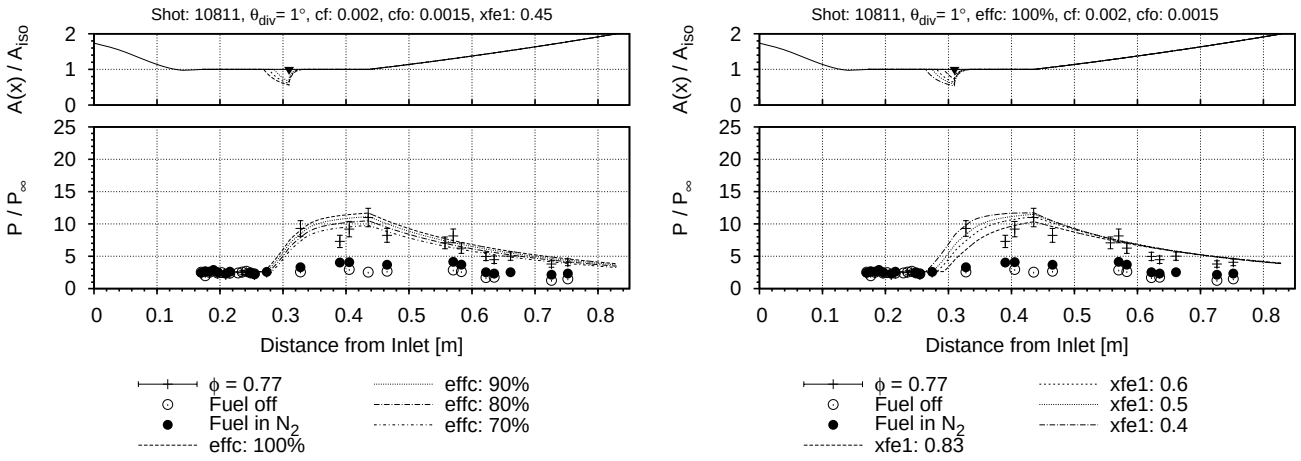

(a) $\eta_{c,f}$ **(b)** x_{fe_1}

Figure E.8: Parameter study of the cycle analysis result of a moderately separated case for the 1° divergent combustor

Highly separated cases

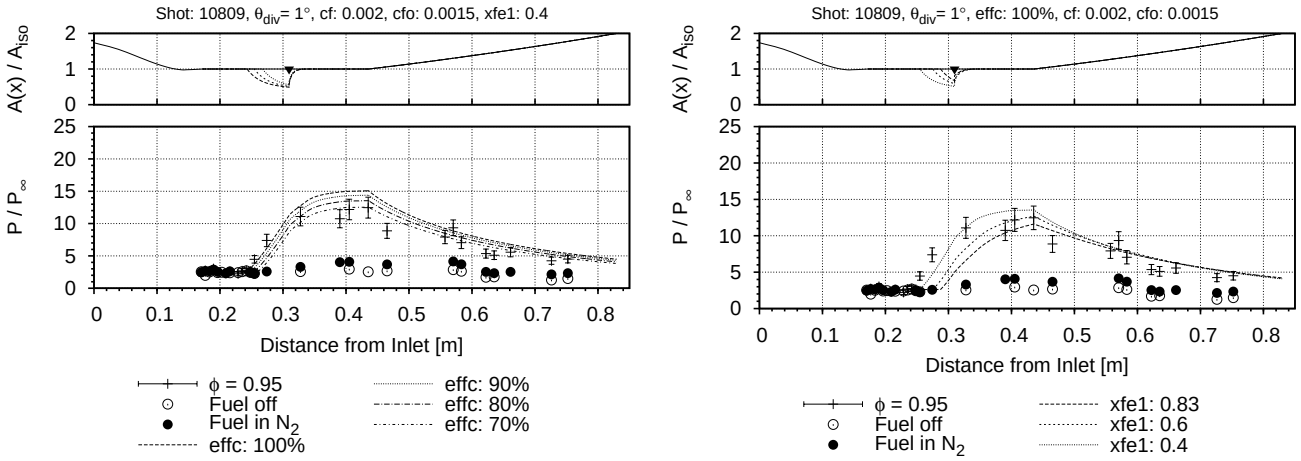

(a) $\eta_{c,f}$ **(b)** x_{fe_1}

Figure E.9: Parameter study of the cycle analysis result of a highly separated case for the 1° divergent combustor

E.1.4 High sensitivity to combustion efficiency and Mach number

It was found in the course of the optimisation that there are cases where the results from the cycle analysis are highly sensitive to the combustion efficiency parameter $\eta_{c,f}$. These are typically for highly separated cases where the shock train is among the longest of the experimental set. An example of this high sensitivity is shown in Figure E.10a. This case is for the maximum fuelling test for the constant area combustor however the flow does not establish within the facility test time. The experimental data presented in these figures is the average of the measured pressure over the conventional test time windows. As such for some of the sensor locations towards the upstream end of the isolator where the leading edge of the shock train is located the pressure shown is an average of the pressure before and after the leading edge of the shock train has travelled past. Despite this transient behaviour, these averaged pressures using the conventional test times still show a typical profile of an established shock train. For this case shown in Figure E.10a, for a minor change in $\eta_{c,f}$ as small as 1 percentage point there is a dramatic change in the result calculated by the cycle analysis code. For example for $\eta_{c,f}$ equal to 48%, 49% and 50%, the separation point moves from 0.26 m to 0.2 m to 0.17 m respectively. The solution also switches from supersonic throughout when $\eta_{c,f}$ = 42% to solutions ($\eta_{c,f} \geq 45\%$) where the core flow is driven to Mach 1 at the exit (such as in the case of $\eta_{c,f}$ = 45%) or is driven below Mach 1 through the shock train ($\eta_{c,f} \geq 49\%$).

A similar sensitivity is found to changes in the flow conditions entering the isolator. These inflow conditions were adjusted by increasing or decreasing the parameter that defines the Mach number of the flow entering the isolator. The parameter introduced to control this change is termed the freestream Mach number factor or $M_{f,f}$. This factor is applied to the Mach number that defines the flow conditions entering the isolator in the cycle analysis code. The results from the study of the sensitivity to this new parameter for a highly separated case for the constant area combustor are shown in Figure E.10b. As an example for how $M_{f,f}$ is applied, for this case the calculated Mach number at the isolator entrance is M_2 = 3.63, so for $M_{f,f}$=0.90 the adjusted value for M_2 equates to 3.27. No other parameters defining the inflow are adjusted to compensate for the change in Mach number, such as pressure or temperature, and so the change in Mach number also changes the mass flow rate and momentum of the incoming flow. For the results presented in Figure E.10b, for a small change in the Mach number of 2% there is a moderate change in the pressure profiles for values of $M_{f,f}$ from 1 to 0.96. Below which there is a dramatic change in the results predicted by the cycle analysis with the separation point advancing far forward to the beginning of the geometry. This is associated with a much larger pressure rise through the shock train. For these latter cases, due to the lower Mach number of the incoming flow, the combustion has driven the Mach number of the core flow below one and this results in non-physical solutions. These results, along with those relating to the high sensitivity to $\eta_{c,f}$ in Figure E.10a, help explain why these tests do not establish within the available test time in the shock tunnel. The explanation is that these engines have choked and that for these cases at

the maximum fuelling rate the beginnings of an engine unstart is observed in the transient plots of the data.

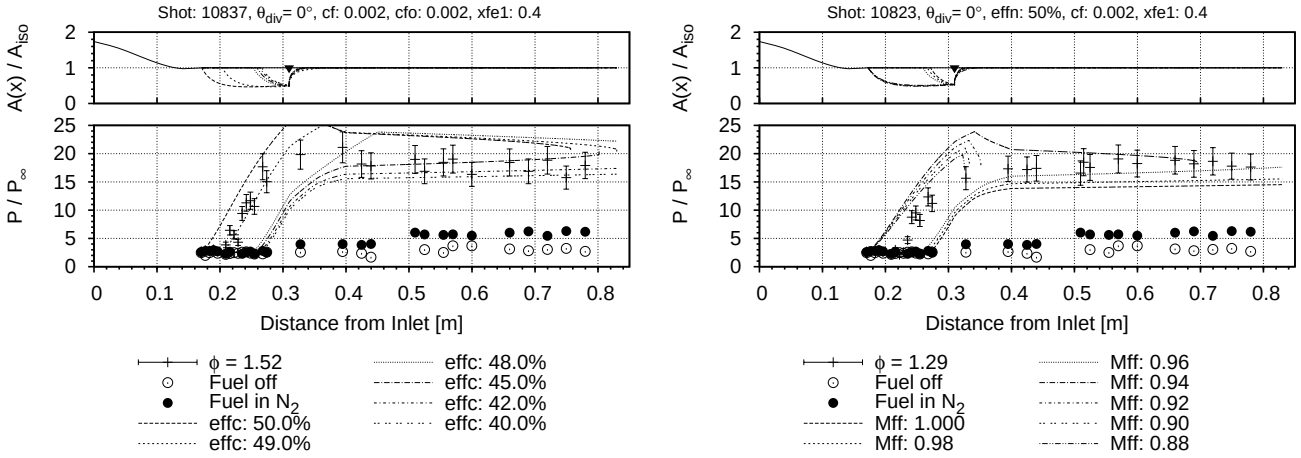

(a) $\eta_{c,f}$ (= *effc*) **(b)** Mach number factor ($M_{f,f}$)

Figure E.10: Parameter study of the cycle analysis results for two highly separated cases for the constant area combustor showing the particularly high sensitivity to: (a) combustion efficiency ($\eta_{c,f}$) and (b) the Mach number of the isolator inflow. The Mach number of the isolator inflow is adjusted by the parameter $M_{f,f}$ - which is the fraction of the Mach number of the flow entering the isolator calculated for that shot.

E.1.5 Non-established maximum fuelling cases

When the approach of adjusting the Mach number of the inflow, as described in Appendix E.1.4, was used in conjunction with adjusting the combustion efficiency, then very good fits were found for the maximum fuelling case for all the combustors in which the flow did not establish in the facility test time. These results are shown in Figure E.11. For the constant area combustor (Figure E.11a), a reduction in the isolator Mach number of just over a 8% yields a pressure profile that fits both the pressures through the shock train as well as along the rest of the engine. The change in the Mach number also had an effect on the combustion efficiency where it reduces from an initial estimate of 49% for the unadjusted condition to 30% for $M_{f,f} = 91.75\%$ condition. Similar results are found for the two divergent combustors. For the 2° divergent combustor the Mach number reduces by 8% and the combustion efficiency subsequently fell from 60% to 38.6%. For the 1° divergent combustors the reduction in Mach number is 6% and the change in combustion efficiency is from 51% to 35%. Interestingly, at these conditions, the cycle analysis predicts for both of the divergent combustors a pressure distribution that fits remarkably well the pressure measurements in the divergent section.

Although a set of parameters have been found for which the result from the cycle analysis fits very well to the experimental data, these are for cases where the flow in the experiment does not reach a steady state. As such the findings from these results should be taken as indicative of the broader dynamics of these dual-mode engines. One indication at least is that for high ϕ cases where the shock train is long, the engine may be very sensitive to inflow conditions. This is particularly true when the engine is running close to the choke point. This provides possible avenues for future studies by manipulating the operating conditions of the facility to further explore the shock train dynamics. The corollary is that the variability and uncertainties of the test flow conditions produced by shock tunnels may be too great to accurately predict the shock train position in subsequent one-dimensional analysis for highly back pressured ducts.

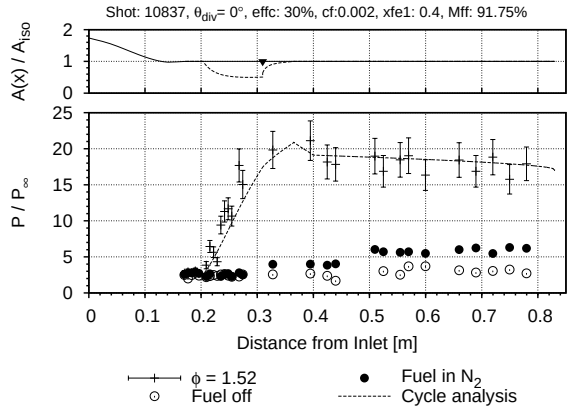

(a) Constant area combustor

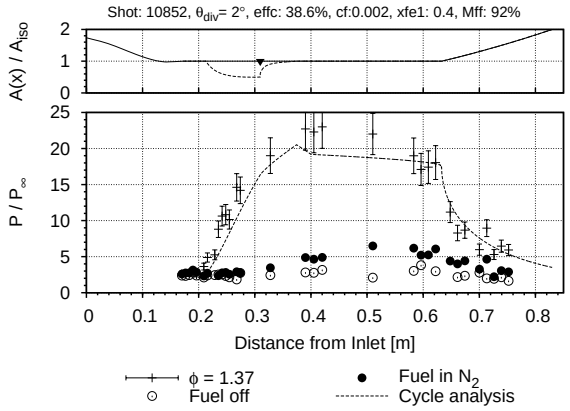

(b) 2° divergent combustor

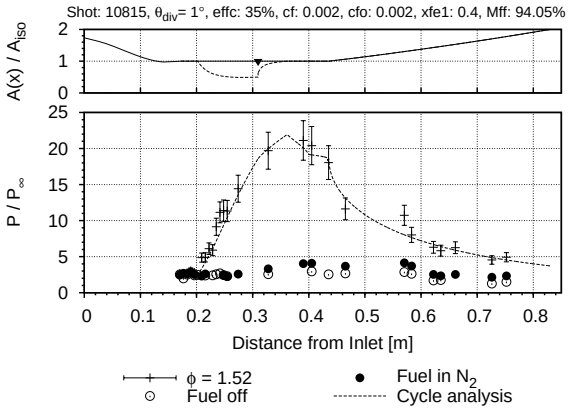

(c) 1° divergent combustor

Figure E.11: Best fit of cycle analysis result of the maximum fuelling case for all three combustors by varying inflow conditions

E.2 Discussion on Mixing Curves

The following figures in Figure E.12 explore the relation between the parameters ϑ and x_{fe_1} with the mixing profile and thereby the effects on combustion efficiency in the cycle analysis code *DMCycle*. These curves are based on equation provided by Heiser and Pratt (1994), which is given in Chapter 5.

Figure E.12a shows the typical combustion efficiency curves along a combustor for values of ϑ between the standard range for scramjets of between 1 and 10 and for extreme values outside that range up $\vartheta = 20$. As shown in the figure, a value of 1 for ϑ is for linear burning typical of a kinetically limited combustion. The next few increments above 1 show a large change in the shape of the curve and as ϑ approaches 10 there is diminishing change in the shape for each successive increment of ϑ.

The next figure, Figure E.12b, shows the relationship between the mixing-length and the parameter x_{fe_1}. In the equation for X, the x_4 term is replaced with x_{fe_1} and so if x_{fe_1} is less than x_4 then mixing is completed (or reaches the specified $\eta_{c,f}$ before then end of the combustor). The curves in Figure E.12b illustrate the effect of varying x_{fe_1} on the mixing curve for a combustor of unit length.

There is some similarity in reducing the mixing-length and increasing the value of ϑ. For a given ϑ shortening the mixing-length is similar to increasing the ϑ as in both approaches the mixing is more rapid. The difference between these two approaches is that reducing x_{fe_1} result in mixing being complete earlier along the combustor, whereas although increasing ϑ increases the initial mixing, mixing is still not complete until the end of the combustor. Comparing the curves from Figures E.12a and E.12b illustrates this point.

A direct comparison of similar curves produced by a combinations of these parameters is shown in Figure E.12c. The mixing curve for $x_{fe_1} = 0.4$ has a ϑ set to a value of 10. Four additional curves are overlaid where the value of x_{fe_1} is constant at a value of 1 and ϑ is varied from 10 through to 40. The initial slope of the first curve (x_{fe_1}=0.4) is best matched by a curve with a ϑ equal to 30. This matches quite well up to a combustion efficiency of 0.8. Beyond this value the two curves begin to diverge. The maximum difference between the two curves is less than 8% which occurs at 0.4 m when the $x_{fe_1} = 0.4$ curve terminates.

This means that considering the simplifications associated with this combustion model for the cycle analysis, the varying if ϑ above the traditional limit of 10 is justified considering that shortening the mixing-length has a very similar effect on the mixing curve. Conclusions drawn from the cycle analysis from fitting to the experimental data regarding the mixing-length parameter x_{fe_1} could, in some cases, equally

be made in relation to the mixing rate parameter ϑ.

However, as the focus of this research is on the effect that dual-mode combustion has on mixing then the conclusions for the most part will be the same regardless of which of these two parameters is chosen. As such, a single parameter, in this case x_{fe_1}, is chosen as a variable and the other held constant.

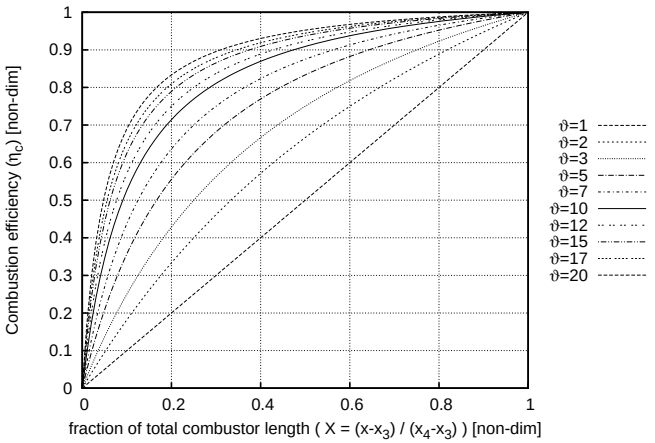

(a) $\eta_{c,f}$ curves for various values of ϑ

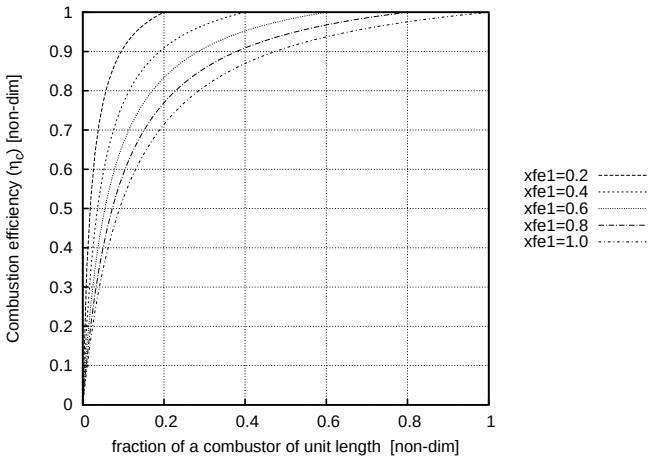

(b) $\eta_{c,f}$ curves for various values of x_{fe_1}

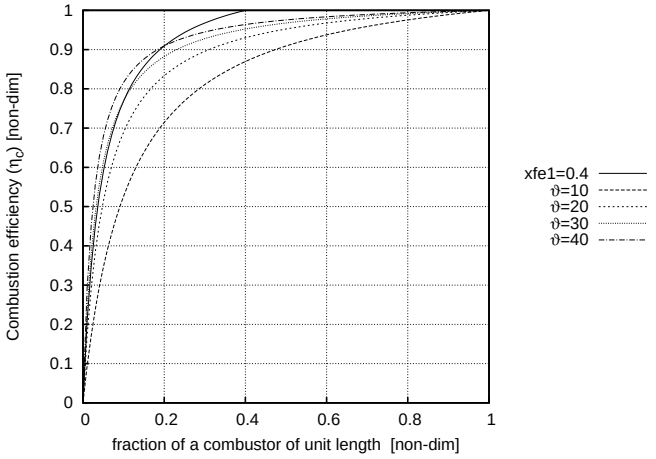

(c) Comparable values of ϑ for a given x_{fe_1}

Figure E.12: Plots showing the effect on the combustion efficiency curve by varying the mixing rate parameter (ϑ) and the mixing length parameter (x_{fe_1}).

Other mixing-combustion models

Noda et al. (2011a) used a quasi-one dimensional chemical kinetic code to estimate the vitiation effects on combustion quantitatively. In their quasi-one dimensional model combustion was initially controlled via a mixing model from Diskin and Northam (1987) which is given below:

$$\eta_{\text{nor}} = 1.01 + 0.176 \cdot \ln\left(x/x_\phi\right) \quad \text{for normal injection} \tag{E.1}$$

$$\eta_{\text{par}} = \left(x/x_\phi\right) \quad \text{for parallel injection} \tag{E.2}$$

$$x_l = 60G \tag{E.3}$$

$$x_\phi = 0.179 \cdot x_l \cdot e^{1.72\phi} \tag{E.4}$$

where η_{nor} and η_{par} are the mixing efficiency for normal and parallel injection respectively, x the distance from the injector, ϕ the equivalence ratio, x_l the mixing-length (at $\phi = 1$), G the gap distance and x_ϕ point of complete mixing as a function of ϕ.

Noda et al. found that the model by Diskin and Northam (1987) underpredicted the mixing efficiency determined by gas sampling for both the supersonic and subsonic combustion cases. They implemented a modification to the Diskin and Northam (1987) mixing model by introducing an additional linear term. This model is provided in Equation (E.5) where x is the distance along the combustor, x_ϕ the complete mixing distance and ξ, ψ and ζ are constants determined from matching the pressure profile from the code to the experiment. The parameters determined from their tests are given in Table E.1.

$$\eta_{mod} = \xi + \psi\frac{x}{x_\phi} + \zeta ln\frac{x}{x_\phi} \tag{E.5}$$

Table E.1: Experimental constants in Equation (E.5) from Noda et al. (2011a)

mode	ξ	ψ	ζ
supersonic	0.9248	0.5289	0.1241
subsonic	1.0979	0.2066	0.1448

The curve using the model by Noda et al. (2011a) for the values they determined from their experiments are plotted in Figure E.13 along with curves using the model by Diskin and Northam (1987) using the same values from Table E.1. Also plotted are curves from the model Heiser and Pratt (1994) both assuming a value for ϑ of 10 with one assuming the point of complete combustion (x_4) is located at end the of the combustor ($x_4 = L_{cc}$) and one where it is located where x_l lies in model from Diskin and Northam (1987) for $\phi = 1$ which is 480H (60*G, G=8H).

Apart from first curve from Heiser and Pratt (1994) model using the long combustion length ($x_4 = x_l$), it is clear that the model by Diskin and Northam (1987) has a much lower terminal combustion efficiency compared with the models from Heiser and Pratt and Noda et al. (2011a). The reason why the model by Diskin and Northam

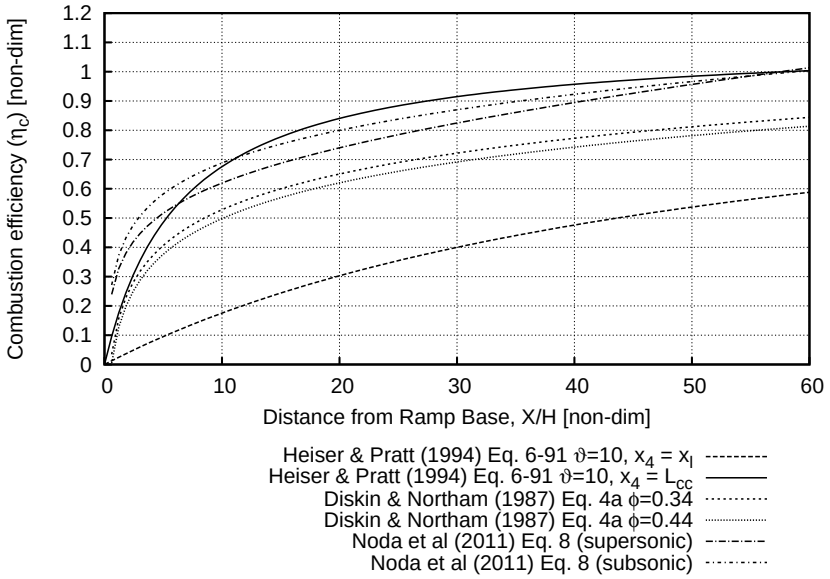

Figure E.13: Plot showing a comparison of common mixing-combustion models used in quasi-one dimensional codes. Models shown are from Heiser and Pratt (1994), Diskin and Northam (1987) and Noda et al. (2011a)

does not reach 100% by the end of the duct stems from the same reason why the first curve from Heiser and Pratt model is far below the others. For both curves the x_l is far downstream of the end of the combustor ($\approx 8.3L_{cc}$). For the Diskin and Northam model the low ϕ brings the point of complete combustion x_ϕ further forward but still remains outside this combustor with x_ϕ equal to $154H$ for $\phi = 0.34$ and $183H$ for $\phi = 0.44$. These last two positions highlights a feature of both the Diskin and Northam and Noda et al. models in that x_ϕ is maximum when $\phi = 1$ and reduces for both leaner and richer mixtures. This is best illustrated in the plot Figure E.14.

Returning to the comparison of the Noda et al. (2011a) model with the Heiser and Pratt (1994) model in Figure E.13 where $x_4 = L_{cc}$ is used in the latter model; here the curves are quite similar in their general rate of mixing across the entire length of the combustor. The curves for the subsonic and supersonic cases from the Noda et al. model both have a very steep gradient at the very start of the combustor but by $X/H = 10$ there is no much difference between the subsonic model by Noda et al. and the model by Heiser and Pratt. This difference at $X/H < 10$ may not though be insignificant if it were to incorporated into a quasi-one dimensional code with a shock train model. Here the more rapid heat release of the Noda et al. model may generate a stronger shock train when compared with Heiser and Pratt for the same terminal combustion efficiency. This discrepancy between these two relatively unsophisticated models highlights again the need for a general improvement in the understanding of the physics pertaining to supersonic combustion in order to improve such combustion models to the level required for the accurate prediction of pre-combustion shock trains.

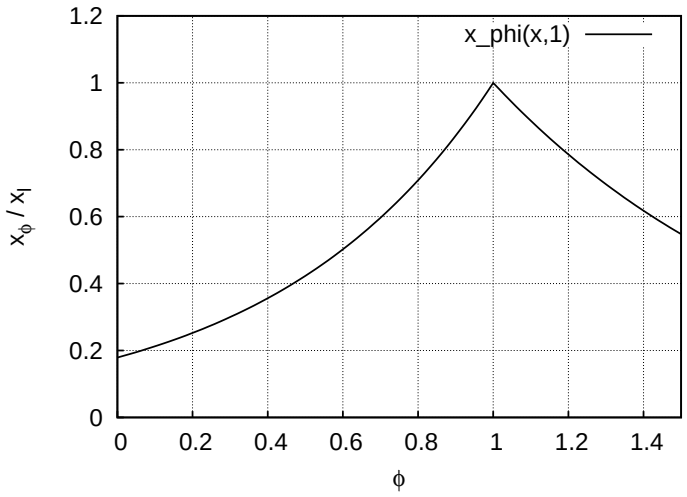

Figure E.14: A plot showing how the point of complete combustion (x_ϕ) in the combustion model by Diskin and Northam (1987) varies with equivalence ratio (ϕ). The variable x_ϕ is normalised by the distance of complete combustion (x_l) as determined for the $\phi = 1$ case.

Appendix F

Technical Drawings

This appendix contains the technical drawings of the parts that were manufactured for the experimental model. Also included are the drawings from original model from Paull (1996) and drawings for subsequent modifications to the original design by Rowan (2003) and Kirchhartz (2009). At the end of this appendix Table F.1 contains the tool path used to machine the diffuser.

REVISION HISTORY			
REV	DESCRIPTION	DATE	APPROVED

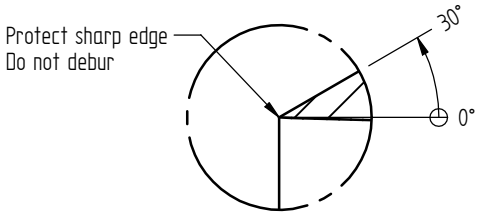

DETAIL B
2:1

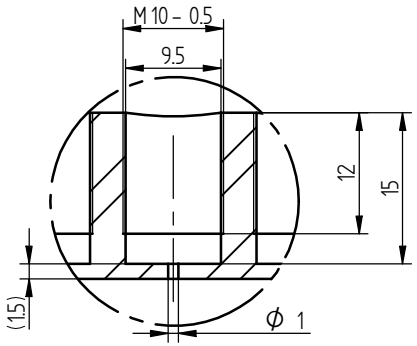

DETAIL C
2:1

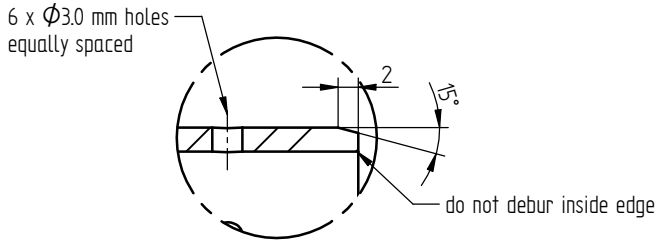

DETAIL D
2:1

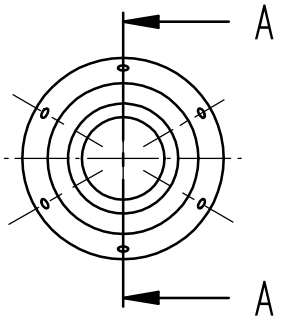

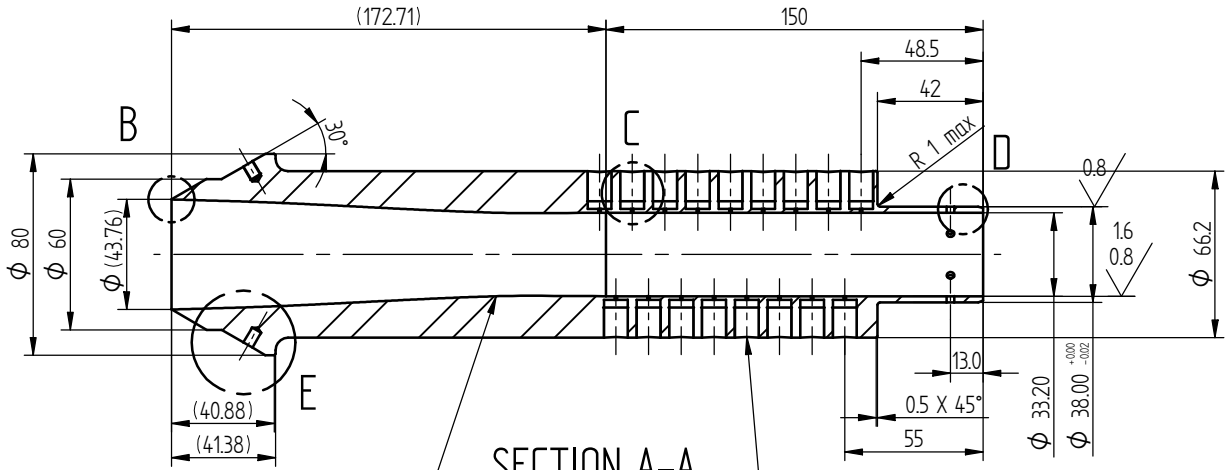

SECTION A–A
1:2

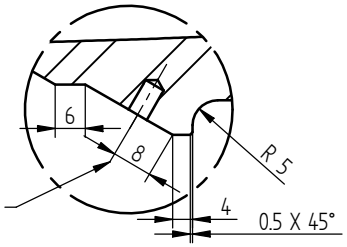

6 x M5 ↧8 mm
equally spaced
drill after assembly

DETAIL E
1:1

Any questions please
call me on x58398
or 0418 440 460

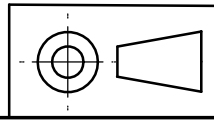

	NAME	DATE
DRAWN	Andrew Ridings	08/06/10
CHECKED		
MGR APPR	Michael Smart	
Material:		
FILE NAME: Inlet_FD_1.dft		

UNLESS OTHERWISE SPECIFIED
DIMENSIONS ARE IN MILLIMETERS
0 PL ± 0.1; 1 PL ± 0.05; 2 PL ± 0.01
ANGLES ±0.1°

THE UNIVERSITY OF QUEENSLAND
AUSTRALIA
Centre for Hypersonics

TITLE: Mach 3.75 Diffuser

PROJECT: Divergent Scramjet Combustors

SIZE	DWG NO	REV
A3	DIFF-1033.2	01

SCALE:	WEIGHT:	SHEET 1 OF 1

NOTES : 1 : DIMENSIONS IN MILLIMETRES EXCEPT WHERE STATED.

THIRD ANGLE PROJECTION

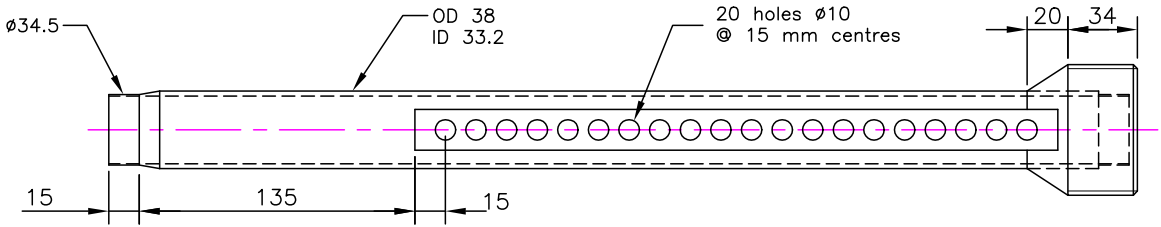

TOP VIEW

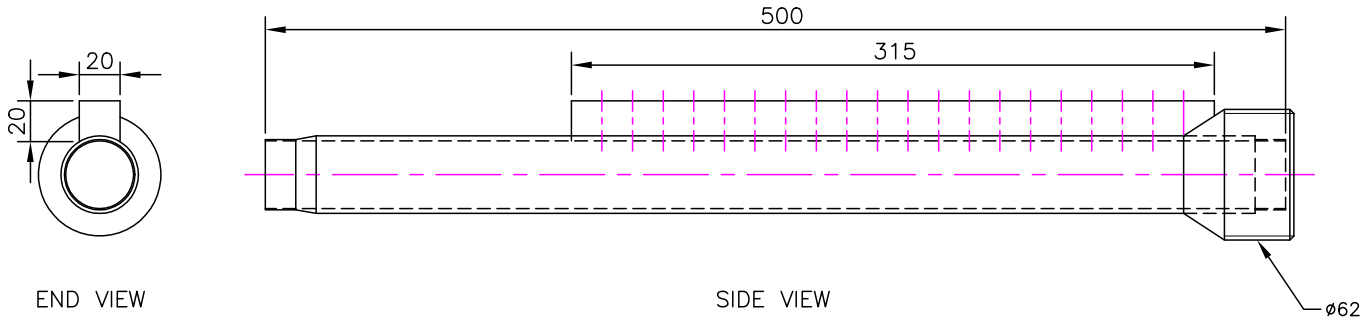

END VIEW

SIDE VIEW

DO NOT SCALE (PRINT MAY BE PHOTO–REDUCED)

2003–3

TOLERANCES	
MILLIMETRES	
NO DECIMAL PLACE	>= 0.0 : ± 0.0 <= 0.0 : ± 0.0
ONE DECIMAL PLACE	: ± 0.0
TWO DECIMAL PLACES	: ± 0.00
ANGLES	: ± 0.0°
EXCEPT WHERE STATED	

THE UNIVERSITY OF QUEENSLAND

DIVISION OF MECHANICAL ENGINEERING

COMBUSTOR MODEL

500 MM – WALL PRESSURE

SCALE : 1 : 2		
DRAFTING STANDARD : AS1100	– 1984	
DRAWN : S A ROWAN		24–08–03
2003–3	SIZE: A3	SHEET: 1 OF 1

REVISION HISTORY			
REV	DESCRIPTION	DATE	APPROVED

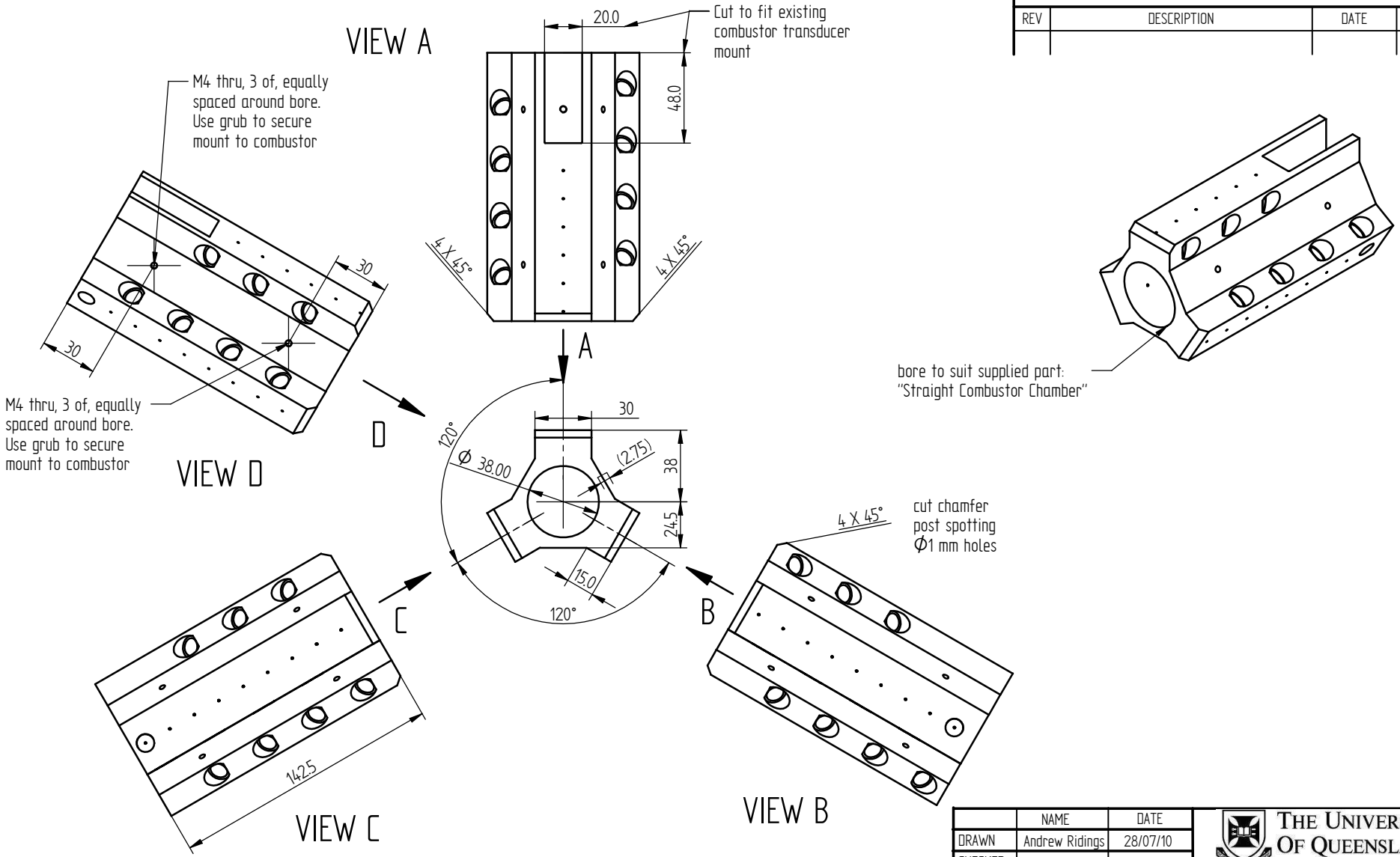

Any questions please call me on x58398 or 0418 440 460

	NAME	DATE
DRAWN	Andrew Ridings	28/07/10
CHECKED		
MGR APPR	Michael Smart	
Material:		
FILE NAME: constArea_CC_fwd_Tri_mount.dft		

UNLESS OTHERWISE SPECIFIED
DIMENSIONS ARE IN MILLIMETERS
0 PL ± 0.1; 1 PL ± 0.1; 2 PL ± 0.01
ANGLES ±0.1°

THE UNIVERSITY OF QUEENSLAND
AUSTRALIA
Centre for Hypersonics

TITLE: Const. Area Combustor Fwd TRI Transducer Mount

PROJECT: Divergent Scramjet Combustors

SIZE	DWG NO	REV
A3	TM-FTRI-CAC	01

SCALE: 1 : 2 | WEIGHT: | SHEET 1 OF 3

REVISION HISTORY			
REV	DESCRIPTION	DATE	APPROVED

Qty: 1
Debur all edges
Cut from Solid Round Bar
(OD = 90 mm) in conjunction
with drawing No. TM-FB-CAC

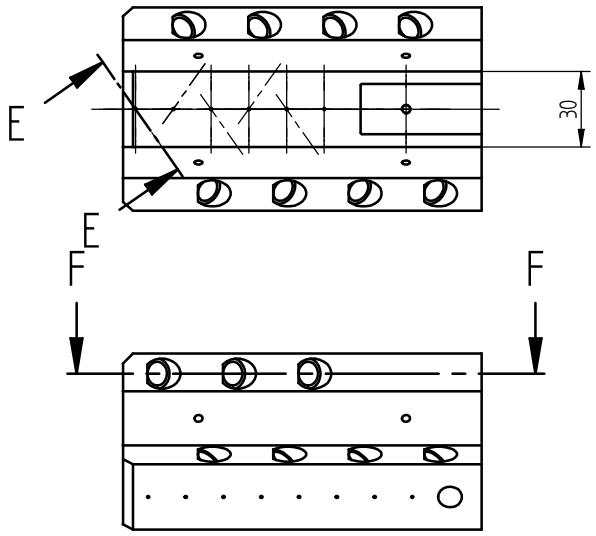

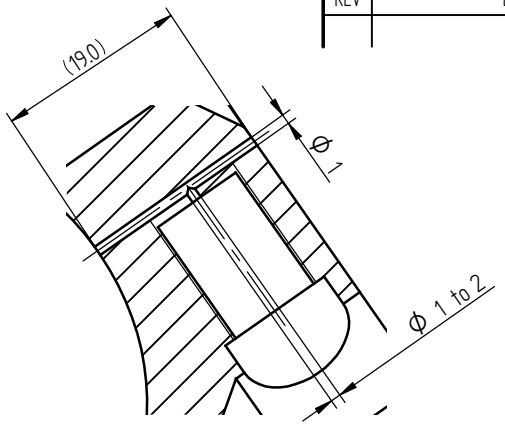

SECTION E-E
2:1

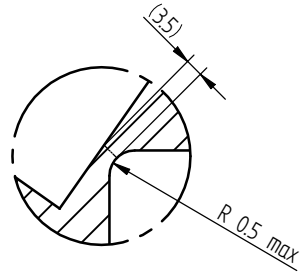

DETAIL G
10:1

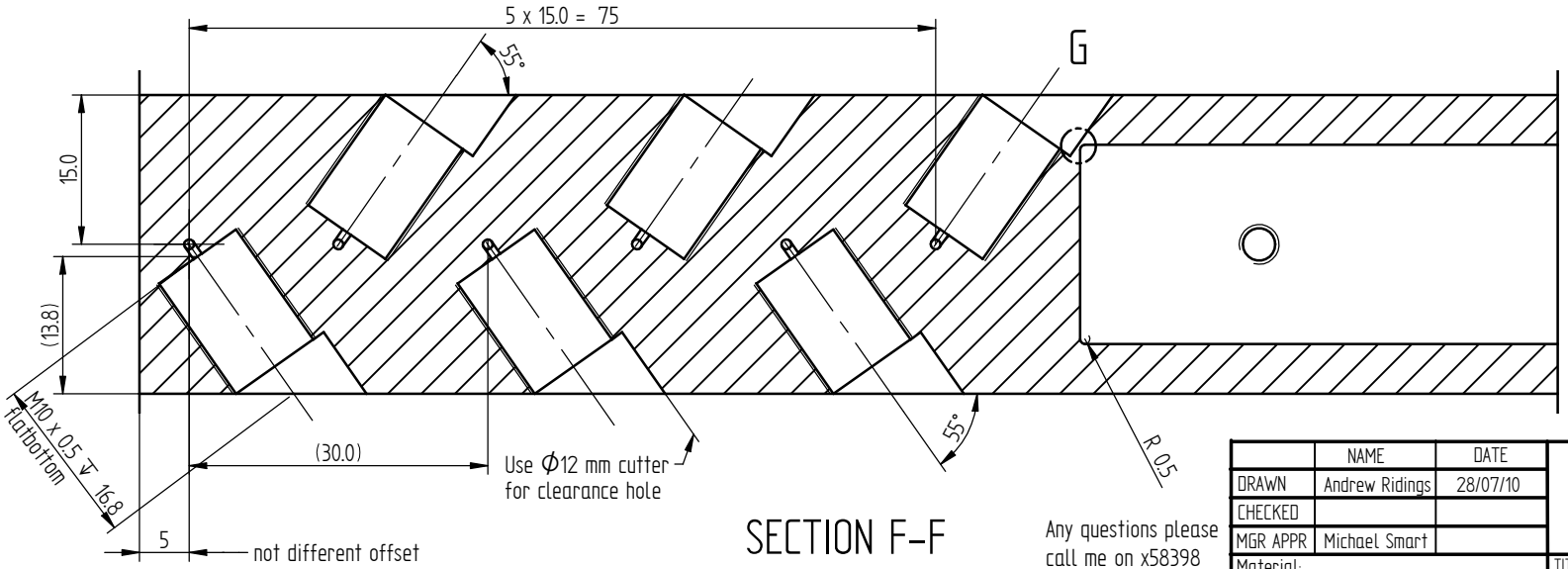

SECTION F-F
2:1

Any questions please
call me on x58398
or 0418 440 460

	NAME	DATE
DRAWN	Andrew Ridings	28/07/10
CHECKED		
MGR APPR	Michael Smart	
Material:		
FILE NAME: constArea_CC_fwd_Tri_mount.dft		

UNLESS OTHERWISE SPECIFIED
DIMENSIONS ARE IN MILLIMETERS
0 PL ± 0.1; 1 PL ± 0.1; 2 PL ± 0.01
ANGLES ±0.1°

THE UNIVERSITY OF QUEENSLAND
AUSTRALIA
Centre for Hypersonics

TITLE: Const. Area Combustor Fwd TRI Transducer Mount

PROJECT: Divergent Scramjet Combustors

SIZE	DWG NO	REV
A3	TM-FTRI-CAC	01

SCALE: 1 : 2 | WEIGHT: | SHEET 2 OF 3

REVISION HISTORY			
REV	DESCRIPTION	DATE	APPROVED

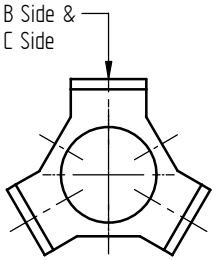

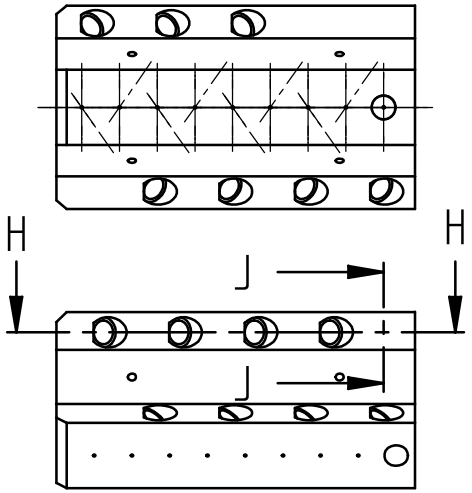

SECTION J-J
2:1

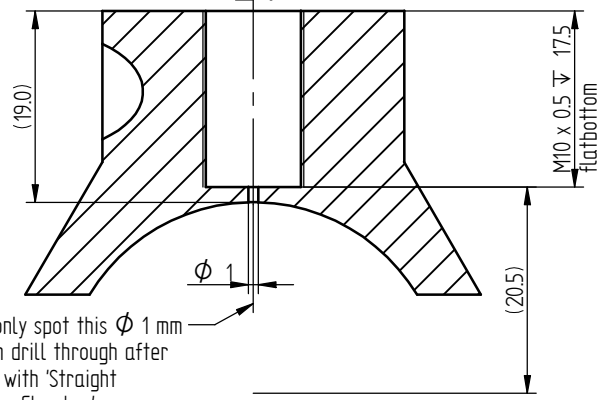

Initially only spot this ϕ 1 mm hole, then drill through after assembly with 'Straight Combustion Chamber'.

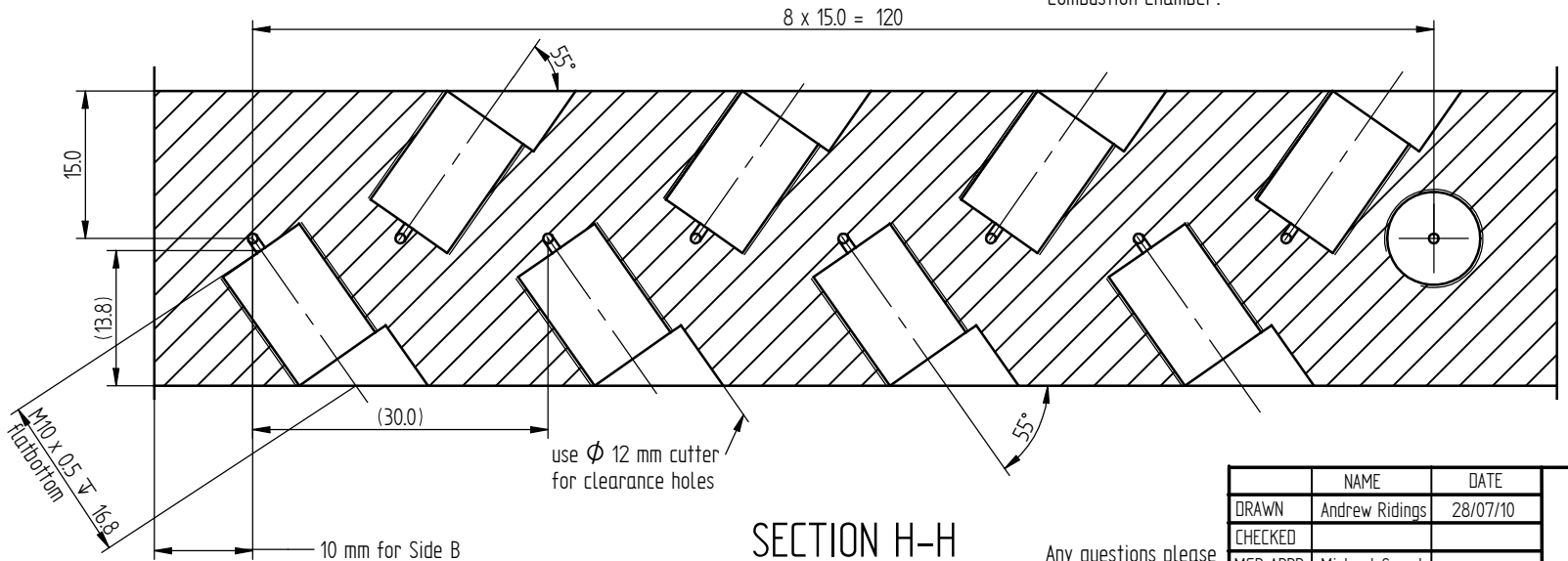

SECTION H-H
2:1

Any questions please call me on x58398 or 0418 440 460

	NAME	DATE
DRAWN	Andrew Ridings	28/07/10
CHECKED		
MGR APPR	Michael Smart	
Material:		
FILE NAME: constArea_CC_fwd_Tri_mount.dft		

UNLESS OTHERWISE SPECIFIED
DIMENSIONS ARE IN MILLIMETERS
0 PL ± 0.1; 1 PL ± 0.1; 2 PL ± 0.01
ANGLES ±0.1°

THE UNIVERSITY OF QUEENSLAND
AUSTRALIA
Centre for Hypersonics

TITLE: Const. Area Combustor Fwd TRI Transducer Mount

PROJECT: Divergent Scramjet Combustors

SIZE	DWG NO	REV
A3	TM-FTRI-CAC	01

SCALE: 1 : 2 | WEIGHT: | SHEET 3 OF 3

REVISION HISTORY			
REV	DESCRIPTION	DATE	APPROVED

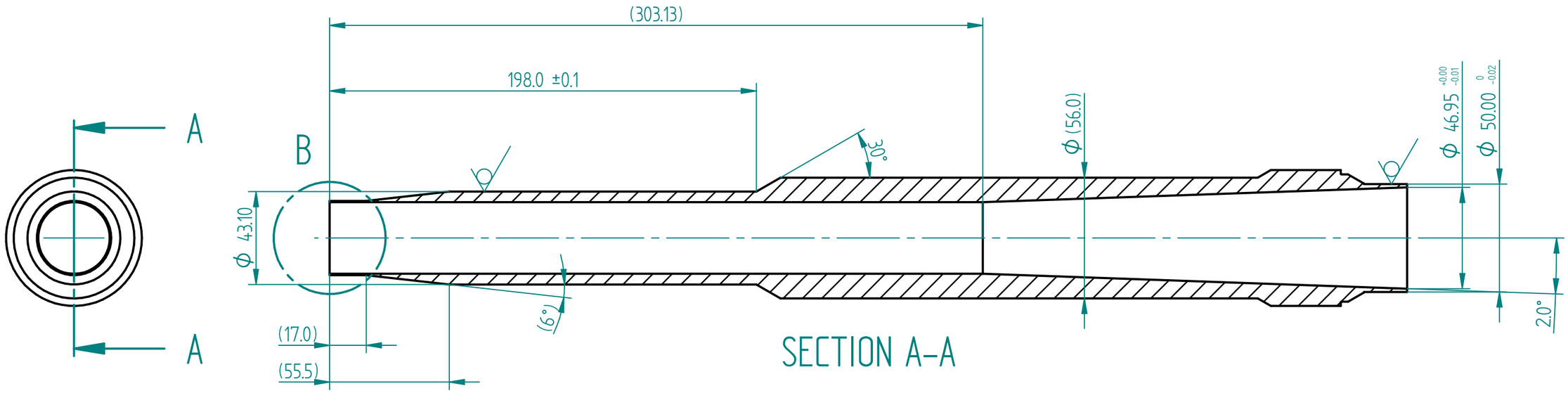

SECTION A–A

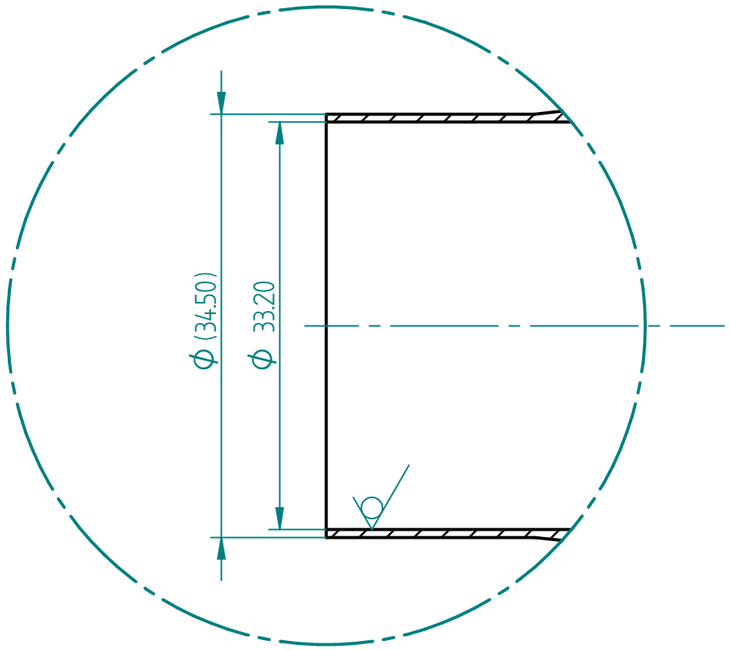

DETAIL B
2:1

N.B. do not debur edges

Any questions please call me on x58398 or 0418 440 460

	NAME	DATE
DRAWN	Andrew Ridings	19/07/10
CHECKED		
MGR APPR	Michael Smart	

Material:

FILE NAME: CC_TSeries_2deg_L500.dft

UNLESS OTHERWISE SPECIFIED
DIMENSIONS ARE IN MILLIMETERS
0 PL ± 0.1; 1 PL ± 0.1; 2 PL ± 0.01
ANGLES ±0.1°

THE UNIVERSITY OF QUEENSLAND
AUSTRALIA
Centre for Hypersonics

TITLE: T-Series 2 deg 500 mm Combustor

PROJECT: Divergent Scramjet Combustors

SIZE	DWG NO	REV
A3	C-T-2-500	01

SCALE: 1 : 2 | WEIGHT: | SHEET 1 OF 1

REVISION HISTORY			
REV	DESCRIPTION	DATE	APPROVED

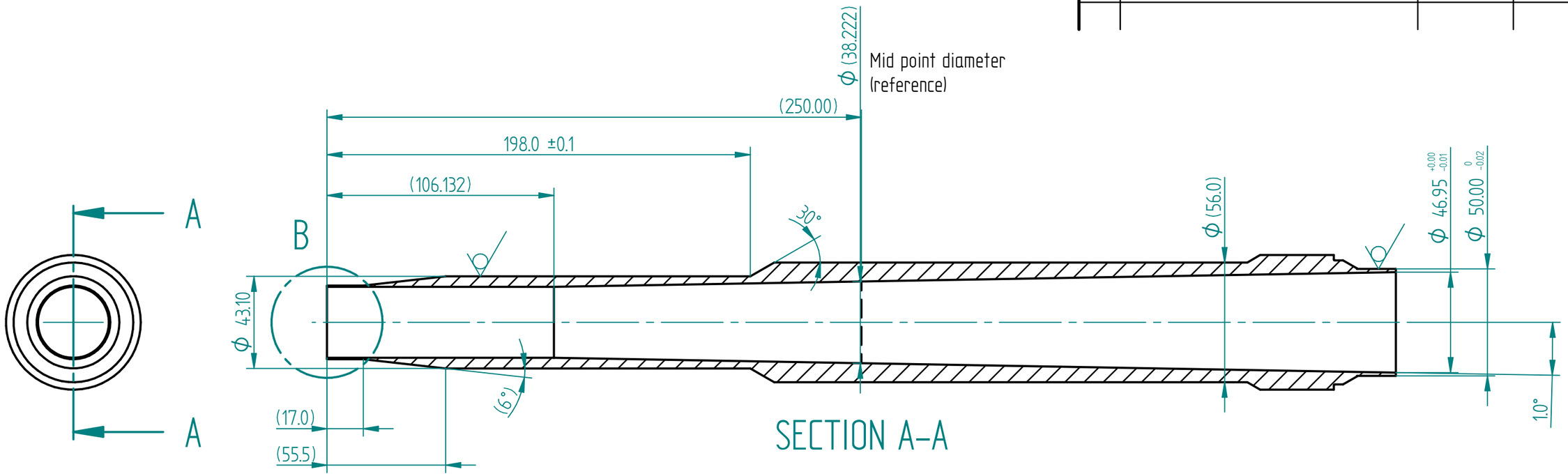

SECTION A–A

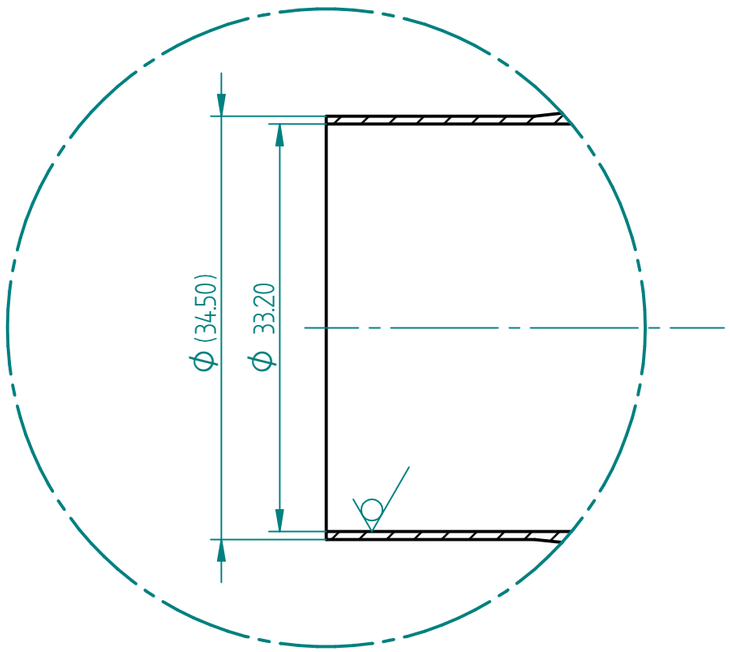

DETAIL B
2:1

N.B. do not debur edges

Any questions please
call me on x58398
or 0418 440 460

	NAME	DATE
DRAWN	Andrew Ridings	03/04/12
CHECKED		
MGR APPR	Michael Smart	

Material:

FILE NAME: CC_TSeries_1deg_L500.dft

UNLESS OTHERWISE SPECIFIED
DIMENSIONS ARE IN MILLIMETERS
0 PL ± 0.1; 1 PL ± 0.1; 2 PL ± 0.01
ANGLES ±0.1°

THE UNIVERSITY OF QUEENSLAND
AUSTRALIA
Centre for Hypersonics

TITLE: T-Series 1 deg 500 mm Combustor

PROJECT: Divergent Scramjet Combustors

SIZE	DWG NO	REV
A3	C-T-1-500	01

SCALE: 1 : 2 | WEIGHT: | SHEET 1 OF 1

REVISION HISTORY			
REV	DESCRIPTION	DATE	APPROVED

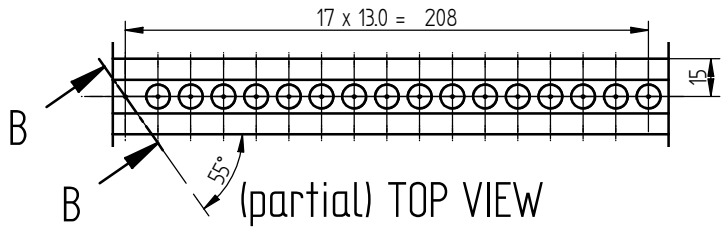

(partial) TOP VIEW

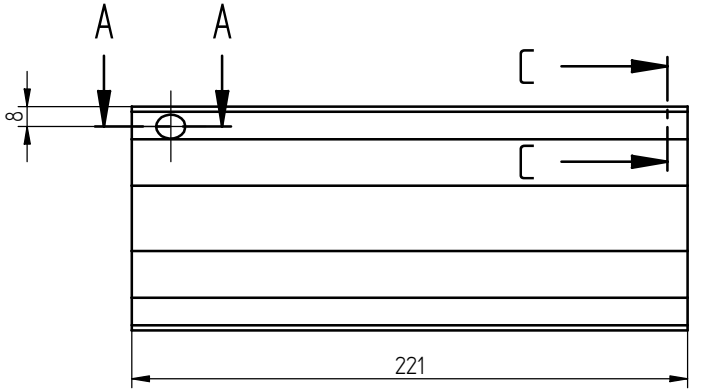

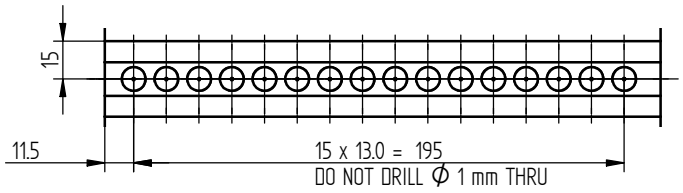

(partial) BOTTOM VIEW

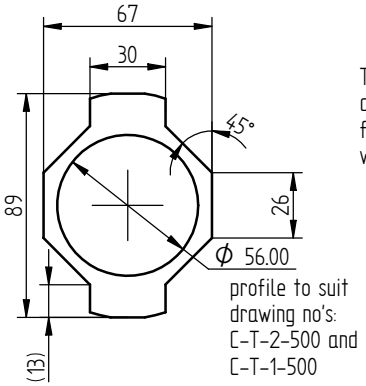

profile to suit drawing no's: C-T-2-500 and C-T-1-500

initially only spot these Φ 1 mm holes, then drill through after assembly with each of the following parts: C-T-1-500 & C-T-2-500

DO NOT DRILL THRU Φ 1 mm HOLES ON BOTTOM SIDE

These rounds are artifacts from cutting from Solid Round Bar with OD = 90mm

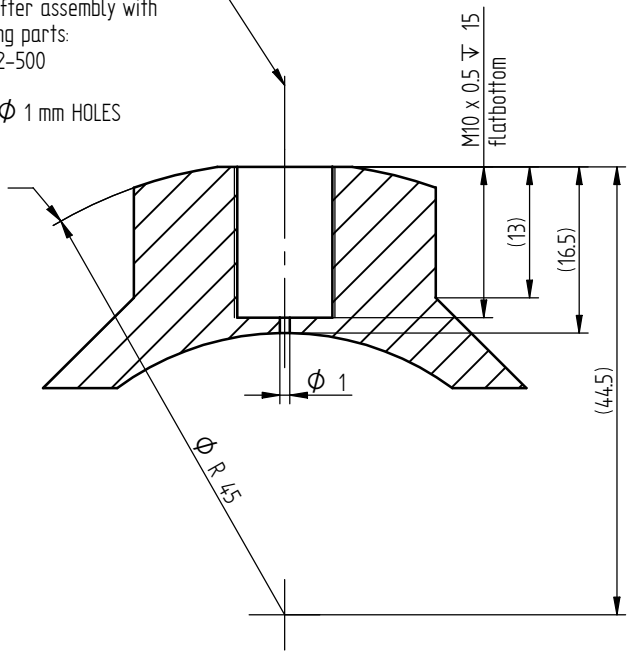

SECTION C-C
2:1

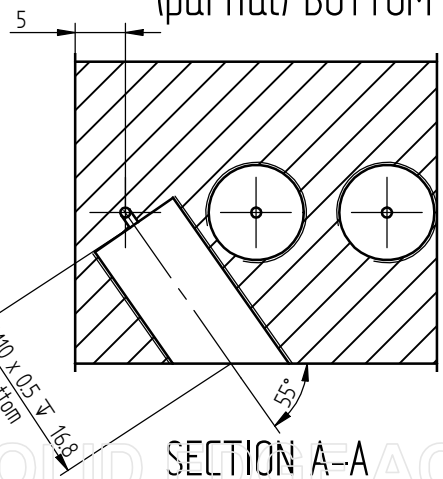

SECTION A-A
2:1

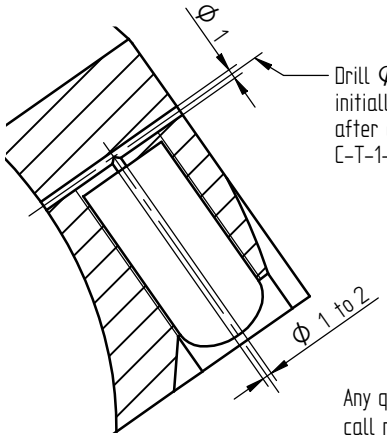

Drill Φ1 mm only ↧ 15 mm initially, then drill through after assembly with parts: C-T-1-500 & C-T-2-500

SECTION B-B
2:1

Qty: 2
Debur all edges
Cut from Solid Round Bar (OD = 90 mm)

Any questions please call me on x58398 or 0418 440 460

	NAME	DATE
DRAWN	Andrew Ridings	28/07/10
CHECKED		
MGR APPR	Michael Smart	
Material: Aluminium		
FILE NAME: TSeries_aft_top_mount.dft		

UNLESS OTHERWISE SPECIFIED
DIMENSIONS ARE IN MILLIMETERS
0 PL ± 0.1; 1 PL ± 0.1; 2 PL ± 0.01
ANGLES ±0.1°

THE UNIVERSITY OF QUEENSLAND
AUSTRALIA
Centre for Hypersonics

TITLE: TSeries Aft Top Transducer Mount

PROJECT: Divergent Scramjet Combustors

SIZE	DWG NO	REV
A3	TM-AT-T	01

SCALE: 1 : 1 | WEIGHT: | SHEET 1 OF 1

REVISION HISTORY			
REV	DESCRIPTION	DATE	APPROVED

VIEW A

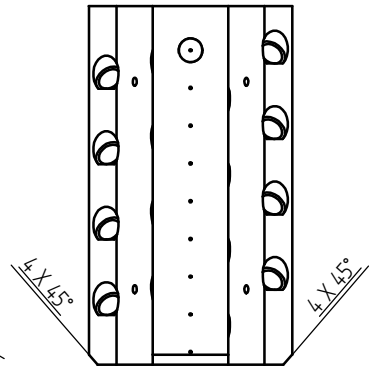

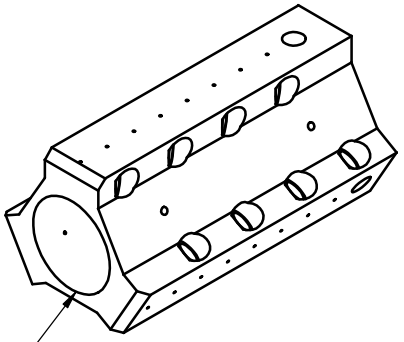

bore to suit
parts: C-T-2-500
and C-T-1-500

M4 thru, 3 of, equally
spaced around bore.
Use grub to secure
mount to combustor

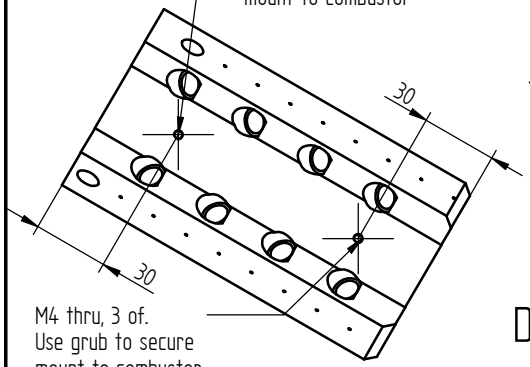

M4 thru, 3 of.
Use grub to secure
mount to combustor

VIEW D

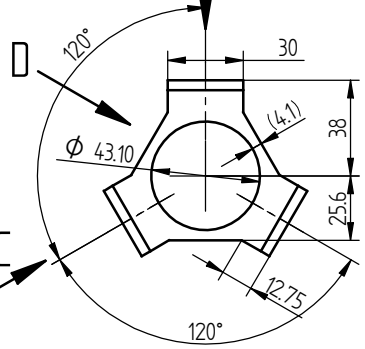

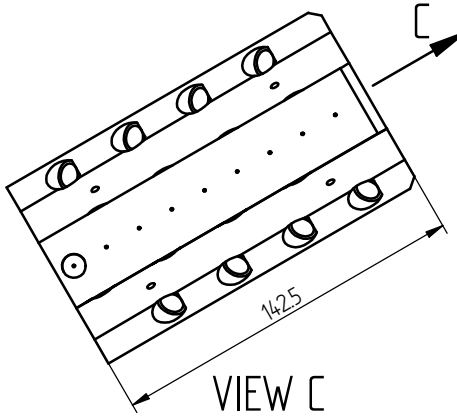

VIEW C

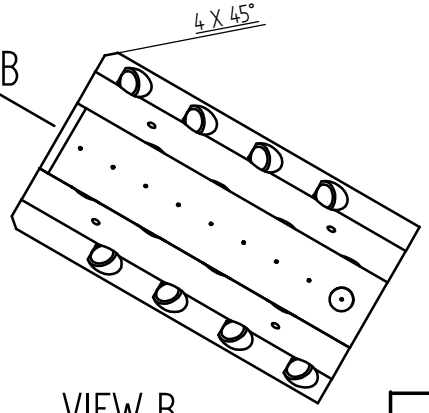

VIEW B

Qty: 2
Debur all edges.
Cut from Solid Round Bar
(OD = 90 mm)

Any questions please
call me on x58398
or 0418 440 460

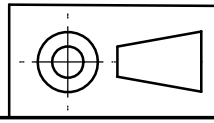

	NAME	DATE
DRAWN	Andrew Ridings	28/07/10
CHECKED		
MGR APPR	Michael Smart	

Material:

FILE NAME: TSeries_fwd_whole_tri_mount.dft

UNLESS OTHERWISE SPECIFIED
DIMENSIONS ARE IN MILLIMETERS
0 PL ± 0.1; 1 PL ± 0.1; 2 PL ± 0.01
ANGLES ±0.1°

THE UNIVERSITY OF QUEENSLAND
AUSTRALIA
Centre for Hypersonics

TITLE: TSeries Forward Tri Transducer Mount

PROJECT: Divergent Scramjet Combustors

SIZE	DWG NO	REV
A3	TM-FTRI-T	01

SCALE: 1 : 2 | WEIGHT: | SHEET 1 OF 2

REVISION HISTORY			
REV	DESCRIPTION	DATE	APPROVED

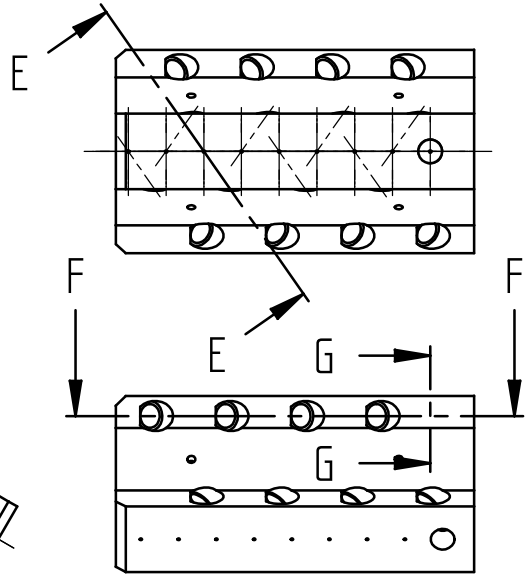

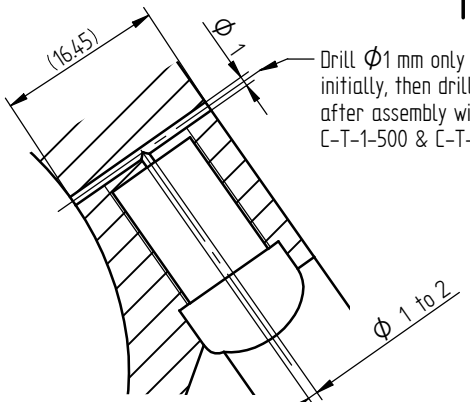

SECTION E-E
2:1

SECTION G-G
2:1

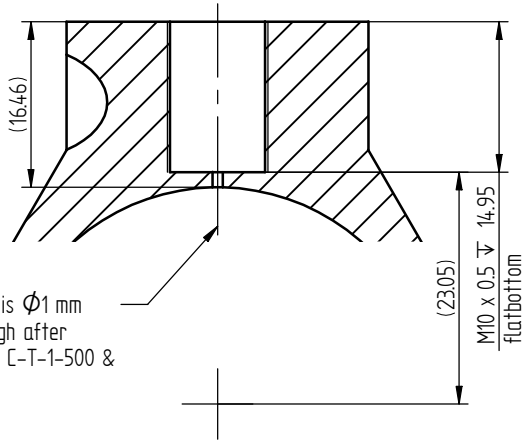

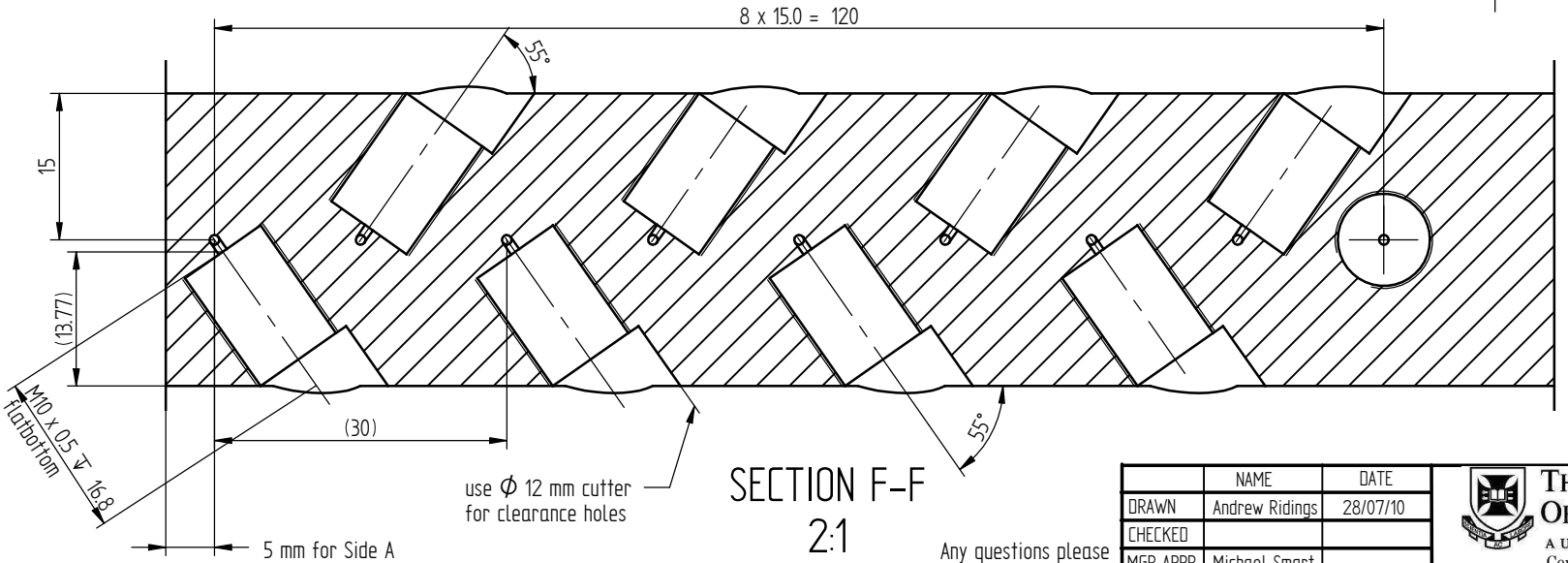

SECTION F-F
2:1

Any questions please call me on x58398 or 0418 440 460

	NAME	DATE
DRAWN	Andrew Ridings	28/07/10
CHECKED		
MGR APPR	Michael Smart	
Material:		
FILE NAME: TSeries_fwd_whole_tri_mount.ipt		

UNLESS OTHERWISE SPECIFIED
DIMENSIONS ARE IN MILLIMETERS
0 PL ± 0.1; 1 PL ± 0.1; 2 PL ± 0.01
ANGLES ±0.1°

THE UNIVERSITY OF QUEENSLAND
AUSTRALIA
Centre for Hypersonics

TITLE: TSeries Forward Tri Transducer Mount

PROJECT: Divergent Scramjet Combustors

SIZE	DWG NO	REV
A3	TM-FTRI-T	01

SCALE: 1 : 2 | WEIGHT: | SHEET 2 OF 2

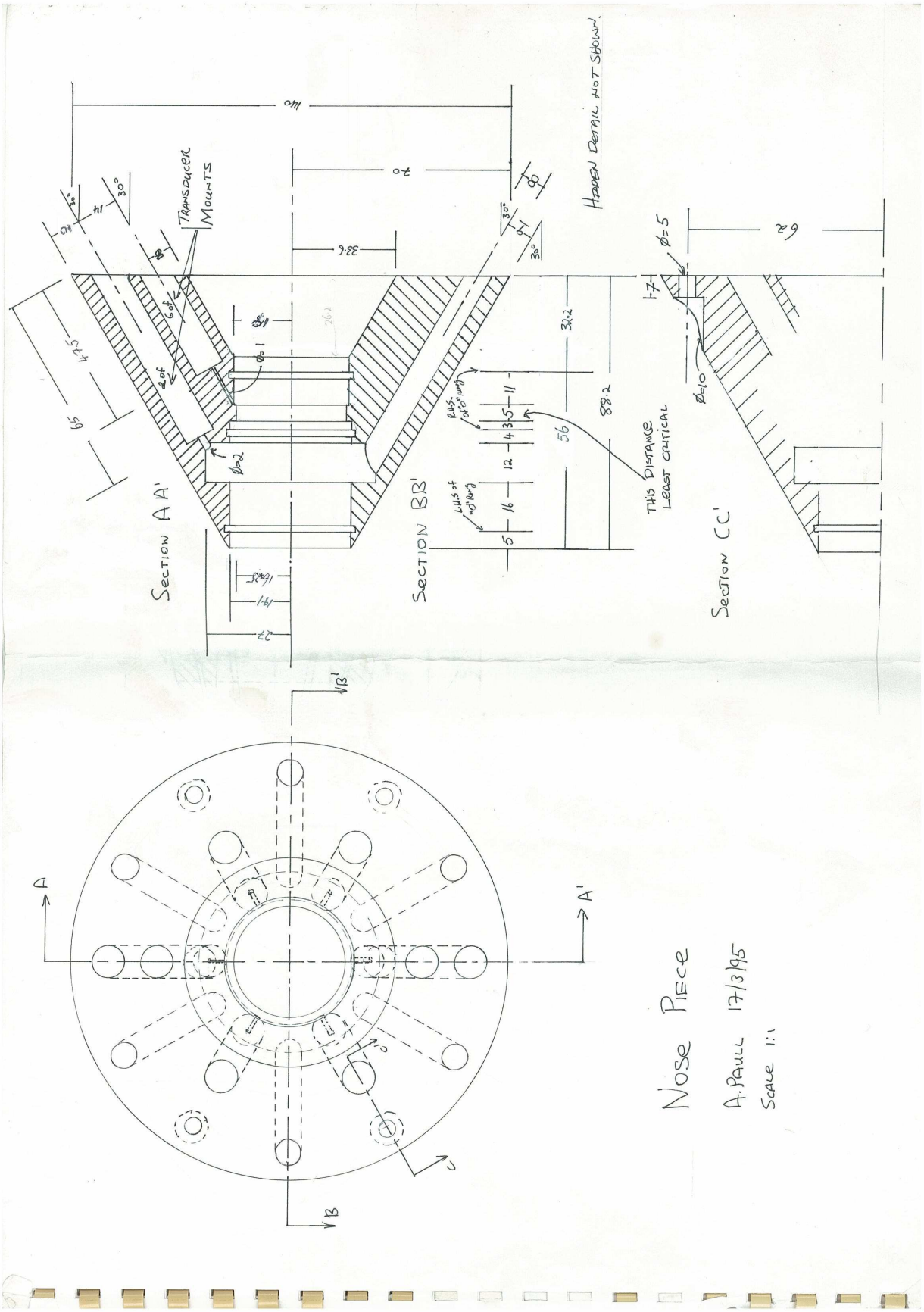
Section A A'
Section BB'
Section CC'
Transducer Mounts
Hidden Detail not shown
This distance least critical
Nose Piece
A. Paull 17/3/95
Scale 1:1

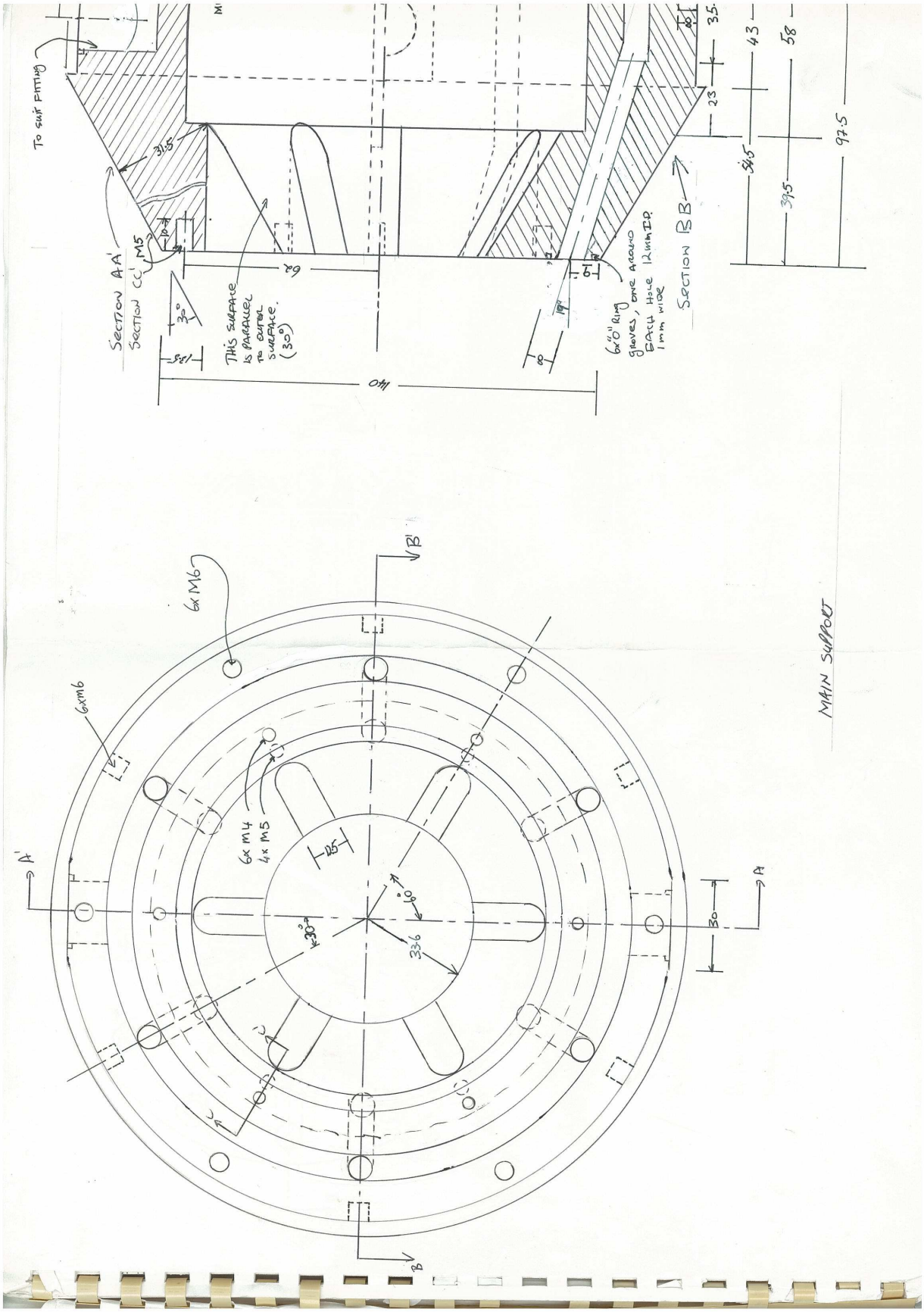
To suit fitting
31.5
SECTION AA'
SECTION CC'
M5
30°
THIS SURFACE IS PARALLEL TO OTHER SURFACE. (30°)
69
140
6x O'RING GROOVES, ONE AROUND EACH HOLE 12mm ID 1mm WIDE
SECTION BB
3.5
23
43
58
34.5
39.5
97.5
6x M6
6xm6
6x M4
4x M5
B'
A'
A
B
25
30°
10°
33.6
30
MAIN SUPPORT

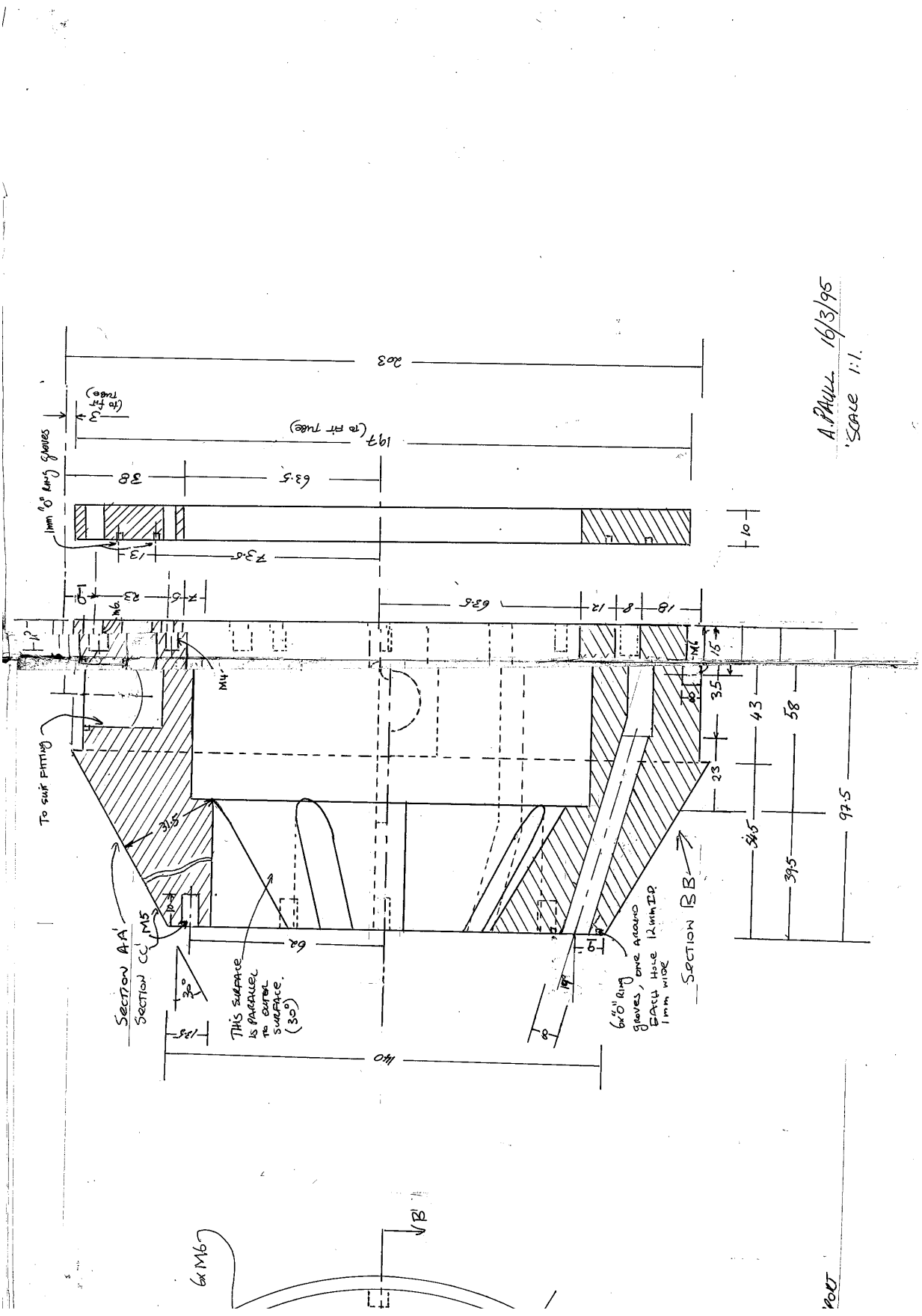
A. PAULL 16/3/95
SCALE 1:1
303
192 (8 FIT Tubes)
(10 FIT Tubes)
63.5
38
1mm 'O' RING GROOVES
73.5
13
10
23
6
4
63.5
18
8
12
15
M4
35
43
58
97.5
31.5
M5
SECTION AA'
SECTION CC'
30°
18.5
THIS SURFACE IS PARALLEL TO OUTER SURFACE. (30°)
68
140
6x 'O' RING GROOVES, ONE AROUND EACH HOLE 1.2mm DP 1mm WIDE
SECTION BB
6xM6
B

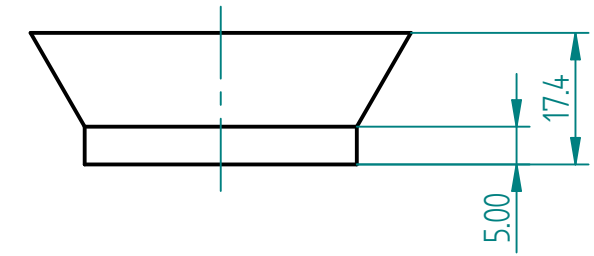

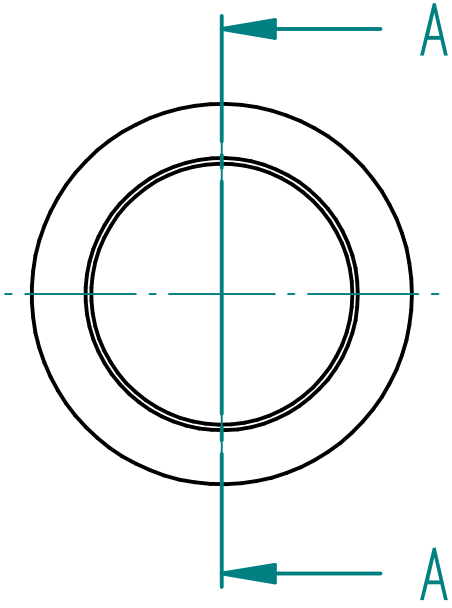

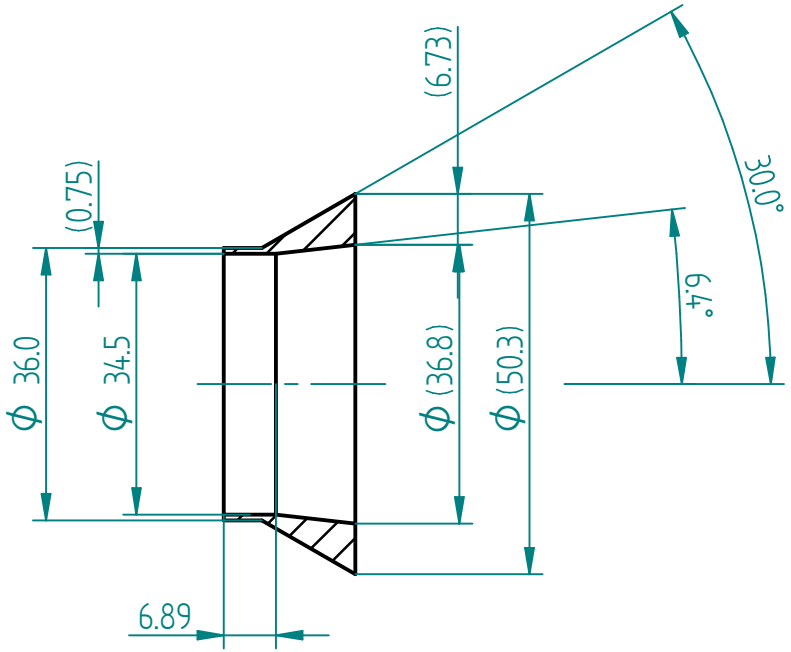

SECTION A–A

Any questions please
call me on x54248
or 0418 440 460

	NAME	DATE
DRAWN	A.Ridings	23/02/13
CHECKED		
ENG APPR	M.Smart	
MGR APPR		

THE UNIVERSITY OF QUEENSLAND
AUSTRALIA

TITLE
Cone Spacer for Divergent Combustors

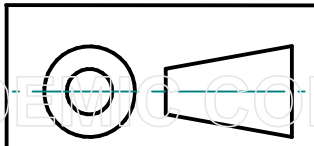

UNLESS OTHERWISE SPECIFIED
DIMENSIONS ARE IN MILLIMETERS
ANGLES ±0.1°
0 PL ± 0.1; 1 PL ± 0.05; 2 PL ± 0.01

SIZE	DWG NO	REV
A4	CS-1dC	01

FILE NAME: cone_spacer_1deg_combustor_V2.dft

SCALE: 1:1	WEIGHT:	SHEET 1 OF 1

Material : Aluminimum

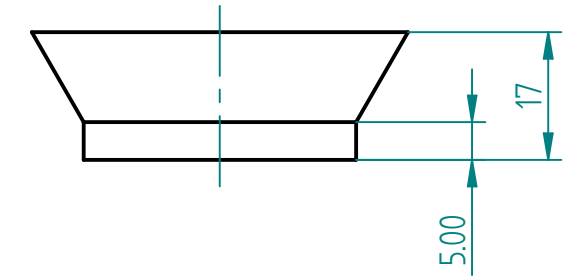

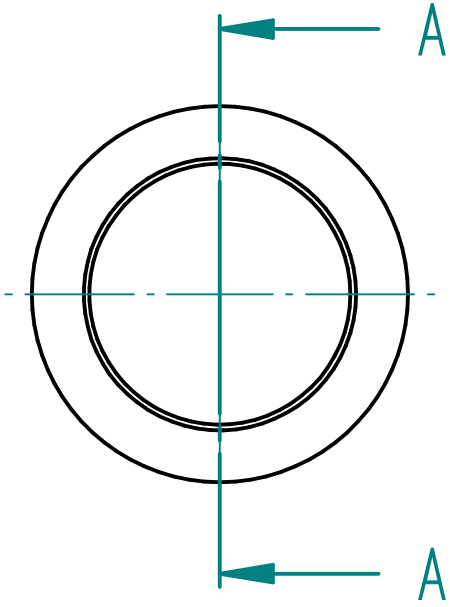

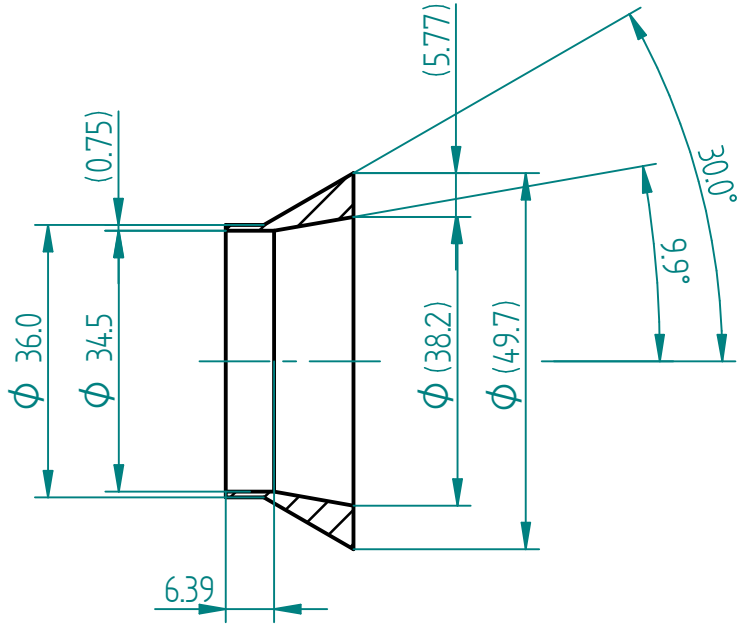

SECTION A-A

Any questions please call me on x54248 or 0418 440 460

	NAME	DATE
DRAWN	A.Ridings	23/02/13
CHECKED		
ENG APPR	M.Smart	
MGR APPR		

THE UNIVERSITY OF QUEENSLAND
AUSTRALIA

TITLE
Cone Spacer for Const. Area. Combustor

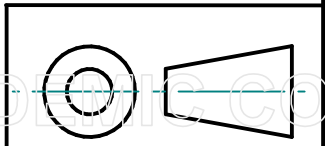

UNLESS OTHERWISE SPECIFIED
DIMENSIONS ARE IN MILLIMETERS
ANGLES ±0.1°
0 PL ± 0.1; 1 PL ± 0.05; 2 PL ± 0.01

SIZE	DWG NO	REV
A4	CS-CAC	01

FILE NAME: cone_spacer_constant_area_combustor_V2.dft

SCALE: 1:1	WEIGHT:	SHEET 1 OF 1

Material : Aluminium

REVISION HISTORY			
REV	DESCRIPTION	DATE	APPROVED

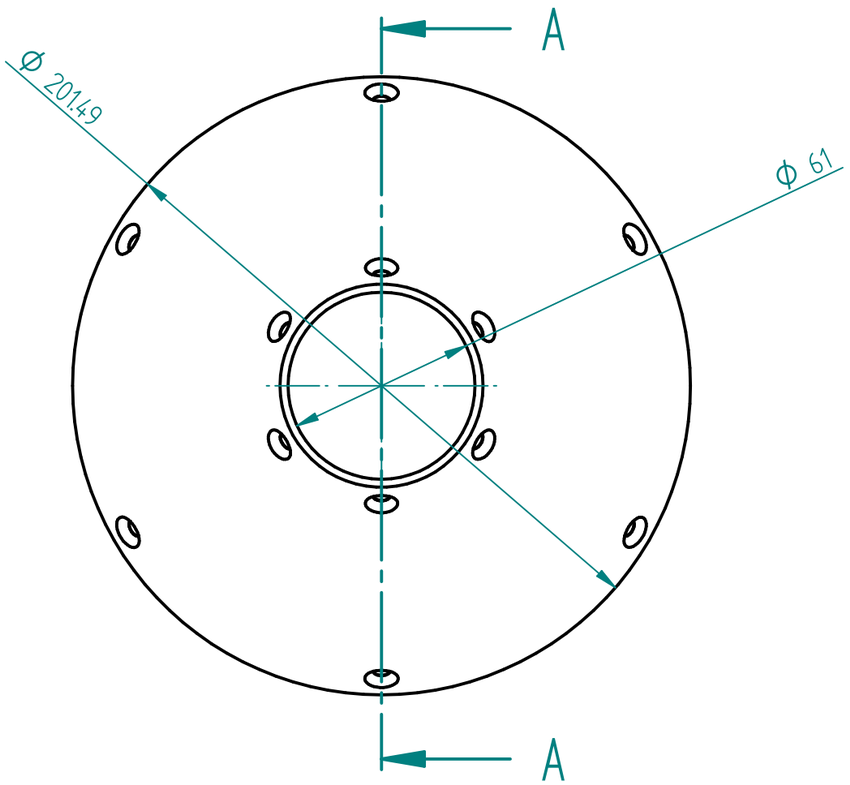

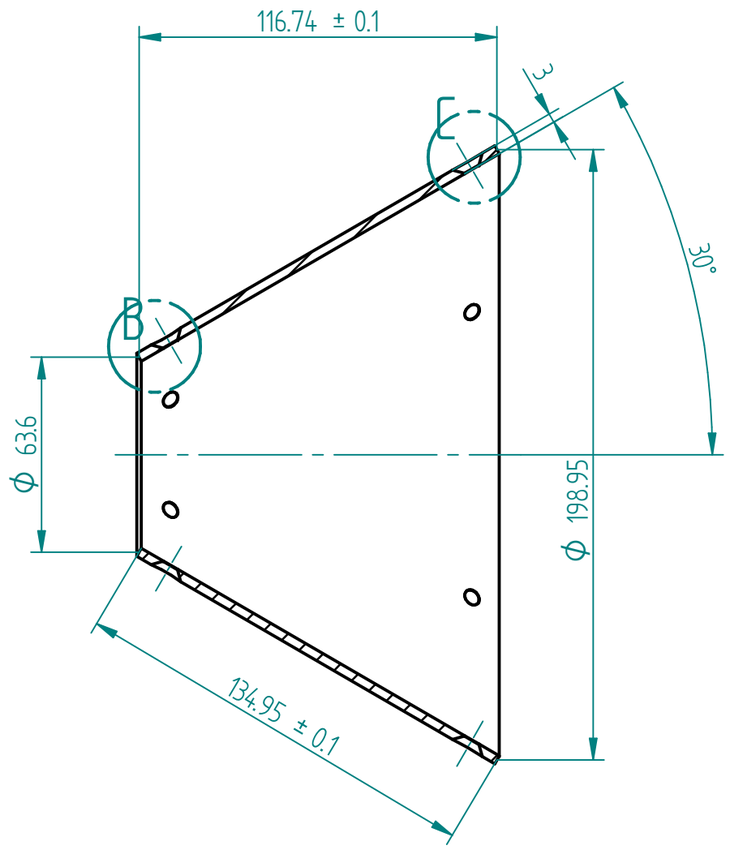

SECTION A-A

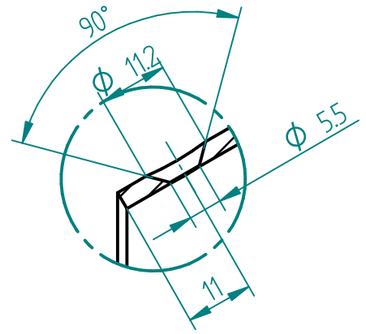

DETAIL B
1:1

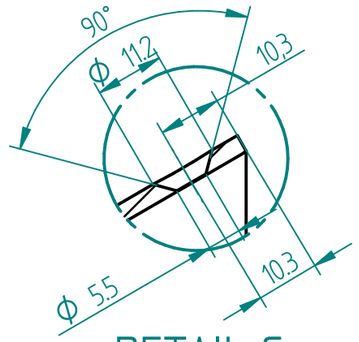

DETAIL C
1:1

	NAME	DATE
DRAWN	Andrew Ridings	10/06/10
CHECKED		
MGR APPR	Michael Smart	

Material: Steel sheet

FILE NAME: Front_cone_V5.dft

UNLESS OTHERWISE SPECIFIED
DIMENSIONS ARE IN MILLIMETERS
0 PL ± 0.1; 1 PL ± 0.1; 2 PL ± 0.01
ANGLES ±0.1°

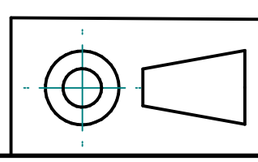

THE UNIVERSITY OF QUEENSLAND
AUSTRALIA
Centre for Hypersonics

TITLE: Front Cone

PROJECT: Divergent Scramjet Combustors

SIZE	DWG NO	REV
A3	FWD-CONE	01

SCALE: 1 : 1	WEIGHT:	SHEET 1 OF 1

REVISION HISTORY			
REV	DESCRIPTION	DATE	APPROVED

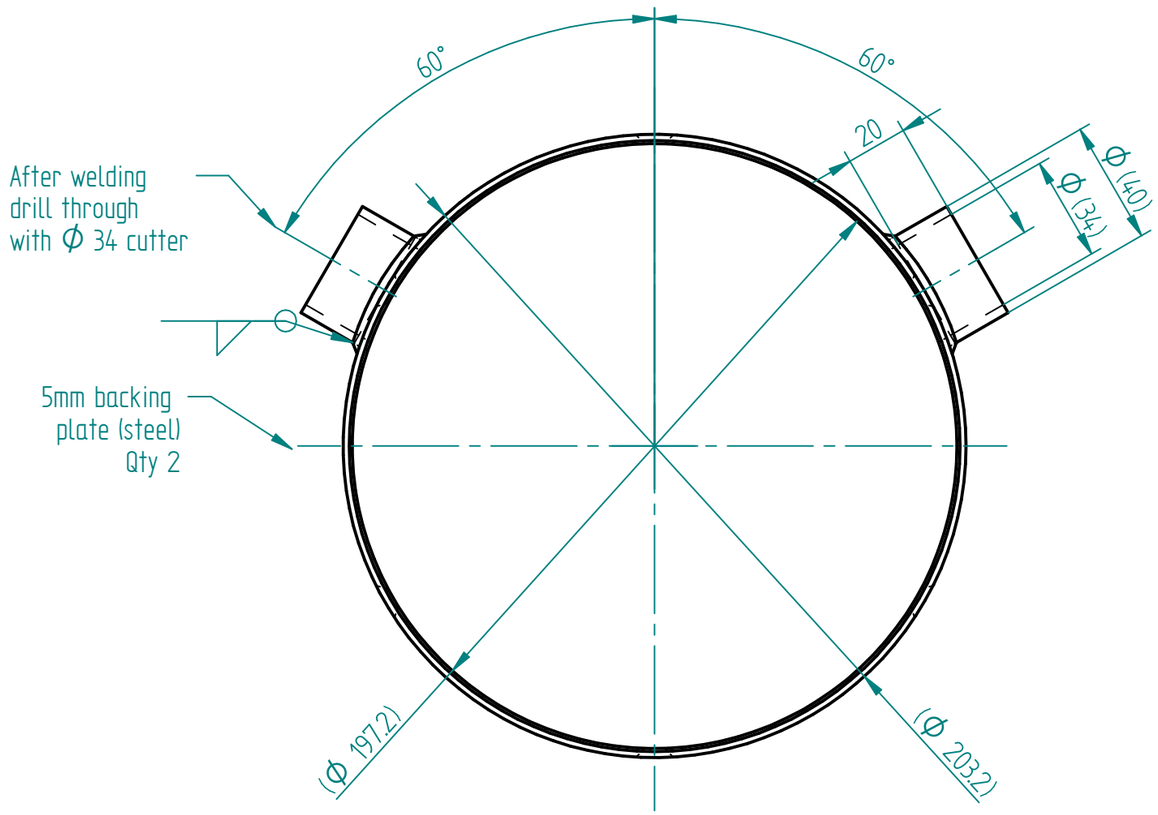

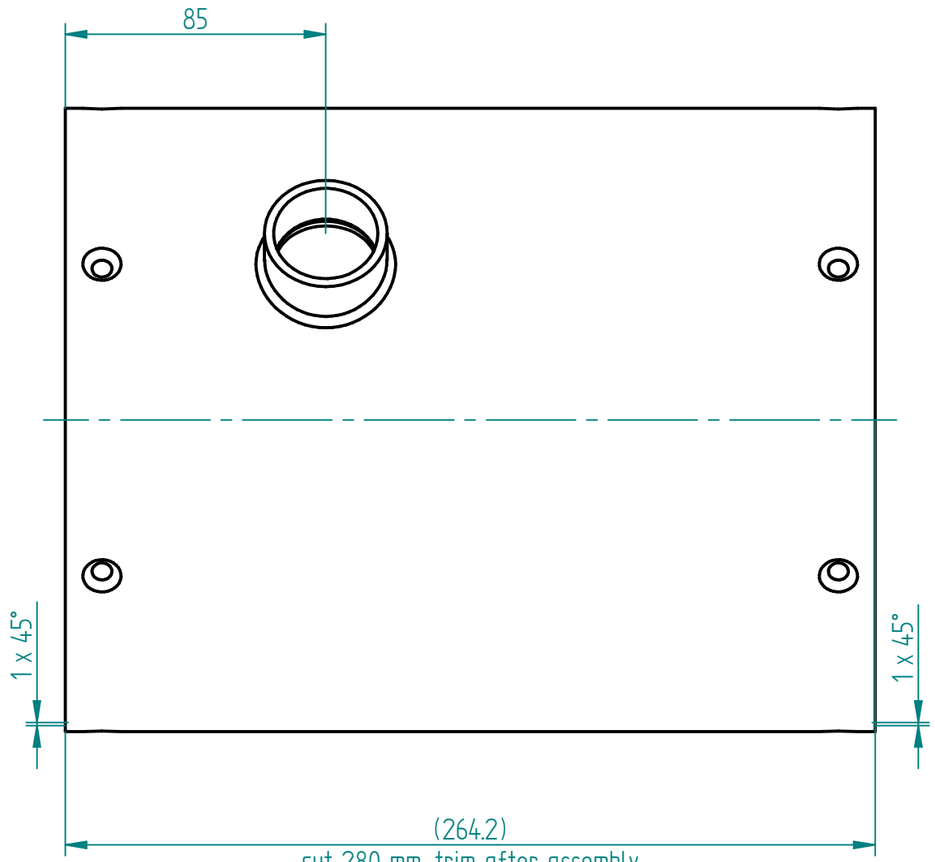

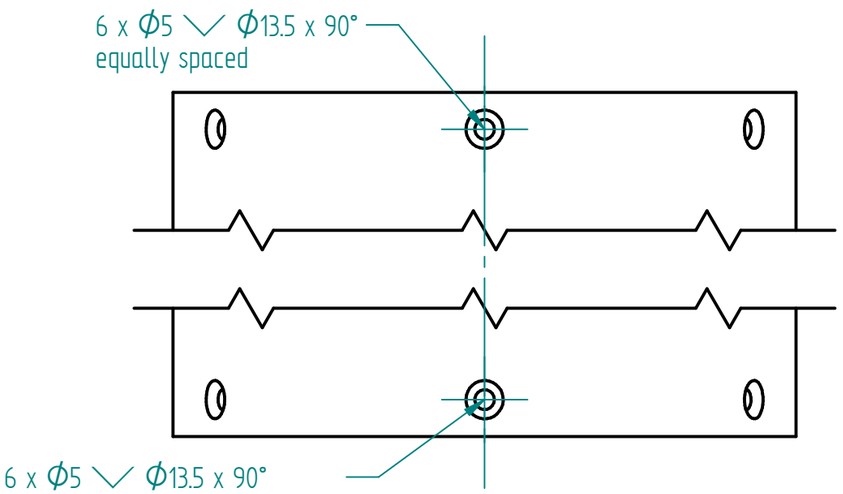

	NAME	DATE
DRAWN	uqaridi1	23/02/13
CHECKED		
MGR APPR	Michael Smart	
Material:	Mild Steel	
FILE NAME: diffuser_outershield_V9_welded.dft		

UNLESS OTHERWISE SPECIFIED
DIMENSIONS ARE IN MILLIMETERS
0 PL ± 0.1; 1 PL ± 0.1; 2 PL ± 0.01
ANGLES ±0.1°

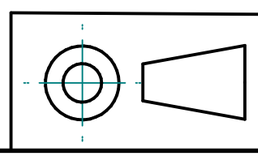

THE UNIVERSITY OF QUEENSLAND
AUSTRALIA
Centre for Hypersonics

TITLE	Diffuser Outershield
PROJECT	Divergent Scramjet Combustors

SIZE	DWG NO	REV
A3	FWD-OUTERSHIELD	01

SCALE: 1 : 1	WEIGHT:	SHEET 1 OF 1

REVISION HISTORY			
REV	DESCRIPTION	DATE	APPROVED

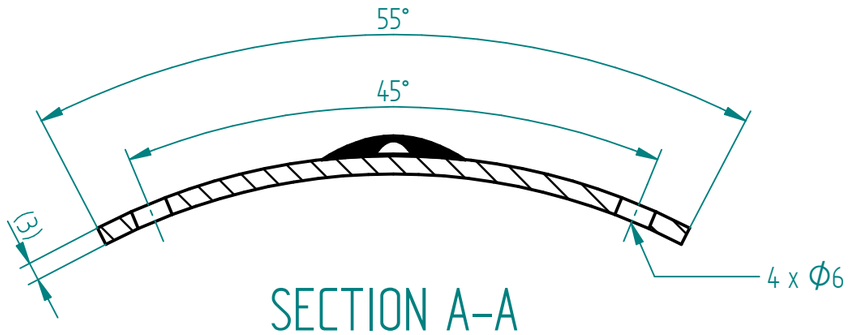

SECTION A–A

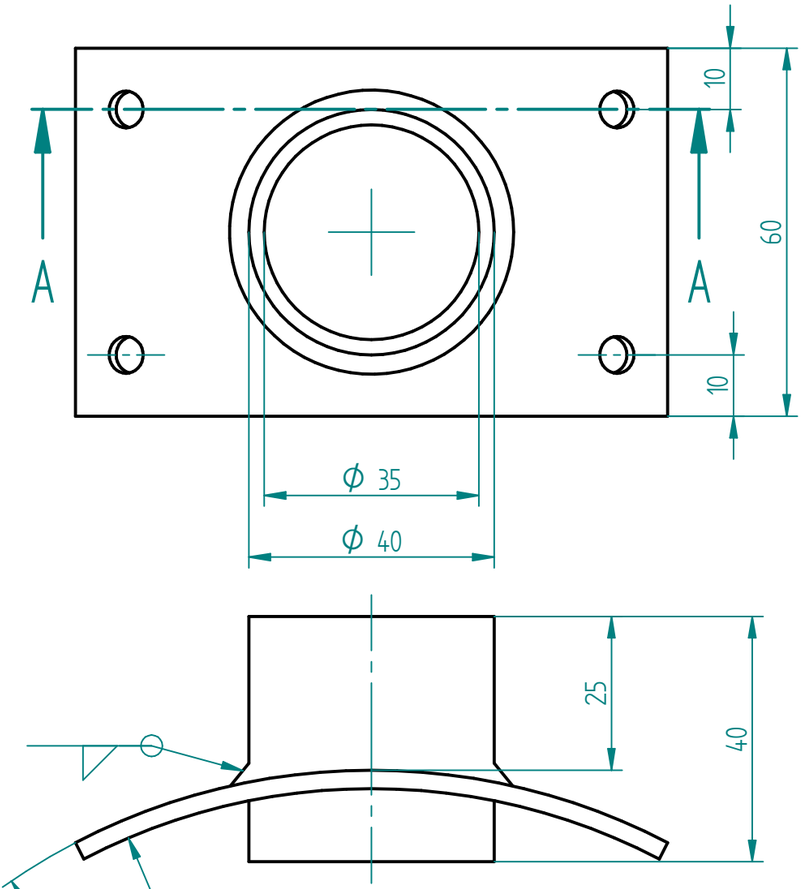

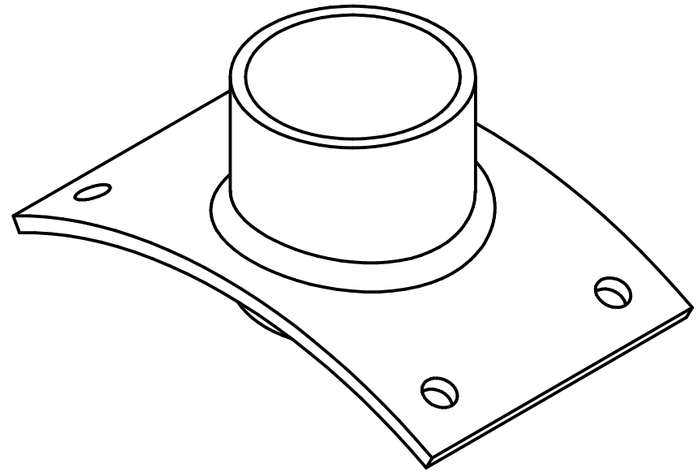

Qty: 2

Any questions please
call me on x54248
or 0418 440 460

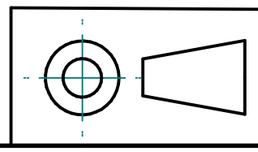

	NAME	DATE
DRAWN	A. Ridings	31/03/11
CHECKED		
MGR APPR	M. Smart	

Material: Aluminium

FILE NAME: data_port_plate_welded.dft

UNLESS OTHERWISE SPECIFIED
DIMENSIONS ARE IN MILLIMETERS
0 PL ± 0.1; 1 PL ± 0.1; 2 PL ± 0.01
ANGLES ±0.1°

THE UNIVERSITY OF QUEENSLAND
AUSTRALIA
Centre for Hypersonics

TITLE: Welded Data Port Insert

PROJECT: Divergent Scramjet Combustors

SIZE	DWG NO	REV
A3	WDP	01

SCALE: | WEIGHT: | SHEET 1 OF 1

REVISION HISTORY			
REV	DESCRIPTION	DATE	APPROVED

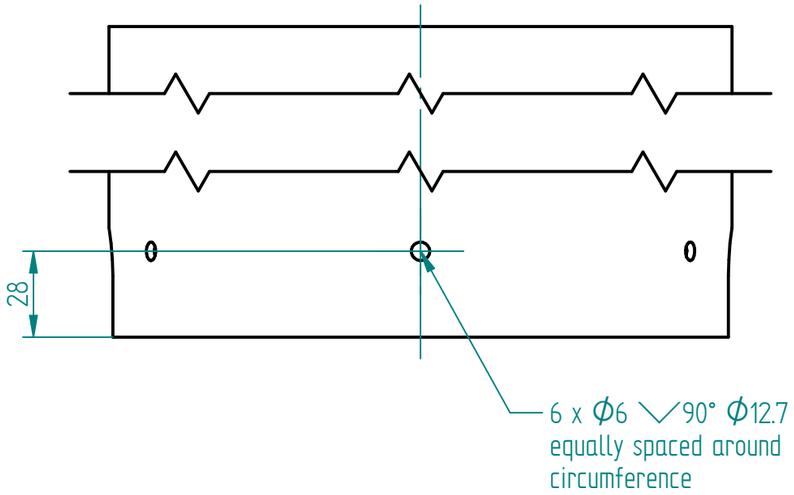

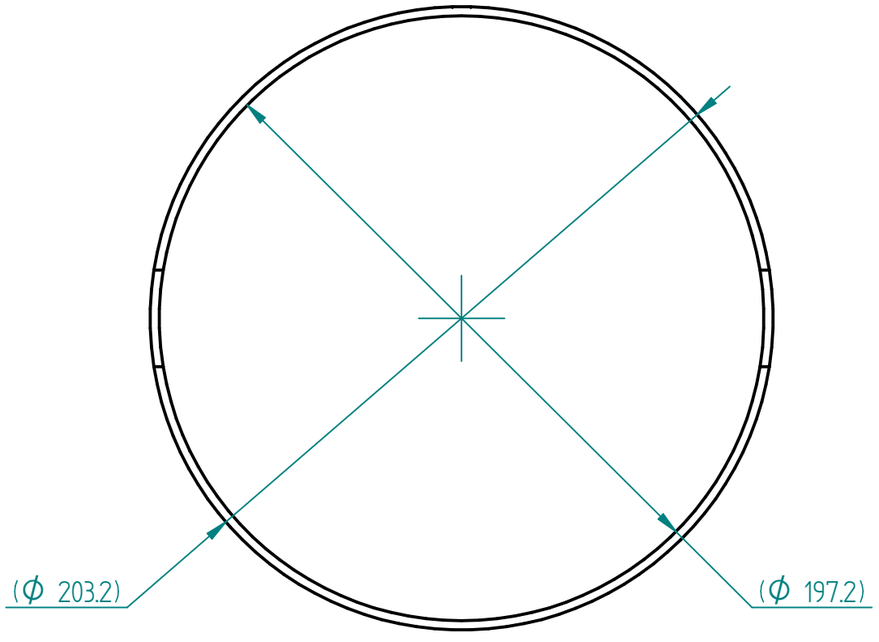

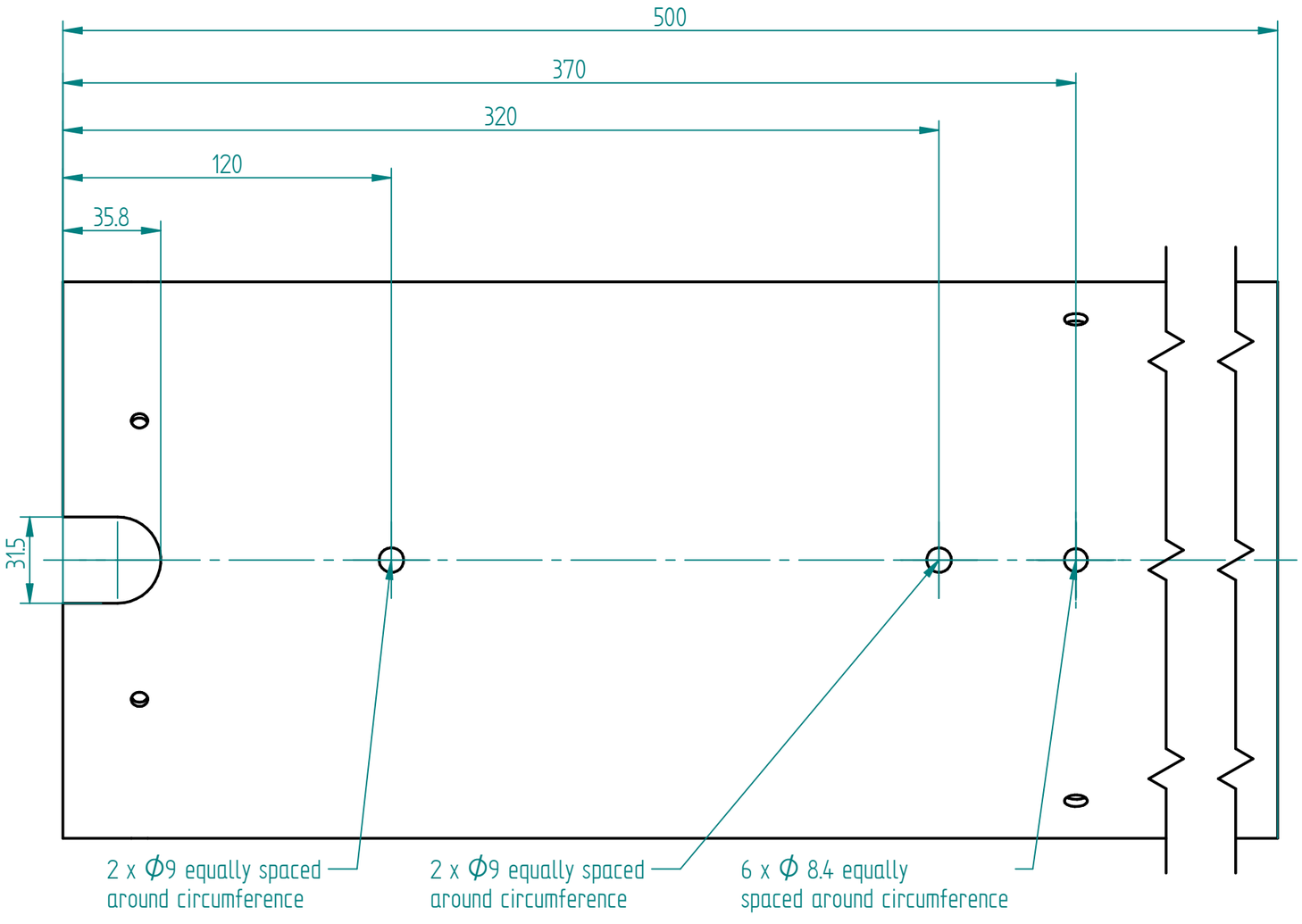

Any questions please
call me on x54248
or 0418 440 460

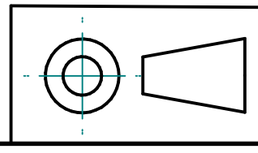

	NAME	DATE
DRAWN	A.Ridings	23/02/13
CHECKED		
MGR APPR	M.Smart	

Material: Aluminium (supplied)

FILE NAME: Rear_Outershield.dft

UNLESS OTHERWISE SPECIFIED
DIMENSIONS ARE IN MILLIMETERS
0 PL ± 0.1; 1 PL ± 0.1; 2 PL ± 0.01
ANGLES ±0.1°

THE UNIVERSITY OF QUEENSLAND
AUSTRALIA
Centre for Hypersonics

TITLE: Rear Outer Shield

PROJECT: Divergent Scramjet Combustors

SIZE	DWG NO	REV
A3	OS-REAR	01

SCALE: | WEIGHT: | SHEET 1 OF 2

REVISION HISTORY			
REV	DESCRIPTION	DATE	APPROVED

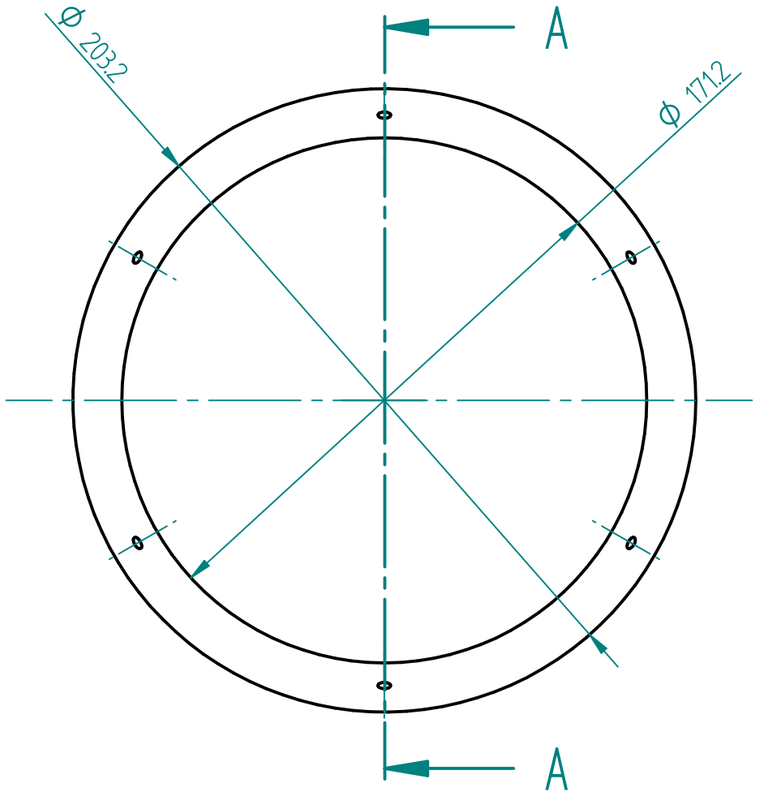

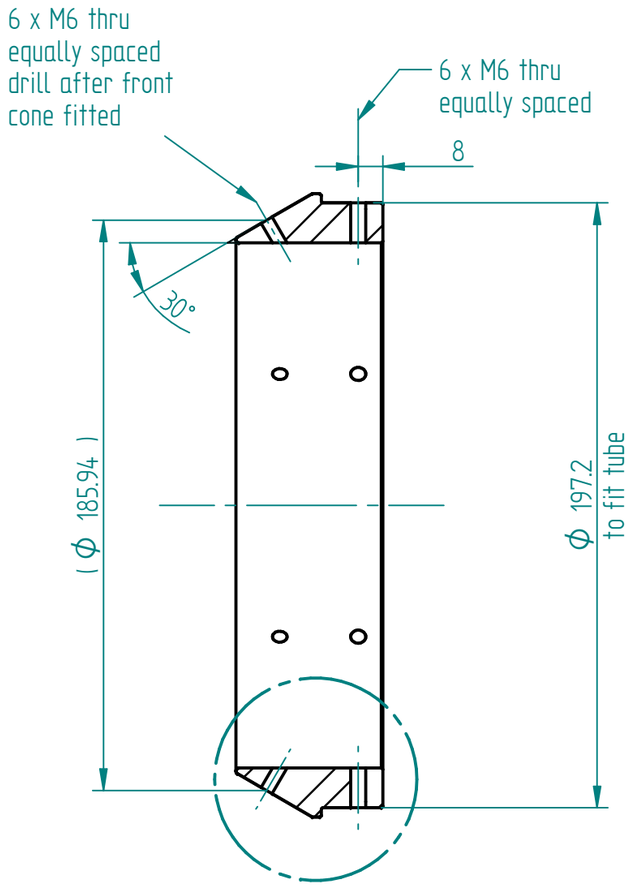

B
SECTION A-A

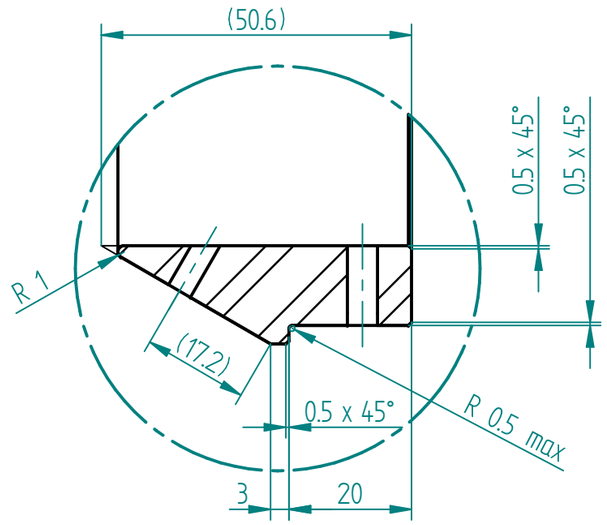

DETAIL B
1:1

Any questions please
call me on x58398
or 0418 440 460

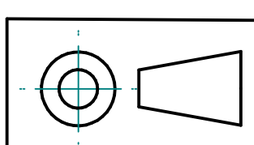

	NAME	DATE
DRAWN	Andrew Ridings	08/06/10
CHECKED		
MGR APPR	Michael Smart	
Material:	Mild Steel	
FILE NAME: Forward_Ring_V5.dft		

UNLESS OTHERWISE SPECIFIED
DIMENSIONS ARE IN MILLIMETERS
0 PL ± 0.1; 1 PL ± 0.1; 2 PL ± 0.01
ANGLES ±0.1°

THE UNIVERSITY OF QUEENSLAND
AUSTRALIA
Centre for Hypersonics

TITLE: Forward Support Ring		
PROJECT: Divergent Scramjet Combustors		
SIZE: A3	DWG NO: FWD-RING	REV: 1
SCALE: 1 : 2	WEIGHT:	SHEET 1 OF 1

REVISION HISTORY			
REV	DESCRIPTION	DATE	APPROVED
02	Holes to clamp to fuel block now align to axial of the ring	08 Jun 10	AR

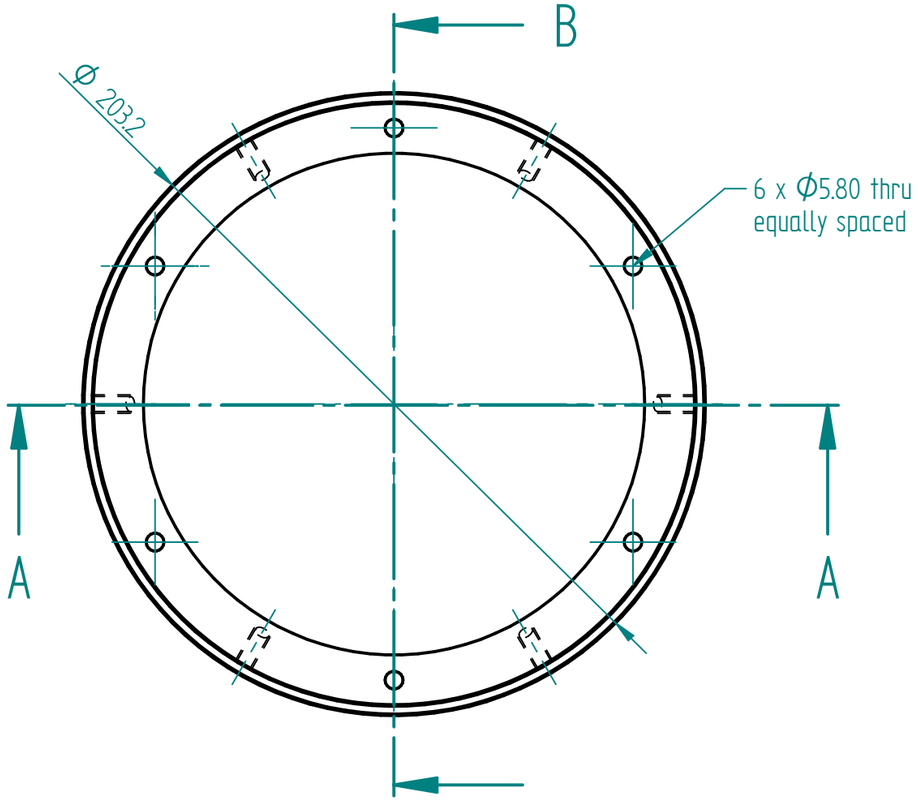

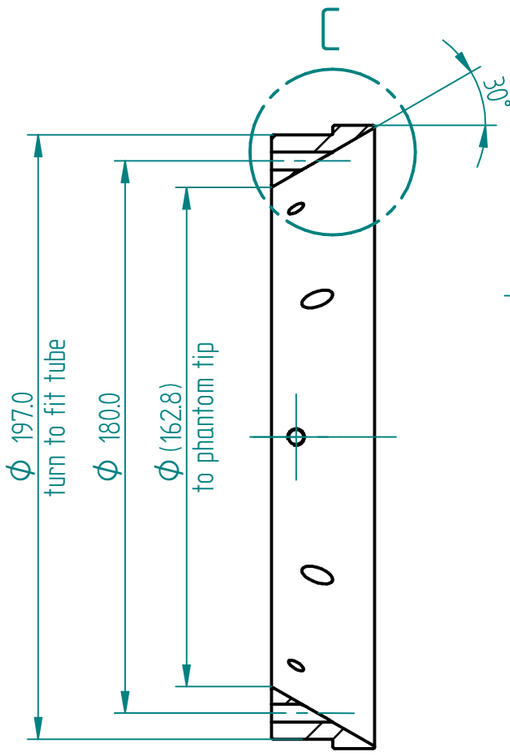

SECTION B-B

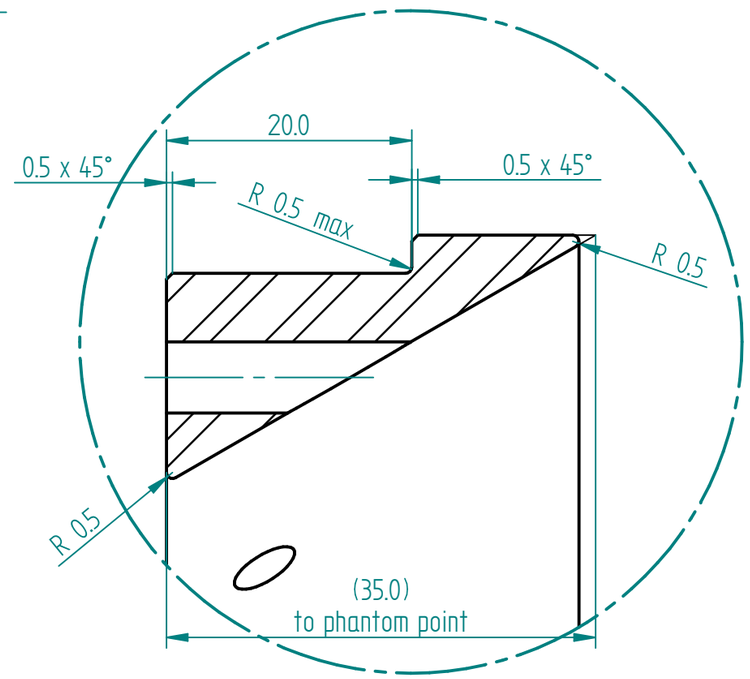

DETAIL C
2:1

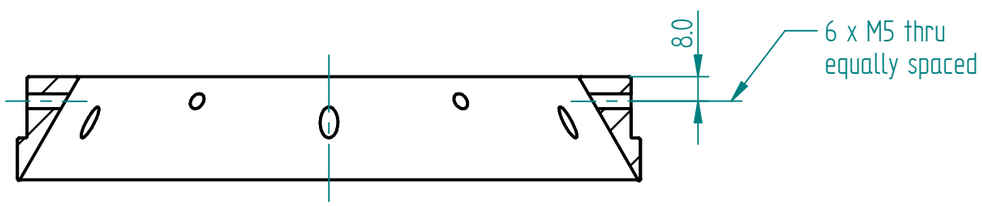

SECTION A-A

Any questions please call me on x58398 or 0418 440 460

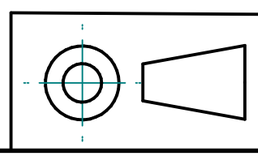

	NAME	DATE
DRAWN	Andrew Ridings	07/07/10
CHECKED		
MGR APPR	Michael Smart	

Material: Steel

FILE NAME: Rear_ring_V5.dft

UNLESS OTHERWISE SPECIFIED
DIMENSIONS ARE IN MILLIMETERS
0 PL ± 0.1; 1 PL ± 0.1; 2 PL ± 0.01
ANGLES ±0.1°

THE UNIVERSITY OF QUEENSLAND
AUSTRALIA
Centre for Hypersonics

TITLE: Rear Adapter Ring

PROJECT: Divergent Scramjet Combustors

SIZE	DWG NO	REV
A3	R-RING-01	02

SCALE: 1 : 2 | WEIGHT: | SHEET 1 OF 1

FILE NAME: fuel_block_front_w_attachment_holes.dft

REVISION HISTORY			
REV	DESCRIPTION	DATE	APPROVED

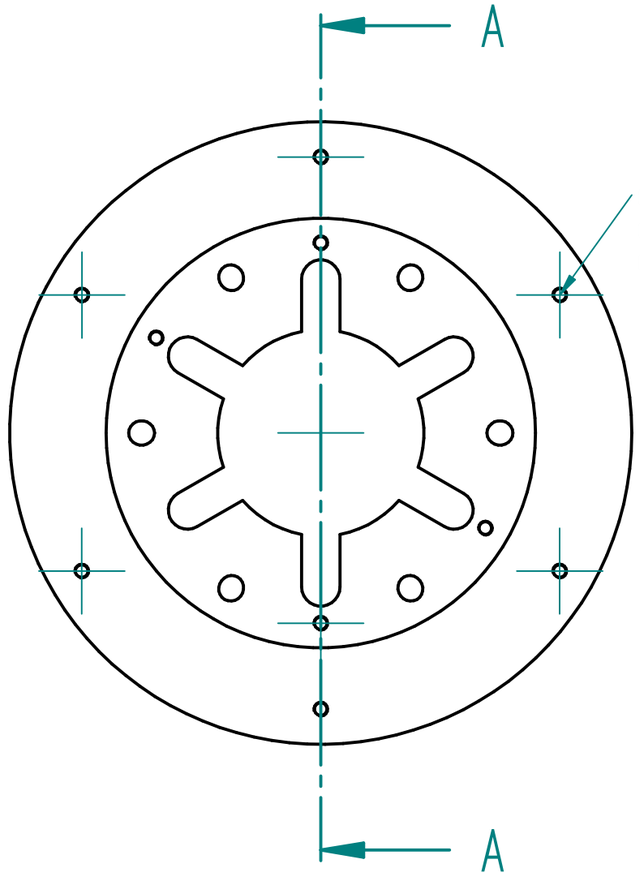

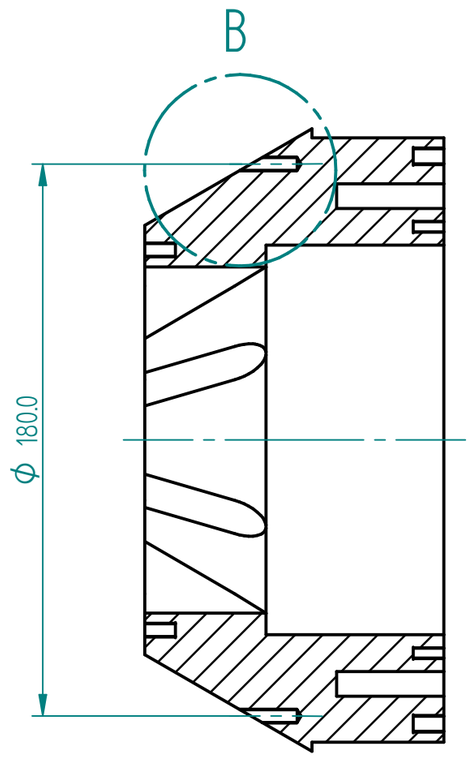

SECTION A-A

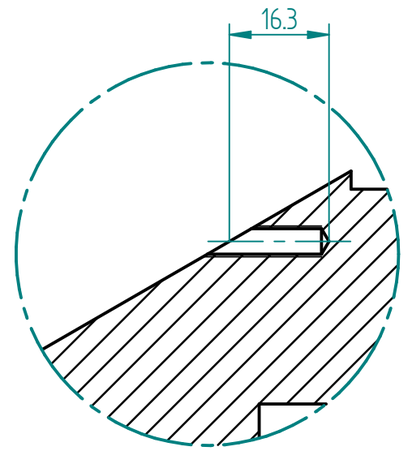

DETAIL B
1:1

Any questions please
call me on x58398
or 0418 440 460

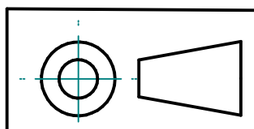

	NAME	DATE
DRAWN	Andrew Ridings	23/02/13
CHECKED		
MGR APPR	Michael Smart	
Material:		

UNLESS OTHERWISE SPECIFIED
DIMENSIONS ARE IN MILLIMETERS
0 PL ± 0.1; 1 PL ± 0.1; 2 PL ± 0.01
ANGLES ±0.1°

THE UNIVERSITY OF QUEENSLAND
AUSTRALIA
Centre for Hypersonics

TITLE: Modifications to Rear Fuel Block

PROJECT: Divergent Scramjet Combustors

SIZE	DWG NO	REV
A3	MOD-RFB	01

SCALE: 1 : 2	WEIGHT:	SHEET 1 OF 1

FILE NAME: fuel_block_front_w_attachment_holes_with_ring.dft

REVISION HISTORY			
REV	DESCRIPTION	DATE	APPROVED

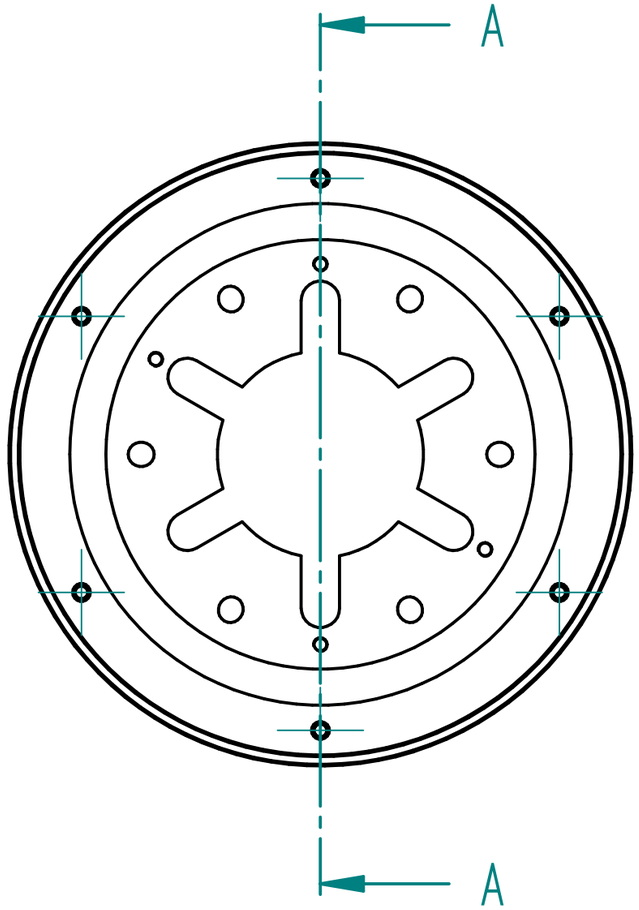

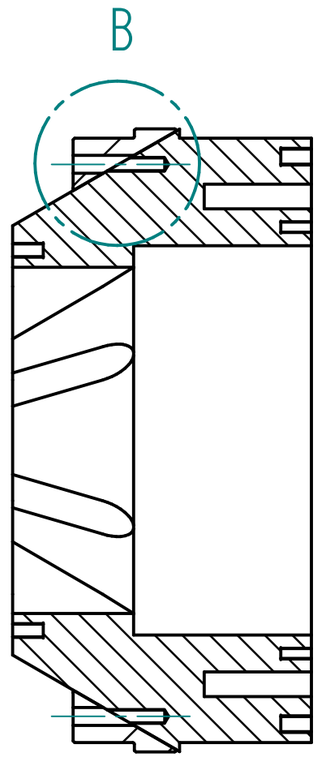

SECTION A-A

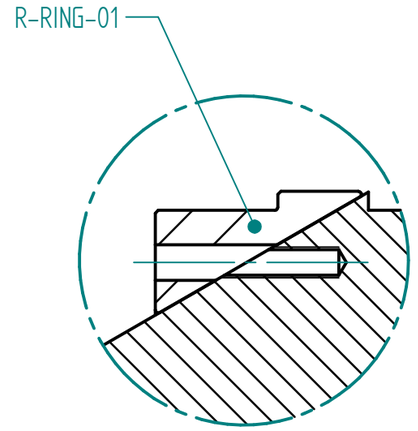

DETAIL B
1:1

Any questions please
call me on x58398
or 0418 440 460

	NAME	DATE
DRAWN	Andrew Ridings	05/07/10
CHECKED		
MGR APPR	Michael Smart	

Material:

UNLESS OTHERWISE SPECIFIED
DIMENSIONS ARE IN MILLIMETERS
0 PL ± 0.1; 1 PL ± 0.1; 2 PL ± 0.01
ANGLES ±0.1°

THE UNIVERSITY OF QUEENSLAND
AUSTRALIA
Centre for Hypersonics

TITLE: Fwd Ring and Fuel Block Assembly

PROJECT: Divergent Scramjet Combustors

SIZE	DWG NO	REV
A3	FR-FB-ASMBLY	01

SCALE: 1 : 2 | WEIGHT: | SHEET 1 OF 1

REVISION HISTORY			
REV	DESCRIPTION	DATE	APPROVED

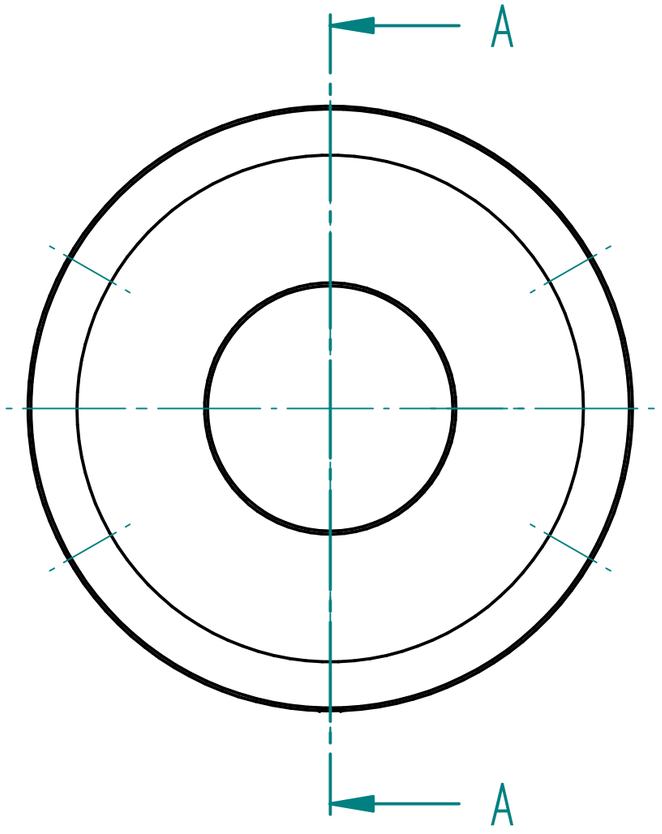

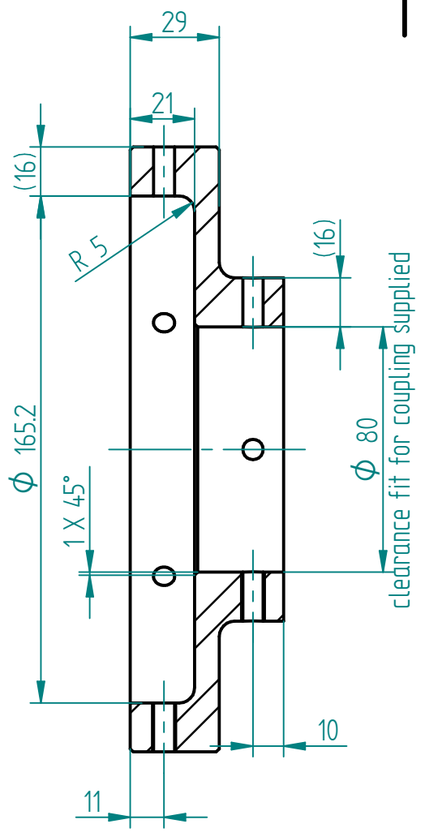

SECTION A-A

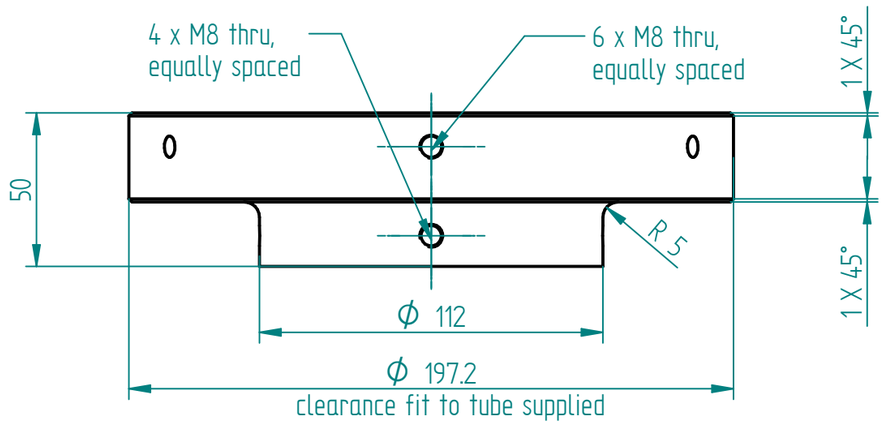

Any questions please call me on x58398 or 0418 440 460

	NAME	DATE
DRAWN	A.Ridings	23/02/13
CHECKED		
MGR APPR	M.Smart	

Material:

FILE NAME: rear_coupling_V4.dft

UNLESS OTHERWISE SPECIFIED
DIMENSIONS ARE IN MILLIMETERS
0 PL ± 0.1; 1 PL ± 0.1; 2 PL ± 0.01
ANGLES ±0.1°

THE UNIVERSITY OF QUEENSLAND
AUSTRALIA
Centre for Hypersonics

TITLE: Rear Aluminium Coupling

PROJECT: Divergent Scramjet Combustors

SIZE	DWG NO	REV
A3	COUPLING-REAR	01

SCALE:	WEIGHT:	SHEET 1 OF 1

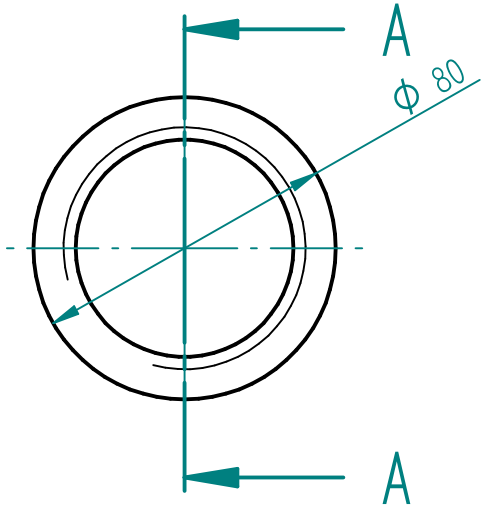

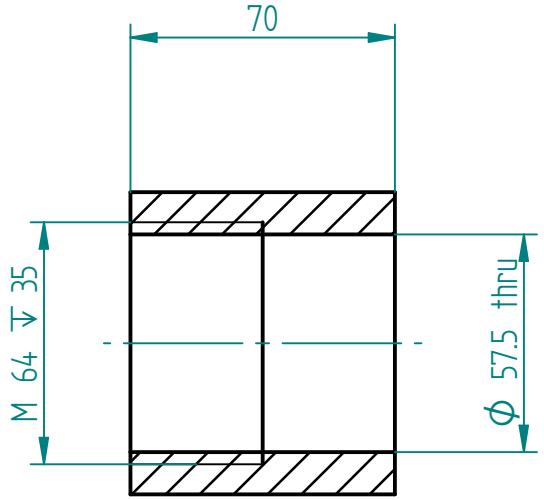

SECTION A-A

Any questions please
call me on x54248
or 0418 440 460

	NAME	DATE
DRAWN	A.Ridings	23/02/13
CHECKED		
ENG APPR	M.Smart	
MGR APPR		

THE UNIVERSITY OF QUEENSLAND
AUSTRALIA

TITLE
Simple Combustor Coupling

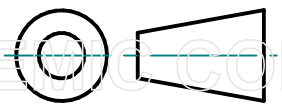

UNLESS OTHERWISE SPECIFIED
DIMENSIONS ARE IN MILLIMETERS
ANGLES ±0.1°
0 PL ± 0.1; 1 PL ± 0.05; 2 PL ± 0.01

SIZE	DWG NO	REV
A4	CC COUPLING	01

FILE NAME: Sting_coupling_simple_small_scale.dft

SCALE: 1:1	WEIGHT:	SHEET 1 OF 1

Material : Mild Steel

REVISION HISTORY			
REV	DESCRIPTION	DATE	APPROVED

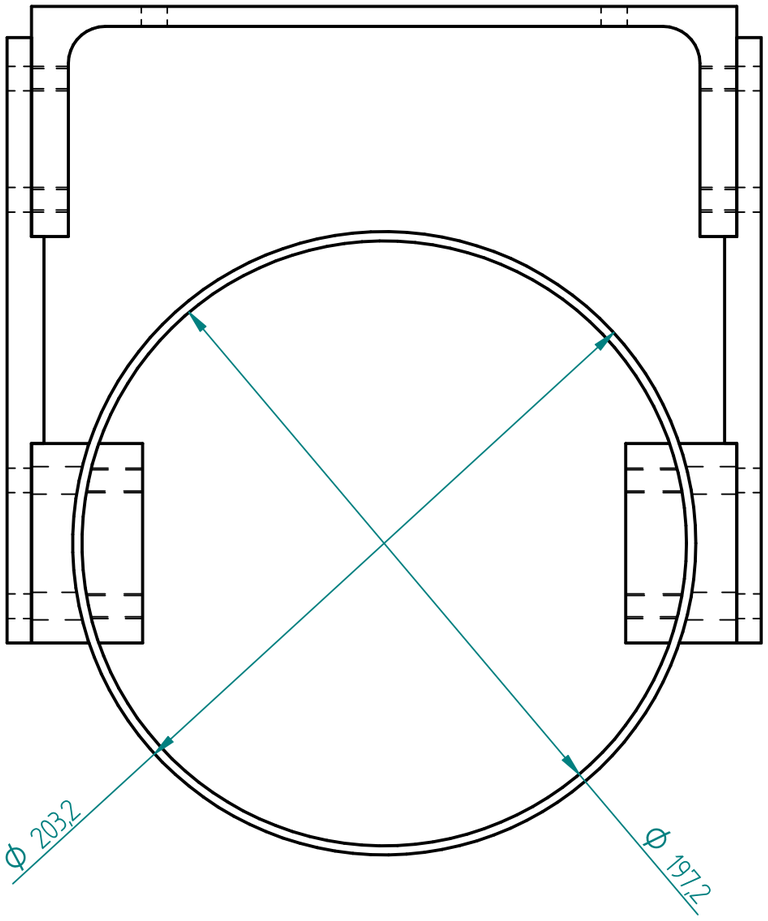

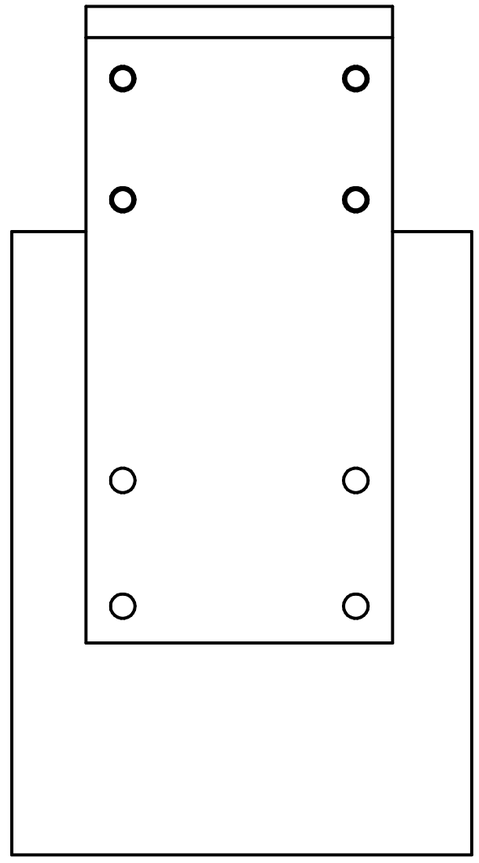

	NAME	DATE
DRAWN	uqaridi1	02/28/11
CHECKED		
ENG APPR		
MGR APPR		

UNLESS OTHERWISE SPECIFIED
DIMENSIONS ARE IN MILLIMETERS
ANGLES ±X.X°
2 PL ±X.XX 3 PL ±X.XXX

SOLID EDGE
UGS - The PLM Company

TITLE

SIZE	DWG NO	REV
A3		

FILE NAME: Support_structure_wide_with_ring.dft

SCALE:	WEIGHT:	SHEET 1 OF 2

REVISION HISTORY			
REV	DESCRIPTION	DATE	APPROVED

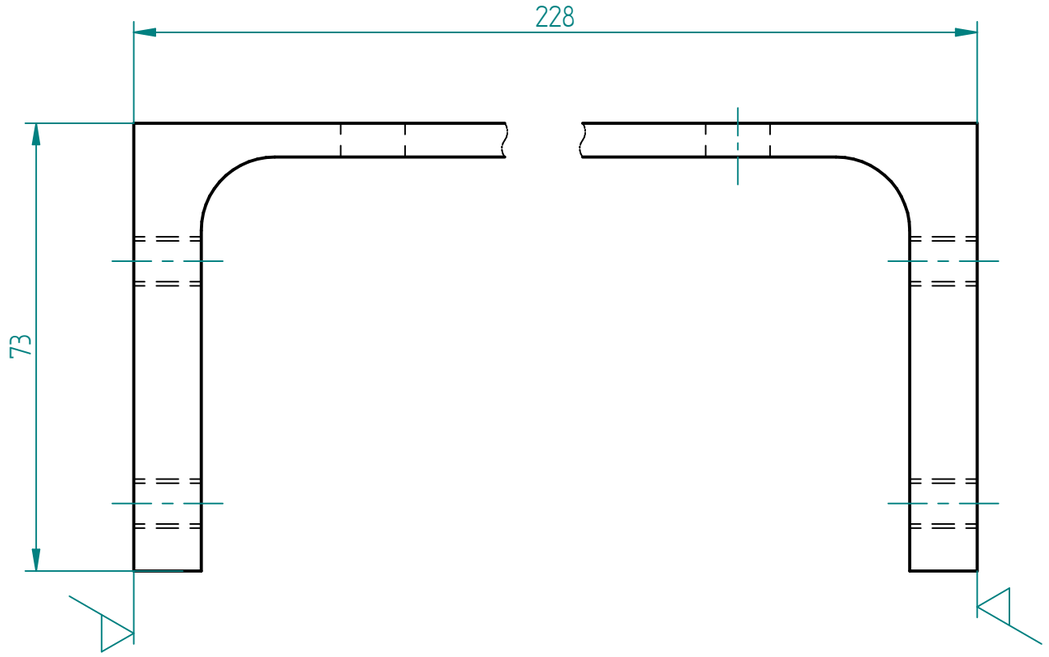

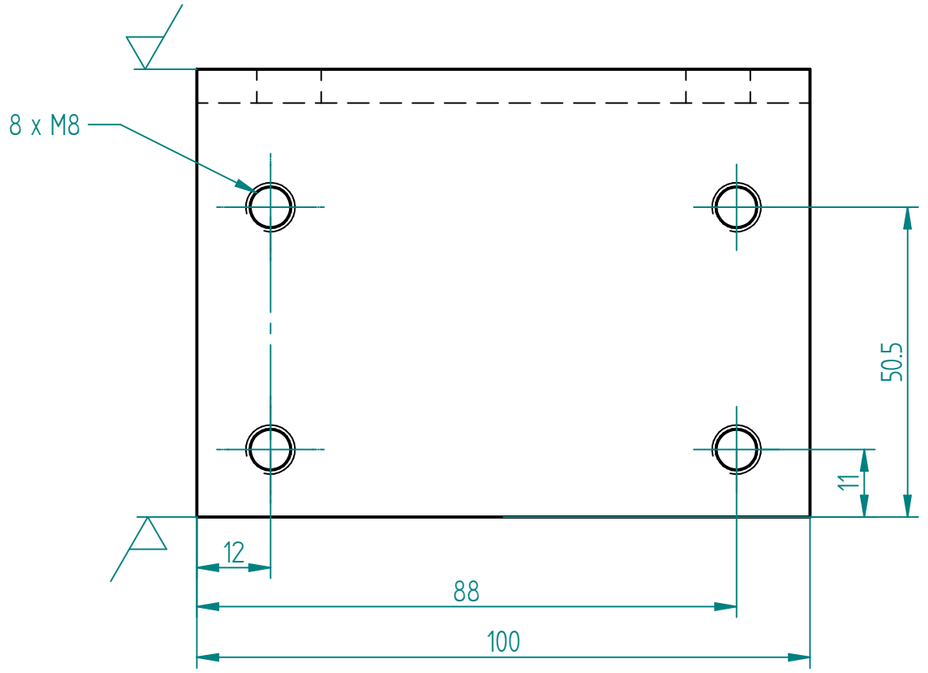

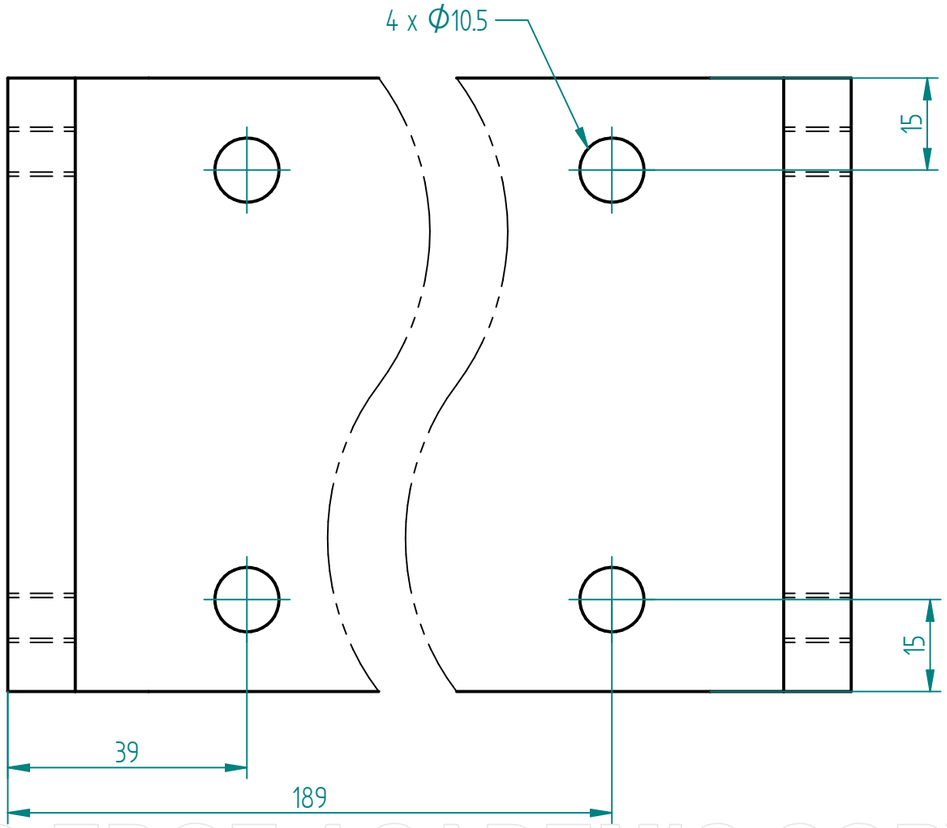

Qty: 1

Any questions please
call me on x54248
or 0418 440 460

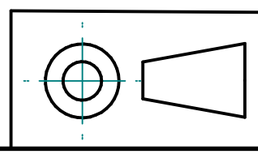

	NAME	DATE
DRAWN	uqaridi1	15/04/11
CHECKED		
MGR APPR	M.Smart	
Material: Mild Steel (Supplied)		
FILE NAME: Top_channel_230PFC_Wide.dft		

UNLESS OTHERWISE SPECIFIED
DIMENSIONS ARE IN MILLIMETERS
0 PL ± 0.1; 1 PL ± 0.1; 2 PL ± 0.01
ANGLES ±0.1°

THE UNIVERSITY OF QUEENSLAND
AUSTRALIA
Centre for Hypersonics

TITLE: Top Channel Support – Wide

PROJECT: Divergent Scramjet Combustors

SIZE	DWG NO	REV
A3	TSC-S	01

SCALE:	WEIGHT:	SHEET 1 OF 1

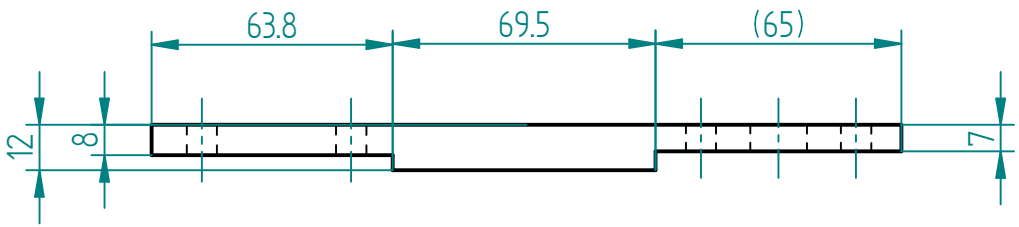

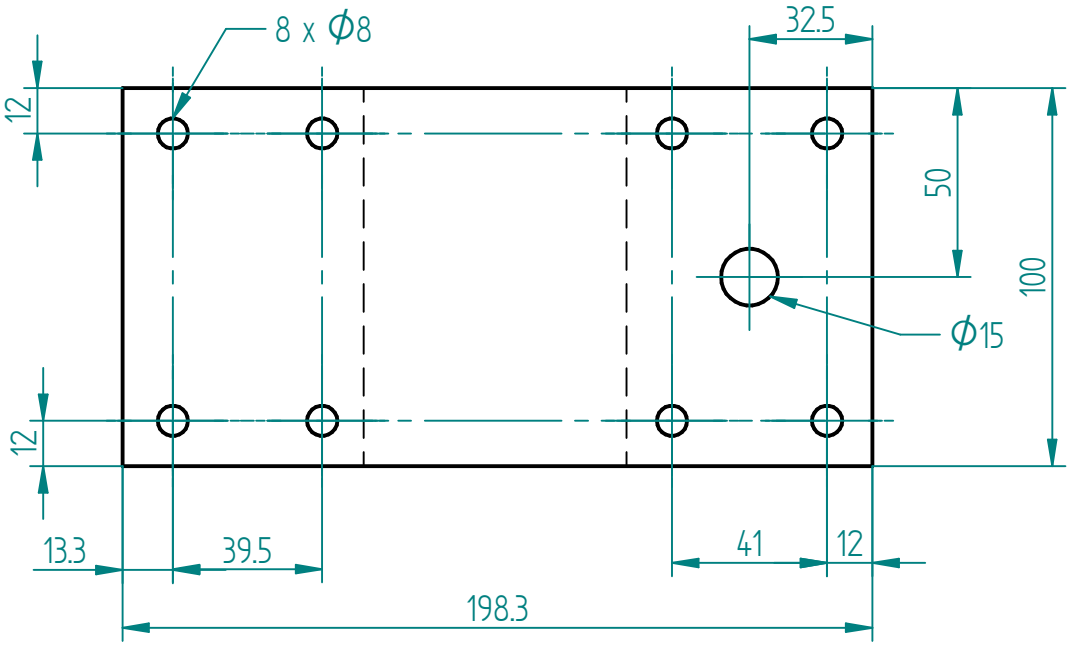

Qty: 2

Any questions please
call me on x54248
or 0418 440 460

	NAME	DATE
DRAWN	A.Ridings	15/04/11
CHECKED		
ENG APPR	M.Smart	
MGR APPR		

THE UNIVERSITY OF QUEENSLAND
AUSTRALIA

TITLE
Strut - Wide

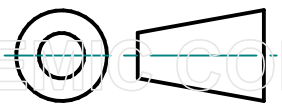

UNLESS OTHERWISE SPECIFIED
DIMENSIONS ARE IN MILLIMETERS
ANGLES ±0.1°
0 PL ± 0.1; 1 PL ± 0.05; 2 PL ± 0.01

SIZE	DWG NO	REV
A4	STRUT-W	01

FILE NAME: Strut_wide.dft

SCALE: 1:1	WEIGHT:	SHEET 1 OF 1

Material : mild steel

Any questions please
call me on
0418 440 460

REVISION HISTORY			
REV	DESCRIPTION	DATE	APPROVED

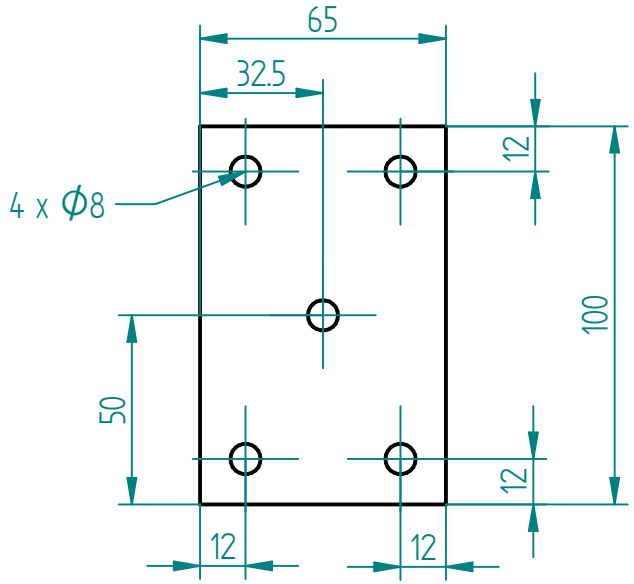

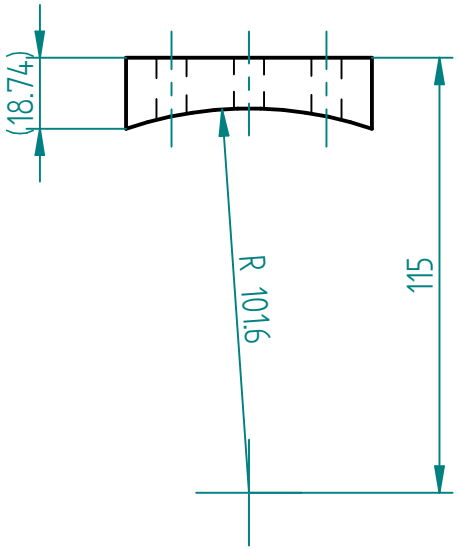

third angle

	NAME	DATE
DRAWN	A. Ridings	02/28/11
CHECKED		
ENG APPR		
MGR APPR		

UNLESS OTHERWISE SPECIFIED
DIMENSIONS ARE IN MILLIMETERS
ANGLES ±X.X°
2 PL ±X.XX 3 PL ±X.XXX

SOLID EDGE
UGS - The PLM Company

TITLE
Outershield Clamps – Outer Piece, Long

SIZE	DWG NO	REV
A4		

FILE NAME: OS_Clamp_outer_piece_long.dft

SCALE:	WEIGHT:	SHEET 1 OF 1

Any questions please
call me on
0418 440 460

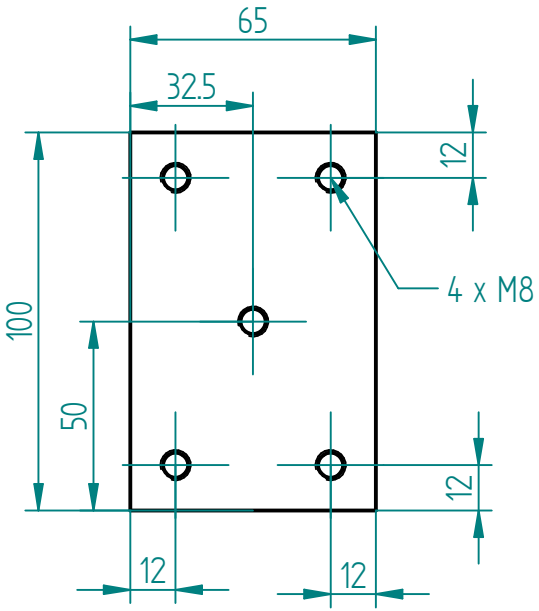

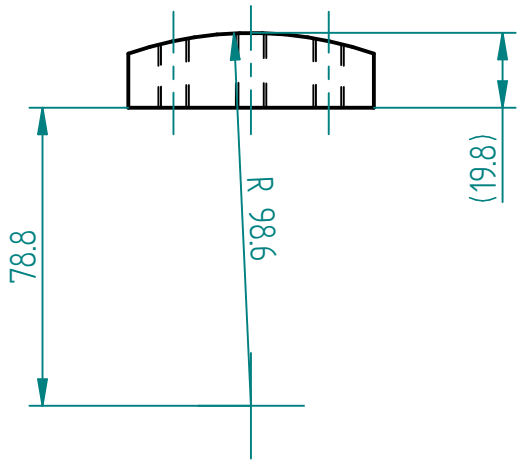

third angle

REVISION HISTORY			
REV	DESCRIPTION	DATE	APPROVED

	NAME	DATE
DRAWN	A. Ridings	02/28/11
CHECKED		
ENG APPR		
MGR APPR		

UNLESS OTHERWISE SPECIFIED
DIMENSIONS ARE IN MILLIMETERS
ANGLES ±X.X°
2 PL ±X.XX 3 PL ±X.XXX

SOLID EDGE
UGS - The PLM Company

TITLE: Outershield Clamp – Inner piece, long

SIZE	DWG NO	REV
A4		

FILE NAME: OS_Clamp_inner_piece_long.dft

SCALE:	WEIGHT:	SHEET 1 OF 1

Table F.1: The tool path for the diffuser. x is the distance from the leading edge and D is the diameter. All dimensions are in millimetres (mm).

x	D	x	D	x	D	x	D	x	D
0.00	43.76	7.04	43.36	42.96	14.10	42.56	21.01	42.16	27.84
0.16	43.75	7.22	43.35	42.95	14.27	42.55	21.20	42.15	28.00
0.34	43.74	7.40	43.34	42.94	14.45	42.54	21.39	42.14	28.15
0.51	43.73	7.57	43.33	42.93	14.63	42.53	21.57	42.13	28.30
0.69	43.72	7.75	43.32	42.92	14.80	42.52	21.76	42.12	28.46
0.87	43.71	7.92	43.31	42.91	14.98	42.51	21.95	42.11	28.61
1.04	43.70	8.10	43.30	42.90	15.16	42.50	22.13	42.10	28.77
1.22	43.69	8.28	43.29	42.89	15.33	42.49	22.31	42.09	28.92
1.40	43.68	8.45	43.28	42.88	15.51	42.48	22.49	42.08	29.07
1.57	43.67	8.63	43.27	42.87	15.69	42.47	22.67	42.07	29.22
1.75	43.66	8.81	43.26	42.86	15.86	42.46	22.85	42.06	29.37
1.93	43.65	8.98	43.25	42.85	16.04	42.45	23.03	42.05	29.52
2.10	43.64	9.16	43.24	42.84	16.21	42.44	23.21	42.04	29.67
2.28	43.63	9.34	43.23	42.83	16.39	42.43	23.38	42.03	29.82
2.46	43.62	9.51	43.22	42.82	16.57	42.42	23.56	42.02	29.97
2.63	43.61	9.69	43.21	42.81	16.74	42.41	23.73	42.01	30.12
2.81	43.60	9.86	43.20	42.80	16.92	42.40	23.90	42.00	30.26
2.98	43.59	10.04	43.19	42.79	17.10	42.39	24.08	41.99	30.41
3.16	43.58	10.22	43.18	42.78	17.28	42.38	24.25	41.98	30.56
3.34	43.57	10.39	43.17	42.77	17.45	42.37	24.42	41.97	30.71
3.51	43.56	10.57	43.16	42.76	17.63	42.36	24.59	41.96	30.85
3.69	43.55	10.75	43.15	42.75	17.80	42.35	24.76	41.95	30.99
3.87	43.54	43.14	10.92	42.74	17.98	42.34	24.93	41.94	31.14
4.04	43.53	43.13	11.10	42.73	18.16	42.33	25.10	41.93	31.28
4.22	43.52	43.12	11.28	42.72	18.33	42.32	25.26	41.92	31.43
4.40	43.51	43.11	11.45	42.71	18.51	42.31	25.43	41.91	31.57
4.57	43.50	43.10	11.63	42.70	18.69	42.30	25.60	41.90	31.71
4.75	43.49	43.09	11.81	42.69	18.86	42.29	25.76	41.89	31.86
4.93	43.48	43.08	11.98	42.68	19.04	42.28	25.92	41.88	32.00
5.10	43.47	43.07	12.16	42.67	19.20	42.27	26.09	41.87	32.14
5.28	43.46	43.06	12.34	42.66	19.34	42.26	26.25	41.86	32.28
5.45	43.45	43.05	12.51	42.65	19.48	42.25	26.41	41.85	32.43
5.63	43.44	43.04	12.69	42.64	19.62	42.24	26.57	41.84	32.57
5.81	43.43	43.03	12.87	42.63	19.76	42.23	26.73	41.83	32.70
5.98	43.42	43.02	13.04	42.62	19.90	42.22	26.89	41.82	32.84
6.16	43.41	43.01	13.22	42.61	20.05	42.21	27.05	41.81	32.98
6.34	43.40	43.00	13.39	42.60	20.24	42.20	27.21	41.80	33.12
6.51	43.39	42.99	13.57	42.59	20.43	42.19	27.37	41.79	33.26
6.69	43.38	42.98	13.75	42.58	20.63	42.18	27.53	41.78	33.40
6.87	43.37	42.97	13.92	42.57	20.82	42.17	27.68	41.77	33.54

Table F.1: continued.

x	D	x	D	x	D	x	D	x	D
41.76	33.68	41.36	38.93	40.96	43.78	40.56	48.36	40.16	52.74
41.75	33.81	41.35	39.05	40.95	43.90	40.55	48.48	40.15	52.85
41.74	33.95	41.34	39.18	40.94	44.02	40.54	48.59	40.14	52.96
41.73	34.09	41.33	39.30	40.93	44.14	40.53	48.70	40.13	53.06
41.72	34.22	41.32	39.43	40.92	44.25	40.52	48.81	40.12	53.17
41.71	34.36	41.31	39.55	40.91	44.37	40.51	48.92	40.11	53.28
41.70	34.49	41.30	39.68	40.90	44.49	40.50	49.03	40.10	53.38
41.69	34.63	41.29	39.80	40.89	44.60	40.49	49.14	40.09	53.49
41.68	34.76	41.28	39.93	40.88	44.72	40.48	49.25	40.08	53.60
41.67	34.90	41.27	40.05	40.87	44.84	40.47	49.36	40.07	53.70
41.66	35.03	41.26	40.17	40.86	44.95	40.46	49.47	40.06	53.81
41.65	35.17	41.25	40.30	40.85	45.07	40.45	49.59	40.05	53.92
41.64	35.30	41.24	40.42	40.84	45.18	40.44	49.70	40.04	54.02
41.63	35.43	41.23	40.54	40.83	45.30	40.43	49.81	40.03	54.13
41.62	35.57	41.22	40.66	40.82	45.41	40.42	49.92	40.02	54.23
41.61	35.70	41.21	40.79	40.81	45.53	40.41	50.03	40.01	54.34
41.60	35.83	41.20	40.91	40.80	45.65	40.40	50.14	40.00	54.45
41.59	35.96	41.19	41.03	40.79	45.76	40.39	50.25	39.99	54.55
41.58	36.10	41.18	41.15	40.78	45.87	40.38	50.35	39.98	54.66
41.57	36.23	41.17	41.27	40.77	45.99	40.37	50.46	39.97	54.76
41.56	36.36	41.16	41.39	40.76	46.10	40.36	50.57	39.96	54.87
41.55	36.49	41.15	41.52	40.75	46.22	40.35	50.68	39.95	54.97
41.54	36.62	41.14	41.64	40.74	46.33	40.34	50.79	39.94	55.08
41.53	36.75	41.13	41.76	40.73	46.45	40.33	50.90	39.93	55.18
41.52	36.88	41.12	41.88	40.72	46.56	40.32	51.01	39.92	55.29
41.51	37.01	41.11	42.00	40.71	46.67	40.31	51.12	39.91	55.39
41.50	37.14	41.10	42.12	40.70	46.79	40.30	51.23	39.90	55.50
41.49	37.27	41.09	42.24	40.69	46.90	40.29	51.34	39.89	55.61
41.48	37.40	41.08	42.36	40.68	47.01	40.28	51.45	39.88	55.71
41.47	37.53	41.07	42.48	40.67	47.13	40.27	51.55	39.87	55.82
41.46	37.65	41.06	42.60	40.66	47.24	40.26	51.66	39.86	55.92
41.45	37.78	41.05	42.72	40.65	47.35	40.25	51.77	39.85	56.03
41.44	37.91	41.04	42.84	40.64	47.47	40.24	51.88	39.84	56.13
41.43	38.04	41.03	42.96	40.63	47.58	40.23	51.99	39.83	56.23
41.42	38.17	41.02	43.07	40.62	47.69	40.22	52.10	39.82	56.34
41.41	38.29	41.01	43.19	40.61	47.80	40.21	52.20	39.81	56.44
41.40	38.42	41.00	43.31	40.60	47.92	40.20	52.31	39.80	56.55
41.39	38.55	40.99	43.43	40.59	48.03	40.19	52.42	39.79	56.65
41.38	38.67	40.98	43.55	40.58	48.14	40.18	52.53	39.78	56.76
41.37	38.80	40.97	43.67	40.57	48.25	40.17	52.63	39.77	56.86

Table F.1: continued.

x	D	x	D	x	D	x	D	x	D
39.76	56.96	39.36	61.07	38.96	65.10	38.56	69.07	38.16	72.99
39.75	57.07	39.35	61.18	38.95	65.20	38.55	69.16	38.15	73.09
39.74	57.17	39.34	61.28	38.94	65.30	38.54	69.26	38.14	73.19
39.73	57.28	39.33	61.38	38.93	65.40	38.53	69.36	38.13	73.29
39.72	57.38	39.32	61.48	38.92	65.50	38.52	69.46	38.12	73.38
39.71	57.48	39.31	61.58	38.91	65.60	38.51	69.56	38.11	73.48
39.70	57.59	39.30	61.68	38.90	65.70	38.50	69.66	38.10	73.58
39.69	57.69	39.29	61.78	38.89	65.80	38.49	69.75	38.09	73.68
39.68	57.79	39.28	61.89	38.88	65.90	38.48	69.85	38.08	73.78
39.67	57.90	39.27	61.99	38.87	66.00	38.47	69.95	38.07	73.87
39.66	58.00	39.26	62.09	38.86	66.10	38.46	70.05	38.06	73.97
39.65	58.11	39.25	62.19	38.85	66.19	38.45	70.15	38.05	74.07
39.64	58.21	39.24	62.29	38.84	66.29	38.44	70.25	38.04	74.17
39.63	58.31	39.23	62.39	38.83	66.39	38.43	70.34	38.03	74.26
39.62	58.41	39.22	62.49	38.82	66.49	38.42	70.44	38.02	74.36
39.61	58.52	39.21	62.59	38.81	66.59	38.41	70.54	38.01	74.46
39.60	58.62	39.20	62.69	38.80	66.69	38.40	70.64	38.00	74.56
39.59	58.72	39.19	62.79	38.79	66.79	38.39	70.74	37.99	74.66
39.58	58.83	39.18	62.89	38.78	66.89	38.38	70.84	37.98	74.75
39.57	58.93	39.17	62.99	38.77	66.99	38.37	70.93	37.97	74.85
39.56	59.03	39.16	63.10	38.76	67.09	38.36	71.03	37.96	74.95
39.55	59.13	39.15	63.20	38.75	67.19	38.35	71.13	37.95	75.05
39.54	59.24	39.14	63.30	38.74	67.29	38.34	71.23	37.94	75.15
39.53	59.34	39.13	63.40	38.73	67.39	38.33	71.33	37.93	75.24
39.52	59.44	39.12	63.50	38.72	67.48	38.32	71.43	37.92	75.34
39.51	59.54	39.11	63.60	38.71	67.58	38.31	71.52	37.91	75.44
39.50	59.65	39.10	63.70	38.70	67.68	38.30	71.62	37.90	75.54
39.49	59.75	39.09	63.80	38.69	67.78	38.29	71.72	37.89	75.63
39.48	59.85	39.08	63.90	38.68	67.88	38.28	71.82	37.88	75.73
39.47	59.95	39.07	64.00	38.67	67.98	38.27	71.92	37.87	75.83
39.46	60.06	39.06	64.10	38.66	68.08	38.26	72.01	37.86	75.93
39.45	60.16	39.05	64.20	38.65	68.18	38.25	72.11	37.85	76.03
39.44	60.26	39.04	64.30	38.64	68.28	38.24	72.21	37.84	76.12
39.43	60.36	39.03	64.40	38.63	68.37	38.23	72.31	37.83	76.22
39.42	60.46	39.02	64.50	38.62	68.47	38.22	72.41	37.82	76.32
39.41	60.57	39.01	64.60	38.61	68.57	38.21	72.50	37.81	76.42
39.40	60.67	39.00	64.70	38.60	68.67	38.20	72.60	37.80	76.51
39.39	60.77	38.99	64.80	38.59	68.77	38.19	72.70	37.79	76.61
39.38	60.87	38.98	64.90	38.58	68.87	38.18	72.80	37.78	76.71
39.37	60.97	38.97	65.00	38.57	68.97	38.17	72.89	37.77	76.81

Table F.1: continued.

x	D	x	D	x	D	x	D	x	D
37.76	76.90	37.36	80.81	36.96	84.75	36.56	88.72	36.16	92.75
37.75	77.00	37.35	80.91	36.95	84.84	36.55	88.82	36.15	92.85
37.74	77.10	37.34	81.01	36.94	84.94	36.54	88.92	36.14	92.95
37.73	77.20	37.33	81.11	36.93	85.04	36.53	89.02	36.13	93.06
37.72	77.29	37.32	81.21	36.92	85.14	36.52	89.12	36.12	93.16
37.71	77.39	37.31	81.30	36.91	85.24	36.51	89.22	36.11	93.26
37.70	77.49	37.30	81.40	36.90	85.34	36.50	89.32	36.10	93.36
37.69	77.59	37.29	81.50	36.89	85.44	36.49	89.42	36.09	93.47
37.68	77.69	37.28	81.60	36.88	85.54	36.48	89.52	36.08	93.57
37.67	77.78	37.27	81.70	36.87	85.64	36.47	89.62	36.07	93.67
37.66	77.88	37.26	81.79	36.86	85.73	36.46	89.72	36.06	93.77
37.65	77.98	37.25	81.89	36.85	85.83	36.45	89.82	36.05	93.87
37.64	78.08	37.24	81.99	36.84	85.93	36.44	89.92	36.04	93.98
37.63	78.17	37.23	82.09	36.83	86.03	36.43	90.02	36.03	94.08
37.62	78.27	37.22	82.21	36.82	86.13	36.42	90.12	36.02	94.18
37.61	78.37	37.21	82.30	36.81	86.23	36.41	90.22	36.01	94.28
37.60	78.47	37.20	82.39	36.80	86.33	36.40	90.32	36.00	94.39
37.59	78.57	37.19	82.48	36.79	86.43	36.39	90.42	35.99	94.49
37.58	78.66	37.18	82.58	36.78	86.53	36.38	90.52	35.98	94.59
37.57	78.76	37.17	82.68	36.77	86.63	36.37	90.63	35.97	94.70
37.56	78.86	37.16	82.78	36.76	86.73	36.36	90.73	35.96	94.80
37.55	78.96	37.15	82.88	36.75	86.83	36.35	90.83	35.95	94.90
37.54	79.05	37.14	82.97	36.74	86.92	36.34	90.93	35.94	95.01
37.53	79.15	37.13	83.07	36.73	87.02	36.33	91.03	35.93	95.11
37.52	79.25	37.12	83.17	36.72	87.12	36.32	91.13	35.92	95.21
37.51	79.35	37.11	83.27	36.71	87.22	36.31	91.23	35.91	95.31
37.50	79.45	37.10	83.37	36.70	87.32	36.30	91.33	35.90	95.42
37.49	79.54	37.09	83.47	36.69	87.42	36.29	91.43	35.89	95.52
37.48	79.64	37.08	83.56	36.68	87.52	36.28	91.53	35.88	95.63
37.47	79.74	37.07	83.66	36.67	87.62	36.27	91.63	35.87	95.73
37.46	79.84	37.06	83.76	36.66	87.72	36.26	91.74	35.86	95.83
37.45	79.93	37.05	83.86	36.65	87.82	36.25	91.84	35.85	95.94
37.44	80.03	37.04	83.96	36.64	87.92	36.24	91.94	35.84	96.04
37.43	80.13	37.03	84.06	36.63	88.02	36.23	92.04	35.83	96.14
37.42	80.23	37.02	84.15	36.62	88.12	36.22	92.14	35.82	96.25
37.41	80.33	37.01	84.25	36.61	88.22	36.21	92.24	35.81	96.35
37.40	80.42	37.00	84.35	36.60	88.32	36.20	92.34	35.80	96.45
37.39	80.52	36.99	84.45	36.59	88.42	36.19	92.45	35.79	96.56
37.38	80.62	36.98	84.55	36.58	88.52	36.18	92.55	35.78	96.66
37.37	80.72	36.97	84.65	36.57	88.62	36.17	92.65	35.77	96.77

Table F.1: continued.

x	D	x	D	x	D	x	D	x	D
35.76	96.87	35.36	101.11	34.96	105.51	34.56	110.11	34.16	115.01
35.75	96.98	35.35	101.22	34.95	105.62	34.55	110.23	34.15	115.14
35.74	97.08	35.34	101.33	34.94	105.73	34.54	110.35	34.14	115.26
35.73	97.19	35.33	101.43	34.93	105.84	34.53	110.47	34.13	115.39
35.72	97.29	35.32	101.54	34.92	105.96	34.52	110.59	34.12	115.52
35.71	97.39	35.31	101.65	34.91	106.07	34.51	110.71	34.11	115.65
35.70	97.50	35.30	101.76	34.90	106.18	34.50	110.83	34.10	115.77
35.69	97.60	35.29	101.87	34.89	106.30	34.49	110.95	34.09	115.90
35.68	97.71	35.28	101.98	34.88	106.41	34.48	111.07	34.08	116.03
35.67	97.81	35.27	102.08	34.87	106.52	34.47	111.19	34.07	116.16
35.66	97.92	35.26	102.19	34.86	106.64	34.46	111.31	34.06	116.29
35.65	98.02	35.25	102.30	34.85	106.75	34.45	111.43	34.05	116.42
35.64	98.13	35.24	102.41	34.84	106.86	34.44	111.55	34.04	116.55
35.63	98.23	35.23	102.52	34.83	106.98	34.43	111.67	34.03	116.68
35.62	98.34	35.22	102.63	34.82	107.09	34.42	111.79	34.02	116.81
35.61	98.44	35.21	102.74	34.81	107.21	34.41	111.91	34.01	116.94
35.60	98.55	35.20	102.85	34.80	107.32	34.40	112.03	34.00	117.07
35.59	98.66	35.19	102.96	34.79	107.44	34.39	112.15	33.99	117.20
35.58	98.76	35.18	103.07	34.78	107.55	34.38	112.27	33.98	117.33
35.57	98.87	35.17	103.18	34.77	107.66	34.37	112.40	33.97	117.47
35.56	98.97	35.16	103.29	34.76	107.78	34.36	112.52	33.96	117.60
35.55	99.08	35.15	103.40	34.75	107.89	34.35	112.64	33.95	117.73
35.54	99.19	35.14	103.51	34.74	108.01	34.34	112.76	33.94	117.86
35.53	99.29	35.13	103.62	34.73	108.13	34.33	112.89	33.93	118.00
35.52	99.40	35.12	103.73	34.72	108.24	34.32	113.01	33.92	118.13
35.51	99.50	35.11	103.84	34.71	108.36	34.31	113.13	33.91	118.26
35.50	99.61	35.10	103.95	34.70	108.47	34.30	113.26	33.90	118.40
35.49	99.72	35.09	104.06	34.69	108.59	34.29	113.38	33.89	118.53
35.48	99.82	35.08	104.17	34.68	108.70	34.28	113.50	33.88	118.67
35.47	99.93	35.07	104.28	34.67	108.82	34.27	113.63	33.87	118.80
35.46	100.04	35.06	104.39	34.66	108.94	34.26	113.75	33.86	118.94
35.45	100.14	35.05	104.50	34.65	109.06	34.25	113.88	33.85	119.07
35.44	100.25	35.04	104.61	34.64	109.17	34.24	114.00	33.84	119.21
35.43	100.36	35.03	104.72	34.63	109.29	34.23	114.13	33.83	119.34
35.42	100.47	35.02	104.83	34.62	109.41	34.22	114.25	33.82	119.48
35.41	100.57	35.01	104.95	34.61	109.52	34.21	114.38	33.81	119.62
35.40	100.68	35.00	105.06	34.60	109.64	34.20	114.50	33.80	119.76
35.39	100.79	34.99	105.17	34.59	109.76	34.19	114.63	33.79	119.89
35.38	100.90	34.98	105.28	34.58	109.88	34.18	114.76	33.78	120.03
35.37	101.00	34.97	105.39	34.57	110.00	34.17	114.88	33.77	120.17

Table F.1: continued.

x	D	x	D	x	D	x	D	x	D
33.76	120.31	33.47	124.52	33.18	129.54	32.89	137.34	33.00	157.51
33.75	120.45	33.46	124.67	33.17	129.75	32.88	137.72	33.01	158.27
33.74	120.59	33.45	124.83	33.16	129.96	32.87	138.14	33.02	159.03
33.73	120.73	33.44	124.98	33.15	130.17	32.86	138.62	33.03	159.80
33.72	120.87	33.43	125.14	33.14	130.39	32.85	139.05	33.04	160.55
33.71	121.01	33.42	125.29	33.13	130.61	32.84	139.55	33.05	161.32
33.70	121.15	33.41	125.45	33.12	130.84	32.83	140.10	33.06	162.07
33.69	121.29	33.40	125.60	33.11	131.06	32.82	140.70	33.07	162.83
33.68	121.44	33.39	125.76	33.10	131.29	32.81	141.42	33.08	163.59
33.67	121.58	33.38	125.91	33.09	131.52	32.80	142.40	33.09	164.35
33.66	121.72	33.37	126.07	33.08	131.76	32.81	143.07	33.10	165.11
33.65	121.86	33.36	126.23	33.07	132.00	32.82	143.83	33.11	165.87
33.64	122.01	33.35	126.39	33.06	132.25	32.83	144.60	33.12	166.63
33.63	122.15	33.34	126.55	33.05	132.50	32.84	145.35	33.13	167.39
33.62	122.30	33.33	126.71	33.04	132.75	32.85	146.11	33.14	168.15
33.61	122.44	33.32	126.87	33.03	133.01	32.86	146.87	33.15	168.92
33.60	122.59	33.31	127.03	33.02	133.27	32.87	147.62	33.16	169.67
33.59	122.73	33.30	127.19	33.01	133.54	32.88	148.38	33.17	170.43
33.58	122.88	33.29	127.36	33.00	133.81	32.89	149.15	33.18	171.19
33.57	123.03	33.28	127.55	32.99	134.09	32.90	149.91	33.19	171.95
33.56	123.17	33.27	127.74	32.98	134.37	32.91	150.67	33.20	172.71
33.55	123.32	33.26	127.93	32.97	134.67	32.92	151.42		
33.54	123.47	33.25	128.12	32.96	134.96	32.93	152.19		
33.53	123.62	33.24	128.32	32.95	135.27	32.94	152.95		
33.52	123.77	33.23	128.51	32.94	135.59	32.95	153.71		
33.51	123.92	33.22	128.72	32.93	135.91	32.96	154.48		
33.50	124.07	33.21	128.92	32.92	136.25	32.97	155.23		
33.49	124.22	33.20	129.12	32.91	136.59	32.98	155.99		
33.48	124.37	33.19	129.33	32.90	136.95	32.99	156.75		